A Study of the Spectroscopy and Collision Dynamics of SiX (X=F,Cl) Radicals

Cameron William Watson

A thesis presented for the degree of
Doctor of Philosophy in the
Faculty of Science at the
University of Edinburgh
1995

Declaration

I declare that this thesis has been composed by me and that the work described in it is my own, except where due acknowledgement is made, and was carried out whilst a member of the laser group at the University of Edinburgh.

Signed:

Date: 16/5/95

" As I always say
'We skipped the light fandango,
Turned cartwheels across the floor,
I was feeling kind of seasick,
But the crowd called out for more.' "
"That's very profound Jimmy, what exactly does it mean?"
"I'm fucked if I know Terry!"

From the film 'The Commitments'.

To Mum and Dad,
thanks for everything

Acknowledgements

I would firstly like to extend my thanks and appreciation to my supervisor Dr Kenneth G. McKendrick for his seemingly endless stream of ideas and plausible explanations. Without you this thesis would have been half as long and at least half as good. We'll always have Naples! I would also like to thank Dr Kenneth P. Lawley for helpful discussions concerning this work. Professor Donovan is also deserving of thanks for the loan of the monochromator used in these studies and for his support and encouragement.

The Science and Engineering Council are duly acknowledged for the provision of a Research grant.

A number of my colleagues deserve recognition for their efforts in assisting me with my studies. Particularly worthy of my gratitude is Dr Graeme Maitland who not only assisted me when I got into difficulty while programming but adapted the existing data acquisition software specifically for the needs of the experiments I was to perform. Thanks also to Neil Jackson who patiently read the first draft of this thesis and spotted a huge catalogue of grammatical and spelling mistakes prior to Ken's red pen treatment. Dr Philip Wilson was of great assistance in discussing the nature of the RKR and Franck-Condon computer programs and hence saved me significant programming time. Andrea Chow assisted me with the work concerning the ΔJ propensities described in chapter 5.

I would also like to acknowledge members of the technical staff for their assistance and good humour throughout my time as a postgraduate student. In particular Stuart Mains for a neverending torrent of anecdotes and football cliches. Derek Burgess and Harry McKenzie also deserve a special mention.

The most enjoyable challenge during the course of my PhD was as a member of the Chemical Society Football team. I would like to extend my thanks to all my team mates both past and present, particularly for letting me play up front.

My residency in that hive of activity and industry, otherwise known as Room 6, was made so much more worthwhile by the friendship shown to me by the other inmates over the last three and a half years. In roughly chronological order; Kev, Jim, Jenny, Charlie, Graeme, Ally, Jonny, Mike, Craig, Bob, Gillian, Bin-Bing, Scott, Neil and Colin - thank you.

Finally, and most importantly, I would like to thank Shona for unofficially supporting me over the final six months of my PhD while I was unemployed, writing up and looking for a *real* job. Your patience and understanding is much appreciated.

Abstract

This thesis concerns the study of state-specific collision-induced energy transfer processes between the SiF $C^2\Delta$ and $B^2\Sigma^+$ and the analogous SiCl $B'^2\Delta$ and $B^2\Sigma^+$ states.

Laser excitation spectra established the wavelengths at which the SiF $B^2\Sigma^+(v' = 0, 1, 2, 4$ and $5)$ and $C^2\Delta(v' = 0, 1)$ levels could be populated selectively. The vibrational transition probabilities of the C - X and B - X systems were measured by observations of the resultant dispersed fluoresence. Comparison with the calculated Franck-Condon factors allowed an assessment of the behaviour of the transition dipole moment functions. The B - X transition moment was essentially invariant with internuclear separation. In contrast, the C - X transition moment was found to be strongly decreasing with increasing internuclear separation. These observations were justified on the basis of simple linear combination of atomic orbitals arguments. The radiative lifetimes of the C and B states were shown to be 94 ± 2 ns and $\leq$ 10 ns respectively by time resolved measurements of the C - X and B - X decays.

Total quenching cross sections for removal of the SiF C (v'=0,1) state were found to be large for the molecular quenchers H_2, N_2, CH_4 and CO_2, although no quenching was observed for Ar and He. A small but quencher dependent fraction of the removed C state molecules was transferred to the $B^2\Sigma^+$ state except for CO_2 as a quencher. The product B state vibrational populations were shown to correlate well with the Franck-Condon overlap between the initial and product vibronic states. The study of the isoelectronic SiCl transfer system produced results in good agreement with, but of improved precision to those of previous studies. The B′ state quenching was efficient for all collision partners with cross sections shown to correlate with long range attractive forces between the collision pair. A large but quencher dependent fraction of the quenched B′ molecules was transferred to the $B^2\Sigma^+$ state. The product state vibrational populations were also highly quencher dependent and the trends could not be attributed to any obvious molecular property.

Laser excitation of specific rotational levels of the SiF C, v′=0 state allowed

an investigation into the J dependence of the total quenching and transfer rates and the product state vibrational populations. None of these aspects exhibited a clear rotational dependence. Higher resolution studies of the collisionally induced B - X fluorescence revealed a surprising propensity for large changes in J upon C - B transfer.

An attempt was made to rationalize the collisional transfer behaviour of both SiF and SiCl in terms of the electronic character of the states involved. It is proposed that the dramatic contrasts between the two systems are related to the detailed differences in the relative arrangements of the potential curves.

Table of Contents

1. Introduction **1**

1.1 Experimental Observations of CIEET 4

1.1.1 Indirect Observations of CIEET 4

1.1.2 Direct Observations of CIEET at the Vibronic Level 7

1.1.3 Direct Observations of CIEET at the Rovibronic Level . . . 16

1.2 Theoretical Investigations 25

1.2.1 Long Range Attractive Intermolecular Interaction 25

1.2.2 Curve Crossing 28

1.2.3 Short Range Repulsive Interaction 30

1.2.4 State Specific Energy transfer 31

1.3 Overview 35

1.4 Proposed Work 36

2. Experimental Apparatus **43**

2.1 Introduction 43

2.2 Laser Systems 43

2.2.1 Nd:YAG Lasers 44

2.2.2 Dye Laser Systems 45

2.2.3 Wavelength Extender Systems 46

2.3 Gas Handling and Radical Production 48

2.3.1 Vacuum Line 48

2.3.2 Flow Control 49

2.3.3 Discharge Flow System 49

2.3.4 Microwave Discharge 52

2.4 Fluorescence Capture and Detection 53

2.4.1 Fluorescence Capture and Wavelength Dispersion 53

2.4.2 Calibration for Spectral Response 56

2.5 Data Acquisition and Experimental Control 57

2.5.1 CAMAC Instrumentation 57

2.5.2 IBM PC-AT Microcomputer 57

2.5.3 Pulse Delay Generator 59

2.5.4 Transient Digitiser 59

2.5.5 Dye Laser Scanning Control 61

3. Spectroscopy of the SiF $B^2\Sigma^+ - X^2\Pi$ and $C^2\Delta - X^2\Pi$ Systems 64

3.1 Introduction 64

3.2 Previous Spectroscopic Observations of the SiF Radical 65

3.3 Interatomic Potentials and Principal Molecular Constants 66

3.4 Diatomic Energy Level Structure 68

3.4.1 Hund's Coupling Case (a) 69

3.4.2 Hund's Coupling Case (b) 70

3.4.3 Λ -type Doubling 72

3.4.4 Transition From Case(a) to Case (b) 72

3.5 Selection Rules and Transition Probabilities 76

3.5.1 Selection Rules for a Rovibronic Transition 76

3.5.2 Vibronic Transition Probabilities 77

3.6 Laser-Induced Fluorescence Excitation Spectra 81

3.6.1 Experimental Method 81

3.6.2 LIF Excitation Spectra of the $B^2\Sigma^+(v' = 0,1,2 \text{ and } 5) - X^2\Pi(v'' = 0)$ Transitions 83

3.6.3 LIF Excitation Spectra of the $C^2\Delta(v' = 0,1) - X^2\Pi(v'' = 0)$ Transitions 84

3.6.4 The $C^2\Delta$ Spin-Orbit Splitting Constant, A. 84

3.7 Dispersed Fluorescence Spectra 91

3.7.1 Experimental Method 91

3.7.2 $B^2\Sigma^+(v' = 0,1,2,(3),4 \text{ and } 5)$ - $X^2\Pi_{\frac{1}{2},\frac{3}{2}}(v'' = 0-12)$ Emission Spectra 93

3.7.3 $C^2\Delta(v' = 0,1) - X^2\Pi_{\frac{1}{2},\frac{3}{2}}(v'' = 0-5)$ Emission Spectra . . . 100

3.8 Discussion 100

3.8.1 $B^2\Sigma^+ - X^2\Pi$ System 100

3.8.2 $C^2\Delta - X^2\Pi$ System 108

3.9 Conclusions 110

4. $^2\Delta - ^2\Sigma^+$ Vibronic Transfer in SiF and SiCl 115

4.1 Introduction 115

4.2 Experimental 119

4.3 Collision Induced $C^2\Delta$ to $B^2\Sigma^+$ Vibronic Energy Transfer in SiF . . 119

4.3.1 Total Collisional Removal of the SiF $C^2\Delta(v' = 0,1)$ States . 120

4.3.2 Specific Collisional Transfer from $C^2\Delta(v' = 0,1)$ to $B^2\Sigma^+$ . . 126

4.3.3 $B^2\Sigma^+$ Vibrational Branching Ratios 137

4.3.4 Correlation of the Nascent $B^2\Sigma^+$ Vibrational Populations with the $C^2\Delta - B^2\Sigma^+$ Franck-Condon Factors. 142

4.4 $B'^2\Delta$ to $B^2\Sigma^+$ Vibronic Energy Transfer in SiCl 143

4.4.1 Total Collisional Removal of SiCl $B'^2\Delta(v' = 0, 1)$ 144

4.4.2 Specific Collisional Transfer from $B'^2\Delta(v' = 0, 1)$ to $B^2\Sigma^+$. 150

4.4.3 Nascent vibrational populations in $B^2\Sigma^+$ following transfer from $B'^2\Delta(v' = 0, 1)$. 155

4.5 Conclusions 159

5. Rotational Effects in SiF $C^2\Delta - B^2\Sigma^+$ Collisional Transfer 162

5.1 Introduction 162

5.2 Rotational energy transfer within the SiF $C^2\Delta$, $v' = 0$ state 164

5.3 ΔJ Propensities upon SiF $C^2\Delta$,$v' = 0$ to $B^2\Sigma^+$, v'' Interstate Transfer. 175

5.4 Rotational Dependence of SiF $C^2\Delta$,$(v' = 0)$ Quenching and Transfer to $B^2\Sigma^+$, (v'') Rates. 182

5.4.1 Introduction 182

5.4.2 J'-Dependent Radiative Lifetimes of the $C^2\Delta$, $v' = 0$ State . 184

5.4.3 Total collisional removal of SiF $C^2\Delta v' = 0$: J' Dependence . 188

5.4.4 Specific collisional transfer SiF $C^2\Delta$, $v' = 0 - B^2\Sigma^+ v''$: J' Dependence 190

5.4.5 J' dependence of the $B^2\Sigma^+$ Vibrational Branching Ratios . . 193

5.5 Conclusions 193

6. The Mechanism of Collision-Induced Energy Transfer between the $^2\Delta$ and $^2\Sigma^+$ States of the Silicon Halides 196

6.1 Total Collision-Induced Electronic Quenching Rates 196

6.1.1 SiCl $B'^2\Delta$,$v' = 0, 1$ Removal 196

6.1.2 SiF $C^2\Delta$,$v' = 0, 1$ Removal 199

6.2 Specific Collisional Transfer from $^2\Delta$ to $^2\Sigma^+$ 200

6.2.1 SiCl $B'^2\Delta$ to $B^2\Sigma^+$ Transfer 200

6.2.2 SiF $C^2\Delta$ to $B^2\Sigma^+$ Transfer 203

6.3 Vibrational Populations in the Product States 204

6.3.1 Vibrational Populations in the SiCl $B^2\Sigma^+$ State 204

6.3.2 Vibrational Populations in the SiF $B^2\Sigma^+$ State 208

6.3.3 Comparison of the Vibrational Populations with Existing Energy Transfer Models 208

6.4 Proposed Mechanism for SiCl and SiF $B', C^2\Delta - B^2\Sigma^+$ Collision-induced Transfer 209

6.4.1 SiF $C^2\Delta$ to $B^2\Sigma^+$ Transfer 212

6.4.2 SiCl $B'^2\Delta$ to $B^2\Sigma^+$ Transfer 228

6.5 Final Conclusions 229

A. Rydberg-Klein-Rees Interatomic Potential Curves **235**

B. Publications **239**

C. Courses Attended **240**

List of Figures

1–1 Schematic representation of the proposed 'cascade' model between the vibrational levels of the $X^2\Sigma^+$ and $A^2\Pi$ states of CN. 6

1–2 Diabatic potential energy as a function of the atom-quencher separation of excited atomic states A' and A'', with an initial energy gap of ΔE, with collision partner M. A curve crossing occurs at r_x. 29

2–1 Cross section of the excitation and observation zone perpendicular to the flow axis. 51

2–2 Schematic of the experimental configuration of the discharge flow apparatus and LIF detection. 54

2–3 Schematic of the CAMAC based experimental control system 58

2–4 Timing sequence for the LeCroy 4222 pulse delay generator used during the experiments 60

3–1 Potential energy curves for the low-lying states of SiF constructed using the Rydberg-Klein-Rees method. 67

3–2 Vector diagram for Hund's coupling case (a) 71

3–3 Vector diagram for Hund's coupling case (b) 73

3–4 Schematic representation of the energy level structures of a $^2\Delta$ state in Hund's case (a) and (b). 75

3–5 Energy level diagram for a $^2\Sigma^+(b) - ^2\Pi(a)$ transition. 78

3–6 Energy level diagram for a $^2\Delta(a) - ^2\Pi(a)$ transition. 79

3–7 LIF excitation spectrum of the $B^2\Sigma^+(v' = 0) - X^2\Pi_{\frac{1}{2}}(v'' = 0)$ sub-band. 85

3–8 LIF excitation spectrum of the $B^2\Sigma^+(v' = 1) - X^2\Pi_{\frac{1}{2}}(v'' = 0)$ sub-band. 86

3–9 LIF excitation spectrum of the $B^2\Sigma^+(v' = 2) - X^2\Pi_{\frac{3}{2}}(v'' = 0)$ sub-band. 87

3–10 LIF excitation spectrum of the $B^2\Sigma^+(v' = 5) - X^2\Pi_{\frac{1}{2}}(v'' = 0)$ sub-band. 88

3–11 LIF excitation spectrum of the $C^2\Delta(v' = 0) - X^2\Pi_{\frac{1}{2}}(v'' = 0)$ sub-band. 89

3–12 LIF excitation spectrum of the $C^2\Delta(v' = 1) - X^2\Pi_{\frac{1}{2}}(v'' = 0)$ sub-band. 90

3–13 LIF excitation spectrum of the P_1 branch of the $C^2\Delta(v' = 0) - X^2\Pi_{\frac{1}{2}}(v'' = 0)$ sub-band. 92

3–14 Dispersed fluorescence spectrum of the $B^2\Sigma^+(v' = 0) - X^2\Pi(v'')$ transition. 94

3–15 Dispersed fluorescence spectrum of the $B^2\Sigma^+(v' = 1) - X^2\Pi(v'')$ transition. 95

3–16 Dispersed fluorescence spectrum of the $B^2\Sigma^+(v' = 2) - X^2\Pi(v'')$ transition 96

3–17 Simulation of the dispersed fluorescence spectrum of the $B^2\Sigma^+(v' = 3) - X^2\Pi(v'')$ transition. 97

3–18 Dispersed fluorescence spectrum of the $B^2\Sigma^+(v' = 4) - X^2\Pi(v'')$ transition 98

3–19 Dispersed fluorescence spectrum of the $B^2\Sigma^+(v' = 5) - X^2\Pi(v'')$ transition 99

3–20 Dispersed fluorescence spectrum of the $C^2\Delta(v' = 0) - X^2\Pi(v'')$ transition. 103

3–21 Dispersed fluorescence spectrum of the $C^2\Delta(v' = 1) - X^2\Pi(v'')$ transition 104

3–22 Schematic molecular orbital diagram for SiF constructed using the linear combination of atomic orbitals approximation. 107

4–1 Potential energy curves for the SiCl $B'^2\Delta$ and $B^2\Sigma^+$ states. 117

4–2 Potential energy curves for the SiF $C^2\Delta$ and $B^2\Sigma^+$ states. 118

4–3 Representative radiative decay plot for the SiF $C^2\Delta - X^2\Pi$ transition. 121

4–4 Plot of the observed first order decay constants for SiF $C^2\Delta(v' = 0)$ as a function of quencher pressure for Ar, H_2, N_2, CH_4 and CO_2. . . 124

4–5 Plot of the observed first order decay constants for SiF $C^2\Delta(v' = 1)$ as a function of quencher pressure for Ar, H_2, N_2, CH_4 and CO_2. . . 125

4–6 Dispersed fluorescence spectra following the initial excitation of SiF $C^2\Delta(v' = 0)$ in the presence of H_2 and Ar. 128

4–7 Dispersed fluorescence spectrum following the initial excitation of SiF $C^2\Delta(v' = 0)$ in the presence of N_2. 129

4–8 Dispersed fluorescence spectrum following the initial excitation of SiF $C^2\Delta(v' = 0)$ in the presence of CH_4. 130

4–9 Dispersed fluorescence spectrum following the initial excitation of SiF $C^2\Delta(v' = 1)$ in the presence of 1 Torr of argon and 0.6 Torr H_2. 131

4–10 Dispersed fluorescence spectrum following the initial excitation of SiF $C^2\Delta(v' = 1)$ in the presence of 1 Torr of argon and 1.3 Torr N_2. 132

4–11 Dispersed fluorescence spectrum following the initial excitation of SiF $C^2\Delta(v' = 1)$ in the presence of 1 Torr of argon and 0.9 Torr CH_4. 133

4–12 a) Time dependent fluorescence profile following excitation of the $B^2\Sigma^+ - X^2\Pi$ (2,0) Q_1 band-head. b) Time dependent profile of the excitation laser pulse intensity. 134

4–13 Dispersed fluorescence spectrum of the SiF $B^2\Sigma^+ - X^2\Pi(0,0)$ transition obtained after the excitation of the $C^2\Delta(v = 0)$ state in the presence of 0.5 Torr H_2 and 1 Torr Ar. 139

4–14 Measured SiF $B^2\Sigma^+$ state product vibrational distributions following excitation of $C^2\Delta$ for H_2, N_2 and CH_4. 141

4–15 Representative radiative decay plot for the SiCl $B'^2\Delta - X^2\Pi$ transition. 146

4–16 Observed first order decay constants for SiCl $B'^2\Delta v' = 0$ as a function of quencher partial pressure. 147

4–17 Observed first order decay constants for SiCl $B'^2\Delta v' = 1$ as a function of quencher partial pressure. 148

4–18 Dispersed fluorescence spectrum following excitation to the SiCl $B'^2\Delta v' = 0$ level in the presence of argon. 151

4–19 Dispersed fluorescence spectrum following excitation to the SiCl $B'^2\Delta v' = 1$ level in the presence of argon. 152

4–20 Dispersed fluorescence spectra following direct initial excitation of SiCl $B^2\Sigma^+ - X^2\Pi$, $(v', 0)$ Q_1 band heads. 156

4–21 Graphic representation of the SiCl $B^2\Sigma^+$ vibrational populations resulting from collisional transfer by each quenching gas from $B'^2\Delta v' =$ 0 and 1 as indicated in figure. 158

5–1 Simulation of the $C^2\Delta - X^2\Pi_{\frac{1}{2}}$ $(0,0)$ excitation spectrum. 165

5–2 Excitation spectrum of the $C^2\Delta - X^2\Pi_{\frac{1}{2}}$ P_1 branch. 166

5–3 'Blue' region of the $C^2\Delta - X^2\Pi_{\frac{1}{2}}$ $(0,0)$ excitation spectrum. 167

5–4 High resolution spectrum of the $C^2\Delta - X^2\Pi_{\frac{3}{2}}$ $(0,0)$ transition recorded after excitation of the $C^2\Delta - X^2\Pi_{\frac{1}{2}}$ $(0,0)$ Q_1 bandhead. 169

5–5 High resolution spectrum of the $C^2\Delta - X^2\Pi_{\frac{3}{2}}$ $(0,0)$ recorded after excitation of the $C^2\Delta - X^2\Pi_{\frac{1}{2}}$ $(0,0)$ P_1 bandhead. 170

5–6 Rotational distributions in the $C^2\Delta$ state used to simulate the $C^2\Delta - X^2\Pi_{\frac{3}{2}}$ fluorescence after excitation of the of relevant bandheads: 172

5–7 High resolution spectrum of the $C^2\Delta - X^2\Pi_{\frac{3}{2}}$ $(0,0)$ transition recorded after excitation of the $C^2\Delta - X^2\Pi_{\frac{1}{2}}$ $(0,0)$ Q_1 bandhead in the presence of H_2. 174

5–8 High resolution spectrum of the collision-induced $B^2\Sigma^+ - X^2\Pi$ $(0,0)$ band recorded after excitation of the $C^2\Delta - X^2\Pi_{\frac{1}{2}}$ $(0,0)$ Q_1 bandhead. 176

5–9 High resolution spectrum of the collision-induced $B^2\Sigma^+ - X^2\Pi$ $(0,0)$ band recorded after excitation of the $C^2\Delta - X^2\Pi_{\frac{1}{2}}$ $(0,0)$ P_1 bandhead. 177

5–10 High resolution spectrum of the collision-induced $B^2\Sigma^+ - X^2\Pi$ $(0,0)$ band recorded after excitation of the $C^2\Delta - X^2\Pi_{\frac{1}{2}}$ $(0,0)$ Q_1 bandhead. 178

5–11 High resolution spectrum of the collision-induced $B^2\Sigma^+ - X^2\Pi$ $(0,0)$ band recorded after excitation of the $C^2\Delta - X^2\Pi_{\frac{1}{2}}$ $(0,0)$ P_1 bandhead. 179

5–12 Rotational distributions used to simulate the $C^2\Delta - X^2\Pi_{\frac{3}{2}}$ and $B^2\Sigma^+ - X^2\Pi_{\frac{1}{2},\frac{3}{2}}$ fluorescence after excitation of the $C^2\Delta - X^2\Pi_{\frac{1}{2}}$ bandheads: 180

5–13 Plot of the observed first order decay constants after excitation of SiF $C^2\Delta_\Omega, v' = 0, J'$ as a function of argon pressure. 185

5–14 Comparison of the temporal profiles of the LIF signal after excitation of (a) $C^2\Delta_{\frac{3}{2}}$ $v' = 0$, $J' = 2.5$ and (b) $C^2\Delta_{\frac{5}{2}}$ $v' = 0$, $J' = 48.5$ states as indicated on the plot. 186

5–15 Observed first order decay rate constants for SiF $C^2\Delta, v' = 0, J'$ as a function of quencher partial pressure. 189

5–16 Dispersed fluorescence spectra following the initial excitation of the $C^2\Delta - X^2\Pi_{\frac{1}{2}}$, $(0,0)$ transition in the presence of 3 Torr H_2 and 1 Torr Ar. 191

5–17 Dispersed fluorescence spectra following the initial excitation of the $C^2\Delta - X^2\Pi$ (0,0) transition in the presence of 3 Torr N_2 and 1 Torr Ar. 192

6–1 Parmenter-Seaver attractive well depth correlation plots of the cross sections for total collisional removal of SiCl $B'^2\Delta$ (a) $v' = 0$ and (b) $v' = 1$. 198

6–2 Plots of the SiF $C^2\Delta - B^2\Sigma^+$ transfer cross section against the collision reduced mass term according to SSH theory. 205

6–3 Parmenter-Seaver correlation plot of specific state-to-state cross sections for the near-resonant collisional collisional transfer from SiCl $B'^2\Delta$, $v' = 0$ to $B^2\Sigma^+$, $v' = 2$. 207

6–4 Schematic representation of the diabatic potential surfaces for the SiX-quencher $C, B'^2\Delta$ and $B^2\Sigma^+$ states. 213

6–5 Plots of the maximum change in the rotational quantum number in SiF for 'hard shape' SiF and 'hard sphere' H_2 collisions as a function of the initial rotational quantum number assuming *no* electronic energy release. 219

6–6 Plots of the maximum δj as a function of the initial rotational quantum number following the collision of SiF and H_2 in an impulsive 'hard-shape' - 'hard-sphere' model. There is an assumed additional energy release of 4816 cm^{-1}, at constant collision velocity for different impact parameters. 221

6–7 Plot of the rotational and translational energy of the SiF - H_2 system before and after a 'hard-shape' - 'hard-sphere' collision accompanied by the additional release of 4816 cm^{-1} energy. 222

6–8 Plots of the maximum δj as a function of the initial rotational quantum number following the collision of SiF and H_2 in an impulsive 'hard-shape' - 'hard-sphere' model, where there is an energy release of 4816 cm^{-1}, at constant impact parameter for different collision velocities. 224

6–9 Plots of the maximum δj as a function of the initial rotational quantum number following the collision of SiF and H_2 in an impulsive 'hard-shape' - 'hard-sphere' model, where there is an energy release of 4816 cm^{-1}, at constant impact parameter for different collision velocities. 225

6–10 Plots of the maximum δj as a function of the initial rotational quantum number following the collision of SiF and N_2 in an impulsive 'hard-shape' - 'hard-sphere' model, where there is an energy release of 4816 cm^{-1}, at constant impact parameter for different collision velocities. 227

List of Tables

2–1 Table of laser dyes with tunable wavelength ranges when operating in fundamental, frequency doubled and frequency doubled / mixed modes. 47

3–1 The principal molecular constants of $^{28}Si^{19}F$ for the $X^2\Pi$, $B^2\Sigma^+$ and $C^2\Delta$ states (from ref. [36]). 68

3–2 Vibrational transition probabilities in the SiF $B^2\Sigma^+$ - $X^2\Pi$ system . 101

3–3 Vibrational transition probabilities in the SiF $C^2\Delta$ - $X^2\Pi$ System. . 102

4–1 Rate constants and thermally averaged cross sections for total removal of SiF $C^2\Delta(v' = 0, 1)$. 123

4–2 Rate constants, thermally averaged cross sections and branching fractions for transfer from SiF $C^2\Delta - B^2\Sigma^+$. 136

4–3 Nascent vibrational populations in SiF $B^2\Sigma^+$ following transfer from $C^2\Delta(v = 0, 1)$. 140

4–4 Rate constants and thermally averaged cross sections for the total collisional removal from SiCl $B'^2\Delta(v' = 0, 1)$. 149

4–5 Rate constants and thermally averaged cross sections for specific transfer from SiCl $B'^2\Delta(v' = 0, 1)$ to $B^2\Sigma^+$. 153

4–6 Nascent vibrational populations in SiCl $B^2\Sigma^+$ following transfer from $B'^2\Delta(v' = 0, 1)$. 157

5–1 Radiative lifetimes for SiF $C^2\Delta v' = 0, J'$. 187

5–2 Rate constants and thermally averaged cross sections for total removal after excitation of SiF $C^2\Delta_{\frac{3}{2}}$ $v' = 0, J'$. 188

6–1 Potential reactive channels available for the quenching of SiF $C^2\Delta$,$v' = 0$ by H_2, CH_4 and CO_2. 201

Chapter 1

Introduction

The factors that govern the exchange of energy as a result of a bimolecular collision are of both fundamental interest and practical importance. Unfortunately these phenomena are still far from being fully understood.

It is well established from a dynamical perspective that chemical reactions can be sensitive to the form of energy possessed by the reagents. The partition of energy in a system produced by a chemical reaction is likely to deviate from the classical Boltzmann distribution. To return to an equilibrated distribution, molecular species must undergo energy transferring collisions in order to lose or gain the required energy to achieve equilibrium with their environment. Thus any intermolecular collisions leading to the transfer of energy, prior to any further reactive steps, could have a significant effect upon the final reaction outcome of a system not initially in thermal equilibrium. A precise knowledge of the simple bimolecular collision event at the molecular level is thus essential if a good understanding of bulk systems is to be achieved.

As diatomic molecules, by definition, are the simplest molecular species, study of their energy transfer behaviour would appear to be the obvious starting point in gaining insight into this complex phenomenon. These molecules can be described well in quantum mechanical terms, hence not only is the analysis of experimental data facilitated but they have the added advantage of being more theoretically tractable than larger systems.

More specifically this thesis concerns the study of collision-induced electronic energy transfer (CIEET) where there is a change in electronic state of one molecule as a result of a collision with another (which remains in the same electronic state), with the possibility of some simultaneous transfer of energy to nuclear framework motions (rotation, vibration and relative translation) *i.e.*

$$AB(T_e', v', J', |m_{J'}|) + M \longrightarrow AB(T_e'', v'', J'', |m_{J''}|) + M \qquad (1.1)$$

Ideally it should be possible to build a predictive universal model as a result of studies of this process.

There already exists a considerable body of work where rate constants have been measured for the total collisional removal of electronically excited species. A number of empirical models have been devised as a result. However, only a small subset of these studies have involved examination of the identity of the product molecules due to a single collision event.

The ideal state-specific energy transfer experiment obviously involves knowledge of the initial and final quantum states of the molecule. With the advent of tunable laser sources it is now routinely possible to selectively populate specific quantum levels, thus facilitating studies of this type. However to date only one experiment has been performed which defines T_e, v, J and $|m_J|$ for both target and product states [1,2]. The majority of state-specific studies have been concerned with collision-induced vibronic energy transfer with increasing attention being focussed at the rovibronic level. As a result there is at present an inadequate quantity of data available from which to draw a fully comprehensive theoretical model.

There are a number of different areas of study which would benefit from an increased understanding of this subject. Perhaps the most obvious application of practical significance is that of gas phase laser systems where high energy species are required which may be populated or depopulated as a result of collisional energy transfer. Hence to build an accurate model of any prospective system under untested conditions would require a complete fundamental theoretical understanding.

The chemistry of the atmosphere has long been the subject of intense research for both environmental and economic motives. Computer based models have been designed to describe and predict energy dispersion in the upper atmosphere. However these models rely mainly upon empirical descriptions of energy transfer which have proved far from satisfactory from a state-to-state perspective.

The pressure dependence of the spectra of chemiluminescent processes is indicative of collision-induced energy transfer, thus a correct interpretation of these spectra requires a knowledge of the potential collisional effects.

Other potential practical applications include the study of plasma processes, combustion, flames and rocket plume emissions *etc.*

The remainder of this chapter is intended as a review of the existing body of relevant experimental and theoretical work followed by a discussion of the different conclusions that have been drawn. This review will be sub-divided into sections dealing with collision-induced electronic energy transfer in different electronic systems of various molecules. These sections will in turn be arranged in order of increasing experimental resolution and chronologically in as much as it is possible.

1.1 Experimental Observations of CIEET

1.1.1 Indirect Observations of CIEET

Much of the present body of existing information was initiated by examination of the collision coupling of the electronically analogous $A^2\Pi$ and $X^2\Sigma^+$ states of CO^+ and CN by Bondybey *et al* [3,4,5]. In these studies direct observations of the time dependence of vibronic populations of a single electronic state were inferred as evidence of collision-induced electronic transfer to at least one other electronic state.

CO^+ $A^2\Pi$ State Quenching

It was observed by Laser-Induced Fluorescence (LIF) that upon selective excitation of the CO^+ $A^2\Pi$, v'=0-3 state vibrational levels in the presence of He that the rate of fluorescent quenching increased with the vibrational quantum number [3,4]. More importantly, part of the fluorescent emission, after excitation of v'=1-3, was found to be from lower lying vibrational levels of the $A^2\Pi$ state. Subsequent time-resolved fluorescent measurements from these lower lying vibronic levels showed that their rate of population was not equal to the rate of removal of the originally populated level. This implied that these vibrational levels were not the result of direct vibrational quenching but rather that of a process whereby molecules were efficiently transferred to the $X^2\Sigma^+$ state and then back to lower lying vibrational levels of the $A^2\Pi$ state as a result of a *second* collision. Collisional coupling between near-isoenergetic vibronic levels was also inferred from the double exponential $A^2\Pi - X^2\Sigma^+$ fluorescent decays which indicated that molecules were transferred to and from the vibronic pairs as a result of sequential collisions with He. By analogy with similar work upon the isoelectronic CN radical in rare gas matrices, the 'cascade' model was proposed as the likely explanation of these observations [6,7,8].

This 'cascade' process, put simply, means that a molecule in an excited electronic state is transferred to the energetically nearest-lying vibrational level of another electronic state after a suitable collision. Hence, in a system containing two vibrational ladders, an excited molecule would step back and forth from one electronic state to another with each collision as shown in figure 1–1.

However, as with the work on the rare gas matrices, the 'cascade' process was not observed directly; it was simply inferred from the $A^2\Pi - X^2\Sigma^+$ decay profiles which could be modelled by a double exponential. There was no suggestion by the authors that a more complicated system could be possible. Transfer to further low-lying levels of the adjacent electronic state as a result of a single collision were not considered.

Quenching cross sections were rationalised [4] by either equating them directly with the Franck-Condon factor or, perhaps more significantly, by pointing out that σ_Q increased as the vibrational level approached the crossing point of the two electronic potentials in the free ion.

CN $A^2\Pi$ State Quenching

The CN $A^2\Pi$ - $X^2\Sigma^+$ transition has been the object of intensive studies as the basis of an electronic molecular predissociation laser[1] [9,10]. A study of the collisional removal of the $A^2\Pi$ (v'=3-9) by Ar also showed that the quenching lifetime decreased with increasing vibrational energy [5]. Cross sections for removal of v'=8, which is near-degenerate with v''=12 of $X^2\Sigma^+$ and coincident with the $A^2\Pi - X^2\Sigma^+$ curve-crossing, were comparable with those for rotational relaxation (where σ values are typically in the range of ~10-100$\AA^2$ [11]).

A simple empirical model was suggested to rationalise these quenching cross-sections based on the assumption that only one quenching channel, to the nearest

---

[1]CN $A^2\Pi_{\frac{3}{2}}$, $v' = 0$ - $X^2\Sigma^+$,$v'' = 0, 1, 2$ laser emission was first observed following photodissociative and predissociative fragmentation of the cyanide parents RCN (R= H, Cl, Br, I, CN, CH_3, CF_3 and C_2F_5) at $\lambda \geq 1550\AA$ [9].

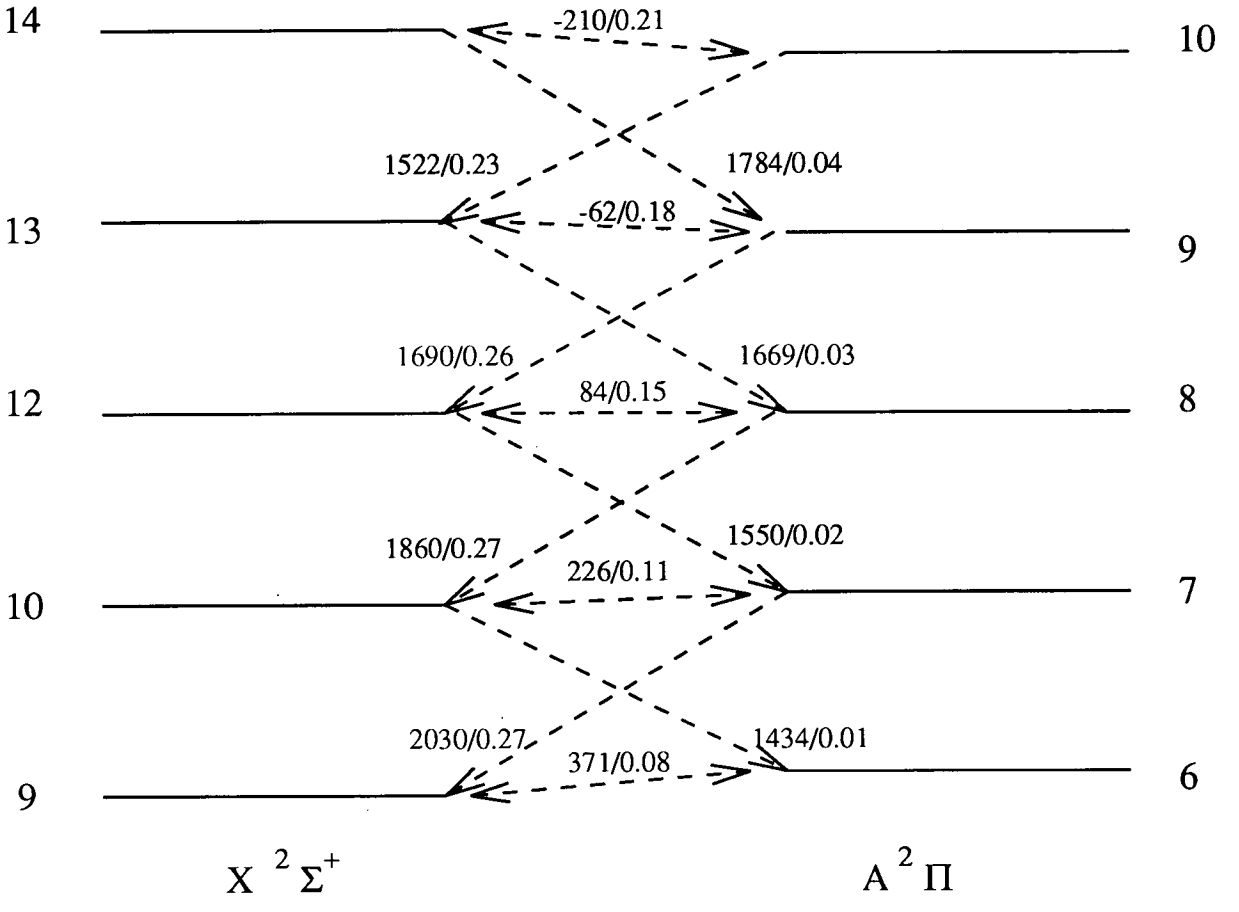

Figure 1–1: Schematic representation of the proposed 'cascade' model between the vibrational levels of the $X^2\Sigma^+$ and $A^2\Pi$ states of CN.

The single-headed arrows refer to single collision transfer from one vibronic level to the adjacent level of the other state. The double-headed arrows indicate collisional coupling, where the adjacent vibronic levels are within kT, thus back transfer to the original state can occur. The figures accompanying each dashed line indicate the energy gap, ΔE, and the Franck-Condon factor, respectively. Extracted from ref. [5].

vibronic level, was available [5]:-

$$\sigma_{obs} = \sigma_{el}.q_{v'v''}.exp(-\Delta E/kT), \tag{1.2}$$

where σ_{obs} is the experimentally determined quenching cross-section, σ_{el} is the hypothetical intrinsic electronic quenching cross section, $q_{v'v''}$ is the Franck-Condon factor and ΔE is the energy gap between the adjacent vibronic levels.

This model had limited success, however, in that it was in crude agreement with σ_Q for the lower vibrational levels but the predicted rise in σ_Q with v' was found to be far too steep.

N_2 $B^3\Pi_g$ State Quenching

Similar work was carried out independently by Setser's group upon molecular nitrogen where vibrational levels v'=0-10 in the $B^3\Pi_g$ state were shown to be collisionally coupled by Ar and Ne to at least one other state, taken to be the $W^3\Delta_u$ state [12,13,14]. The multi-exponential decays were shown to be often greater than second order thus implying that a third and/or fourth vibronic state was involved in the quenching mechanism, the most likely candidates being the $A^3\Sigma_u^+$ and $B'^3\Sigma^-$ states. Transfer to any of the near-lying singlet states was precluded by the absence of any $a^1\Pi_g$ or $a'^1\Sigma_u^-$ to $X^1\Sigma_g^+$ fluorescence.

Although in this case Setser acknowledged that the 'cascade' process was an unverified assumption, the experimental results were well reproduced using this kinetic model. Thus there appeared to be no evidence from this study and the other contemporary data to indicate that inter-electronic collisional energy transfer is possible between all but adjacent vibronic levels.

1.1.2 Direct Observations of CIEET at the Vibronic Level

The work described in this section concerns CIEET where the collisionally produced electronic states have been observed directly either by LIF or Optical-Optical Double-Resonance (OODR). These studies examined the transfer propensities where only vibronic transfer can be ascribed as a single collision process

although some include an investigation of the effect of varying the initial rotational quantum number.

N_2^+ $A^2\Pi_u$ - $X^2\Sigma_g^+$

For many years it was also thought that collisional transfer between vibronic states was possible *only* where there existed mutually perturbed rotational levels[2]. There are known to be rotational perturbations between the $A^2\Pi$ and $X^2\Sigma^+$ states for the vibrational for CO^+ ($v' = 0,1,2,3, v'' = v' + 10$) and CN ($v' = 3,7,8, v'' = v' + 4$) although these perturbations are generally weak and occur only at high rotational levels. Although the results of the J' dependent quenching of the $A^2\Pi$ states indicated [3,4,5] that they did not play a major role in CIEET, a study of the N_2^+ ion [43] proved an unambiguous test of the necessity of perturbations for this process. Due to the homonuclear nature of the ion, perturbations between the $A^2\Pi_u$ and $X^2\Sigma_g^+$ states are forbidden and hence can play no role in the transfer event.

The technique of OODR is a classic example of a 'pump and probe' experiment. Put quite simply, target molecules are first laser excited to the required quantum level and after a specific time delay a second laser is used to 'probe' the identity of the collision-induced product molecules by exciting them to a further excited electronic state. Any signal that results from probe excitation of quantum levels other than the initially prepared level is the result of energy transfer.

The first OODR study in this field was performed on N_2^+ $A^2\Pi_u$ - $X^2\Sigma_g^+$ transfer [43]. This was successful in showing that the ions originally pumped into the $A^2\Pi_u$ state were deactivated by collisions with He into high lying vibrational levels of the $X^2\Sigma_g^+$ state, and hence conclusively disproved the 'gateway' theory for the

---

[2]This 'gateway' model was first proposed by Gelbert and Freed after studies on the $^2B_1$ and $^2B_2$ states of NO_2 [15]. This model will be discussed later in more detail. Other examples where this behaviour was also observed include the $B^2\Sigma^+$ and $A^2\Pi$ states of CN [16] and $B^2\Sigma_u^+$ and $A^2\Pi_u$ states of CO_2^+ [17].

first time [18]. However the experiment was too crude to cast doubt upon the assumption that direct transfer is possible only between near-adjacent vibronic levels. This was because the pump-probe pulse delays were on the microsecond time scale and hence could not distinguish between multiple and single collision processes.

Cross sections for removal were five and ten times greater than for CO^+ and CN, respectively. These differences were attributed mainly to the small Franck-Condon overlap for the CO^+ system and the neutral charge of the CN radical (hence no long range ion-molecule attraction) [18]. The magnitudes of the cross sections were again not quantitatively well predicted by the exponential energy gap model.

The role of the energy gap was the basis for a comparative study of the $^{14}N_2^+$ and $^{15}N_2^+$ $A^2\Pi_{ui}$ (v'=4) - $X^2\Sigma_g^+$ (v''=7,8) transfer processes [19,20]. Although the magnitudes of the rotationless energy gaps between the respective levels were not significantly different for the two molecules, the endothermicity of the $^{14}N_2^+$ transition appeared to have a substantial effect upon the product vibronic branching ratios. These were found to differ dramatically, with $\frac{k_{4\to 8}}{k_{4\to 7}} \approx 2$ and 6 for $^{14}N_2^+$ and $^{15}N_2^+$, respectively. In both cases, transfer was found to be faster for the smaller energy gap transition. A subsequent study of the relative transfer rates from $^{15}N_2^+$ $A^2\Pi_{ui}$ (v'=3) to $X^2\Sigma_g^+$ (v''=6,7) led to the development of another phenomenological model based on the energy gap and the Franck-Condon overlap. This model predicts that the branching ratio for transfer to vibronic levels j and k in the product state from level i in the initial state is

$$\frac{k_{i\to j}}{k_{i\to k}} = R\frac{FCF_{ij}}{FCF_{ik}} \tag{1.3}$$

where R is a linear function of the energy gap, ΔE_1, between i and the nearer vibronic level, j, where

$$R = A + B(\Delta E_1) \tag{1.4}$$

and A and B are constants. Although this model appears to have had some success in describing the relative transfer probabilities for the $^{14}N_2^+$ and $^{15}N_2^+$ transfer systems it can be shown that a reasonable correlation is also achieved even when

the larger energy gap, ΔE_2, is chosen. The contribution of the smaller energy gap to the branching fraction is therefore contentious.

N_2 $B^3\Pi_g$ - $B'^3\Sigma_u^-$

Nitrogen was also the subject of directly observed collision-induced electronic transitions from laser excited $B^3\Pi_g$, v'=7-9 to $B'^3\Sigma_u^-$, $v = v' + 4$ [14,21,22]. Fluorescence was observed directly from lower lying vibrational levels of the $B'^3\Sigma_u^-$ state in the presence of N_2, Ar and Ne though again the width of the detection gate was too long to determine the effect of single collisions. The decay profiles indicated that the mechanism for this transition involves at least one additional level, the $W^3\Delta_u$ state being the most likely candidate (as previously mentioned in section 1.1.1).

CH $A^2\Delta$ - $B^2\Sigma^-$

The diatomic hydrides have probably attracted the most attention for kinetic studies of electronic quenching due to their relevance in flames and combustion processes [23]. Despite the large volume of work concerning quenching rates of electronically excited states there is surprisingly little data available on state-to-state transfer effects despite the obvious advantages for theoretical study of these molecules.

A LIF study has been made of the CH radical in atmospheric pressure flames of CH_4, O_2 and N_2 mixtures where CIEET was observed [24,25]. Rovibronic levels in v'=0 and 1 were selectively populated in the $A^2\Delta$ and $B^2\Sigma^-$ states with the resulting fluorescence being time and wavelength resolved. After excitation of $A^2\Delta$ v'=0 or 1, fluorescence was detected from the adjacent $B^2\Sigma^-$ v'=0 level. However, upon excitation of $B^2\Sigma^-$ v=0, only fluorescence from it and $A^2\Delta$ v'=1 could be observed. The CIEET cross-sections for these transfer channels were equivalent to about 20% of those for total quenching of the excited states.

The results implied that in this case the Franck-Condon factor between the vibrational levels does not play an important role. The overlap between the $A^2\Delta$

v=0 and $B^2\Sigma^-$ v=0 wavefunctions is almost an order of magnitude greater than that between $A^2\Delta$ v=1 and $B^2\Sigma^-$ v=0 though this is not reflected in the relative transfer rates. Rather, these experiments appeared to show increasing transfer efficiency between levels with small energy gaps.

Although the relative CIEET cross sections appear to have a small rotational level dependence, where σ decreases with J', the relative rotational populations in the final state appeared to be statistical. This is despite the fact that pure rotational energy transfer (RET), although approximately an order of magnitude greater than CIEET in this case, was shown to be insufficient to produce a Boltzmann distribution within the radiative lifetimes (where $A^2\Delta$ $\tau_{rad} \approx$ 540 ns and $B^2\Sigma^-$ $\tau_{rad} \approx$ 340 ns [24,25]).Thus there appears to be no propensity for retention of the rotational quantum number during an electronic state changing collision.

Obviously, due to the combination of high pressure and the relatively long radiative lifetimes, the affect of single collisions could not be ascertained.

OH $A^2\Sigma^+$ - $X^2\Pi_i$

Collisional quenching of OH $A^2\Sigma^+$ has been probably the most extensively investigated electronically excited diatomic though only one study has attempted to investigate the dynamics, as opposed to the kinetics, of this process [26].

Upon laser excitation of OH $A^2\Sigma^+$, v'=0 produced in a flowing discharge of H_2O vapour, the excited radicals were collisionally quenched. The product $X^2\Pi_i$ vibrational levels v''= 1,2 and 4 were monitored by LIF. The time dependent populations were inferred to indicate that the majority of product molecules were not the result of a direct collision but rather of a long-lived collisional complex.

This was consistent with an earlier study where the quenching cross section was shown to decrease with increasing rotational angular momentum and hence was indicative of complex formation [27].

NH $c^1\Pi$ - $A^3\Pi$

It has been observed that upon 193.3 nm photolysis of HN_3, the addition of O_2, NO, Xe or N_2O decreases the NH($c^1\Pi$ - $a^1\Delta$) fluorescence intensity but increases the amount of NH($A^3\Pi_i$ - $X^3\Sigma^-$) fluorescence [28]. These 'forbidden' $c^1\Pi$ - $A^3\Pi$ collision-induced spin conversions are extremely efficient and approach the gas kinetic rate for O_2 and NO.

A more recent study established the kinetics and specific products of this process [29]. Not only was the NH molecule transferred over a very large electronic energy gap ($\Delta E \approx 15000$ cm^{-1}) but the product state vibrational distributions showed an interesting quencher dependence. For quenching with O_2 the relative vibrational populations in the $A^3\Pi_i$ state for v=0-2 were 64:12:24, respectively, yet for NO no $A^3\Pi_i$ v=2 fluorescence was observed at all with populations being 85:15:0.

This observation was rationalised by a resonant transfer mechanism in which singlet O_2 is generated as the co-product of the NH $c^1\Pi$ - $A^3\Pi$ conversion thus conserving total spin for the system. The three O_2 vibronic ($a^1\Delta$, v=0,2,4) products are in near resonance with NH $A^3\Pi_i$ v=0-2.

The crossing induced by the paramagnetic NO was also deduced to take place with total spin conversion though the excess energy loss by NH was assumed in this case to be taken up by vibrational energy in the NO X, v=6,8 respectively. There was, however, no direct evidence for these products.

There is no spin conservation process possible for singlet to triplet transfer with Xe as the collision partner, though spin is not necessarily a good quantum number in collisions with such heavy atoms. As the transfer efficiency appeared to be greater than one, a further collision induced transition was implied, such as NH $b^1\Sigma^+$ - $A^3\Pi_i$, where the NH $b^1\Sigma^+$ is also produced by the 193.3 nm photolysis of HN_3, though again there was no direct evidence for this system.

The NH products of all the above processes were all shown to be rotationally very hot with Boltzmann temperatures of approximately 1500, 4000, 1500 and 3000 K for O_2, NO, Xe and N_20, respectively. This contrasts with the rotational

temperature for the photolytically produced NH $c^1\Pi$ which was found to be only about 800 K. Thus the CIEET process causes substantial rotational excitation in the NH products.

Unlike the previously studied systems this was the first case where CIEET was observed between non near-isoenergetic vibronic levels. More significantly there appeared to be *no* propensity for transfer over the approximately isoenergetic channels.

NH $a^1\Delta$ - $X^3\Sigma^-$

Studies of NH $a^1\Delta$ - $X^3\Sigma^-$ transfer have shown a propensity for collisional electronic transfer over a large energy gap similar to those observed for NH $c^1\Pi - A^3\Pi$.

The NH $a^1\Delta$ produced by 266 nm laser photodissociation of HN_3 has been found to be predominately in v'=0-3 [30]. Collisional quenching of this $a^1\Delta$ vibrational distribution by N_2, O_2, CO and Xe (where quenching by N_2 and Xe only was the result of pure physical quenching) has been observed to result in intersystem crossing to the $X^3\Sigma^-$ state with v''=0-2 being detected by LIF, after a 90μs photolysis-probe delay, via the $A^3\Pi$ state [31]. The relative $X^3\Sigma^-$ vibrational populations were found to decrease monotonically with v'' though for N_2 the NH $X^3\Sigma^-$ state was predominately in v''=0. Obviously this is again a very exothermic process with the maximum energy gap, ΔE_{max}, about 8000 cm^{-1}.

Quenching cross sections for Xe were large and invariant with v', of the order of 10% gas kinetic, being 1000 times the quenching cross sections of Kr and 10^4 times that of Ar and He.

A similar study on this collision-induced system was performed with a photolysis wavelength of 308 nm [32]. In this case NH $a^1\Delta$ was produced with greater than 95% in v'=0. Collisions of NH $a^1\Delta$, v'=0 with the quenchers Xe and N_2 produced *only* $X^3\Sigma^-$, v''=0. Therefore it was shown that any vibrationally excited $X^3\Sigma^-$ produced from NH $a^1\Delta$ state molecules by collisions with Xe state in the previous study [31] must have been channeled from vibrational levels greater than 0.

As the internuclear separation in the NH $X^3\Sigma^-$ and $a^1\Delta$ states is very similar, it was proposed that the product NH $X^3\Sigma^-$ vibrational distribution is consistent with a Franck-Condon model [54]. However, this remains to be shown conclusively, requiring further state-specific information from selectively populated vibrationally excited levels in $a^1\Delta$.

O_2 $b^1\Sigma_g^+$ - $a^1\Delta$

Surprisingly, the physical quenching dynamics of electronically excited molecular oxygen has attracted little attention despite its obvious potential significance in photochemical and atmospheric systems.

The one study that has been carried out concerns the quenching of the $^{16}O_2$ $b^1\Sigma_g^+$, v'=0-2 vibronic levels which were selectively populated by laser excitation [34]. Fluorescence was observed from the $b^1\Sigma_g^+$ states of $^{16}O_2$ *and* $^{18}O_2$ (in a 1:1 mixture of the two isotopes) and from $a^1\Delta$, v''=0. The CIEET process was found to have an efficiency of about 90% for a range of simple quenchers despite the large energy gap of $\Delta E \approx 7000$ cm^{-1}.

NS $B^2\Pi$ - $B'^2\Sigma^+$, $b^4\Sigma^-$

The first lifetime measurements for the quenching of NS $B^2\Pi$ v'=6-12 by N_2 revealed that the perturbed levels v'= 8,10 and 11 showed evidence of collisional coupling to other electronic states because the fluorescence decays were multi-exponential [35]. Subsequently, the quenching of laser excited rovibronic levels of NS $B^2\Pi$ v'=3-8 has been studied by time and wavelength resolved LIF [36]. It is known that $B^2\Pi$ v=3 is perturbed by the quartet states $b^4\Sigma^-$ and $a^4\Pi$ and $B^2\Pi$ v=8 is known to be perturbed by the doublet $B'^2\Sigma^+$, v=0 [37].

The behaviour for v'=4-7 is quencher dependent. The cross sections showed a dramatic oscillatory behaviour with increasing v' for a large variety of quenchers with the exception of O_2 which showed a monotonic increase. Unfortunately there was nothing to suggest the identity of the quenching channel itself [36].

Excitation of v'=3 showed multi-exponential decay behaviour suggesting collisional coupling between it and some other vibronic state(s) [36]. However, this was only observed after excitation to perturbed rotational levels thus exhibiting 'gateway' type behaviour.

After excitation of $B^2\Pi$ v'=8, fluorescence was also observed from the near isoenergetic $B'^2\Sigma^+$, v''=0 [36]. However, in contrast to v' = 3, rapid collisional coupling occurs from all rotational levels of the $B^2\Pi$, v'=8 and $B'^2\Sigma^+$, v''=0 states followed by radiative and collisional removal of this coupled manifold.

NO $a^4\Pi$ - $b^4\Sigma^-$, $B^2\Pi$

A study of the collisional relaxation of the $a^4\Pi$ state of NO investigated competing energy transfer channels involving the $B^2\Pi$ and $b^4\Sigma^-$ states [38]. An NO molecular beam with a velocity of 960 ms^{-1} was passed through a dc discharge, producing highly vibrationally excited NO $a^4\Pi$, v' = 0 to > 8, and into a cell containing the collision partner. Collision-induced emission was observed from at least $b^4\Sigma^-$, v=2-5 (higher vibrational levels are predissociated) for the quenching species He, Ar, Xe, N_2, O_2 and NO. Spontaneous emission was observed from the perturbed B state levels $^2\Pi_{3/2}$ v''=0, J''=10.5 and $^2\Pi_{1/2}$ v''=3, J''=17.5. Collision induced transfer to the $B^2\Pi$ state, however, was only observed for NO, O_2 and Xe.

This quencher specificity was rationalised by considering the paramagnetic character of O_2 and NO which could more easily induce the spin-changing transition. Spin-changing energy transfer is also known to be facilitated by a heavy atom collision partners such as Xe.

SiCl $B'^2\Delta$ - $B^2\Sigma^+$

The CIEET of the SiCl $B'^2\Delta$ (v'=0 and 1) states showed perhaps the most surprising quencher dependent product distributions observed so far. Transfer from these states to the $B^2\Sigma^+$ state (where v''=2 is near isoenergetic with $B'^2\Delta$ v'=0) has been studied using the inert gases He, Ar [39,40,41] and Ne [39] as well as the simple non-polar molecules H_2, N_2, CO_2, CH_4 and CF_4. [40,41].

For this system the disparity in the radiative lifetimes of the states in question was exploited to allow examination of the vibronic transfer under pseudo-single collision conditions. The experimental pressure ($\sim$ 1-5 Torr) was arranged such that laser excited SiCl $B'^2\Delta$ ($\tau_{rad} \sim 1$ μs [39]) molecules were likely to undergo collisions prior to emission though any collision-induced $B^2\Sigma^+$ ($\tau_{rad} \sim 10$ ns [39]) would be unlikely to be involved in any further collisions prior to radiation.

Rate constants for the total quenching process were found [40,41] to correlate approximately with the intermolecular attractive force model developed by Parmenter and Seaver [42]. However, the fraction of molecules transferred to the nearby $B^2\Sigma^+$ state was highly quencher dependent, varying from 5 - 100% [39,40, 41].

The product vibrational distributions $B^2\Sigma^+$ (v''=0,1 and 2) varied widely with quencher identity. The maximum product population occurred in all three vibronic levels for different collision partners. This surprising variation is perhaps most striking upon comparison of the $B^2\Sigma^+$ state $v' = 0 : 1 : 2$ branching ratios for He and Ar quenchers (from $B'^2\Delta$ v'=0) which were 9:60:31 and 9:27:64 respectively [40,41]. There was no obvious molecular property that could be used to rationalise these observations although cross sections for the near resonant $B'^2\Delta$ (v'=0) - $B^2\Sigma^+$ (v''=2) channel were found to be roughly correlated with attractive forces.

The limited rotationally resolved measurements showed no significant J' dependence for the specific or total quenching cross sections [40,41]. As this system is the subject of in-depth interest to this thesis it will therefore be discussed in more detail in the following chapters.

1.1.3 Direct Observations of CIEET at the Rovibronic Level

This section deals with CIEET where the specific rovibronic channels have been examined as a result of a single collision.

N_2^+ $A^2\Pi_{ui}$ - $X^2\Sigma_g^+$

The most rigorous series of experiments performed to date concerns the analogous studies upon N_2^+ $A^2\Pi_{ui}$ - $X^2\Sigma_g^+$ and CN $A^2\Pi$ - $X^2\Sigma^+$ transfer in which the initial and product rovibronic populations were determined by OODR under essentially single-collision conditions [19,20,43,44,45,46,47,48,49,50].

The first such study on N_2^+ $A^2\Pi_{ui}$ (v'=4;J') - $X^2\Sigma_g^+$ (v''=7,8,J'') transfer with He as the collision partner was performed using 20 ns wide pump and probe laser pulses [43,44]. These pulses were coincident in time to minimise the effects of multiple collisions. The results showed that there was a strong propensity to conserve rotational angular momentum over both near-isoenergetic and the large energy gap (ΔE = 1760 cm^{-1}) vibronic channels; however, although $\Delta J \approx 0$ is preferred, higher ΔJ's ($\sim \pm 1, 2$) were observed. The collision-induced transitions were also shown to be strictly governed by the optical-like selection rules $s \leftrightarrow s$, $a \leftrightarrow a$ and $s \not\leftrightarrow a$. The transfer rates were observed to be as fast or faster than typical pure RET rates. A subsequent study on the fine structure propensities of the $X^2\Sigma_g^+$ (v''=7) products showed that generally the same intensity pattern results from the initial population of e or f rotational sub-levels [45].

Transfer from the $A^2\Pi_{ui}$ (v'=3) state to $X^2\Sigma_g^+$ (v''=6,7) showed the same propensity for $\Delta J \approx 0$ for both channels, where the energy gaps are approximately 1950 and -23cm^{-1}, respectively [20]. Despite the large difference in energy gaps, the transfer rate is only three times greater for the near-resonant $A(v'=3)$ to $X(v''=7)$ process. It was noted that the quenching rate may be enhanced by an increased Franck-Condon factor for the larger energy gap $A(v'=3)$ to $X(v''=6)$ transition. However, the absolute rates anticipated by the crude exponential energy gap model discussed earlier (see equation 1.2) are several orders of magnitude too small for the larger energy gap transition.

CN $A^2\Pi$ - $X^2\Sigma^+$

The isoelectronic CN $A^2\Pi$ - $X^2\Sigma^+$ collision-induced transition was the subject of OODR studies by Dagdigian *et al* [46,47,48,49,50]. The initial work investigated

transfer from CN $A^2\Pi$ (v'=7,J') to $X^2\Sigma^+$ (v''=11, J'') in the presence of Ar (rotationless $\Delta E \approx 50$ cm^{-1}) [47,46]. Both $A^2\Pi$ and $X^2\Sigma^+$ rovibronic manifolds were probed by LIF via the $B^2\Sigma^+$ state.

Collision-induced transfer rates were shown to be comparable to those for pure CN $A^2\Pi$ - $A^2\Pi$ RET and largely J' independent regardless of the degree of X state character of the initial rovibronic level. The $X^2\Sigma^+$ rotational populations showed significant even-odd alternations of the final rotational quantum number indicative of the near homonuclear character of the Ar-CN molecule in analogy with the complete absence of $s \leftrightarrow a$ transitions in the N_2^+ $A^2\Pi_{ui}$ - $X^2\Sigma_g^+$ system. Again the largest CIEET cross sections are for transitions with small changes in rotational angular momentum of $\Delta J = \pm 0, 1, 2$.

The CN $A^2\Pi$ (v'=3,J') to $X^2\Sigma^+$ (v''=7,J'') transition where the energy gap $\Delta E \approx$640 cm^{-1} showed the same propensity for rotational angular momentum conservation seen with N_2^+ [48]. Despite this much larger energy gap and a considerably smaller Franck-Condon overlap the rate of transfer was comparable to that of the CN $A^2\Pi$ (v'=7,J') to $X^2\Sigma^+$ (v''=11,J'') collision induced transition. Product rotational populations showed an even more enhanced even-odd alternation than that seen previously for CN. On this occasion the transfer propensity to lower-lying $X^2\Sigma^+$ vibrational levels *was* investigated: however, no direct transfer was observed under single-collision conditions.

The rotational product branching oscillations were not observed for $A^2\Pi$ (v'=8,J') to $X^2\Sigma^+$ (v''=12,J'') transfer where the vibronic levels are near isoenergetic [49]. This was deemed to show that the degree of homonuclear character of the CN-Ar system decreases sharply with the C-N separation.

One further study on CN $A^2\Pi$ (v'=7,J') to $X^2\Sigma^+$ (v''=11,J'') transfer was carried out using He as the quenching species (in order to tie in with the parallel theoretical investigations into this same system which will be discussed later) [50]. As before, a similar even-odd alternation of rotational populations was observed though the rotational populations had different peak positions. The ratio of CIEET to pure RET was found to be roughly half that of the corresponding value for Ar quenching.

CN $A^2\Pi$ - $B^2\Sigma^+$

The anomalous intensities of specific rotational lines of the CN $B^2\Sigma^+$ - $X^2\Sigma^+$ in the emission spectra in flames has historically been regarded as evidence for the necessity of 'gateway' states to facilitate collision-induced electronic transitions [16]. It was proposed that preferentially formed CN $A^2\Pi$ populates the $B^2\Sigma^+$, v=0 level by collisionless state mixing and by collisional transfer selectively from perturbed rotational levels in the isoenergetic $A^2\Pi$ v'=10 level.

Dagdigian *et al* used the OODR technique to study this process in detail under the same conditions as that of the CN $A^2\Pi$ - $X^2\Sigma^+$ system [51]. Upon excitation of perturbed $A^2\Pi$ v'=10 rotational levels, fluorescence was observed immediately from the corresponding $B^2\Sigma^+$ v''=0 levels. However, it was observed that even after excitation of *unperturbed* levels, emission was observed from the $B^2\Sigma^+$ state after a delay consistent with single collisions. There was no evidence to support the theory that perturbation enhances this collisional process. The results implied that the observed anomalous intensities in the CN-containing flames are merely due to the large fraction of B state character of the perturbed A state levels.

CO^+ $A^2\Pi$ - $X^2\Sigma^+$

A similar study to the CN and N_2^+ $A^2\Pi$ to $X^2\Sigma^+$ investigations was performed for the isoelectronic CO^+ $A^2\Pi$ (v'=0) - $X^2\Sigma^+$ (v''=10) transfer process where the vibronic levels are nearly isoenergetic [52]. However, unlike the N_2^+ and CN analogues, rapid collision transfer between unperturbed rotational levels was *not* observed. Collision-induced transfer was only observed through the *perturbed* levels. It was noted, perhaps significantly, that the Franck-Condon factor between the two manifolds is substantially smaller than for any previously examined transfer system.

N_2 $a^1\Pi_g$ - $a'^1\Sigma_u^-$

Preliminary research into the N_2 - He $a^1\Pi_g$ (v'=0,J') - $a'^1\Sigma_u^-$ (v''=0,J'') transfer process (where the rotationless $\Delta E \approx 1212$ cm^{-1}) is in qualitative agreement with the analogous N_2^+ - He and CN - Ar experiments [53]. In this experiment the initial N_2 $a^1\Pi_g$ was populated by two-photon excitation and the product states probed by resonance-enhanced multiphoton ionisation (REMPI). CIEET was shown to be as fast or faster than RET, with the same propensity for small ΔJ (though again higher ΔJ's were observed). More importantly, this work demonstrated how REMPI could be exploited for studies of this sort. Due to a combination of the low pressures required and the high sensitivity of REMPI the study of single collision events is much facilitated.

NH $c^1\Pi$ - $A^3\Pi$

A crossed-beam study of NH $a^1\Delta$ electronic quenching by Xe and CO provided rovibrational and fine structure information [54] for this transfer process (previously discussed in section 1.1.2). The Boltzmann temperature of the product NH $X^3\Sigma^-$ rotational distribution was found to be quite cold ($\sim$ 100 K, consistent with the reagent rotational temperature) and to decrease with v'', despite the large energy gap. More significantly, population of all three fine structure levels (F_1,F_2 and F_3) was detected, with the distributions being nearly statistical. This is in complete contrast to the observed absence of F_2 levels in the NH $X^3\Sigma^-$ fragments from the spin-forbidden decomposition of HN_3 [33].

In a diabatic representation of the wavefunctions involved in the quenching process, the presence of the perturber will induce admixtures of other electronic states into the initial and final electronic states [54]. Spin-orbit coupling may then be allowed between states that would otherwise be forbidden from coupling. It has been found from this study [54] of the decomposition process of HN_3 that the singlet electronic wavefunction could be described as an approximately equal mixture of NH($a^1\Delta$)-N_2 and NH($b^1\Sigma^+$)-N_2. Spin-orbit coupling to the triplet

NH($X^3\Sigma^-$)-N_2 state is thus allowed by this singlet component, $b^1\Sigma^+$. The $^1\Sigma^+$ - $^3\Sigma^-$ mixing allows formation of only the symmetric F_1 and F_3 levels.

It has been inferred [54] that as the collision partner is not restricted to a single angle of approach (by contrast with a 'half-collision'), it also affects the triplet state whereby an admixture of $^3\Pi$ character is induced in the NH($X^3\Sigma^-$)-M wavefunction. A second coupling mechanism is thus allowed through the $^1\Delta$ - $^3\Pi$ spin-orbit interaction allowing the formation of symmetric and anti-symmetric NH ($X^3\Sigma^-$) fine-structure levels.

Na_2 $B^1\Pi_u$ - $(2)^1\Sigma_g^+$

The collisional relaxation of Na_2 $B^1\Pi_u$ to $(2)^1\Sigma_g^+$ has been the subject of two independent sets of observations, which have led to conflicting interpretations [55, 1,2]. In the analogous studies a heated cell containing sodium vapour in an argon bath (10 Torr) was excited by exploiting various emission lines of an Ar ion laser to populate rovibronic levels of the $B^1\Pi_u$ state of the sodium dimer.

Hussein *et al* observed the collision-induced infra-red emission attributed to the $(2)^1\Sigma_g^+$ - $A^1\Sigma_u^+$ system [55,1]. Cross sections for $B^1\Pi_u$ to $(2)^1\Sigma_g^+$ transfer were found to be exceptionally large, approaching $2000\mathring{A}^2$ for some channels, and are orders of magnitude greater than typical gas kinetic values. The relative magnitudes of the transfer cross sections were dependent upon ΔE and were found to be negligible for $\Delta E \geq 300$ cm^{-1} at a cell temperature of 770 K.

Due to the short lifetimes of the two states the product rovibronic populations could safely be attributed to single collision events. Upon excitation of $B^1\Pi$ v'=6, J'=43 emission was observed from $(2)^1\Sigma_g^+$ v''=23-26 with $\Delta J''$=0. However, transfer from v'=7, J'=43 produced $(2)^1\Sigma_g^+$ v''=25-29 with $\Delta J''=\pm 1$. This behaviour pattern was attributed to conservation of nuclear spin symmetry [55,1].

The theoretical model developed by Hussein *et al* to describe this system led to the conclusion that the collision partner must be excited Na ($3p^2P$) atoms [55]. This was based on the assumption of a long range quadrupole-dipole interaction therefore on this basis the quencher must possess non-zero electronic angular mo-

mentum and hence cannot be either the argon bath gas or ground state Na ($3s^2S$) atoms.

A subsequent study by McCaffery and co-workers came to a rather different conclusion concerning the identity of the quencher [1,2]. This investigation monitored the $A^1\Sigma_u^+$ - $X^1\Sigma_g^+$ fluorescence which followed the $(2)^1\Sigma_g^+$ - $A^1\Sigma_u^+$ emission. The $A^1\Sigma_u^+$ state populations were found to be vibrationally inverted peaking at v=5. This observation was consistent with the inferred populations of the $(2)^1\Sigma_g^+$ state from the previous infra-red measurements and the Franck-Condon factors for the $(2)^1\Sigma_g^+$ - $A^1\Sigma_u^+$ transition.

For the first, and only, time to date in an electronic energy transfer experiment, the fluorescence polarisation was also monitored. The linear polarisation of the emission was found to be negative with respect to the laser linear polarisation. As the excitation step Σ - Π is a perpendicular transition and the observed Σ - Σ fluorescence is a parallel transition there must be a considerable propensity to conserve the molecular alignment, expressible through the M_J distribution, as a result of the collision induced $B^1\Pi$ - $(2)^1\Sigma_g^+$ crossing. By analogy with studies of pure RET, where the conservation of plane of rotation is also observed [56], the transfer process was attributed to that of a 'sudden' interaction, the dynamical opposite of the long range interaction [2].

McCaffery's group argued that the concentration of excited Na atoms would be too low to account for the observed fluorescence. As transfer also occurred in the absence of the bath gas, the collision partner was deduced to be ground state Na ($3s^2S$) atoms.

Na_2 $A^1\Sigma_u^+$ - $b^3\Pi_u$

As a result of a spectroscopic study of the Na_2 Rydberg states it was observed that efficient state-specific collision-induced transitions occurred between the mutually perturbing Na_2 $A^1\Sigma_u^+$ and $b^3\Pi_u$ states [57]. This was subsequently investigated in more detail by cw OODR from which it was proposed that a perturbation is

essential for CIEET between two electronic states connected by a dipole-forbidden transition [58].

Excitation of $A^1\Sigma_u^+$, $v' = 26$ resulted in transfer to the near isoenergetic $b^3\Pi_u$, $v'' = 28$ level ($\Delta E \leq 10$ cm^{-1}) only via perturbed a-symmetry $A^1\Sigma_u^+$ parent levels. However, regardless of which a-symmetry $A^1\Sigma_u^+$ level is populated the product population is always centered about $b^3\Pi_u$, J=16e,a which is significantly perturbed by the isoenergetic $A^1\Sigma_u^+$, J'=16,a level. Hence inter-system crossing between these two vibronic levels was inferred as occurring only through this strongly perturbed 'gateway' level.

Li_2 ^1R_g - ^3R_g

Following the two-step laser excitation of five Li_2 Rydberg states ^1R_g ($5d\delta^1\Delta_g$, $5d\pi^1\Pi_g$, $5d\sigma^1\Sigma_g^+$, $6d\delta^1\Delta_g$ and $6s\sigma^1\Sigma_g^+$) collisional-induced fluorescence was observed from the neighbouring triplet Rydberg state ^3R_g, respectively [59]. Transfer from $5d\pi^1\Pi_g$ v'=0-5, J'=30 was studied in greater detail, with the identity of the product state deduced to be a previously unobserved $^3\Delta_g$ state. The propensity for small ΔE, which varied between 0-30 cm^{-1}, appeared to be greater than that for the conservation of J: hence, transfer was only observed between near-isoenergetic rovibronic levels.

K_2 $^1\Delta_g$ - $^1\Sigma_g^+$

The most recent investigation of collisional induced electronic energy transfer in an alkali diatomic is that of the $^1\Delta_g$ (v'=0) - R_1 $^1\Sigma_g^+$ (v''=0) and $^1\Delta_g$ (v'=2) - R_2 $^1\Sigma_g^+$ (v''=2), R_3 $^1\Sigma_g^+$ (v''=2) Rydberg states of K_2 ($\Delta E \leq 10$ cm^{-1}) which have been studied by continuous wave (cw) OODR [60].

For all three transfer processes there was a greater propensity to conserve rotational angular momentum than to conserve energy. The rate of transfer from $^1\Delta_g$ (v'=2) - R_2 $^1\Sigma_g^+$ (v''=2) was found to be greater than for the larger ΔE, $^1\Delta_g$ (v'=2) - R_3 $^1\Sigma_g^+$ (v''=2) process. Again there are rigorous selection rules, corresponding to the conservation of nuclear spin for the CIEET process in that for

odd J_e $^1\Delta_g$ levels, $\Delta J = 0,\pm 2$, and for *even* J_f levels, $\Delta J = \pm 1$. The fluorescence intensities indicated that the collision-induced transition probability was quite large.

I_2 $E(0_g^+)$ - $D(0_u^+)$

The collisional relaxation of I_2 has been studied for a single rovibrational quantum state, $E(0_g^+)$, v'=8, J'=56 [61]. This state was produced by two-colour OODR of I_2 vapour and followed by dispersion of the resultant fluorescence.

The collisional electronic relaxation process was found to be remarkably state specific and efficient with no rotational relaxation observed. Fluorescence was monitored in the $D(0_u^+)$ - $X(0_g^+)$ system from v''=10, J''=56 when only I_2 was present and from v''=11 and 12, J''=56 states as well in the presence of O_2 or N_2. Obviously this process shows a remarkable propensity for the selection rule $\Delta J = 0$.

1.2 Theoretical Investigations

Theoretical investigations into CIEET have been somewhat limited in the past both in terms of abundance and universal success. The majority of studies have concentrated upon the role of the intermolecular forces on the rate of electronic quenching. The two different approaches for this type of description of energy transfer is that the dominant intermolecular interaction are either that of a short range repulsive or a long range attractive interaction. Unfortunately only small subset of the existing theoretical work has attempted to rationalise the propensities for the state-specific transfer channels for specific CIEET processes.

1.2.1 Long Range Attractive Intermolecular Interaction

The majority of the experimental investigations into the role of long range forces in quenching of diatomic molecules have examined the dependence of the quenching rate upon the rotational angular momentum of the excited species.

Due to the typically anisotropic nature of the intermolecular potential there will be particular collision orientations which will preferentially lead to the electronic quenching event. Hence as J is increased these preferred 'valleys' of approach will become averaged out resulting in a decrease in the quenching cross section. A good example of this dependence is the study on the quenching of OH $A^2\Pi$ where the quenching rate was found to decrease with J [27].

The presence of long-range interactions can also be deduced by comparison of the electronic quenching cross-sections for a range of quenchers with those predicted by various existing empirical models. These have been constructed in slightly different ways but all are essentially based on some measure of the long range forces.

The model developed by Selwyn and Steinfield was based on the assumption that dispersion forces dominate the quenching process [62]. The cross section σ

for quenching of A by quencher M is given by

$$\sigma \propto \mu^{1/2} I_M \alpha_M R_c^{-3} \tag{1.5}$$

where μ is the reduced collision mass, I_M is the ionisation potential of the quencher, α_M is the polarisability of the quencher and R_c is the hard sphere collision radius.

A less general model developed by Thayer and Yardley [63] accounted both for polar-nonpolar (pn) and polar-polar (pp) interactions such that

$$\sigma_{pn} = A\mu^{1/2} I_A^2 I_M^2 (I_A + I_M)^{-2} \alpha_M^2 R_c^{-9} + C \tag{1.6}$$

$$\sigma_{pp} = B\mu^{1/2} D_M^2 R_c^{-3} \tag{1.7}$$

where D_M is the permanent dipole moment of the quencher and A, B and C are constants. The total quenching cross section is obviously the sum of σ_{pn} and σ_{pp}.

The well depth of the collisional pair interaction was the basis of the empirical model proposed by Parmenter and Seaver [42] where σ scales as

$$ln(\sigma) = lnC + \varepsilon_{AM}/kT \tag{1.8}$$

C is a constant and ε_{AM} is the intermolecular well depth which is calculated by assuming the geometric mean of the molecule-molecule and molecule-quencher well depths, ε_{AA} and ε_{MM}, respectively

$$\varepsilon_{AM} \approx (\varepsilon_{AA}\varepsilon_{MM})^{1/2} \tag{1.9}$$

The magnitude of ε_{AA} will be the same for studies of quenching rates for different quenchers, thus equation 1.8 can be modified to

$$ln(\sigma) = lnC + \beta(\varepsilon_{MM}/k)^{1/2} \tag{1.10}$$

where β is a constant given by

$$\beta = (\varepsilon_{AA}/kT^2)^{1/2} \tag{1.11}$$

This relationship will hold assuming there are no resonant or chemical reaction channels available.

More recent work by Crosley *et al* [64] attempted to describe this interaction potential by the combination of all physical intermolecular forces. These multipole attractive forces are described by a one-dimensional potential, given by

$$V_r = -C_3/r^3 - C_4/r^4 - C_6/r^6 \tag{1.12}$$

where r is the collision pair separation, C_3/r^3 the dipole-dipole, C_4/r^4 the dipole-quadrupole and C_6/r^6 the sum of the dipole-induced dipole (C_6'/r^6) and dispersion interactions (C_6''/r^6). These parameters are approximated as the magnitudes at the orientation of maximum interaction. They are therefore given as

$$C_3 = 2\mu_A\mu_M \tag{1.13}$$

$$C_4 = 3/2(\mu_A Q_M + \mu_M Q_A) \tag{1.14}$$

$$C_6' = 2(\mu_A^2\alpha_M + \mu_M^2\alpha_A) \tag{1.15}$$

$$C_6'' = 3/2\frac{I_A I_M}{I_A + A_M}\alpha_A\alpha_M \tag{1.16}$$

where in this case μ_A and μ_M are the dipole moments and Q_A and Q_M the quadrupole moments of the collision partners.

Taking account of the centrifugal barrier for the approach of the quencher, equation 1.12 should be modified to that of the effective potential, V_{eff}, where

$$V_{eff} = V_r + \frac{Eb^2}{r^2} \quad , \tag{1.17}$$

b is the collision impact parameter and E is the kinetic energy of the collision. Thus the centrifugal barrier will occur at r_{max}, defined by

$$\frac{d}{dr}\left[V_{eff}(r)\right]_{r_{max}} = 0. \tag{1.18}$$

Only when the molecules can approach within this value of r_{max} can they experience the effect of the attractive forces. This will occur when

$$\left[E - V_r + \frac{Eb^2(E)}{r^2}\right]_{r_{max}} \geq 0. \tag{1.19}$$

The value of r_{max}, which can be evaluated by solving equation 1.18, thus determines b_{max} through

$$b_{max}^2(E) = r_{max}^2(1 - \frac{V_r}{E}). \tag{1.20}$$

and hence defines the classical cross-section σ_E where

$$\sigma_E = \pi b_{max}^2(E). \tag{1.21}$$

This well known approach is otherwise called the 'line-of-centres' model.

From this the thermally averaged cross-section $\sigma(T)$ can be calculated for a given temperature T by

$$\sigma(T) = \frac{1}{(kT)^2}\int_0^\infty \sigma_E E exp(\frac{-E}{kT})dE \tag{1.22}$$

assuming that all collisions which cross the effective barrier result in a quenching interaction.

This model predicted σ's which correlated well, for example, with experimental cross sections for the quenching of OH $A^2\Pi$ for a range of molecular quenchers [64].

1.2.2 Curve Crossing

The long range attractive force models discussed above were developed to describe resonant and/or near-resonant energy transfer processes. One qualitative model devised to justify non-resonant transfer is the 'curve crossing' mechanism which was applied to describe collisional quenching of excited atomic species [65]. A simple approach to this model would be to consider two electronic states A' and A'' separated by energy ΔE. With the approach of collider M a differential interaction between the two states and M could lead to a potential curve crossing at r_x as depicted in figure 1–2.

Thus a perturbation which might not be strong enough to couple A' and A'' at large ΔE may be sufficient at the crossing point of the diabatic potentials which *exclude* the coupling, where ΔE is zero, to allow coupling. This assumes that there is sufficient kinetic energy available for this crossing point to be reached during a collision.

If the A-M separation could be varied infinitely slowly it would be found that the potential curves will *not* cross, if a perturbation couples the states, resulting

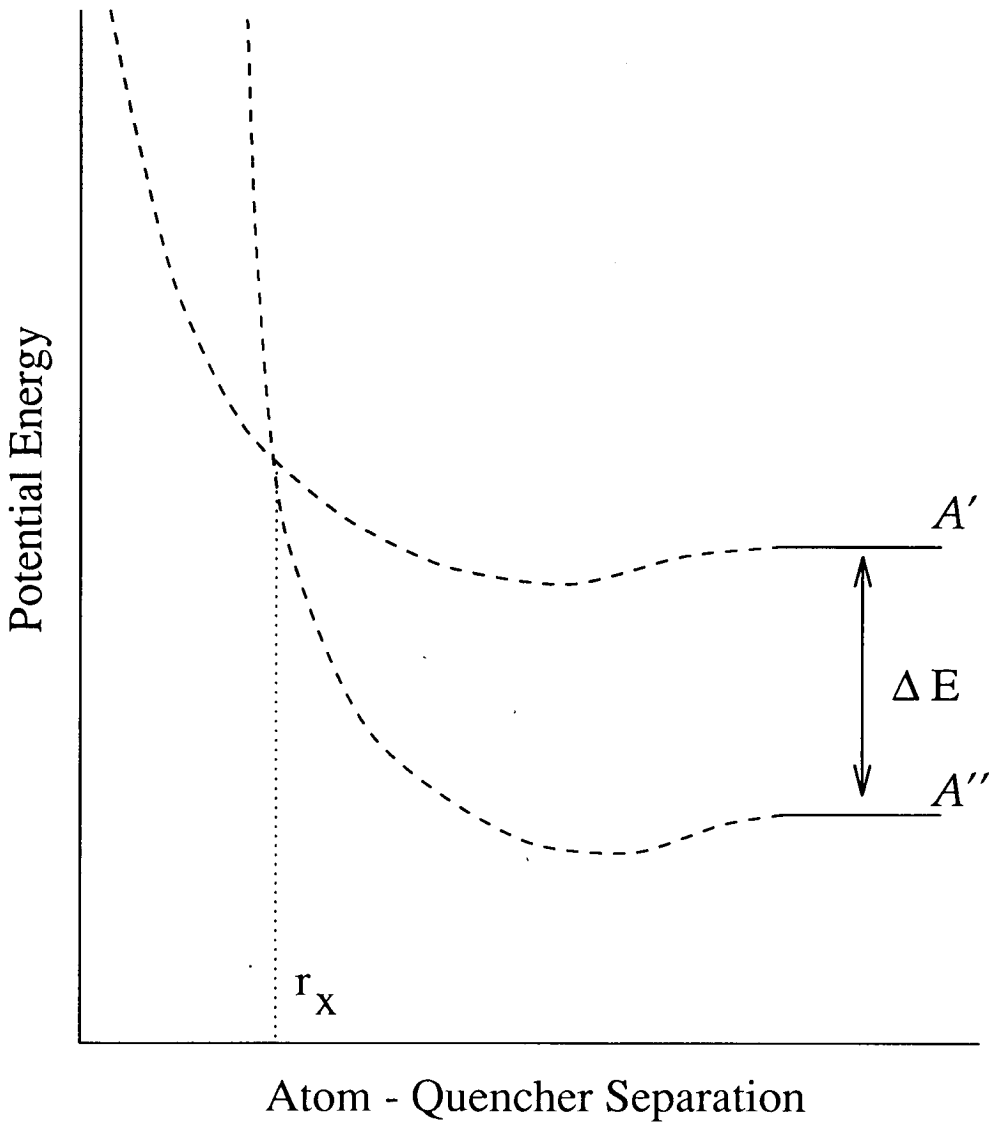

Figure 1–2: Diabatic potential energy as a function of the atom-quencher separation of excited atomic states A' and A'', with an initial energy gap of ΔE, with collision partner M. A curve crossing occurs at r_x.

in two *adiabatic* curves due to the 'non-crossing' rule [66]. However if the A-M motion is sufficiently fast that the interaction does not have 'time' to act then the motion will follow the 'original' *diabatic* curves.

A successful model used to justify the non-adiabatic transition is the approximate probability function developed by Landau and Zener [67,68]. The probability of crossing between the *diabatic* surfaces (*i.e.* remaining on the same *adiabatic* surface) is given by

$$P_{LZ} = 1 - exp(-w), \tag{1.23}$$

where

$$w = \left[\frac{-2\pi U_{12}^2}{\hbar|F_2 - F_1|v_x}\right]. \tag{1.24}$$

U_{12}^2 is the square of the interaction matrix element between the states, v_x is the collision velocity and $|F_2 - F_1|$ is the modulus of the difference between the slopes of the two *diabatic* surfaces. Hence the probability of a non-adiabatic transition (*i.e.* remaining on the same *diabatic* surface) is

$$P = 1 - P_{LZ} = exp(-w). \tag{1.25}$$

For any real collision the system must an approach and return passage through the crossing point. Assuming that the transition probability remains constant at both crossing events, the probability of an overall $A'' \longrightarrow A'$ transition is equal to the product of the probabilities of $A'' \longrightarrow A'$ and $A' \longrightarrow A'$ plus $A'' \longrightarrow A''$ and $A'' \longrightarrow A'$ which gives

$$P_{A''-A'} = 2exp(-w)\left[1 - exp(-w)\right]. \tag{1.26}$$

1.2.3 Short Range Repulsive Interaction

The universally accepted model for energy transfer processes in small molecules dominated by a repulsive interaction is one devised by Schwartz, Slawsky and Herzfeld (SSH) [69]. This describes the vibration-to-translation energy transfer due to a collinear collision between a diatomic molecule AB and an atom C.

The probability, P, of a transition between two vibrational levels m and n of a diatomic induced by an atomic collision (where the atomic masses are M_A, M_B and M_C, respectively) is given by [67]

$$\begin{aligned} P_{nm} &= \left[\frac{4M_A^2 M_B M_C}{(M_B+M_C)(M_A+M_B)^2}\mu\right]\frac{1}{2}(\frac{2\pi}{3})^{1/2}(\frac{\theta'}{\theta})(\frac{\theta'}{T})^{1/6} \\ &\times exp\left[-3/2(\frac{\theta'}{T})^{1/3}\right] exp(\frac{\theta}{2T}) exp(\frac{\varepsilon}{kT}), \end{aligned} \tag{1.27}$$

where

$$\theta' = 4\pi^2\mu L^2\omega^2/k \quad , \tag{1.28}$$

and

$$\theta = \frac{h\omega}{2\pi k} \quad . \tag{1.29}$$

ε is the well depth of the interaction, ω is the diatomic oscillator frequency in s^{-1}, L is the distance of approach at which energy transfer occurs and μ is the collision reduced mass. Fortunately, under isothermal experimental conditions, equation 1.27 is dominated by the term $exp\left[-3/2(\frac{\theta'}{T})^{1/3}\right]$ so that the probability scales as

$$ln(P_{nm}) = A - \mu^{1/3} \tag{1.30}$$

where A is a combination of three terms which are approximately constant.

1.2.4 State Specific Energy transfer

The formative theoretical work on state specific electronic energy transfer tended to focus upon the necessity for non Born-Oppenheimer state mixing between rovibronic levels in the isolated molecule *prior* to collision with the quencher. As noted in section 1.1.2, Gelbert and Freed [15] developed a simple model to describe transitions of this type. Their work was inspired by observation of the anomalously large intensities of specific rotational lines of the CN $B^2\Sigma^+$ - $X^2\Sigma^+$ transition in the emission spectra of organic/nitrogen flames [16]. As described in section 1.1.3, it was proposed that preferentially formed CN $A^2\Pi$ populates the $B^2\Sigma^+$, v=0 level by collisionless state mixing and by collisional transfer selectively from perturbed rotational levels in the isoenergetic $A^2\Pi$ v=10 level.

They proposed that the rate of inter-electronic transfer, k, between pure $^2\Pi$ and perturbed $^2\Sigma$ levels will be

$$k = z\frac{|< \ ^2\Pi \mid V_{coll}(\Delta E') \mid \rho \ ^2\Pi + (1-\rho^2)^{1/2} \ ^2\Sigma^+ >|^2}{\hbar^2} \qquad (1.31)$$

where z is the gas-kinetic collision rate, $V_{coll}(\Delta E')$ is the Fourier transform of the intermolecular interaction potential (depending on time through the classical trajectory) evaluated at the energy difference in question, ΔE. ρ is the state mixing coefficient. The transfer process from unperturbed levels was therefore deemed to be dependent upon the rate of rotational energy transfer within the initial vibronic level because transfer was predicted to be significantly faster via the perturbed rotational levels.

This model was extended by Alexander *et al* [70] for the theoretical study of collision-induced transitions between the low-lying $^1\Sigma^+$ and $^1\Pi$ state of CaO where it had been suggested that perturbations played a role [71].

Since it has now been established experimentally that perturbations are *not* a requirement for CIEET, as noted extensively in section 1.1, there have been further, alternative major theoretical contributions to the study of state-to-state collision-induced transitions between electronic states of diatomic molecules. These were initiated by the development of an exact quantum description of CIEET between $^2\Pi$ and $^2\Sigma$ states of a diatomic molecule by Alexander and Corey to enable the necessary *ab initio* calculations to produce the relevant potential energy surface (PES) [72]. This description was done while ignoring the effects of non Born-Oppenheimer state mixing in the isolated molecule (*i.e.* abandoning the 'gateway' requirement).

The basis of this description is the lifting of the cylindrical symmetry of the diatomic by the approach of the collision partner (except for a collinear approach). Thus the $^2\Sigma$ wavefunctions have A' symmetry in the C_s point group whereas the $^2\Pi$ wavefunctions are split into A' and A'' symmetry species. It is the mixing of the two A' states that results in the transfer between the two electronic states.

Upon transformation to a diabatic basis, *four* potential energy functions V_Σ, V_Π, V_1 and V_2 are required to describe the interaction of the $^2\Sigma$ and $^2\Pi$ with

the collision partner [72]. V_Σ represents the interaction of the $^2\Sigma$ state with the perturber. Two surfaces (denoted V_Π-V_2 and V_Π+V_2 for A' and A'' components, respectively) are required to describe the interaction of the $^2\Pi$ state with the perturber. V_1 is the potential energy function of the perturber-induced coupling between the Σ and Π (A') components.

One of the main conclusions of this work was that for collisions involving a homonuclear diatomic, s/a symmetry will be rigorously conserved. It was also proposed that the use of the Franck-Condon approximation could *not* be justified. This is because the collisions could neither be described by a perturbative, weak limit nor by a sudden approximation in which collisions occur on a time scale where the vibrational motion could be described as 'frozen'.

Two collisional propensity rules were developed as a result of this work:
1. cross sections for $^2\Pi$ - $^2\Sigma$ $\Delta J = 0$ transitions will become vanishingly small for transitions which conserve the e/f symmetry index of the molecular wavefunction (where e represents the Λ-doublet symmetric with respect to reflection in the plane of molecular rotation).
2. $^2\Pi$ - $^2\Sigma$ transitions from initial high J levels, for which a Hund's case(b) description of the $^2\Pi$ state is appropriate, will occur only via F_1, f - $^2\Sigma^+, e$ (or $^2\Sigma^-, f$) and F_2, e - $^2\Sigma^+, f(^2\Sigma^-, e)$ levels.

Using this approach, potential energy surfaces were computed for the collision of CN ($X^2\Sigma^+$, $A^2\Pi$) with He [73] from *ab initio* MCSCF and MCSCF-CI wavefunctions using an extensive basis set. The coupling potential was shown to be only weakly dependent upon the CN internuclear separation and exponentially decreasing with CN - He distance.

These surfaces were consequently used to calculate cross sections for rovibronic collision-induced energy transfer for this CN - He system [74] and compared with the experimental cross sections for the analogous CN - Ar system measured by Dagdigian *et al* [46,47,48,49] (as discussed in section 1.1.3). The cross sections calculated for $A^2\Pi, (v' = 7)$ - $X^2\Sigma^+, (v'' = 11)$ and $A^2\Pi, (v' = 8)$ - $X^2\Sigma^+, (v'' = 12)$ transfer were of comparable magnitude to Dagdigian *et al*'s experimental values [46,47,48,49]. Both transitions, however, were predicted to display oscillatory

structure as a function of the final state rotational quantum number (where the phase of this alternation is dependent upon whether the initial Λ doublet level is e or f). This contrasts with the experimental observation of the absence of the oscillatory structure in the $A^2\Pi(v' = 8)$ - $X^2\Sigma^+(v'' = 12)$ system [49].

The most striking differences between cross sections emerged from comparison of the values for $A^2\Pi$ (v'=3) - $X^2\Sigma^+(v'' = 7)$ transfer where the calculated cross-sections were found to be $\sim 10^{-5}\mathring{A}$. These were significantly smaller than the experimental values which had been shown experimentally to be equivalent to those for $A^2\Pi, (v' = 7)$ - $X^2\Sigma^+, (v'' = 11)$ and $A^2\Pi, (v' = 8)$ - $X^2\Sigma^+, (v'' = 12)$ transfer. The failure of the calculation in this case was attributed to the significantly larger energy gap for this transition.

To resolve this discrepancy between the calculated and experimental values *ab initio* potential energy surfaces were computed for the equivalent CN - Ar system [74]. The calculations were then repeated using the new surfaces but although there was an enhancement for the $A^2\Pi$ (v'=3) - $X^2\Sigma^+(v'' = 7)$ transfer cross sections, relative to the CN - He values, they were still orders of magnitude smaller than the experimental results [49].

Subsequently, a tandem experimental and theoretical reinvestigation of the CN $A^2\Pi$, $v' = 7$ to $X^2\Sigma^+$, v''=11 transition induced by collisions with He has been performed (as previously mentioned in section 1.1.3) [50]. For the first time non-Born-Oppenheimer mixing between the $A^2\Pi$ and $X^2\Sigma^+$ states in the isolated CN molecule was included in the quantum scattering calculations. Generally there was a good agreement between the experimental results and the calculated values. The experimentally determined even-odd alternation in the final rotational state distribution was somewhat reduced compared to the calculated (and the previously measured CN - Ar $A^2\Pi$, $v' = 7$ to $X^2\Sigma^+$, v''=11 [46,47,48,49]) values though this was attributed mainly to multiple collision effects although it was assumed that the He partner did *not* affect the CN fine structure levels.

The total $A - X$ transfer cross sections were measured to be approximately a factor of two smaller for He as the collision partner [50] compared to the previous Ar measurements [46,47,48,49]. This was shown to be consistent with the

calculations where the V_1 coupling potential for CN - Ar was approximately twice as large as the equivalent CN - He potential at their respective 300 K classical turning points.

1.3 Overview

Upon examination of the available experimental data it is apparent that there are many factors governing collision-induced intramolecular electronic energy transfer.

Isoenergetic transfer has traditionally been seen as the major transfer channel such that the theoretical studies have been largely constrained to this approach. Indeed much of the experimental work, particularly the OODR studies, have focussed entirely upon it and no other. However, although isoenergetic transfer is often the favoured channel there is a growing body of data which shows appreciable transfer rates over considerable energy gaps. More significantly, a subset of this data also demonstrates that the isoenergetic channel is often secondary or even negligible when compared to larger energy gap transitions.

The Franck-Condon overlap is currently not considered to play a significant role in determining the specific transfer channels both due to theoretical considerations and lack of any substantial experimental evidence. However, the case of NH $a^1\Delta$ -$X^3\Sigma^-$ transfer [32] did appear to show some correlation though the data set was somewhat limited. The crude attempts made to correlate transfer cross sections with the Franck-Condon overlap and the energy gap have proved far from successful, though the absence of isoenergetic transfer in the CO^+ $A^2\Pi$ ($v' = 0$) - $X^2\Sigma^+$ ($v'' = 10$) (where the Franck-Condon factor is $\sim 10^{-5}$), with the exception of the rotationally perturbed levels, would seem to indicate that the overlap may play some role [52].

Although it is well established that perturbations in the isolated molecule are not a general requirement for CIEET it is apparent that they are necessary for some specific transfer systems. Unfortunately there is again not sufficient evidence to draw any absolute conclusions.

There is also conflicting evidence for the J' dependence upon the transfer cross sections and for the propensity to conserve the rotational angular momentum after collision over both small and large vibronic energy gaps. It is not immediately apparent why J' should be significant in some cases but not in others where the systems would appear to be similar.

The significance of the identity of the collision partner is something which has not been investigated rigorously for the majority of systems studied. Although it is well established that the identity will affect the transfer cross sections, there has been little attention paid to any variation in their rovibronic product state distributions. This is obviously an aspect of the field which requires more attention.

Unfortunately, due to the lack of rigorous tandem state-to-state theoretical and experimental investigations (with the obvious exception of the CN $A^2\Pi$ - $X^2\Sigma^+$ system by Alexander *et al* and Dagdigian *et al*, respectively) it is impossible to establish a general predictive model for specific channel propensities and cross sections. Such a model would need to be based upon *all* the variable parameters such that

$$\sigma_{i\rightarrow f} \propto f(J', J'', v', v'', \Delta E, q_{v'v''}, V), \tag{1.32}$$

where V is represents the potential energy surfaces between the quencher and the molecule in the initial and final states and the quencher-induced coupling between them.

1.4 Proposed Work

The aim of this work was to extend the existing data set such that the prospects for the formulation of a predictive model for CIEET might be enhanced.

As the majority of the prior work on the SiCl $B'^2\Delta$ - $B^2\Sigma^+$ system was carried out at this university [40,41] and (coincidentally) produced perhaps the most intriguing set of results, it was decided to investigate the electronically analogous system of the related silyl halide, SiF $C^2\Delta$ - $B^2\Sigma^+$. It was hoped that this study might reveal the degree to which SiCl transfer system is a true anomaly.

For more practical reasons, the SiF transfer system was particularly attractive because it was anticipated that that there would be a similar disparity between the relative radiative lifetimes of the $C^2\Delta$ and $B^2\Sigma^+$ states (as observed in SiCl). In this event, the transfer system could be studied under pseudo-single collision conditions using readily available equipment and without the need for a second probe laser (as required, for example, in OODR). Thus the proposed series of experiments could be performed more simply and without further expenditure.

The experimental equipment used for the studies described in the remainder of this thesis will be discussed in detail in the following chapter. Chapter three concerns the preliminary spectroscopic studies of the SiF $B^2\Sigma^+ - X^2\Pi$ and $C^2\Delta - X^2\Pi$ transitions required for the analysis of the subsequent energy transfer data. The results for the collision-induced *vibronic* energy transfer process for SiF $C^2\Delta$ to $B^2\Sigma^+$ are discussed in chapter four. This chapter also includes the results for the repeated measurements of some of quenching and transfer rates for the analogous SiCl electronic states. The preliminary results of work investigating the J' dependence and the ΔJ propensities of the SiF $C^2\Delta$ to $B^2\Sigma^+$ transfer process are reported in chapter five. Finally, the implications of the energy transfer results reported in this thesis are discussed in chapter six.

Bibliography

[1] A.G Astill. A.J. McCaffery and B.J. Whitaker, Chem. Phys. Letts. **125** (1986) 33.

[2] A.G Astill. A.J. McCaffery, S.C. Taylor, B.J. Whitaker and M.J. Wynn, J. Chem. Phys. **89** (1989) 184.

[3] T.A. Miller and V.E. Bondybey, Chem. Phys. Letts. **50** (1977) 275.

[4] V.E. Bondybey and T.A. Miller, J. Chem. Phys. **69** (1978) 3597.

[5] D.H. Katayama, T.A. Miller and V.E. Bondybey, J. Chem. Phys. **71** (1979) 1662.

[6] V.E. Bondybey, J. Chem. Phys. **63** (1977) 794.

[7] V.E. Bondybey and N. Nitzen, Phys. Rev. Letts. **38** (1977) 889.

[8] H. Dubost and R. Charneau, Chem. Phys. **12** (1976) 407.

[9] G.A. West and M.J. Berry, J. Chem. Phys. **61** (1974) 4700.

[10] G.A. West and M.J. Berry, Chem. Phys. Letts. **56** (1978) 423.

[11] R.Fei, D.E. Adelman, T. Carrington, C.H. Dugan and S.V. Filseth, Chem. Phys. Letts. **232** (1995) 547.

[12] N Sadeghi and D.W. Setser, Chem. Phys. Letts. **77** (1981) 304.

[13] N Sadeghi and D.W. Setser, J. Chem. Phys. **79** (1983) 2710.

[14] A. Rotem, I. Nadler and S. Rosenwaks, Chem. Phys. Letts. **83** (1981) 281.

[15] W.M. Gelbert and K.F. Freed, Chem. Phys. Letts. **18** (1973) 470.

[16] D.W. Pratt and H.P. Broida, J. Chem. Phys. **50** (1969) 2181.

[17] S. Leach, M. Devoret and J. Eland, Chem. Phys. **33** (1978) 113.

[18] D.H. Katayama, T.A. Miller and V.E. Bondybey, J. Chem. Phys. **72** (1980) 5469.

[19] D.H. Katayama, A.V. Dentamaro and J.A. Welsh, J. Chem. Phys. **87** (1987) 6983.

[20] D.H. Katayama and A.V. Dentamaro, J. Chem. Phys. **91** (1989) 4571.

[21] A. Rotem, I. Nadler and S. Rosenwaks, J. Chem. Phys. **76** (1982) 2109.

[22] A. Rotem and S. Rosenwaks, Optical Engineering **22** (1983) 564.

[23] D.R. Crosley, J. Chem. Phys. **93** (1984) 295.

[24] N.L. Garland and D.R. Crosley, Applied Optics **24** (1985) 4229.

[25] K.J. Rensberger, M.J. Dyer and R.A. Copeland, Applied Optics **27** (1988) 3679.

[26] D.R. Crosley, R.A. Copeland and J.B. Jeffries, SRI International Report, (1988).

[27] R.A. Copeland and D.R. Crosley, Chem. Phys. Letts. **107** (1984) 295.

[28] H. Okabe, J. Chem. Phys. **49** (1968) 2726.

[29] F. Rohrer and F. Stuhl, J. Chem. Phys. **86** (1987) 226.

[30] H.H. Nelson and J.R. McDonald, J. Chem. Phys. **93** (1990) 8777.

[31] J.S. Adams and L. Pasternack, J. Phys. Chem. **95** (1991) 2975.

[32] W. Hack and K. Rathmann, J. Phys. Chem. **96** (1992) 47.

[33] M.H. Alexander, H.-J. Werner and P.J. Dagdigian, J. Chem. Phys. **89** (1989) 1388.

[34] J. Wildt, G. Bednarek and E.H. Fink, Chem. Phys. **122** (1988) 463.

[35] Y. Matsumi, T. Munakata and T.Kasuya, J. Phys. Chem. **88** (1984) 264.

[36] I.J. Wysong, J.B. Jeffries and D.R. Crosley, J. Chem. Phys. **91** (1989) 5343.

[37] A. Jenouvier and B. Pascat, Can. J. Phys. **58** (1980) 1275.

[38] Ch. Ottinger and A.F. Vilesov, J. Chem. Phys. **100** (1994) 1805.

[39] J.B. Jeffries, J. Chem. Phys. **95** (1991) 1628.

[40] S. Singleton, Laser Based Studies of Transient Species in a Discharge Flow Apparatus, PhD Thesis, University of Edinburgh, (1990).

[41] K.G. McKendrick and S. Singleton, J. Phys. Chem. **97** (1993) 1389.

[42] H.M. Lin, M. Seaver, K.Y. Lang, A.E.W. Knight and C.S. Parmenter, J. Chem. Phys. **70** (1979) 5442.

[43] D.H. Katayama, J. Chem. Phys. **81** (1984) 3495.

[44] D.H. Katayama, Phys. Rev. Letts. **54** (1985) 657.

[45] D.H. Katayama and A.V. Dentamaro, J. Chem. Phys. **85** (1986) 2595.

[46] N. Furio, A. Ali and P.J. Dagdigian, Chem. Phys. Letts. **125** (1986) 561.

[47] N. Furio, A. Ali and P.J. Dagdigian, J. Chem. Phys. **85** (1986) 3860.

[48] G Jihua, A. Ali and P.J. Dagdigian, J. Chem. Phys. **85** (1986) 7098.

[49] A. Ali, G Jihua and P.J. Dagdigian, J. Chem. Phys. **87** (1987) 2045.

[50] P.J. Dagdigian, D. Patel-Misra, A. Berning, H.-J. Werner, M.H. Alexander, J. Chem. Phys. **98** (1993) 8580.

[51] A. Ali, G Jihua and P.J. Dagdigian, Chem. Phys. Letts. **131** (1986) 331.

[52] A.V. Dentamaro and D.H. Katayama, J. Chem. Phys. **90** (1989) 91.

[53] D.H. Katayama and A.V. Dentamaro, J. Chem. Phys. **97** (1992) 2820.

[54] D. Patel-Misra and P.J. Dagdigian, J. Chem. Phys. **97** (1992) 4871.

[55] K. Hussein, M. Aubert-Frécon, O. Babaky, J. D'Incan, C. Effantin and J. Vergès, J. Mol. Spec. **114** (1985) 105.

[56] A.J. McCaffery, M.J. Proctor and B.J. Whitaker, Ann. Rev. Phys. Chem. **37** (1986) 223.

[57] L. Li and R.W. Field, J. Mol. Spec. **117** (1986) 245.

[58] L. Li, Q. Zhu, A.M. Lyyra, T.-J. Whang, W.C. Stwalley, R.W. Field and M.H. Alexander, J. Chem. Phys. **97** (1992) 8835.

[59] S.B. Rai, B. Hemmerling and W. Demtröder, Chem. Phys. **97** (1985) 127.

[60] L. Li, A.M. Lyyra, H. Wang and W.C. Stwalley, Chem. Phys. Letts. **179** (1991) 417.

[61] W. Ubachs, I. Aben, J.B. Milan, G.J. Somsen, A.G. Stuiver and W. Hogervorst, Chem. Phys. **174** (1993) 285.

[62] J.E. Selwyn and J.I. Steinfeld, Chem. Phys. Letts. **4** (1969) 217.

[63] C.A. Thayer and J.T. Yardley, J. Chem. Phys. **57** (1972) 3992.

[64] P.W. Fairchild, G.P. Smith and D.R. Crosley, J. Chem. Phys. **79** (1983) 1795.

[65] J.J. Kaufman, Adv. Chem. Phys. **28** (1975) 113.

[66] G. Herzberg, Molecular Spectra and Molecular Structure I. Spectra of Diatomic Molecules 2nd Edition (Van Nostrand, New York, 1950).

[67] J.T. Yardley, Introduction to Molecular Energy Transfer (Academic Press, New York 1980).

[68] J.C. Tully and R.K. Preston, J. Chem. Phys. **55** (1971) 562.

[69] R.N. Schwartz, Z.I. Slawsky and K.F. Herzfeld, J. Chem. Phys. **20** (1952) 1591.

[70] M.H. Alexander and M. Osmolovsky, J. Chem. Phys. **77** (1982) 839.

[71] C.J. Hsu, W.D. Krugh and H.B. Palmer, J. Chem. Phys **60** (1974) 5118.

[72] M.H. Alexander and G.C. Corey, J. Chem. Phys. **84** (1986) 100.

[73] H.-J. Werner, B. Follmeg and M.H. Alexander, J. Chem. Phys. **89** (1988) 3139.

[74] H.-J. Werner, B. Follmeg, M.H. Alexander and D. Lemoine, J. Chem. Phys. **91** (1989) 5425.

Chapter 2

Experimental Apparatus

2.1 Introduction

The apparatus used in the studies of the state-specific energy transfer processes of SiF (and SiCl) had to be capable of fulfilling three basic requirements:-

- production of the molecule under study.
- excitation of the molecule to the required rovibronic level.
- detection of the product molecules upon undergoing a single collision.

The technique chosen was that of laser induced fluorescence (LIF) in conjunction with a discharge flow system. The remainder of this chapter will give detailed descriptions of the apparatus used in the course of the experimental studies.

2.2 Laser Systems

The laser systems which were utilised in this work were both Neodymium : Yittrium Aluminium Garnet (Nd:YAG) pumped dye-lasers with wavelength extension (WEX) units.

2.2.1 Nd:YAG Lasers

The Nd:YAG Lasers, manufactured by Spectron Laser Systems Ltd., were type SL803 'Q' switched lasers [1]. They consisted of a pair of Neodymium doped YAG rods arranged as an oscillator and amplifier system, each pumped by a separate flash lamp.

The oscillator fundamental wavelength of 1064.8 nm is induced by producing gain between electronic energy levels of the Nd^{3+} ion embedded in the glass matrix. Nd^{3+} has the ground electronic configuration $[Kr]4d^{10}4f^{3}5s^{2}5p^{6}$ where lasing occurs between the $^4F_{3/2}$ and $^4I_{11/2}$ states [2] (labelled within to the Russell-Saunders approximation [3]).

In the free Nd^{3+} ion the $^4F_{3/2}$ - $^4I_{11/2}$ transition is doubly forbidden due to the atomic selection rules for an electronic transition where $\Delta l = \pm 1$ and $\Delta J = 0, \pm 1$. However in the YAG matrix the atomic terms are split into several non-degenerate components by crystal field interactions whereby eight different transitions are allowed of which the transition at 1064.8 nm is dominant at room temperature [4].

The laser output power is enhanced by 'Q' switching whereby the 'Q' factor of the laser cavity is reduced during and beyond the flashlamp pulse which allows the build up of the upper state population of the two active levels [2]. This is done by use of a Pockel's cell in the laser cavity. This cell consists of the electro-optic material potassium dihydrogen phosphate (KDP) which becomes birefringent upon application of a voltage. Following a chosen time delay, the cell is triggered whereby there is a change in the voltage across the optic. The 'Q' factor is thus suddenly restored and there is a resultant rapid pulse of photon density.

The oscillator and amplifier flashlamps and 'Q' switch delay could be controlled internally or externally (as will be described in section 2–3). Triggering the oscillator flashlamp initiated the charging of the Pockel's cell which was itself triggered after a delay of 200 μs. The resultant, approximately gaussian, beam pulse ($\sim 14 - 16$ ns full width half maximum (FWHM)) of ~ 1 J was emitted at a repetition rate of 10 Hz.

For the laser system used to produce the data discussed in chapters 3 and 4, the fundamental output of the oscillator / amplifier unit was frequency doubled using a KDP crystal to produce output at 532 nm, with a pulse energy of $\sim$ 300 mJ which in turn was used to pump the dye laser. The residual fundamental radiation was separated from the doubled output using a dichroic optic and could then be used, if required, for mixing with the doubled-dye output.

The laser system used in chapter 5 differed from the original system in that the doubled Nd:YAG output was mixed with the fundamental output using a further KDP crystal, to produce $\sim$ 140 mJ of laser radiation at 355 nm.

2.2.2 Dye Laser Systems

The Spectron Laser System Ltd. dye lasers (SL4000) were used to produce tunable laser radiation, which was subsequently doubled, or doubled and mixed with the Nd:YAG fundamental, to provide laser light of the appropriate wavelength. As discussed previously, the laser was pumped using the 532 nm or 355 nm harmonic from the Nd:YAG laser depending on the system in question.

A methanol solution of the dye molecules represented the active laser medium. Typical dyes are large organic molecules which exhibit high absorption in the visible spectral region. Generally the molecules are excited from the (usually) singlet ground state to the first excited state *ie.* $S_1 \longleftarrow S_0$ [2].

Upon excitation the molecules undergo rapid collisional relaxation among the S_1 rotational and vibrational levels to produce a thermal distribution. The molecules will generally fluoresce back to vibrationally excited levels of the ground state (typical lifetimes $\tau_{rad} \approx 10ns$) due to the Franck-Condon principle. Fluorescence and absorption will occur at different wavelengths thus reducing the associated problem of reabsorption.

Both systems consisted of an oscillator and two amplifier stages where a small fraction of the incident pump beam was used to pump the oscillator cavity. The remainder of the pump beam was split equally and used to pump the amplifier cells.

In both cases the oscillator consisted of a transversely pumped flowing dye cell module, an output coupler, a master holographic grating, a tuning mirror and prism beam expander. The grating was used in a grazing incidence configuration with wavelength tuning achieved using the tuning mirror. This was operated by a sine drive incorporating a stepper motor which was controlled by a microcomputer (PC-AT compatible) via a scan controller(SL4000SC). The resultant beam was horizontally polarised due to the combination of the beam expanding prisms and the diffraction grating.

The 532 nm pumped laser amplifier system consisted of two longitudinally pumped dye cells set at Brewsters angle and a pump beam splitter. Amplification was achieved by overlapping the oscillator output beam with the amplification pump beams. The 355 nm pumped laser system differed in that the amplifier cells were transversely pumped.

The oscillator and amplifier dye solutions were contained in one litre reservoirs and were continuously circulated through the dye cells. The oscillator dye solutions were of generally more concentrated than those used in the amplifier cells.

The output energy of the two systems were $\leq$ 30 mJ at 560 nm and $\leq$ 15 mJ at 510 nm for the 532 nm and 355 nm pumped lasers respectively. For both systems the pulse duration was typically of 12 - 14 ns with a linewidth of $\geq$ 0.1cm^{-1} according to the manufacturers specifications.

The laser dyes and their respective tunable wavelength ranges used in this thesis are listed in table 2–1.

2.2.3 Wavelength Extender Systems

The tunable dye laser output was frequency doubled or frequency doubled and mixed using the Spectron Laser Systems Ltd SL4000EX and SL4000D-FM4A wavelength extension units, respectively.

These units comprised two stepper-motor driven, temperature controlled crystal housings. The frequency doubling and frequency mixing crystals were con-

Dye	Fundamental/nm	Doubled/nm	Mixed/nm
Rhodamine 560 (a)	540 - 582	270 - 291	(c)
Rhodamine 575 (a)	544 - 570	272 - 285	(c)
Rhodamine 590 (a)	550 - 590	275 - 295	(c)
Rhodamine 610 (a)	580 - 606	290 - 303	(c)
DCM (a)	605 - 672	302 - 336	235 - 255
LDS 698 (a)	660 - 740	330 - 370	252 - 275
Coumarin 500 (b)	485 - 550	243 - 275	(c)

Table 2–1: Table of laser dyes with tunable wavelength ranges when operating in fundamental, frequency doubled and frequency doubled / mixed modes.
Dyes were supplied by Exciton. (a) Oscillator pumped with 532 nm Nd:YAG harmonic (b) Oscillator pumped with Nd:YAG 355nm harmonic. (c) Frequency mixing not used with this dye. The fundamental ranges are as quoted in reference [6].

tained within the housings in tandem with a plain quartz compensating block to correct the resultant beam path.

When frequency mixing was required the Nd:YAG fundamental beam was passed through an optical delay line to ensure temporal overlap with the dye output beam.

The doubled and mixed output powers were monitored by splitting a small fraction of the respective ultraviolet (UV) output onto a photodiode. The output powers could then be continually optimised by angle tuning the crystals using a dedicated computer.

The output beam bandwidths, estimated from simulations of laser excitation spectra, were approximately ≥ 0.4 cm^{-1} and 0.5 cm^{-1} for the doubling and mixing operations, respectively.

2.3 Gas Handling and Radical Production

2.3.1 Vacuum Line

A gas handling line was built to introduce the precursor and bath gas mixtures into the discharge-flow system in a controlled manner. The vacuum line was constructed from Pyrex glass and contained eight independently isolable arms incorporating Young's greaseless taps.

The line was evacuated using a liquid N_2-trapped single stage mercury diffusion pump backed by a rotary oil pump. The line pressure was measured using an MKS Baratron 222BA gauge (0-1000Torr) with the base pressure found to be less than 0.005 Torr.

The various gases used were transferred to and from the vacuum line using either teflon or nylon 1/4″ diameter tubing, depending on the nature of the gas in question. Gas mixtures were stored in a 10 litre glass bulb.

2.3.2 Flow Control

Gases were passed from the vacuum line (and from gas cylinders) to the flow system via mass flow controllers (Advanced Semi-conductor Materials Int., type AFC-260). The three controllers used in this thesis measured and controlled flow rates in the ranges 0-20, 0-500 and 0-2000 standard cubic centimetres per second (sccm), respectively.

The flow controllers operated by monitoring the rate of heat exchange between a series of thermal sensors, on either side of variable aperture, with flow. The aperture size was varied automatically to ensure a constant temperature profile and hence a steady flow rate.

The controllers themselves were not accurately calibrated as a precise knowledge of the flow rate was not required for the experiments performed in this thesis. Rather, the controllers were used to ensure a constant gas flow, regardless of changes in the backing pressure, and hence constant pressure in the flow tube.

2.3.3 Discharge Flow System

The discharge flow system consisted of a silica quartz inlet incorporating a microwave discharge, a quenching gas inlet and an excitation and detection zone. The majority of the 25 mm diameter flow system was again constructed using Pyrex glass with each section connected with an appropriate cone/socket joint using high vacuum silicone grease. The system was continuously pumped via a liquid N_2-cooled cold-trap using a high throughput pump (Alcatel mechanical pump 2063, 1100 $Lmin^{-1}$) with the pressure monitored using an MKS Baratron 127A capacitance manometer (0-10 Torr).

The pumping efficiency was highly dependent upon the oil temperature with the result that after a period of about four hours the pump had to be allowed to cool as it was unable to sustain a constant pressure at any given flow rate. The oil itself needed to be changed periodically as it became contaminated thus again reducing pumping efficiency. The pressure stability ranged from about ± 0.005

Torr at a flow rate of $\sim$ 500 sccm to about $\pm$0.1 Torr for flows greater then 2000 sccm. Typical pressures in the system for the experiments performed ranged from 1 to 6 Torr. An input flow rate of about 500 sccm of Ar produced a pressure of around 1 Torr. Under these conditions it can be shown that the molecules will travel through the flow system at a speed of approximately 13 ms^{-1}.

The detection / excitation zone could be isolated from the pump (and atmosphere) by a 25 mm bore Springham tap. When all sections were connected the flow system was approximately one metre in length.

The detection and excitation zone consisted of a six way cross. Molecules were excited by passing the laser beam vertically through the flow axis via two arms with quartz windows set at Brewster's angle. Mutually perpendicular to this and the flow axis was another quartz window through which the resultant fluorescence was observed. A schematic representation of this section can be seen in figure 2–1.

It was necessary to observe the resultant laser induced fluorescence at the point of excitation due to the short lifetimes of the species investigated in this thesis, where typical radiative lifetimes were $\leq$ 1 μsec. Therefore, assuming the estimated flow speed to be uniform, in this time the bulk flow will travel a distance of $\sim 1.3 \times 10^{-2}$ mm. As the laser beam diameter is approximately 5 mm the point of laser excitation and fluorescent emission are essentially overlapped.

The major problem with the discharge flow technique is due to heterogenous effects involving collisions between the radical species and the walls of the flow system. As this could lead to radical recombination processes it is important to minimise these effects.

There are two obvious methods by which this can be achieved:-

- maximise the molecular flow rate through the system thus reducing the number of molecule / wall collisions.

- coat the wall surfaces with an agent to inhibit surface recombination.

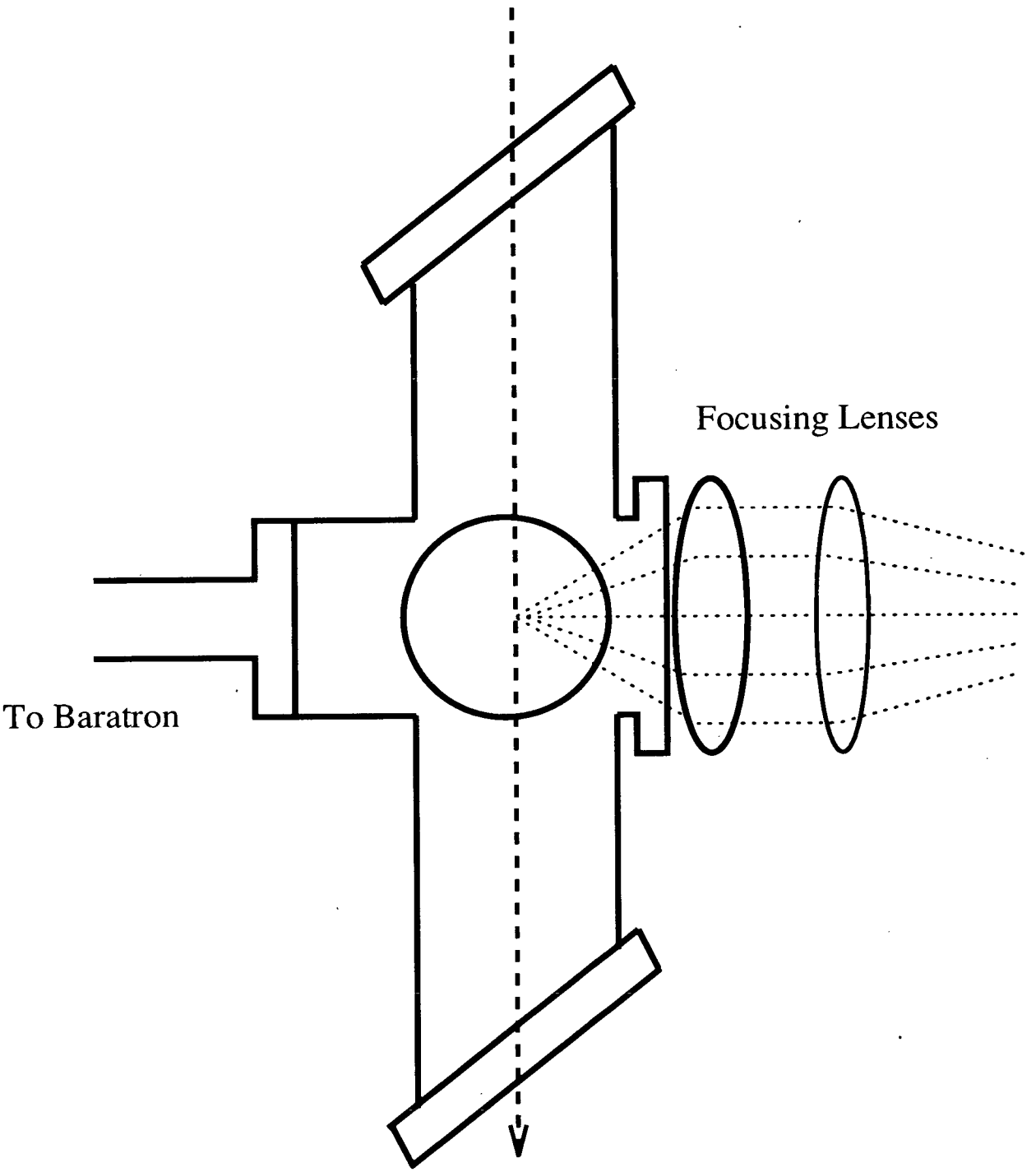

Figure 2–1: Cross section of the excitation and observation zone perpendicular to the flow axis.

The laser excitation beam is represented by the dashed line (- - -) and the resultant fluorescence by the dotted lines (· · ·). The excitation and observation axes are mutually perpendicular to the flow axis.

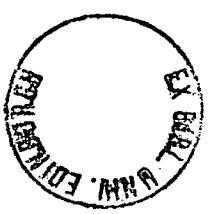

The apparatus was designed specifically to maximise the flow rate by using a large uniform internal diameter and by minimising the number of turns in the flow system itself.

Surface reaction inhibitors which have previously been used include $HClO_4$, sulphuric acid, phosphoric acid, teflon and halocarbon wax [7,8,9,10]. Previous work in this field showed that halocarbon wax and phosphoric acid were good inhibiting agents and suitable for these studies [11]. Due to its low melting point ($\sim 60°C$) ,hence ease of application, and inert nature, halocarbon wax was used to coat the reactor walls.

It is apparent that the halocarbon wax is not suitable when the surface temperature increases much above ambient levels however in the discharge arm, local surface temperatures may be as high as several thousand Kelvin. The discharge arm was therefore coated with phosphoric acid. The coating was applied by first ensuring the surface walls were clean by washing with hot potassium hydroxide solution (5 M). Phosphoric acid was then run through the arm before heating to $\sim$ 1000 K using a blue Bunsen flame. A uniform white coating could be achieved by slowly rotating the arm in the flame before baking overnight in an oven at $\sim$ 700 K. This method had been previously found to significantly increase the radical concentration [11].

2.3.4 Microwave Discharge

The silicon halide species required for these studies were produced by use of a microwave discharge apparatus. An EMS Microtron Mk 3 microwave power supply producing microwaves at 2450 MHz was used to produce discharge powers of $\sim$ 10 Watts through a microwave discharge cavity, EMS 214L, which enclosed the quartz discharge arm. The cavity was continuously cooled using compressed air and the reflected power was found to be typically $\sim$ 25%.

2.4 Fluorescence Capture and Detection

A schematic representation of the apparatus used in all the experiments performed in this thesis can be seen in figure 2–2. The features of this set-up that will be discussed in this section are:-

- capture and optimisation of the fluorescence signal.
- calibration of the system's wavelength-dependent response.

2.4.1 Fluorescence Capture and Wavelength Dispersion

Optimisation of the fluorescence signal-to-noise ratio requires that the number of photons gathered from the excitation zone must be maximised. Due to the nature of the isotropic gas mixture, photons will be emitted over all solid angles (ignoring any possible laser polarisation effects). In an effort to 'capture' as many photons as possible a 'condenser' lens of equal height to the observation aperture was placed at a distance equal to its focal length, *ie.* 5 cm, from the point of interaction of the excitation laser beam and the target molecules. The lens was chosen to allow it to be placed as close as possible to the aperture so as to ensure maximum collection of photons transmitted through the quartz window as can be seen in figure 2–1.

The resultant collimated beam of light was then focussed using a second 'field' lens onto the entrance slit of the monochromator. By ensuring that the back mirror is fully filled by the 'field' lens the diffraction grating is fully illuminated and hence optimum wavelength resolution can be achieved. The appropriate focal length of the 'field' lens was calculated by proportion of the monochromator focal length and mirror diameter to the diameter of the 'field' lens.

Initial lens system alignment was performed by use of a small electric light bulb placed in the excitation zone. The relative lens positions were then adjusted to produce a sharp focussed image of the filament on the entrance slit (and exit slit if the monochromator is set to zero order) of the monochromator.

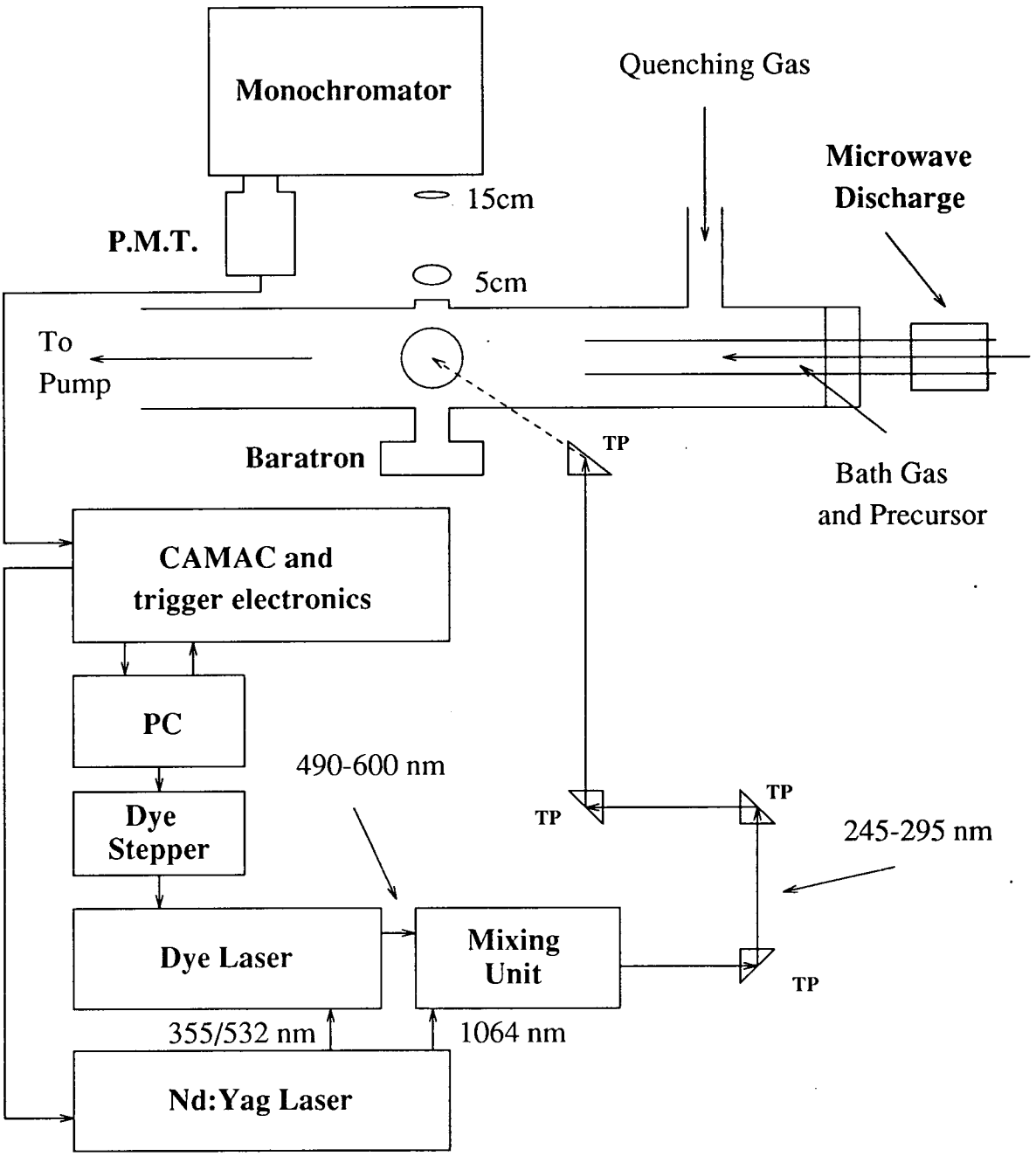

Figure 2–2: Schematic of the experimental configuration of the discharge flow apparatus and LIF detection.

(TP = turning prism) The laser beam entered the observation zone vertically as shown in more detail in figure 2–1.

The monochromator used in all experiments was a Monospek 1000 D400 grating spectrometer (Hilger and Watts) which had a focal length of 1000 mm, a relative aperture of$\sim f/10$ (102 mm$\times$ 102 mm grating) and was set up in the Czerny-Turner configuration [5]. The kinematically mounted, holographic type grating had 1200 grooves per mm and could be automatically or manually rotated to 'scan' the incident radiation. The monochromator entrance and exit slits were precision engineered and bi-lateral opening.

The monochromator wavelength accuracy was measured against the known wavelengths of a group of emission lines emitted from a low pressure mercury lamp [12]. As a result the monochromator was found to read approximately 6 nm too low.

Previous studies involving this same monochromator had shown the dispersion of the instrument was 0.82 nm/mm slit width [11].

Photons transmitted through the monochromator were detected using a single photomultiplier tube (PMT) (Thorn EMI 9558QB, power supply PM28R). The tube had a variable wavelength response from $\sim$200 - 900 nm. In the region of interest for these studies *ie.* between 250 and 340 nm, the quantum efficiency of the spectral response was around 20%. The PMT had a nominal response time of 10 ns and a pulse width of 22 ns (FWHM) according to the manufacturers specifications. The tube incorporated a venetian blind dynode system (11 stages) and a 45 mm CsSb effective photocathode diameter. PMT output signals were amplified using a ten times amplifier (Thorn EMI A2 (C633)).

The PMT was shielded from room light and scattered laser light by constructing a mount whereby the tube was enclosed and fixed flush with the exit slits of the monochromator. To further ensure the omission of extraneous light the entire monochromator and PMT system were covered with a heavy black cloth with the collimated incident radiation enclosed within a beam tube. It was found that these measures significantly reduced the amount of background radiation detected.

2.4.2 Calibration for Spectral Response

Use of a standard lamp of known spectral irradiance (Optronic Laboratories Inc, model 245 A, 45 W quartz-halogen coiled filament lamp standard) allowed the calibration of the wavelength response of the optical detection system.

The lamp was supplied with a set of irradiance data for a range of specific wavelengths. The values assigned have an estimated uncertainty of $\pm 2\%$ relative to National Bureau of Standards (NBS) reference data.

As only the relative wavelength response function of the apparatus was required, and not the absolute response, the system was calibrated by measuring the relative photon intensity at each specific wavelength and comparing those with the specified absolute value. The ratio of spectral response against spectral irradiance was then used to determine the response for any wavelength in the calibrated range by fitting a 'spline' function through the experimentally determined points.

The calibration test was performed by placing the lamp in the excitation zone of the flow apparatus. The wavelength dependent intensities were then recorded using the same conditions for light gathering, dispersion and detection as was used in the subsequent experiments.

A requirement of the calibration test was that constant current of 12 A had to be used. According to the manufacturers report, a 1% error in the current setting results in a 12% error in the spectral irradiance at 250 nm. This problem was overcome by using a Farnell B30/10 stabilised power supply in conjunction with a Fluke 75 digital multimeter to monitor the current drawn.

2.5 Data Acquisition and Experimental Control

The experiments were controlled using a CAMAC system (Computer Aided Monitoring And Control) interfaced to an IBM compatible PC-AT implementing software written by Maitland [13]. This software was able to control device triggering sequences as well as processing and storing experimental data using the first output serial port via the CAMAC crate. The software simultaneously had control over the dye laser wavelength directly through the second output serial port.

The major feature of the software was the interrupt mechanism of the PC-AT. As the experimental cycle operated at 10Hz, the interrupt was generated at 20Hz hence on alternate interrupts the software could switch between experimental control and data processing.

2.5.1 CAMAC Instrumentation

The function of the CAMAC apparatus is to allow the interface of a range of instrumentation to a controlling computer via a common dataway.

The common dataway, consisting of 24 read/write lines, is incorporated into the backplane of the CAMAC crate (Optima 860) into which modules can be placed at a specific station address. These stations are controlled via a dedicated crate controller module (DSP 6001) which is programmed through a DSP PC004 interface card which was inserted in an 8 bit expansion card slot in the computer.

A schematic representation of the CAMAC system and associated devices can be seen in figure 2–3.

2.5.2 IBM PC-AT Microcomputer

The IBM compatible (Dell System 486/MX Optiplex) PC-AT contained an Intel 80486 (16 bit) processor and 8Mb of RAM. Experimental data were displayed on

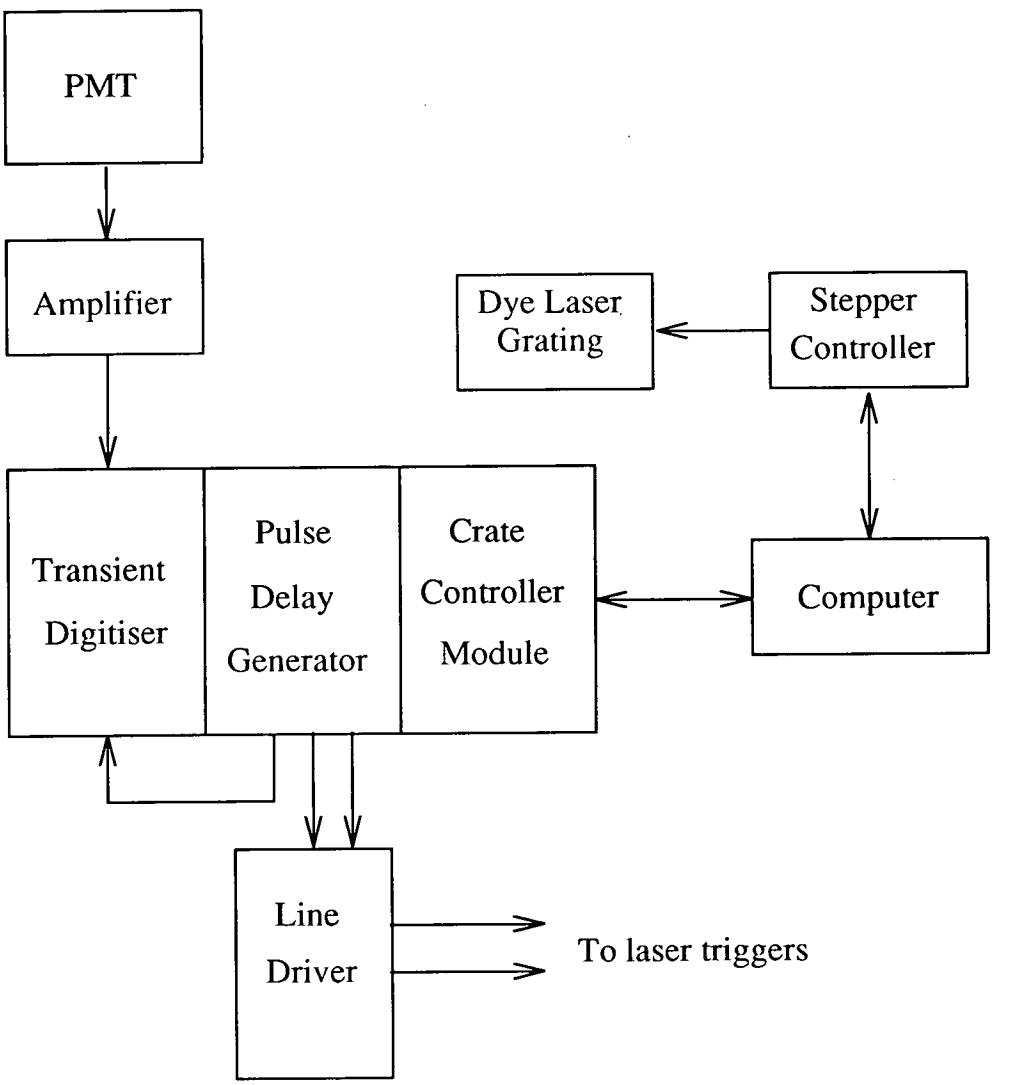

Figure 2–3: Schematic of the CAMAC based experimental control system

a high resolution VDU, driven by an SVGA 1Mb graphics card. A 170 Mb hard disk and a 1.44 Mb floppy drive allowed storage of software and data.

2.5.3 Pulse Delay Generator

Control of the experimental apparatus required that a series of separate trigger pulses be sent to the laser flashlamps, 'Q'-switch and transient digitiser. This task was performed using a pulse delay generator (PDG) (LeCroy model 4222). This four channel module could generate four separate 100ns FWHM pulses of 5V amplitude with delays specified by four 24 bit inputs via the CAMAC controller. Figure 2–4 shows a schematic representation of the timing sequences for the trigger pulses.

The PDG output triggers were incompatible with the voltage logic of the laser flashlamps and 'Q' switch. Therefore the signals were enhanced and, in the 'Q' switch case, inverted using a custom built 8 channel line driver unit, housed in a Nuclear Interface Module (NIM) fitted with a CAMAC adapter. This could produce the appropriate 15 V, 50 μs pulses required.

2.5.4 Transient Digitiser

Upon the detection of signal by the photomultiplier tube, a negative-going voltage is generated at the anode. To store this data in the computer this signal must be digitised. This function is performed using a 100MHz transient digitizer (Transiac 2001A). Waveforms could thus be recorded with a minimum resolution of 10 ns with the number of samples stored ranging from 256 to 32768.

The unit continuously digitizes and stores the required number of samples whereupon receiving a trigger signal from the pulse delay generator the samples are sent to the controlling computer. Thus the laser induced signal could be monitored in real time.

The controlling software allowed five gates (four signal and one background) to be set up. Signal could then be integrated over gates with any signal recorded

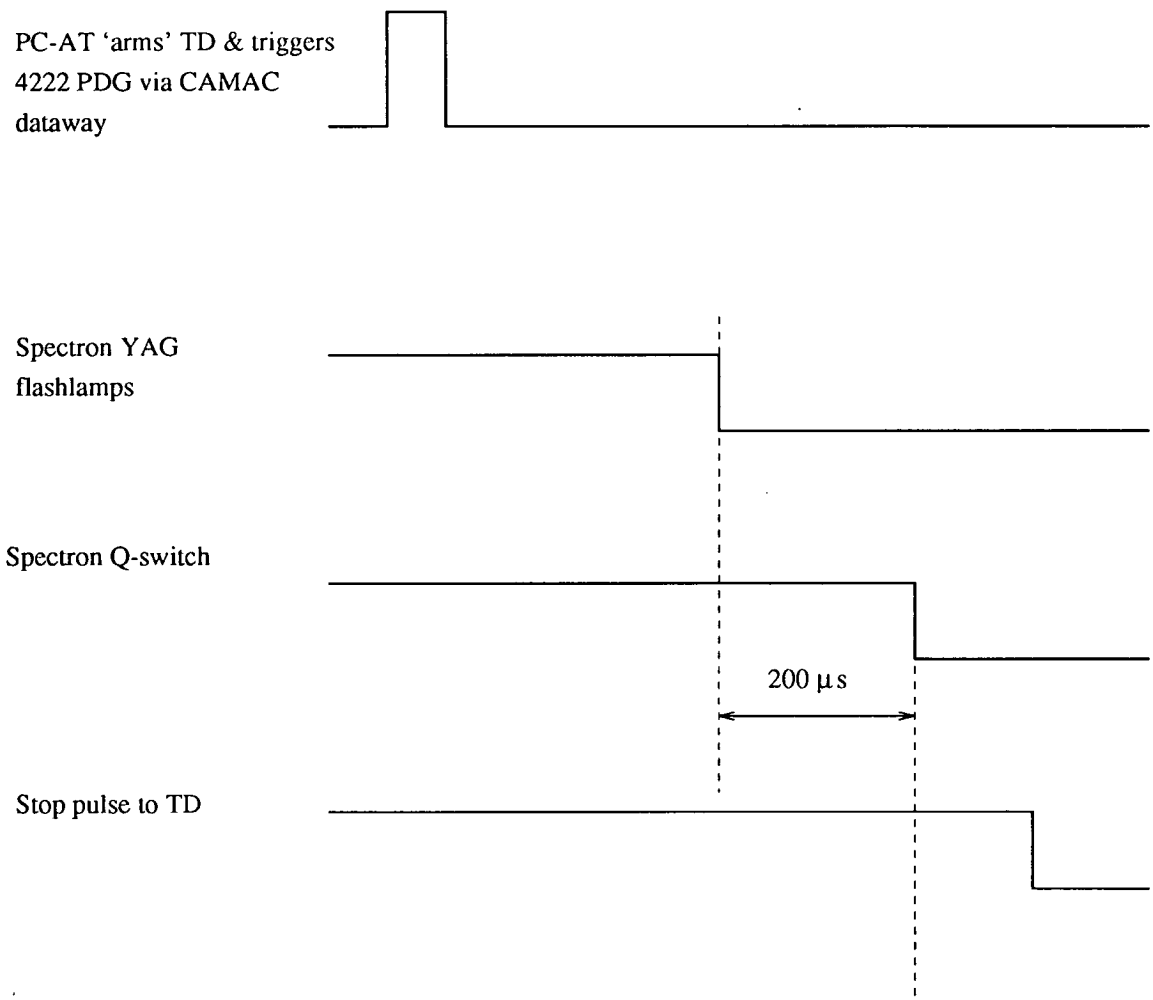

Figure 2–4: Timing sequence for the LeCroy 4222 pulse delay generator used during the experiments

between the background gate subtracted. This allowed spectra to be recorded over different time intervals within a digitised waveform.

2.5.5 Dye Laser Scanning Control

As mentioned earlier in section 2.2.2, the dye laser scanning was performed using the PC-AT to operate the laser scan controller (SL4000SC). Unlike the other devices, this was not done via the CAMAC controller module but by incorporating the remaining RS-232 port.

The required mode of operation for laser scanning involved the dye laser stepping to a predefined wavelength followed by data collection over a set number of laser shots. The laser grating then stepped to the next wavelength and the cycle was repeated.

Bibliography

[1] Nd:YAG Laser User Manual, Spectron Laser Systems Ltd.

[2] J.M. Hollas, High Resolution Spectroscopy (Butterworths, London 1982).

[3] G. Herzberg, Spectra of Diatomic Molecules, Molecular Spectra and Molecular Structure, 2nd Edition (D. Van Nostrand Company, New York 1950).

[4] W. Demtröder, Laser Spectroscopy, 2nd Edition (Springer-Verlag, Berlin 1982).

[5] F.A. Jenkins and H.E. White, Fundamentals of Optics, 4th Edition (McGraw Hill, New York 1976).

[6] Laser Dye Catalog, Exciton Chemical Company (1990).

[7] J.G. Anderson, J.J. Margitan and F. Kaufman, J. Chem. Phys., **60** (1974) 3310.

[8] P.E. Debely, Rev. Sci. Instrum.,**41** (1970) 1290.

[9] M.A.A. Clyne and P.M. Holt, J. Chem. Soc. Far. Trans. II, **75** (1979) 569.

[10] M.A.A. Clyne and P.M. Holt, J. Chem. Soc. Far. Trans. II, **75** (1979) 582.

[11] S. Singleton, Laser Based Studies of Transient Species in A Discharge Flow Apparatus (PhD Thesis, University of Edinburgh 1990).

[12] C.R.C. Handbook of Chemistry and Physics, 70th Edition (CRC Press Inc., Florida 1989-90).

[13] G. Maitland, Spectroscopic Studies for State-To-State Reaction Dynamics (PhD Thesis, University of Edinburgh 1993).

Chapter 3

Spectroscopy of the SiF $B^2\Sigma^+ - X^2\Pi$ and $C^2\Delta - X^2\Pi$ Systems

3.1 Introduction

The main objective of this thesis was to investigate collision-induced energy transfer processes between rovibronic levels of the SiF $C^2\Delta$ and $B^2\Sigma^+$ states. As discussed previously in chapter 1, the experimental methodology requires the laser excitation of specific rovibronic levels of the $C^2\Delta$ state from the $X^2\Pi$ state followed by observation of the resultant $C^2\Delta$ - $X^2\Pi$ and any collision-induced $B^2\Sigma^+$ - $X^2\Pi$ fluorescence. Therefore, to quantitatively analyse the resultant spectra and hence derive the relevant product distributions, a thorough knowledge of the spectral band positions and transition probabilities was essential.

In parallel, any spectroscopic study of these transitions can also yield information on the geometry and electronic structure of the states involved. The internuclear potential curves for a diatomic can be inferred from a measurement of the band positions which will give the vibronic eigenvalues. This information can be extended by measuring the relative band intensities which will be affected by the nuclear and electronic wavefunction overlap.

In this chapter, the excitation spectra of the $B^2\Sigma^+$ ($v' = 0, 1, 2, 4$ and 5) - $X^2\Pi$ ($v'' = 0$) and $C^2\Delta$ ($v' = 0, 1$) - $X^2\Pi$ ($v'' = 0$) transitions and the dispersed

fluorescence spectra of the $B^2\Sigma^+$ ($v' = 0, 1, 2, 4$ and 5) - $X^2\Pi$ ($v' = 0 - 9$) and $C^2\Delta$ ($v' = 0, 1$) - $X^2\Pi$ ($v' = 0 - 5$) transitions will be presented.

3.2 Previous Spectroscopic Observations of the SiF Radical

The SiF radical has been the subject of many extensive spectroscopic and theoretical studies over the last eighty years. It has been of general scientific interest for a variety of reasons. The molecule is of astrophysical importance as it has been detected in stellar atmospheres [1] and it may be a constituent of the Sun [2]. Of more technological importance, the SiF $a^4\Sigma^-$ - $A^2\Sigma^+$ transition has been successfully exploited as a chemical laser system [3] and it has been shown that SiF occurs during the plasma etching of silicon in the manufacture of integrated circuits [4].

The first observation of SiF was performed by Porlezza in 1911 [5,6] since when a large number of different electronic states have been identified and reported. The ground state has been established to be a $^2\Pi$ state [7], as have the C', $D(2)$, D', $D''(2)$, $D''(3)$, E, H' and I states [8,9,10,11,12,13,14]. The A, B, C'', $D''(1)$, D''', F, G, G' and H'' states have been shown to have $^2\Sigma^+$ symmetry [7,8,9,11,12,13, 15,16,17,18]. Also located and identified are a low-lying $a^4\Sigma^-$ state [19,20]; the $D^2\Sigma^-$ state [16]; the C, H and $M(2)$ $^2\Delta$ states [7,12,21,22]; and the $M(1)^4\Delta$ state [22]. The J, M and N states have also been observed but at present have not been unambiguously identified [12,22].

Some of the more recent work has been performed using the technique of resonance enhanced multi-photon ionisation (REMPI) where the intermediate states have been the A, C' and C'' states [13,23,24].

Theoretical calculations have been performed on the $X^2\Pi$ state [25,26] and on the $X^2\Pi$ and $a^4\Sigma^-$ states [27] using self-consistent-field (SCF) wavefunctions. A contemporary minimal basis full-valence configuration interaction (FV CI) study

showed the lowest $^2\Sigma^+$ and $^2\Delta$ states to be repulsive [28]. More recent CI studies have compared calculated spectroscopic constants with experimental values, with good agreement, for eight low-lying valence and Rydberg states ($X^2\Pi$, $A^2\Sigma^+$, $a^4\Sigma^-$, $B^2\Sigma^+$, $C'^2\Pi$, $C^2\Delta$, $C''^2\Sigma^+$ and $E^2\Pi$) as well as predicting constants for a further eight states [29,30,31].

3.3 Interatomic Potentials and Principal Molecular Constants

As stated previously, the electronic states relevant to this work are the $X^2\Pi$, $B^2\Sigma^+$ and $C^2\Delta$ states. The potential energy curves for these states and for the near-lying $A^2\Sigma^+$ and $a^4\Sigma^-$ states can be seen in figure 3–1 . These potentials were calculated using the well established Rydberg-Klein-Rees (RKR) procedure[1] [32, 33,34]. To facilitate these calculations a computer program written by Lawley [35] was exploited. This program required as input the atomic masses and the vibrational and rotational molecular constants of each electronic state. The constants used were those experimentally derived by Houbrechts *et al* [36] and are listed in table 3–1. From table 3–1 it is apparent from the principal rotational constants that r_e, the equilibrium internuclear separation, for the $C^2\Delta$ state is marginally shorter than that of the $X^2\Pi$ state. This will result in a slightly off-diagonal $C-X$ system (in terms of vibronic transition probabilities) due to the Franck-Condon principle. The $B^2\Sigma^+$ state equilibrium internuclear separation is shorter still than that of the $C^2\Delta$ state which implies that the $B-X$ system will more off-diagonal still.

It should be noted that the value of A_e, the spin-orbit splitting constant, for the $C^2\Delta$ state is not well defined in table 3–1: this will be discussed in section 3.4.4.

---

[1]For a summary of this method see Appendix A.

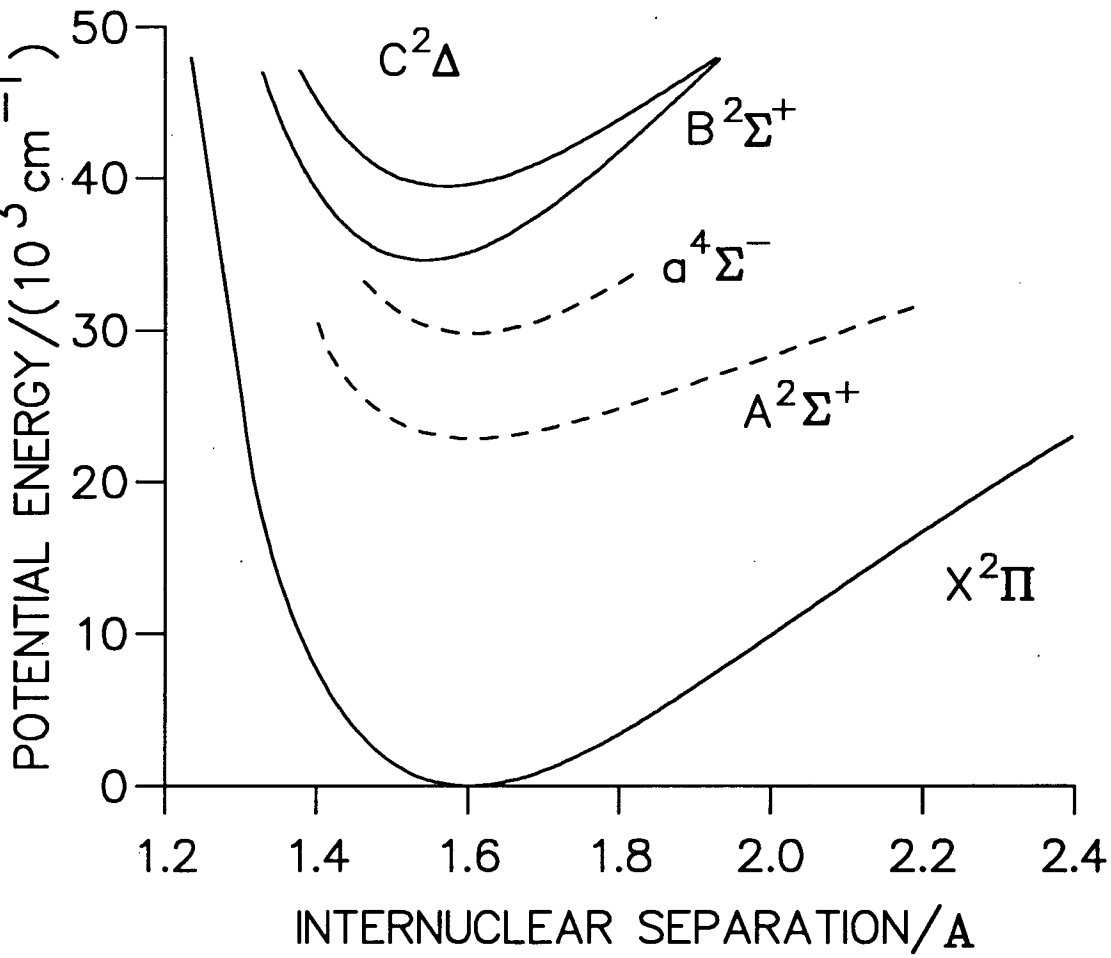

Figure 3–1: Potential energy curves for the low-lying states of SiF constructed using the Rydberg-Klein-Rees method.

The solid lines indicate the states of direct interest in this work.

State	$T_e^{(a)}$	$A_e^{(b)}$	$\omega_e^{(c)}$	$\omega_e x_e^{(d)}$	$\omega_e y_e^{(e)}$	$B_e^{(f)}$	$D_e \times 10^{6(g)}$
$X^2\Pi$	0	161.689	857.31	4.83	0.018	0.58116	1.07
$B^2\Sigma^+$	34561.57	-	1011.16	4.84	0.012	0.62675	0.96
$C^2\Delta$	39438.07	0/2.46	889.70	5.62	-0.044	0.60380	1.09

Table 3–1: The principal molecular constants of $^{28}Si^{19}F$ for the $X^2\Pi$, $B^2\Sigma^+$ and $C^2\Delta$ states (from ref. [36]).

All values are in wavenumbers (cm^{-1}). a) the electronic term value corresponding to the zero point energy difference between the ground state and the excited state. b) the spin-orbit interaction energy for the theoretical vibrationless energy level of the state. c) the vibration wavenumber which a classical oscillator would have for an infinitesimal displacement from equilibrium. d) the first anharmonicity correction constant. e) the second anharmonicity correction constant. f) the rotational constant for the state in the hypothetical vibrationless energy level. g) centrifugal distortion constant.

3.4 Diatomic Energy Level Structure

To fully understand, analyse and simulate the electronic spectra recorded in the course of this thesis it was important to understand the laws governing the various transition probabilities.

The energy of any transition is, quite simply, the energy difference between the two connected levels,

$$\Delta E = E' - E'' \tag{3.1}$$

where E' and E'' denote the energy of the upper and lower states, respectively. The energy of a particular level in a $^1\Sigma$ state can be expressed as,

$$E_v = T_e + \omega_e(v+\frac{1}{2}) - \omega_e x_e(v+\frac{1}{2})^2 + \omega_e y_e(v+\frac{1}{2})^3 - .... + B_v J(J+1) - D_v J^2(J+1)^2 + ... \tag{3.2}$$

where v and J are the vibrational and rotational quantum numbers, respectively. The higher anharmonicity and centrifugal distortion coefficients have been ignored in equation 3.2.

However for a state of any other symmetry, equation 3.2 is an oversimplification as the energy level structure is significantly affected by the coupling of the various forms of angular momentum present in the molecule. These momenta, neglecting the nuclear hyperfine spin, are defined as

- **L**, the total electron orbital angular momentum.
- **S**, the total electron spin angular momentum.
- **R**, the total nuclear rotation angular momentum.

The ways in which these momenta couple together to form the total angular momentum, **J**, in diatomic molecules was first described by Hund [37].

3.4.1 Hund's Coupling Case (a)

In Hund's coupling case (a) the interaction of the nuclear rotation, **R** and electronic 'motion', **L** and **S**, is very weak. However, the electronic 'motion' *is* strongly coupled to the internuclear axis. Due to the cylindrical symmetry of the diatomic, only the axial projection of the electronic angular momentum is generally well defined. The precession of **L** and **S** about the internuclear axis is represented by the components of these momenta projected along the internuclear axis. These projections are termed Λ and Σ respectively. The magnitude of the total electronic angular momentum is thus represented by Ω where

$$\Omega = \Lambda + \Sigma \quad . \tag{3.3}$$

Λ can take the values

$$\Lambda = 0, 1, 2.....L \tag{3.4}$$

and Σ can be

$$\Sigma = S, S-1, S-2, ... - S \quad . \tag{3.5}$$

In all cases where $\Lambda \neq 0$, the states are doubly degenerate as these correspond to the two senses of classical rotation of the electron about the internuclear axis. The total angular momentum **J** is therefore the resultant of Ω and the angular momentum of the nuclear rotation **R**. This coupling scheme is shown in figure 3–2.

The electronic energy levels in case (a) are thus split into multiplets where

$$T_e = T_0 + A\Lambda\Sigma \tag{3.6}$$

where T_0 is the zero point electronic energy. The rotational energy levels, neglecting centrifugal stretching terms are given by

$$F_v(J) = B_v[J(J+1) - \Omega^2]. \tag{3.7}$$

3.4.2 Hund's Coupling Case (b)

If the orbital angular momentum is zero, *ie.* $\Lambda = 0$, and $\mathbf{S} \neq 0$, then the spin vector **S** is not coupled to the internuclear axis and therefore Ω is not defined. In this situation Hund's case (a) does not apply. (This is also true if $\Lambda \neq 0$ and **S** is only very weakly coupled to the internuclear axis). This situation is characteristic of Hund's case (b) where the angular momenta Λ (when $\Lambda \neq 0$) and **R** form a resultant which is termed **N**, the total angular momentum apart from spin **N** can have values

$$N = \Lambda, \Lambda + 1, \Lambda + 2..... \tag{3.8}$$

J is therefore the resultant of **N** and **S** as is shown in figure 3–3.

The molecular rotation produces a very slight magnetic moment which may cause coupling between **S** and **N** thus inducing a splitting of levels with equal N but different J. In the case of $^2\Sigma$ states the rotational energy levels are given by

$$F_1(N) = B_v N(N+1) + \frac{1}{2}\gamma N \tag{3.9}$$

and

$$F_2(N) = B_v N(N+1) + \frac{1}{2}\gamma(N+1). \tag{3.10}$$

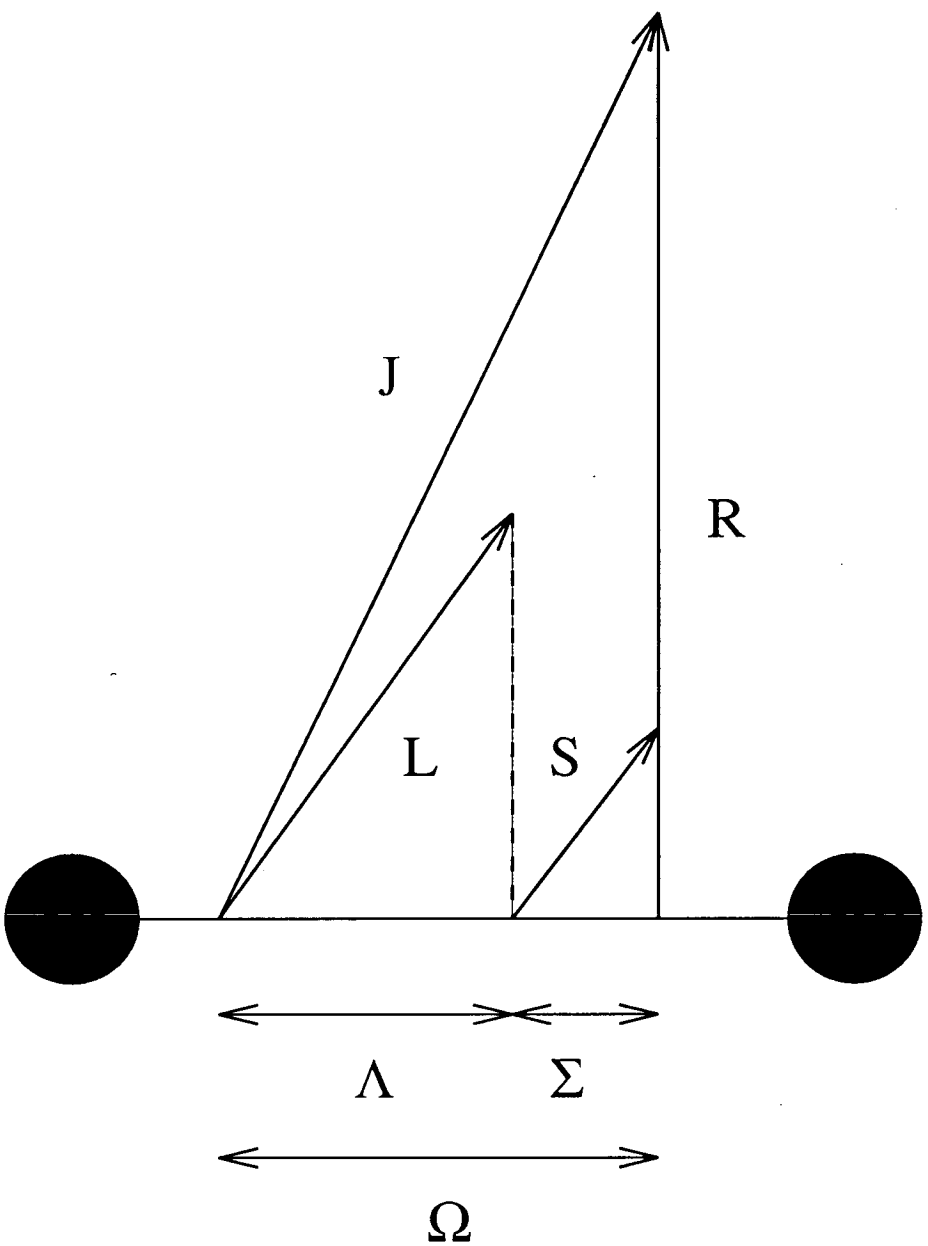

Figure 3–2: Vector diagram for Hund's coupling case (a)

where F_1 refers to $J = N + \frac{1}{2}$, F_2 refers to $J = N - \frac{1}{2}$ and γ is the spin splitting constant.

For both case (a) and (b) the convention for labeling each electronic state is ${}^{2S+1}\Lambda_\Omega$

3.4.3 Λ -type Doubling

For situations where $\Lambda \neq 0$ the phenomenon of Λ doubling must be taken into consideration. This occurs due to the splitting of the degenerate Λ doublet pair, comprising $\pm\mathbf{L}$. This splitting can be thought of as due to the molecular spin being either in the plane or perpendicular to the orbital motion and therefore the cylindrical symmetry of the degenerate pair is broken. The magnitude of this splitting is however very small and is generally only significant in the high J limit.

3.4.4 Transition From Case(a) to Case (b)

In situations where $\Lambda \neq 0$, the states often belong to cases intermediate between case(a) and case (b). Case (a) is usually considered a good approximation for very small rotation such that **S** can be coupled with Λ so as to define Ω. However, as the molecular rotation increases **S** will become uncoupled from the internuclear axis the vector **N** is formed which corresponds to case (b).

The term values for a doublet state for any magnitude of coupling between **S** and Λ (but neglecting coupling between **S** and **N**) have been theoretically shown by Hill and Van Vleck [38] to be

$$F_1(J) = B_v\left\{(J+\frac{1}{2})^2 - \Lambda^2 - \frac{1}{2}\sqrt{4(J+\frac{1}{2})^2 + Y(Y-4)\Lambda^2}\right\} - D_v J^4 \qquad (3.11)$$

and

$$F_2(J) = B_v\left\{(J+\frac{1}{2})^2 - \Lambda^2 + \frac{1}{2}\sqrt{4(J+\frac{1}{2})^2 + Y(Y-4)\Lambda^2}\right\} - D_v(J+1)^4 \qquad (3.12)$$

where $Y = A/B_v$.

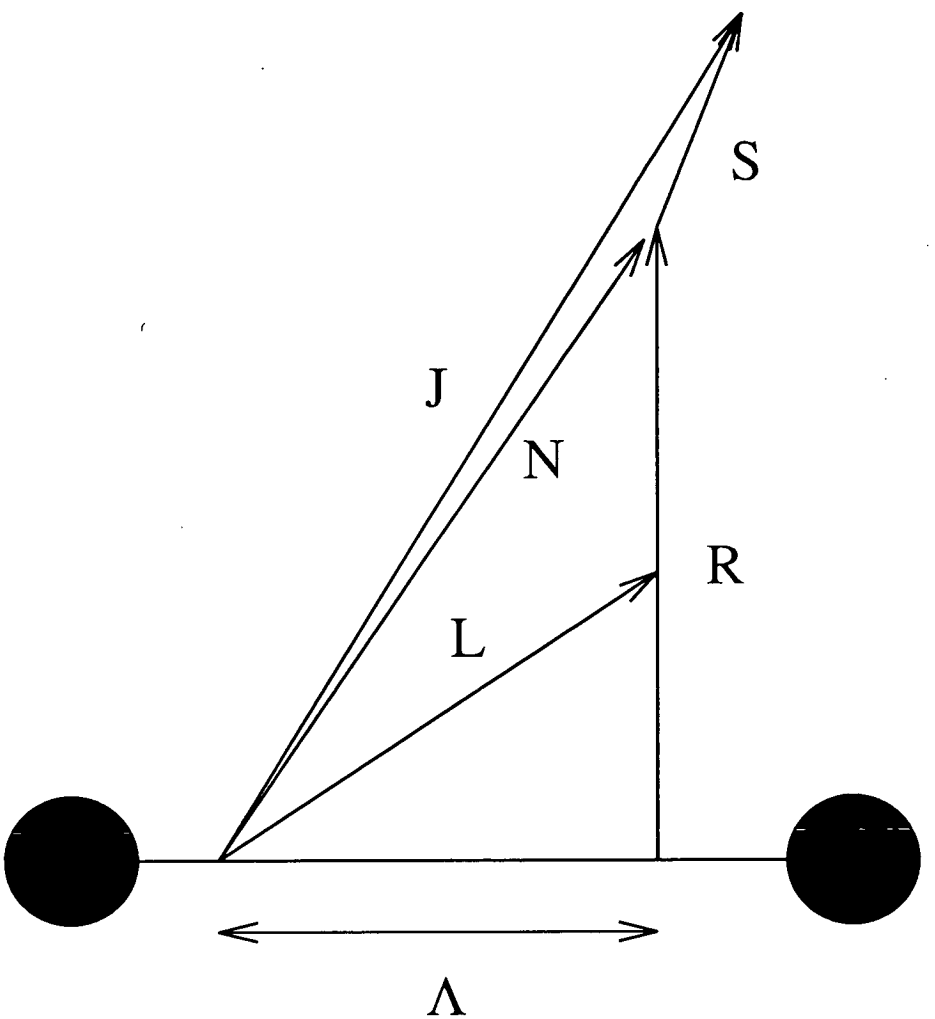

Figure 3–3: Vector diagram for Hund's coupling case (b)

In the case of SiF it has been shown conclusively that the SiF X state corresponds to Hunds case (a) ($X^2\Pi_{\frac{1}{2},\frac{3}{2}}$) and that the B state corresponds to case (b) ($^2\Sigma^+$) [15]. However, studies by Appelblad *et al.* upon the $C - X$ dispersed fluorescence spectrum have revealed that there is some ambiguity as to the correct assignment of the spin-orbit splitting constant, A, and hence the coupling case, due to the strict coincidence between the $\Delta_{\frac{3}{2}}(J)$ and $\Delta_{\frac{5}{2}}(J)$ levels for all except the lowest J values [21] .

The reason for this coincidence is apparent upon examination of equations 3.11 and 3.12. Substitution of $J = N + \frac{1}{2}$ and $J = N - \frac{1}{2}$, respectively, results in $F_1 = F_2$ for the same N if either $Y = 0$ or $Y = 4$ the it is impossible to say whether $A = 0$ or $4B$. These two alternative resultant energy level structures are shown in figure 3–4.

It is immediately obvious that the two systems depicted in figure 3–4 differ only in the position of the $J = \frac{3}{2}$ levels. Hence to prove conclusively the magnitude of the spin-orbit splitting it is necessary to examine the spectral lines involving these levels. Unfortunately, it was shown in the study by Appelblad *et al.* that in the $C - X$ system the relevant spectral lines occur in a highly congested part of the spectrum and hence they could not be positively identified due to the inadequate resolution of the experiment [21]. However by analogy with the isoelectronic SiCl $B' - X$ system, where the $B'^2\Delta$ state spin-orbit splitting constant has been shown to have a small finite value, ($A = -2.729cm^{-1}$ [39,40]), it is perhaps more likely that the SiF $C^2\Delta$ state is in fact transitional between pure Hund's case (a) and (b) and therefore it will be assumed that the spin-orbit splitting constant is $2.46cm^{-1}$ which is approximately $4B$. This could be proved beyond doubt by using a higher resolution technique than that of Appelblad *et al.* In that study the third order spectral lines lines were photographed using a 30ft concave grating spectrograph. It was suggested by Appelblad *et al.* that this question could be settled by the observation of the absorption spectrum of cold SiF (produced in flash photolysis). This method is obviously analogous to study by laser-induced fluorescence.Therefore it is conceivable that it may be possible to determine to true value of A from a laser excitation study of the $C^2\Delta - X^2\Pi$ transition.

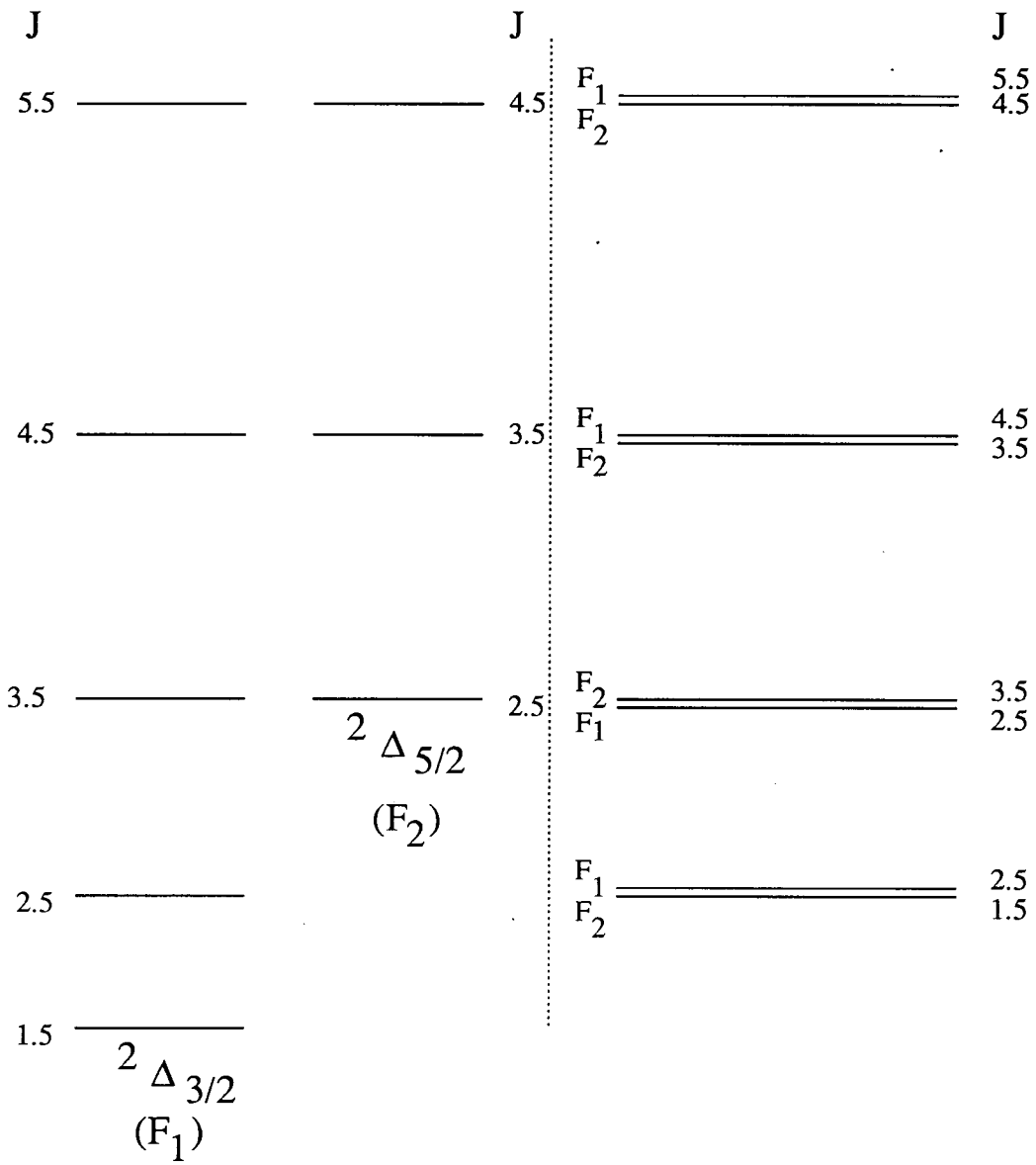

Figure 3–4: Schematic representation of the energy level structures of a $^2\Delta$ state in Hund's case (a) and (b).

The lefthand side of the figure represents a regular case (a) structure with $A = 4B$ and the righthand side represents the analogous structure for case (b) where $A = 0$. If the spin splitting constant γ is zero in the case (b) structure then there will be no splitting between the pairs $J = K \pm \frac{1}{2}$. In both cases the negligible splitting of all levels due to Λ doubling has been ignored.

3.5 Selection Rules and Transition Probabilities

Using the procedure briefly outlined in section 3.4 it should be possible to construct the rovibronic energy levels for the states under study. However, the appropriate transition probabilities and selection rules must also be understood to correctly interpret and simulate any spectrum.

3.5.1 Selection Rules for a Rovibronic Transition

The selection rules for an electric dipole allowed rovibronic transition are [37]

- $\Delta J = 0, \pm 1$
- $\Delta\Lambda = 0, \pm 1$ (in cases where Λ is well defined).
- $\Delta S = 0$ (in cases S is well defined).
- $+ \not\leftrightarrow + \; ; - \not\leftrightarrow - \; ; + \leftrightarrow -$ (only levels of opposite parity are connected.)
- $g \not\leftrightarrow g \; ; \; u \not\leftrightarrow u \; ; \; g \leftrightarrow u$ (for molecules containing a centre of inversion *i.e.* homonuclear diatomics.)

By applying the selection rules to the energy level structures for the $B - X$ and $C - X$ systems it is possible to predict the occurrence of the various rotational branches. The branches are labelled principally according to ΔJ with a preceeding superscript indicating ΔN[2]. The subscript indicates the F_1 and F_2 spin rotation and spin-orbit components in the upper and lower state, respectively[3]. Energy

---

[2]N values for the case (a) state are obtained by extrapolation from high J (where N is defined as case (b) is approached) to low J where N is not a good quantum number.

[3]Where both labels are the same only one is used.

level diagrams for the $^2\Sigma^+ - ^2\Pi$ and $^2\Delta - ^2\Pi$ transitions are thus shown in figures 3–5 and 3–6, respectively.

The relative transition intensities can be derived by calculating the line strength $S(J' : J'')$ for a single photon transition between an upper state J' and a lower state J'' where

$$S(J' : J'') = \sum_{m_{J'} m_{J''}} |\langle J' m_{J'} | \mu | J'' m_{J''} \rangle|^2 \tag{3.13}$$

These calculations were performed by using a general simulation program written by Zare [41]. The program required as input values for Λ, Σ, spectroscopic constants and state symmetries as well nuclear masses and sample temperature. The program calculated all the allowed transitions between two vibronic states and the corresponding line strengths and intensities.

3.5.2 Vibronic Transition Probabilities

The probability of spontaneous emission an upper rovibronic state, v', J', and a lower state, v'', J'', is given by the Einstein coefficient, $A_{v'v''}$ where

$$A_{v'v''} = \frac{64\pi^4\nu^3}{3h} \left\{ \frac{S_{J'J''}}{2J'+1} \right\} |R_{ev}|^2 \tag{3.14}$$

and

- $S_{J'J''}$ is the rotational line strength;
- $R_{ev}(r)$ is the transition moment integral;
- ν is the transition frequency (s^{-1}).

Hence, in the simple case of a two level system, after a time, $\tau = \frac{1}{A_{v'v''}}$, the number of molecules remaining in state v' is $\frac{1}{e}$ of the original number. In all real cases, the total radiative rate is the sum of all individual $A_{v'v''}$'s, and hence $\tau = \frac{1}{\sum_{v''} A_{v'v''}}$.

In this thesis, the low experimental spectral resolution used for the measurements of vibrational band intensities was such that it was possible to neglect

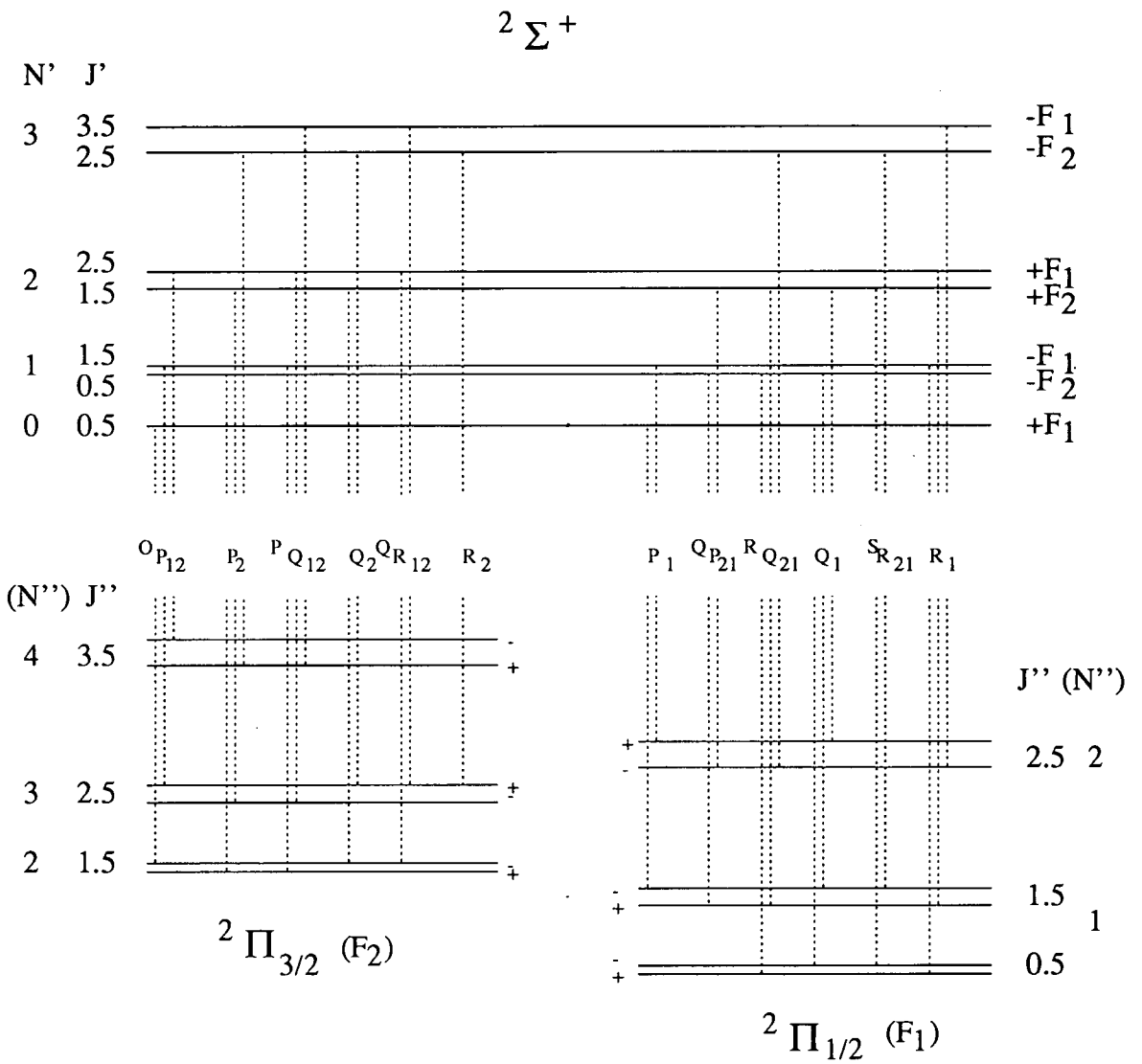

Figure 3–5: Energy level diagram for a $^2\Sigma^+(b) - ^2\Pi(a)$ transition. All 12 identifiable branches are shown

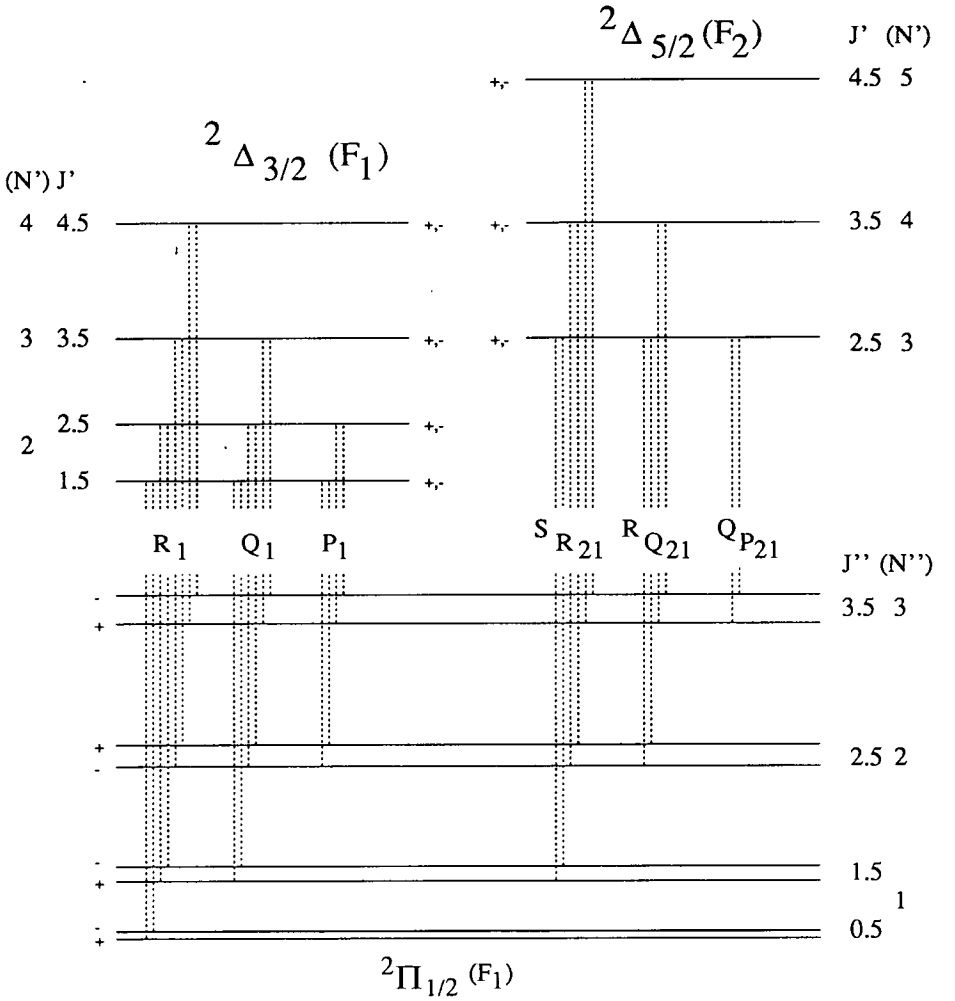

Figure 3–6: Energy level diagram for a $^2\Delta(a) - ^2\Pi(a)$ transition.

For simplicity, the figure only shows transitions from the $X^2\Pi_{\frac{1}{2}}$ spin-orbit state. The (negligible) Λ doubling of the $^2\Delta$ state has also been omitted. There are therefore 12 identifiable branches within the $^2\Delta - ^2\Pi_{\frac{1}{2}}$ subsystem and a further 12 (not shown) in the $^2\Delta - ^2\Pi_{\frac{3}{2}}$ subsystem.

rotational effects because the vibronic intensities were the sum over all rotational lines of the band. This leads to equation 3.14 simplifying to

$$A_{v'v''} = \frac{64\pi^4\nu^3}{3h}|R_{ev}(r)|^2 \tag{3.15}$$

The absolute vibrational transition probability can thus be defined as $p_{v'v''}$, where

$$p_{v'v''} = \{|R_{ev}(r)|\}^2 . \tag{3.16}$$

The transition moment integral, as shown in equation 3.17, is the integral over all electronic and vibrational coordinates of the product of the upper and lower state wavefunctions and the electric dipole moment operator, μ:

$$R_{ev} = \int \psi'_{ev}\mu\psi''_{ev}d\tau_{ev} \tag{3.17}$$

As the vibronic state wavefunctions are the product of the electronic and vibrational wavefunctions within the Born-Oppenheimer approximation, then ψ_{ev} can be expressed as the product of $\psi_e\psi_v$. Equation 3.17 now becomes

$$R_{ev} = \int\int \psi'_e\psi'_v\mu\psi''_e\psi''_v d\tau_e dr \tag{3.18}$$

where τ_e represents the electronic coordinates and r is the internuclear separation.

Upon integration over all electronic coordinates, equation 3.18 yields

$$R_{ev} = \int \psi'_v R_e \psi''_v dr \tag{3.19}$$

where R_e is the electronic transition moment given by

$$R_e = \int \psi'_e\mu\psi''_e d\tau_e. \tag{3.20}$$

The vibrational transition probability is therefore defined as

$$p_{v'v''} = \left\{\int \psi_{v'}R_e(r)\psi_{v''}dr\right\}^2 . \tag{3.21}$$

If the electronic transition moment function $R_e(r)$ happens to be independent of the internuclear distance, r, then the vibrational transition probability is directly proportional to the Franck-Condon factor, $q_{v'v''}$, which is the square of the vibrational wavefunction overlap

$$q_{v'v''} = \left\{\int \psi_{v'}\psi_{v''}dr\right\}^2 . \tag{3.22}$$

It is possible to calculate the form of these vibrational wavefunctions using the molecular potentials derived using the RKR procedure (see Appendix A) by solving the radial Schrödinger equation [42]:

$$\frac{\delta^2\psi}{\delta r^2} + \frac{8\pi^2\mu}{h^2}\{E_{vJ} - U_J(r)\}\psi_{vJ} = 0 \tag{3.23}$$

where E_{vJ} is the eigenvalue for the wavefunction ψ_{vJ} and $U_J(r)$ is the molecular potential as a function of r and J. The vibrational transition probabilities were calculated by solving equation 3.23 and hence exploiting equation 3.21 using a program written by Lawley and Wheeler [43]. As well as the molecular state potentials the program required as input a chosen form of the electronic transition dipole moment function.

The program also served as a check upon the accuracy of the RKR molecular potentials because it produced the term values of the vibronic transitions and the values of $p_{v'v''}$. It was found that these calculated values were in good agreement with the observations from which the spectroscopic constants were derived [36].

3.6 Laser-Induced Fluorescence Excitation Spectra

The reason for recording the LIF excitation spectra was mainly to establish the wavelengths at which specific (ro)vibronic levels of the $C^2\Delta$ and $B^2\Sigma^+$ states could be populated. These scans could also reveal the characteristic pattern of rovibronic transitions, proving unambiguously the identity of the states under study. From the experimental rotational intensities it was also possible to estimate the rotational temperature of the sample.

3.6.1 Experimental Method

The excitation spectra were obtained using the equipment described in chapter 2. The SiF radicals were typically generated by combining a flow of argon (500

SCCM) and a 10% mixture of SiF_4 in argon (10 SCCM) well before entering the discharge region. The mixture then passed through the microwave cavity operating at $\sim$ 15 Watts where the plasma could be seen to produce a deep violet emission. This flow produced a steady state pressure of about 1 Torr in the excitation zone.

It was found that increasing the pressure of the argon flow significantly increased the amount of SiF present in the excitation zone, probably due to the argon acting as a buffer to reduce diffusion of the radical species to the flow system walls. Therefore when it was necessary to maximise the LIF signal the flow rate of the argon carrier was increased to produce pressures of up to 5 Torr.

The mixtures of 10% SiF_4 in argon were prepared, using the vacuum line, in a $10dm^3$ Pyrex bulb. The bulb was initially filled with approximately 76 Torr of SiF_4 before adding argon to produced a combined pressure of 760 Torr. The mixture was left to equilibrate for a number of hours (generally overnight) to allow complete mixing. The gases used in this chapter were SiF_4 (Union Carbide, 99.99%) and argon (BOC, 99.99%).

The LIF excitation spectra were obtained in the region 250-290 nm. Excitation was performed from the lower, $^2\Pi_{\frac{1}{2}}$, spin-orbit component of $v'' = 0$ of the ground state to $v' = 0, 1$ and 5 of the $B^2\Sigma^+$ state and to $v' = 0$ and 1 of the $C^2\Delta$ state. Unfortunately, due to wavelength restrictions of the laser system used for this section of work, $v' = 2$ of the $B^2\Sigma^+$ state could only be accessed from the $^2\Pi_{\frac{3}{2}}$ spin orbit component (a factor of $\sim$ 2 less populated than the $^2\Pi_{\frac{1}{2}}$ component) whereas the $v' = 3$ level could not be populated at all[4].

Although it could be accessed, an excitation spectrum for $v' = 4$ was not recorded as the computer controlling the WEX unit crystals was unable to track the doubled output at this wavelength due to a combination of low dye output

[4]As mentioned in chapter 2, the laser system used in this particular study was the 532 nm pumped dye laser. Unfortunately when working in this mode it was impossible to attain lasing in the dye laser to produce the appropriate dye laser output which could either be doubled or mixed to excite these transitions.

power and an unsuitable filter on the doubled monitor photodiode. An automatic laser scan, therefore, was not possible. Nevertheless, the $v' = 4$ level could be excited (for the purposes of recording a dispersed fluorescence spectrum) by manually tuning the dye laser to the appropriate wavelength.

The excitation spectra were recorded by scanning the laser through the appropriate wavelength region with the monochromator set (in first order) to collect the resultant emission in a region of maximum fluorescence. This region chosen such that it was isolated from the position of the laser excitation wavelength to reduce the detection of scattered radiation.

As typical laser pulses energies were of ~1 - 10 mJ it was anticipated that this high intensity of radiation could result in optical saturation of the stronger transitions. From initial runs it became apparent that this was indeed the case. Therefore, to reduce this effect, the laser beam was attenuated by replacing one of the turning prisms in the optical line with a glass slide. Pulse energies were correspondingly reduced to typically ~ 25 μJ by this measure.

3.6.2 LIF Excitation Spectra of the $B^2\Sigma^+(v' = 0, 1, 2$ and $5) - X^2\Pi(v'' = 0)$ Transitions

The LIF excitation spectra for the $B^2\Sigma^+(v' = 0, 1, 2$ and 5) states are shown in figures 3–7 to 3–10 respectively. Each spectrum is presented with the appropriate simulation which was generated from the rotational line strengths calculated using the method discussed in section 3.5. A further (simple) program, written by Singleton [44] was employed to convolute the simulated spectrum with an assumed the laser band-width. A value of ~ 0.5 cm^{-1} was found to give the best agreement between experiment and simulation.

Excitation of the $B^2\Sigma^+(v' = 5) - X^2\Pi_{\frac{1}{2}}(v'' = 0)$ sub-band was impossible without simultaneously exciting the tail of the $C^2\Delta(v' = 0) - X^2\Pi_{\frac{3}{2}}(v'' = 0)$ transition which is much stronger due to a more favourable Franck-Condon factor. This problem was alleviated by observing only the fluorescence on the relatively intense $B - X(5, 8)$ band which is spectroscopically isolated from any significant

$C - X$ emission. However, from examination of spectrum 3–10 it can be seen that there is still evidence of direct $C - X$ excitation, particularly in the region of the P_1 branch. It should be noted that the strong transition in the region of the P_1 band head is most likely due to the excitation of an atomic Si electronic transition [45].

In all the $B^2\Sigma^+ - X^2\Pi$ LIF excitation spectra the characteristic Q_1 and P_1 heads can easily be located as well as the partially resolved rotational structure. It is thoroughly apparent from figures 3–7 to 3–10 that the experimentally measured spectra are well matched by the simulations, thus confirming the state assignments.

3.6.3 LIF Excitation Spectra of the $C^2\Delta(v' = 0, 1) - X^2\Pi(v'' = 0)$ Transitions

The analogous $C^2\Delta(v' = 0, 1) - X^2\Pi_{\frac{1}{2}}(v'' = 0)$ LIF excitation spectra can be seen in figures 3–11 and 3–12. The most obvious features of these spectra are the strong Q_1 band head (which is coincident with the weaker ${}^QP_{21}$ branch) and the P_1 branch which is spectroscopically isolated from the remainder of the spectrum and extends to form a band head. Again there is good agreement between experiment and simulation thus confirming that it is possible to populate these $C^2\Delta$ state vibrational levels without simultaneously exciting $B - X$ transitions.

3.6.4 The $C^2\Delta$ Spin-Orbit Splitting Constant, A.

It was impossible from examination of these $C - X$ excitation spectra to resolve unambiguously the question of the value of the SiF $C^2\Delta$ state spin-orbit splitting parameter, A *ie.* whether $A = 0$ or $4B$. The band width of the laser's doubled output was too broad to isolate the spectral lines in question (as discussed in section 3.4.4). However, the relative rotational line strengths are also related to the value of A and hence can be used as an indicator of the most likely solution of the two alternatives. This is best illustrated by examining the theoretically

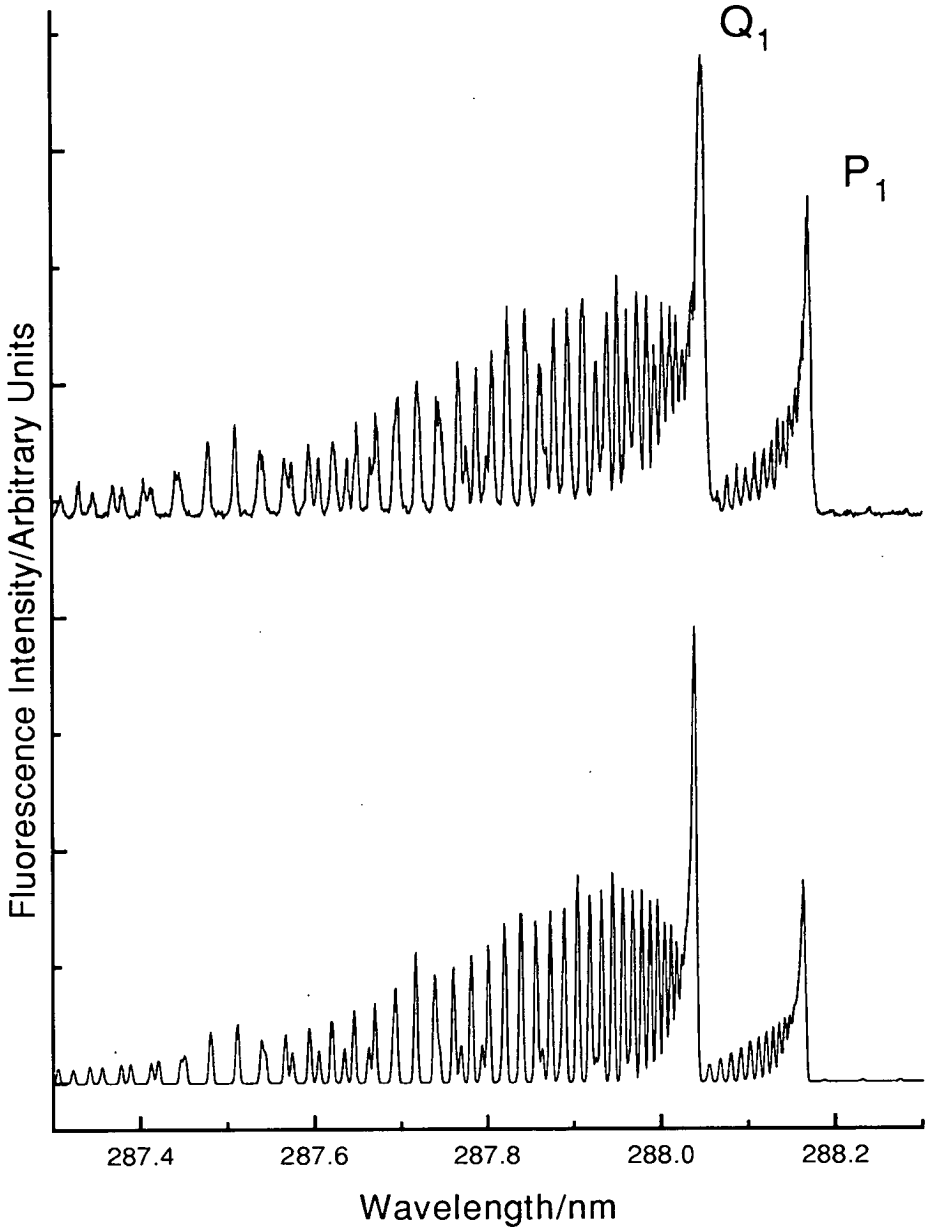

Figure 3–7: LIF excitation spectrum of the $B^2\Sigma^+(v' = 0) - X^2\Pi_{\frac{1}{2}}(v'' = 0)$ sub-band.

The upper trace shows the experimentally observed spectrum (laser pulse energy $\sim 25\mu J$ in $\sim$ 10 ns with a $\sim$1 cm^2 spot size) with the lower trace showing a simulation where the assumed bandwidth is 0.5 cm^{-1} and the rotational temperature is $300K$.

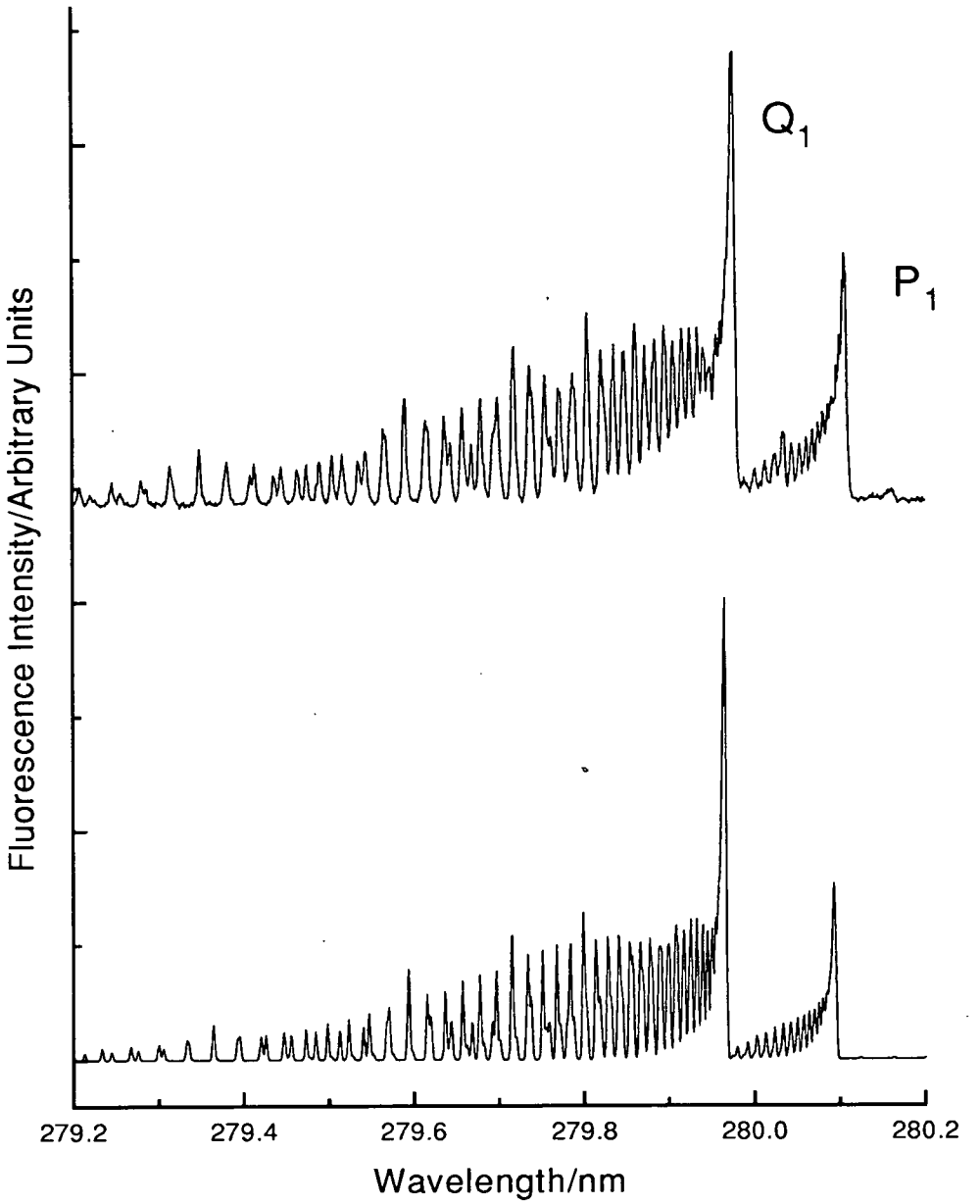

Figure 3–8: LIF excitation spectrum of the $B^2\Sigma^+(v' = 1) - X^2\Pi_{\frac{1}{2}}(v'' = 0)$ sub-band.

Conditions as in figure 3–7.

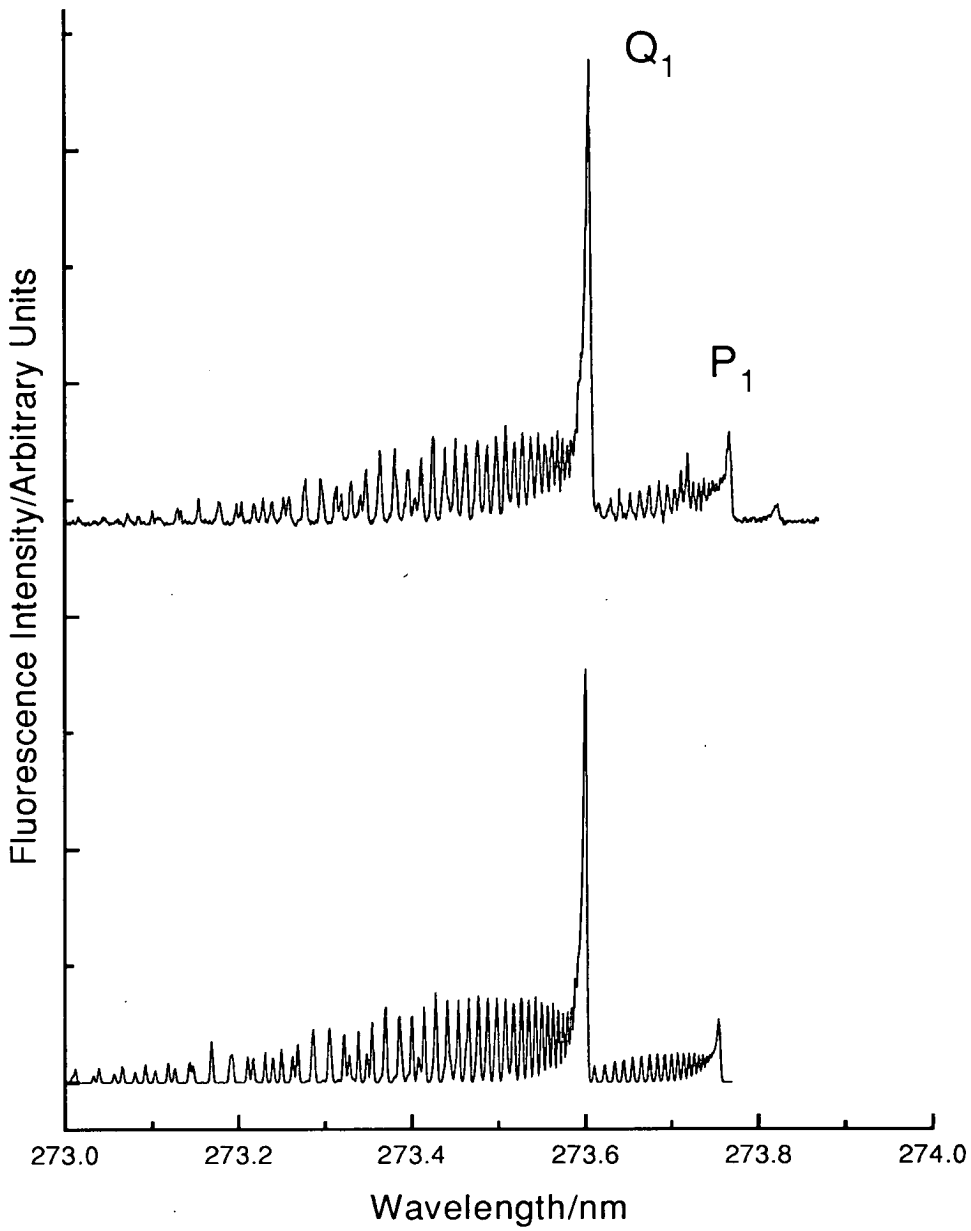

Figure 3–9: LIF excitation spectrum of the $B^2\Sigma^+(v' = 2) - X^2\Pi_{\frac{3}{2}}(v'' = 0)$ sub-band.

Conditions as in figure 3–7.

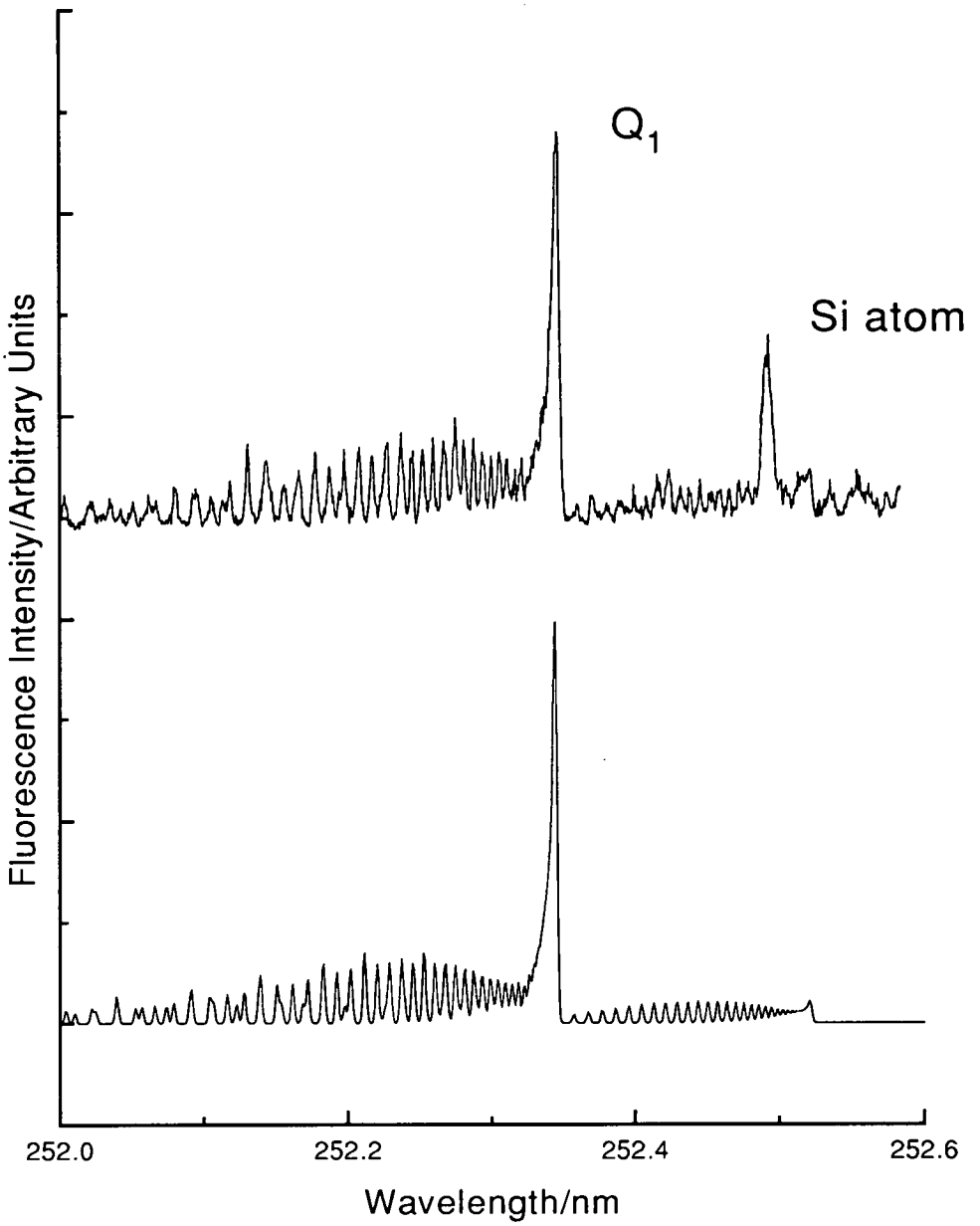

Figure 3–10: LIF excitation spectrum of the $B^2\Sigma^+(v' = 5) - X^2\Pi_{\frac{1}{2}}(v'' = 0)$ sub-band.

Conditions as in figure 3–7. Interference due to directly excited $C - X$ (0,0) fluorescence can be seen at the higher wavelength region of the spectrum. The sharp feature in the region of the P_1 band head is most probably due to the excitation of silicon electronic transition [45].

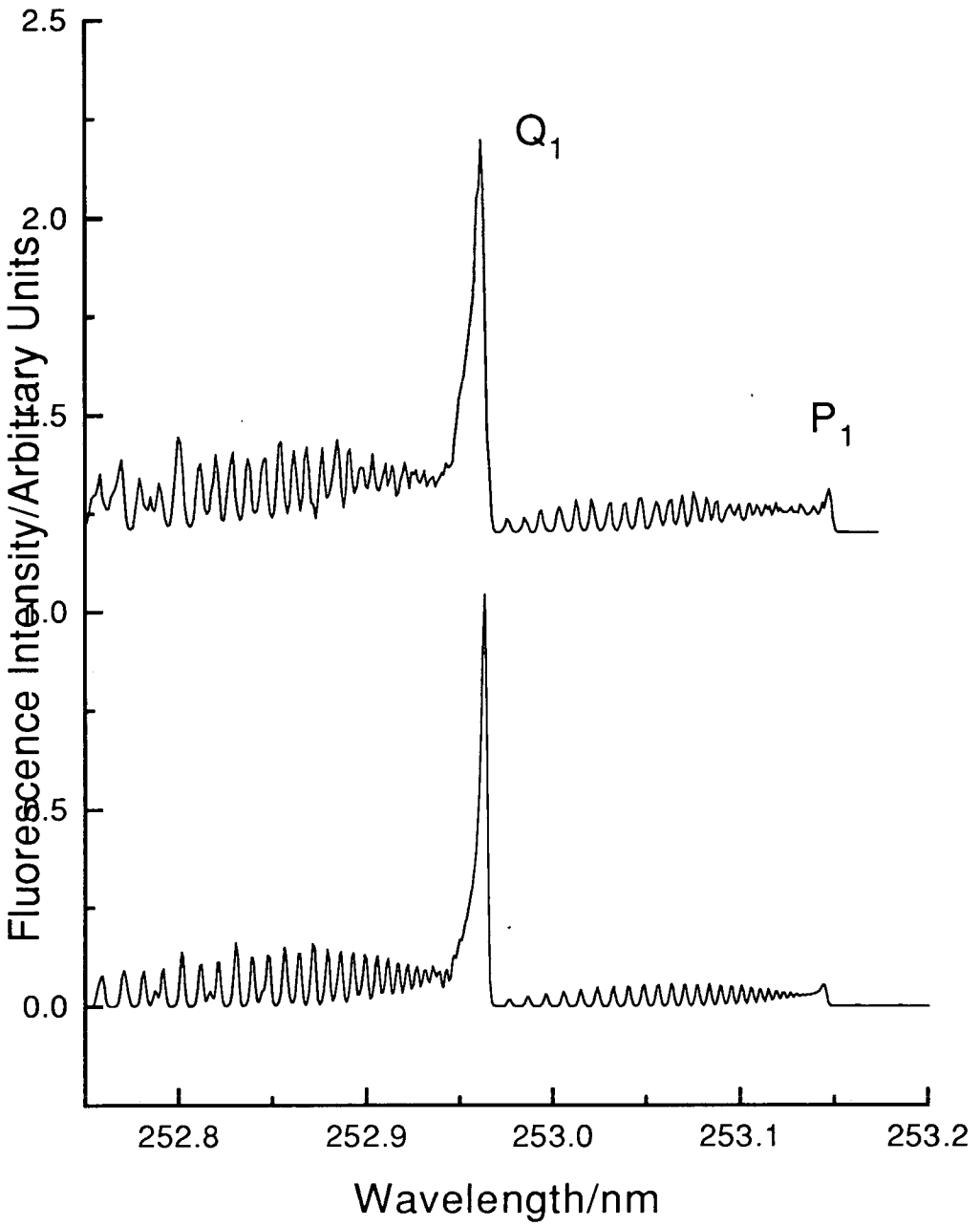

Figure 3–11: LIF excitation spectrum of the $C^2\Delta(v' = 0) - X^2\Pi_{\frac{1}{2}}(v'' = 0)$ sub-band.

Upper trace shows the experimentally measured spectrum (laser pulse energy $\sim 25\mu J$ in $\sim 10ns$ with a ~ 1 cm^2 spot size). The lower trace shows a simulation where the assumed bandwidth is 0.5 cm^{-1} and the rotational temperature is $300K$.The spin-orbit splitting parameter, A ,of the $C^2\Delta$ state is taken to be 2.46 cm^{-1}

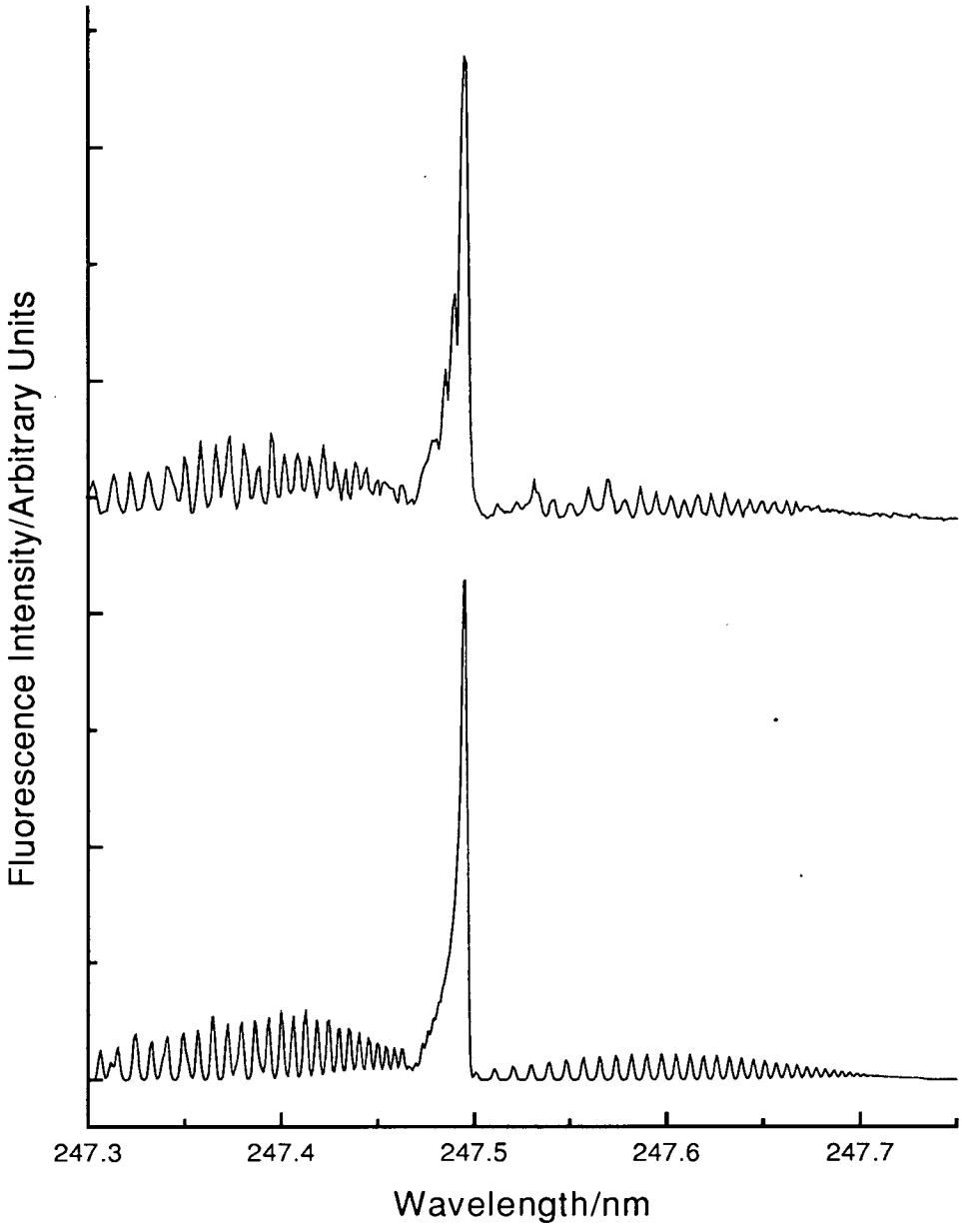

Figure 3–12: LIF excitation spectrum of the $C^2\Delta(v' = 1) - X^2\Pi_{\frac{1}{2}}(v'' = 0)$ sub-band.

Conditions as in figure 3–11.

obtained intensities of the P_1 branch which appears in isolation in the $C - X$ excitation spectra.

Figure 3–13 shows a comparison of two simulated and the experimentally measured versions of the P_1 branch of the $C^2\Delta(v' = 0) - X^2\Pi_{\frac{1}{2}}(v'' = 0)$ transition. The spectra have been normalised against the strong Q_1 band head (not shown in figure 3–13). It is apparent that the relative transition intensities of the experimental spectrum are better matched by the simulation where $A = 2.46$ cm^{-1} thus perhaps indicating that this is its true value. This point could be settled more conclusively by recording a higher resolution spectrum.

3.7 Dispersed Fluorescence Spectra

To establish the vibronic transition probabilities relevant to this thesis it was necessary to examine the resultant fluorescence upon selective excitation of each vibronic state.

3.7.1 Experimental Method

The dispersed fluorescence spectra reported in this chapter were recorded under essentially identical conditions to the excitation spectra. In each case the laser was tuned to the intense Q head of the $B - X$ or $C - X$ transition under study. This was done purely to maximise the signal intensities: excitation to another part of the same vibronic transition produced no observable change in the relative fluorescence intensities. Likewise, optical saturation was no longer a consideration therefore maximum laser pulse energies were employed.

The resultant fluorescence was dispersed in first order by the monochromator which scanned over all wavelength regions in which there was measurable emission. In all cases the the monochromator slit widths were set at 0.4mm, which is equivalent to a resolution of 0.3 nm.

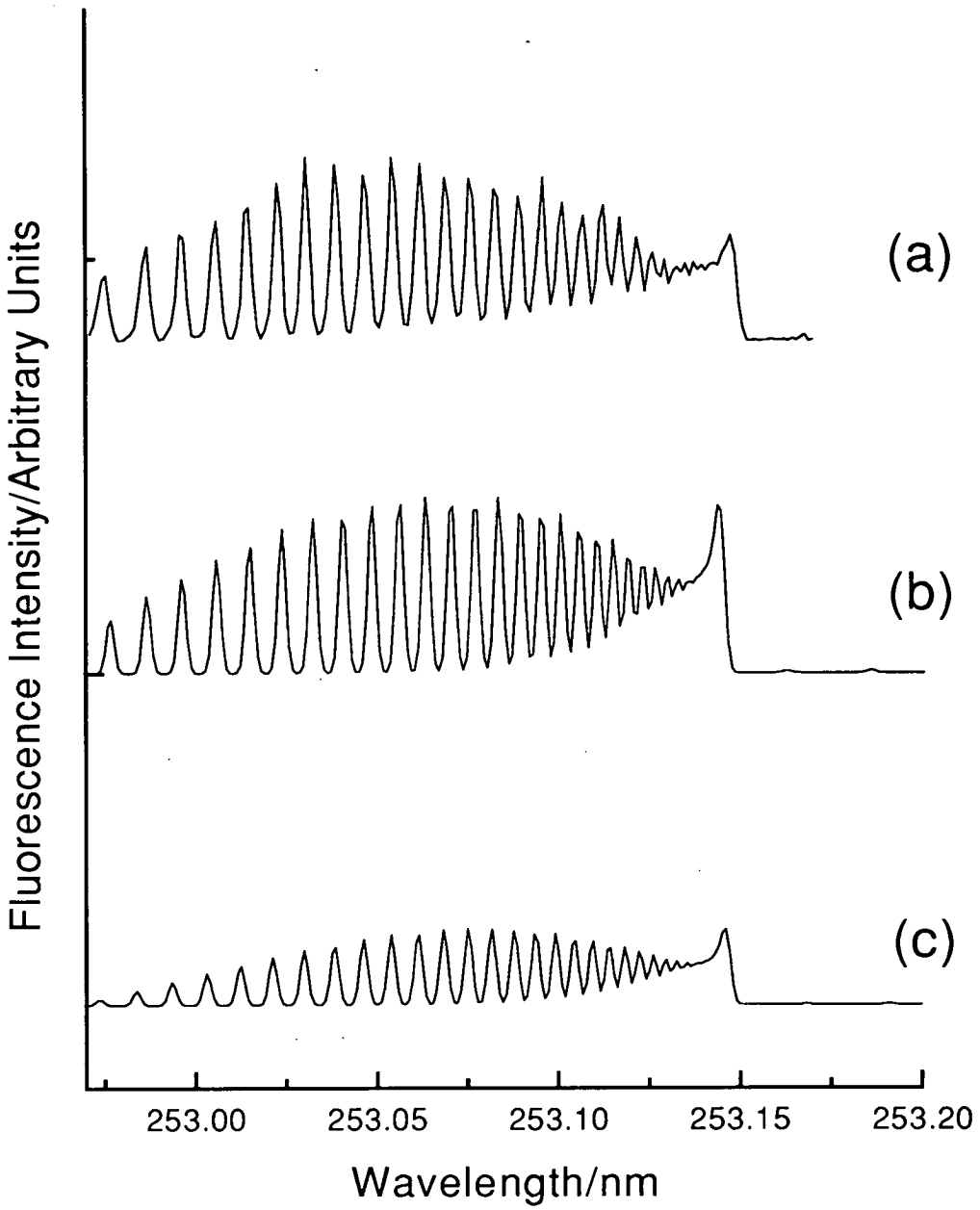

Figure 3–13: LIF excitation spectrum of the P_1 branch of the $C^2\Delta(v' = 0) - X^2\Pi_{\frac{1}{2}}(v'' = 0)$ sub-band.

(a) Experiment (conditions as in figure 3–11). (b) Simulation, $A = 2.46cm^{-1}$. (c) Simulation, $A = 0$.

3.7.2 $B^2\Sigma^+(v' = 0, 1, 2, (3), 4$ and $5)$ - $X^2\Pi_{\frac{1}{2},\frac{3}{2}}(v'' = 0 - 12)$ Emission Spectra

Fluorescence spectra for the $B^2\Sigma^+(v' = 0, 1, 2, (3), 4$ and $5)$ - $X^2\Pi_{\frac{1}{2},\frac{3}{2}}(v'' = 0 - 12)$ transitions can be seen in figures 3–14 to 3–19, respectively, alongside the spectral simulation (outlined in section 3.5.2). Because $B^2\Sigma^+(v' = 3)$ could not be accessed only the predicted spectrum is presented.

It can be seen from the spectra that the peaks appear as a series of doublets due to the spin-orbit splitting of the $^2\Pi$ ground state. The transitions can be seen to be significantly off-diagonal, indicated by the length of the progressions.

As mentioned in section 3.6.2 it was impossible to prepare $B^2\Sigma^+(v' = 5)$ without simultaneously exciting the $C^2\Delta(v' = 0)$ state. The contribution of the resultant $C - X$ emission to the dispersed spectrum was reduced by exploiting the disparity in the radiative lifetimes of the $B^2\Sigma^+$ ($\tau_{rad} \leq 10ns$) and $C^2\Delta$ ($\tau_{rad} \approx 94ns$) states[5]. The LIF was thus gated electronically so that signal was only collected during a 10 ns period immediately after the initial laser excitation step. Therefore virtually all the $B^2\Sigma^+$ emission could be collected whereas the $C^2\Delta$ state contribution would be substantially reduced. Unfortunately, as can be seen from figure 3–19, there is still evidence of $C - X$ emission in the shorter wavelength region of the spectrum.

The intensities for each transition were then integrated to yield the vibronic transition probabilities $p_{v'v''}$ as defined in equation 3.21 after correction for the wavelength response of the system and for the frequency dependent term, ν^3, shown in equation 3.14. The *relative* vibronic transition probability is therefore

$$p_{v'v''} \propto \frac{A_{v'v''}}{\nu^3_{v'v''}} C(\nu) \tag{3.24}$$

where $C(\nu)$ is a frequency dependent correction factor for the detection system response.

---

[5]This will be discussed in more detail in chapter 4

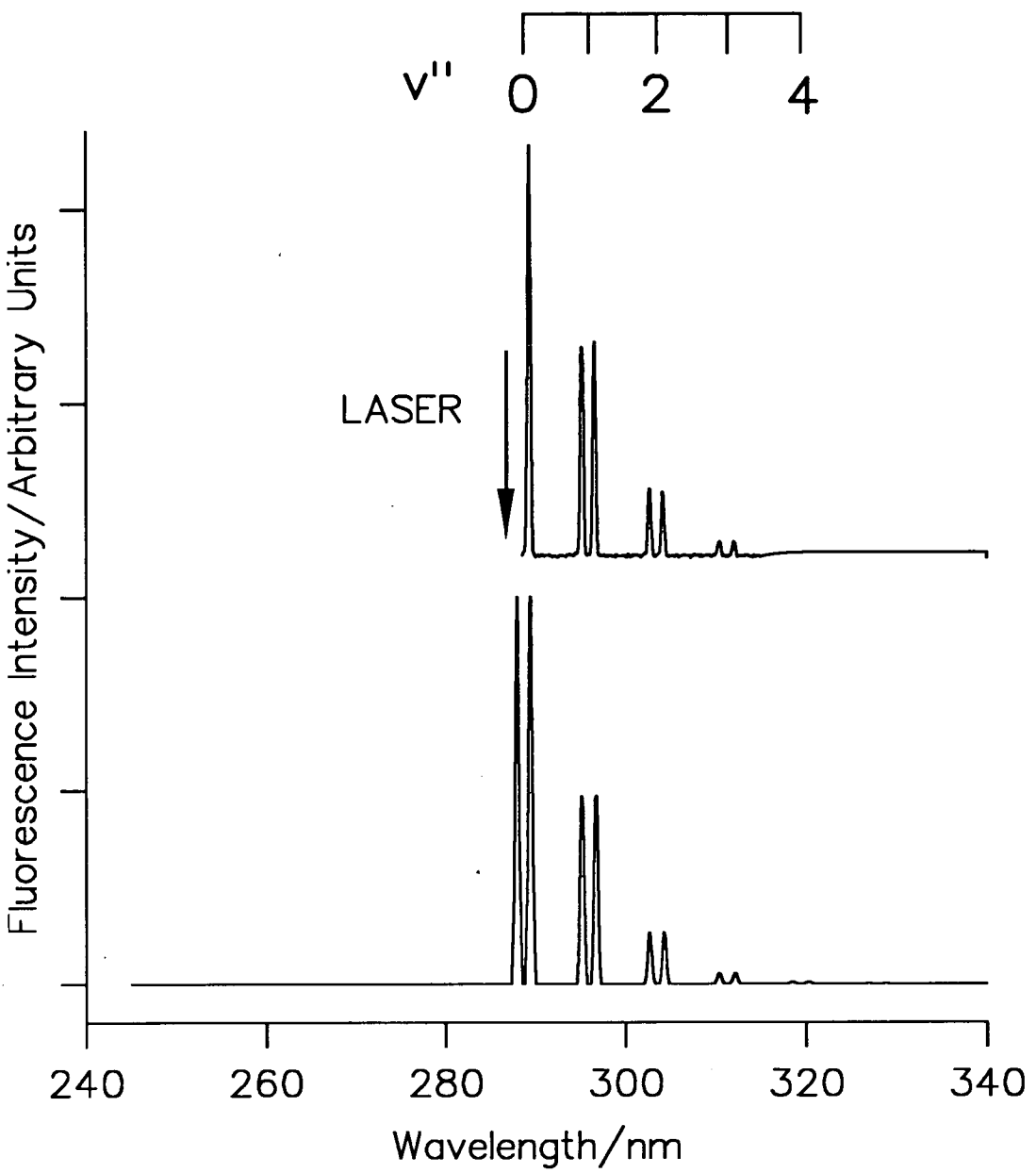

Figure 3–14: Dispersed fluorescence spectrum of the $B^2\Sigma^+(v' = 0) - X^2\Pi(v'')$ transition.

The upper trace is the experimentally produced spectrum and the lower trace is the simulation using calculated Franck-Condon factors as described in section 3.5.2 (*i.e* $R_e(r)$=constant). The assumed bandwidth of 0.3 nm adequately matches that of the experiment. The position of the excitation wavelength is indicated by the vertical arrow. Signals over this region were not recorded to avoid the detection of scattered laser light.

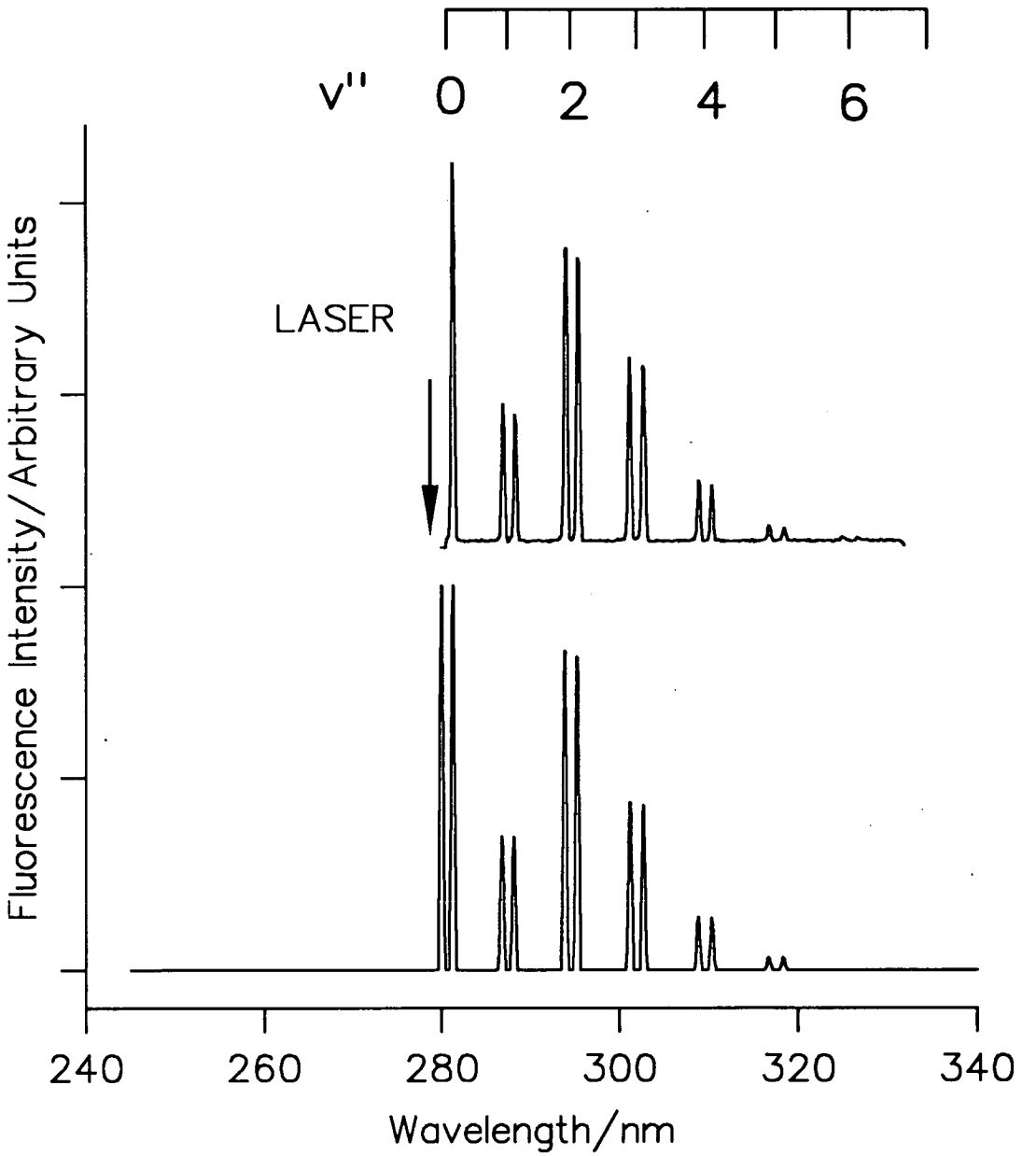

Figure 3–15: Dispersed fluorescence spectrum of the $B^2\Sigma^+(v' = 1) - X^2\Pi(v'')$ transition.

The experimental conditions are essentially the same as described for figure 3–14.

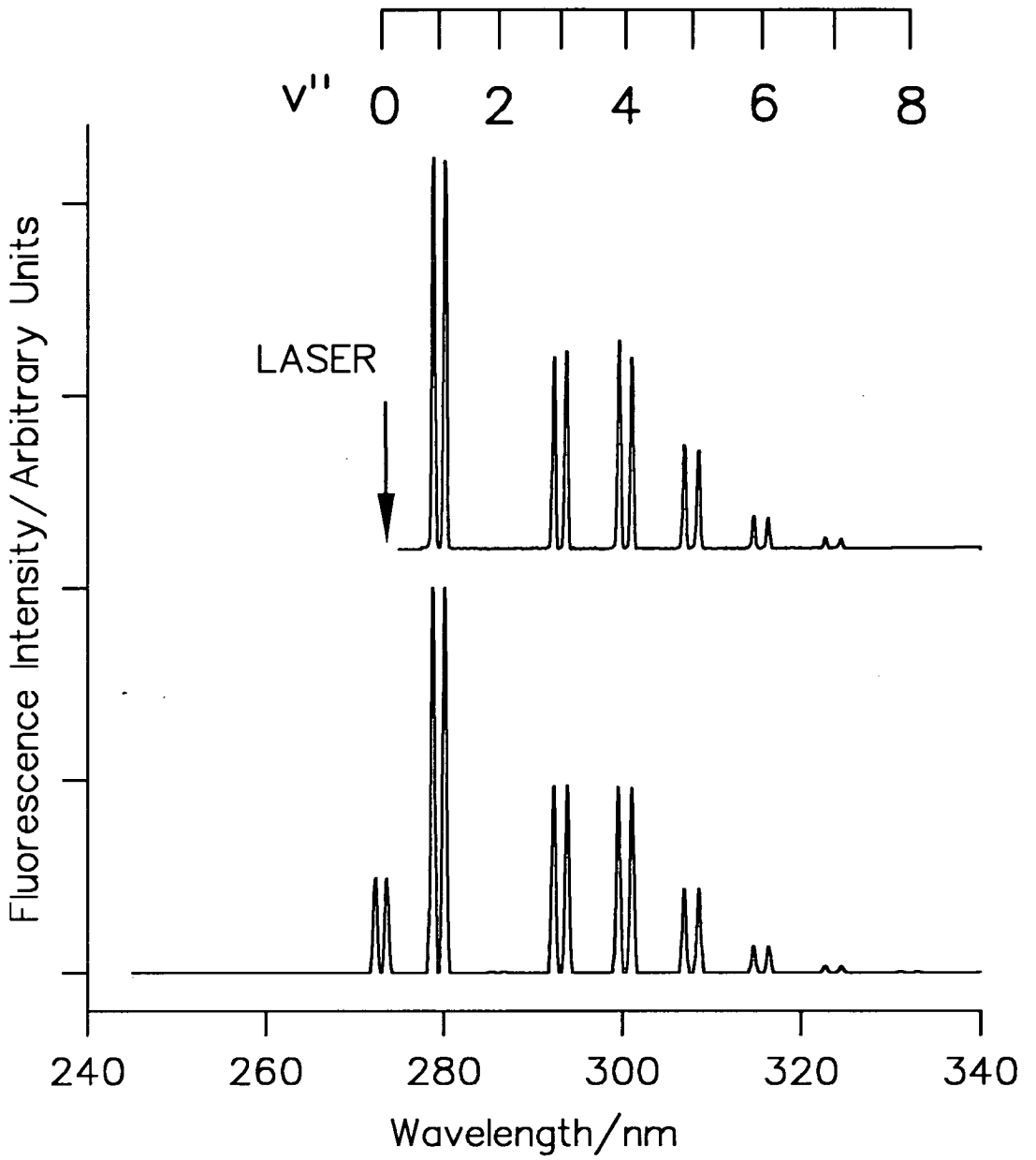

Figure 3–16: Dispersed fluorescence spectrum of the $B^2\Sigma^+(v' = 2) - X^2\Pi(v'')$ transition

The experimental conditions are essentially the same as described in figure 3–14 with the exception that the $B^2\Sigma^+(v' = 2)$ level was excited via the $X^2\Pi_{\frac{3}{2}}(v'' = 0)$ spin-orbit component.

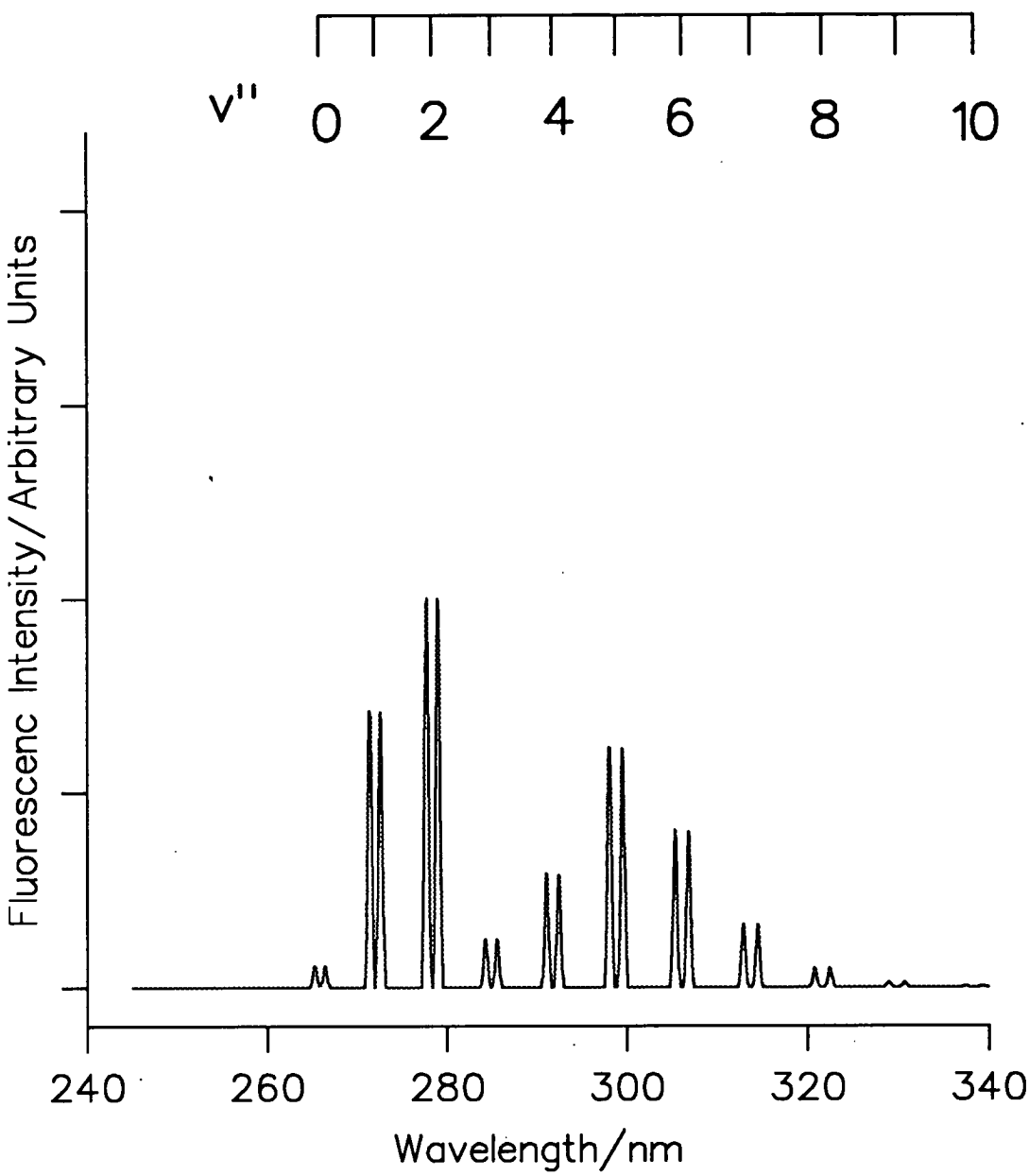

Figure 3–17: Simulation of the dispersed fluorescence spectrum of the $B^2\Sigma^+(v' = 3) - X^2\Pi(v'')$ transition.

As noted in the text, it was not possible to obtain an experimental spectrum for this transition. Simulation performed assuming the same conditions as described in figure 3–14.

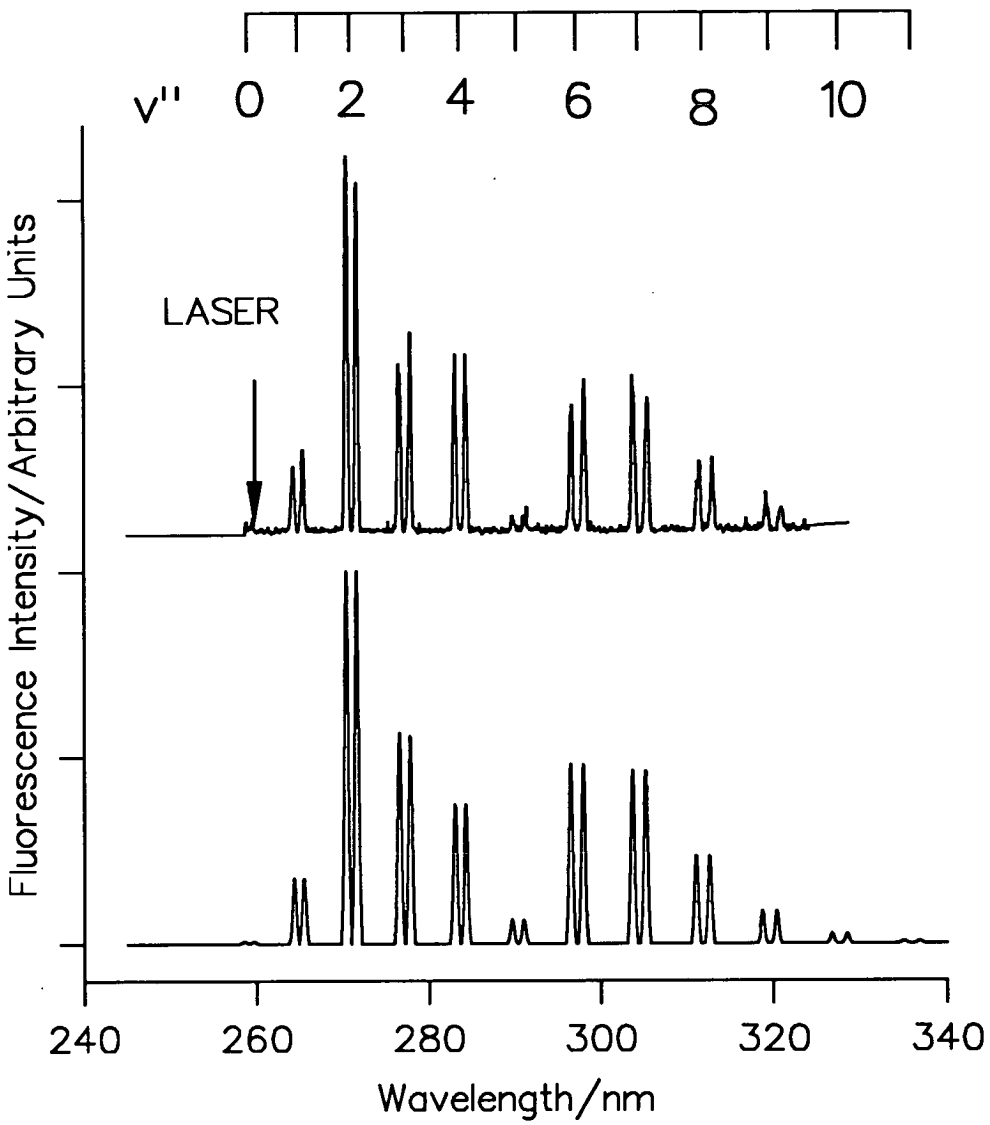

Figure 3–18: Dispersed fluorescence spectrum of the $B^2\Sigma^+(v' = 4) - X^2\Pi(v'')$ transition

The experimental conditions are essentially the same as described for figure 3–14.

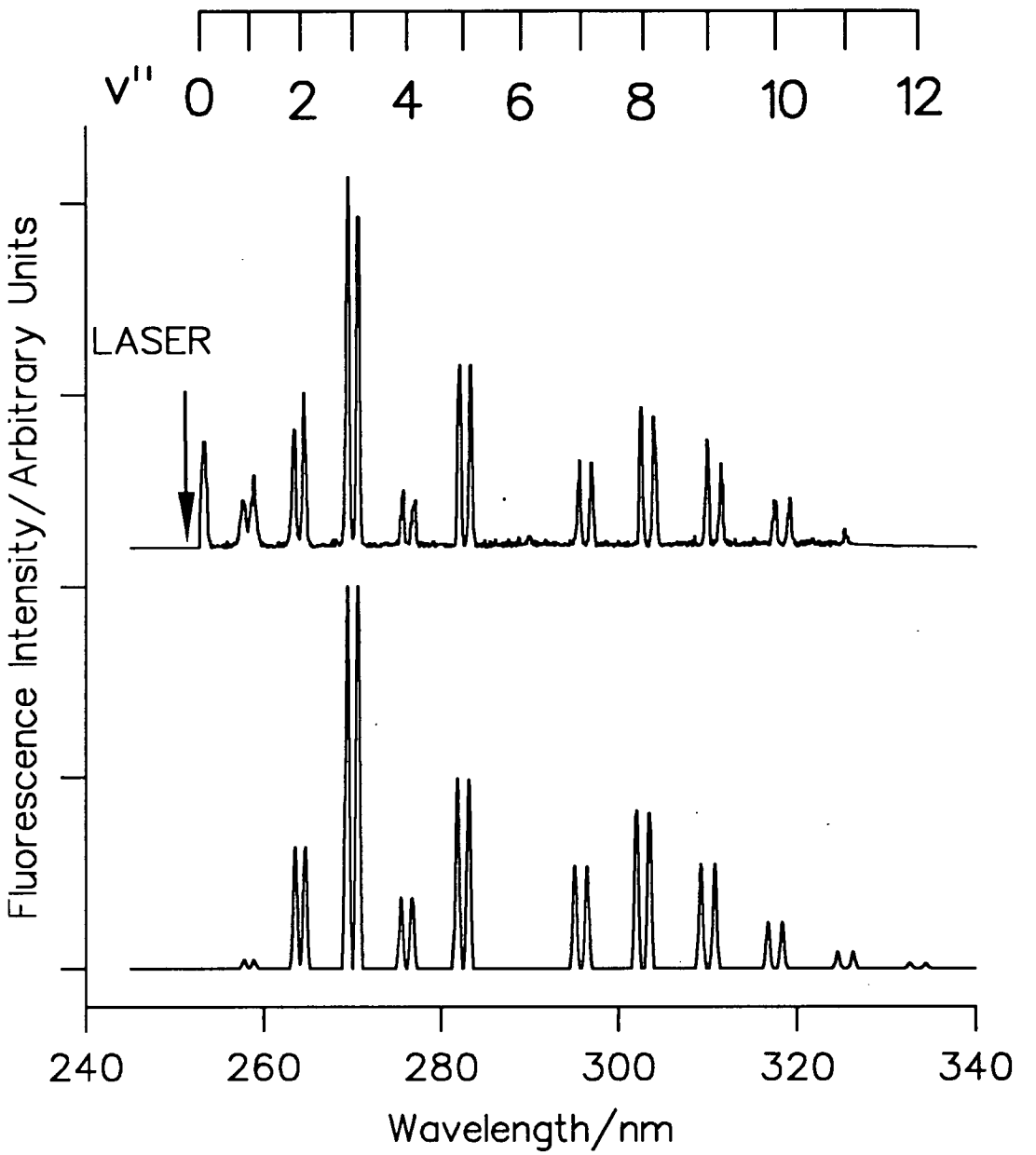

Figure 3–19: Dispersed fluorescence spectrum of the $B^2\Sigma^+(v' = 5) - X^2\Pi(v'')$ transition

Fluorescence was collected over the first $\sim$ 10 ns following the laser pulse. Otherwise, conditions were the same as in figure 3–14. The bands to short wavelength present in the experimental but not the simulated spectrum result from the simultaneously directly excited $C^2\Delta(v' = 0)$ state.

These results for the vibrational transition probabilities are presented in table 3–2, where the sums of $p_{v'v''}$ have been normalised to 1000. For the case of $B^2\Sigma^+(v' = 5)$, the intensities of the bands overlapping with the $C - X$ emission were estimated from the Franck-Condon factors for the purposes of the normalisation step. This was justified by the lack of an appreciable $R_e(r)$ dependence as will be demonstrated in section 3.8.

3.7.3 $C^2\Delta(v' = 0, 1) - X^2\Pi_{\frac{1}{2},\frac{3}{2}}(v'' = 0 - 5)$ Emission Spectra

The corresponding $C^2\Delta(v' = 0, 1) - X^2\Pi_{\frac{1}{2},\frac{3}{2}}(v'' = 0 - 5)$ emission spectra, recorded in the presence of 1 Torr argon, are shown with the relevant simulations in figures 3–20 and 3–21, respectively. As will be discussed in greater detail in chapter 4, there is no evidence of collisional transfer to vibrational levels of the $B^2\Sigma^+$ state. This is in contrast to the analogous SiCl cases where vibronic transfer was observed from the $B'^2\Delta$ to the $B^2\Sigma^+$ state in the presence of argon [44,46,47]. For excitation of $v' = 1$, there was no evidence for any relaxation to $v' = 0$. Again, as anticipated, the spectra can be seen to be significantly more diagonal than the $B - X$ transitions. The corrected vibrational probabilities are presented in table 3–3.

3.8 Discussion

3.8.1 $B^2\Sigma^+ - X^2\Pi$ System

It can be seen from table 3–2 that there is an excellent agreement between the experimentally derived vibrational transition probabilities, $p_{v'v''}$, and the Franck-Condon factors, $q_{v'v''}$. These Franck-Condon factors, which were derived using RKR potentials, are also compared with the only previous reported calculation of these values derived from the less exact Morse potential functions [48]. It is apparent that there is a reasonable correlation between the two sets of values. The discrepancies are probably due to the different type of molecular potentials

(v',v")	$p_{v'v"}$(expt)[a]	$q_{v',v"}$[b] Ed[c]	$q_{v'v"}$[b] RNN[d]	(v',v")	$p_{v'v"}$(expt)[a]	$q_{v'v"}$[b] Ed[c]	$q_{v'v"}$[b] RNN[d]
(0,0)	589(4)	582	568	(1,0)	322(5)	323	327
(0,1)	300(6)	303	311	(1,1)	112(2)	119	104
(0,2)	88(3)	90	94	(1,2)	301(14)	307	306
(0,3)	19(2)	20	21	(1,3)	187(5)	174	181
(0,4)	4(1)	4	3	(1,4)	60(1)	58	61
(0,5)	-	-	-	(1,5)	18(1)	15	15
(2,0)	85(4)	81	87	(3,0)	f)	12	14
(2,1)	354(13)	357	347	(3,1)	f)	175	183
(2,2)	-	1	-	(3,2)	f)	265	243
(2,3)	179(7)	200	197	(3,3)	f)	34	43
(2,4)	210(13)	212	218	(3,4)	f)	88	79
(2,5)	125(3)	103	107	(3,5)	f)	200	203
(2,6)	40(1)	34	e)	(3,6)	f)	140	e)
(2,7)	7(1)	9	e)	(3,7)	f)	60	e)
(4,0)	2(2)	1	1	(5,0)	-	-	-
(4,1)	42(4)	40	45	(5,1)	5(1)	5	6
(4,2)	255(4)	242	246	(5,2)	79(2)	80	89
(4,3)	147(6)	146	122	(5,3)	268(7)	268	262
(4,4)	130(6)	104	128	(5,4)	45(5)	53	36
(4,5)	13(1)	19	14	(5,5)	171(16)	152	153
(4,6)	138(8)	154	e)	(5,6)	5(3)	-	e)
(4,7)	153(7)	158	e)	(5,7)	85(8)	95	e)
(4,8)	82(4)	87	e)	(5,8)	153(14)	155	e)
(4,9)	38(5)	34	e)	(5,9)	109(15)	110	e)
-	-	-	e)	(5,10)	62(7)	53	e)
-	-	-	e)	(5,11)	16(3)	20	e)

Table 3–2: Vibrational transition probabilities in the SiF $B^2\Sigma^+$ - $X^2\Pi$ system a) Vibrational transition probabilities. Numbers in parentheses represent 1σ uncertainties in the last digit. The sum of $p_{v'v'}$ for a given v' has been normalised to 1000. b) Franck-Condon factors. The sum of $q_{v'v''}$ for a given v' has been normalised to 1000. c) Calculated from RKR potentials, this work. d) Calculated from Morse potentials, ref. [48]. e) Not calculated in ref. [48]. f) Due to wavelength restrictions of the laser system, it was not possible to access $B^2\Sigma^+(v' = 3)$.

(v',v")	$p_{v'v"}$ (expt)[a]	$q_{v'v"}$ [b] Ed[c]	$q_{v'v"}$ [b] SM[d]	$p_{v'v"}$ (calc)[e]
(0,0)	686(27)	885	886	690
(0,1)	253(3)	103	107	252
(0,2)	53(1)	11	3	49
(0,3)	7(1)	1	-	8
(0,4)	1(1)	-	-	1
(1,0)	7(4)	112	100	3
(1,1)	472(5)	690	690	467
(1,2)	381(8)	168	197	388
(1,3)	109(3)	26	8	112
(1,4)	25(3)	3	-	25
(1,5)	6(3)	-	-	5

Table 3–3: Vibrational transition probabilities in the SiF $C^2\Delta$ - $X^2\Pi$ System. a) Vibrational transition probabilities. Figures in parenthesis represent 1σ uncertainty in the last digit, calculated from statistical variations in the measurements between runs. b) Franck-Condon factors. The sum of $q_{v'v''}$ for a given v' has been normalised to 1000. c) Calculated from RKR potentials, this work. d) Calculated from Morse potentials, ref [49]. e) Calculated according to equation 3.17, using the best-fit functional form of $R_e(r)$ expressed in equation 3.20. The sum of $p_{v',v''}$ for a given v' has been normalised to 1000.

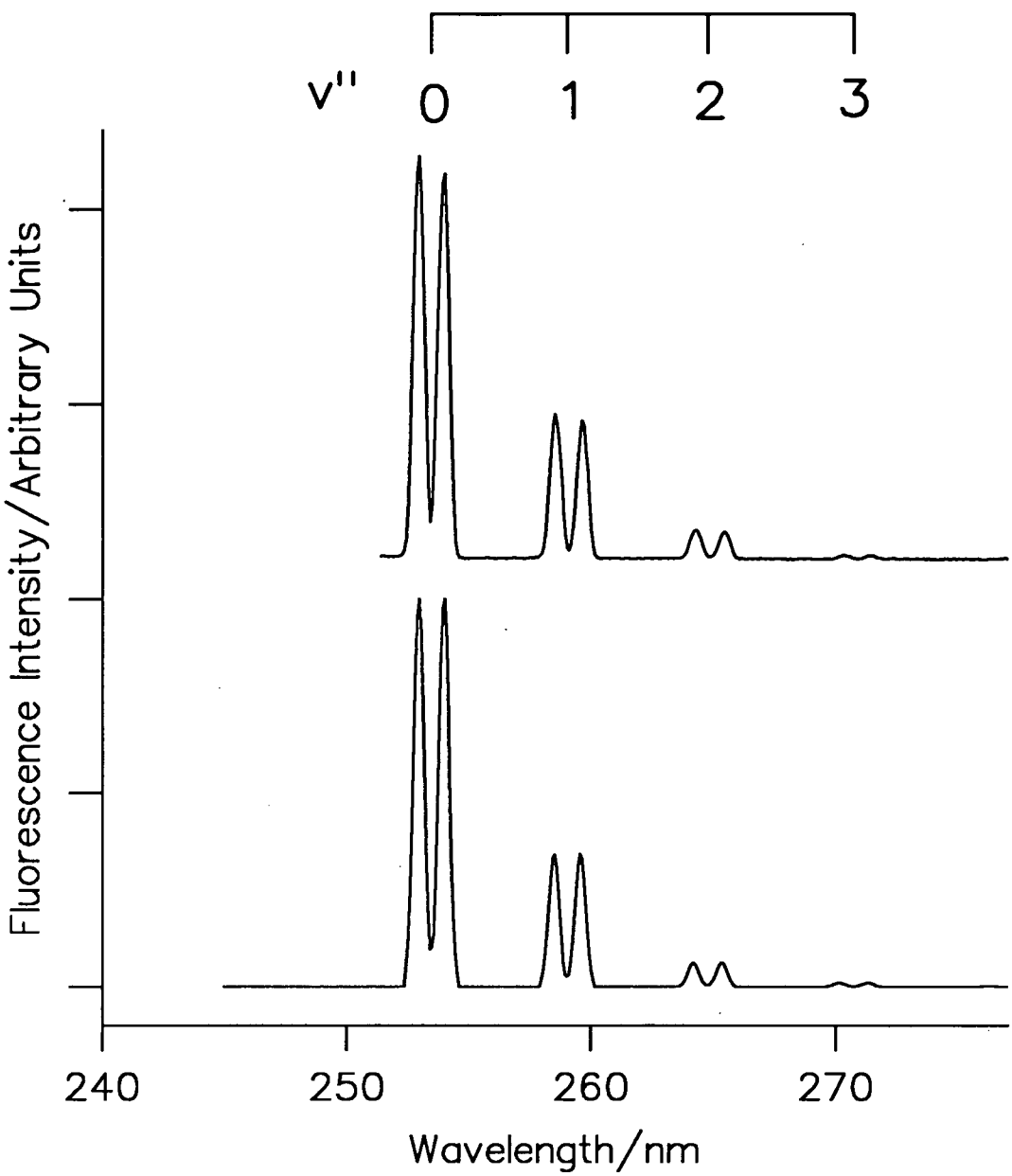

Figure 3–20: Dispersed fluorescence spectrum of the $C^2\Delta(v' = 0) - X^2\Pi(v'')$ transition.

Spectrum recorded in the presence of 1 Torr argon. The upper trace is the experimentally produced spectrum and the lower trace is the simulation using calculated Franck-Condon factors and a variable $R_e(r)$ function as described in section 3.5.2. A bandwidth of 0.5 nm is required to adequately match the simulation with the experimental spectrum. Signal was collected over all regions of the spectrum including the excitation region since the scattered laser light was found to give a negligible contribution.

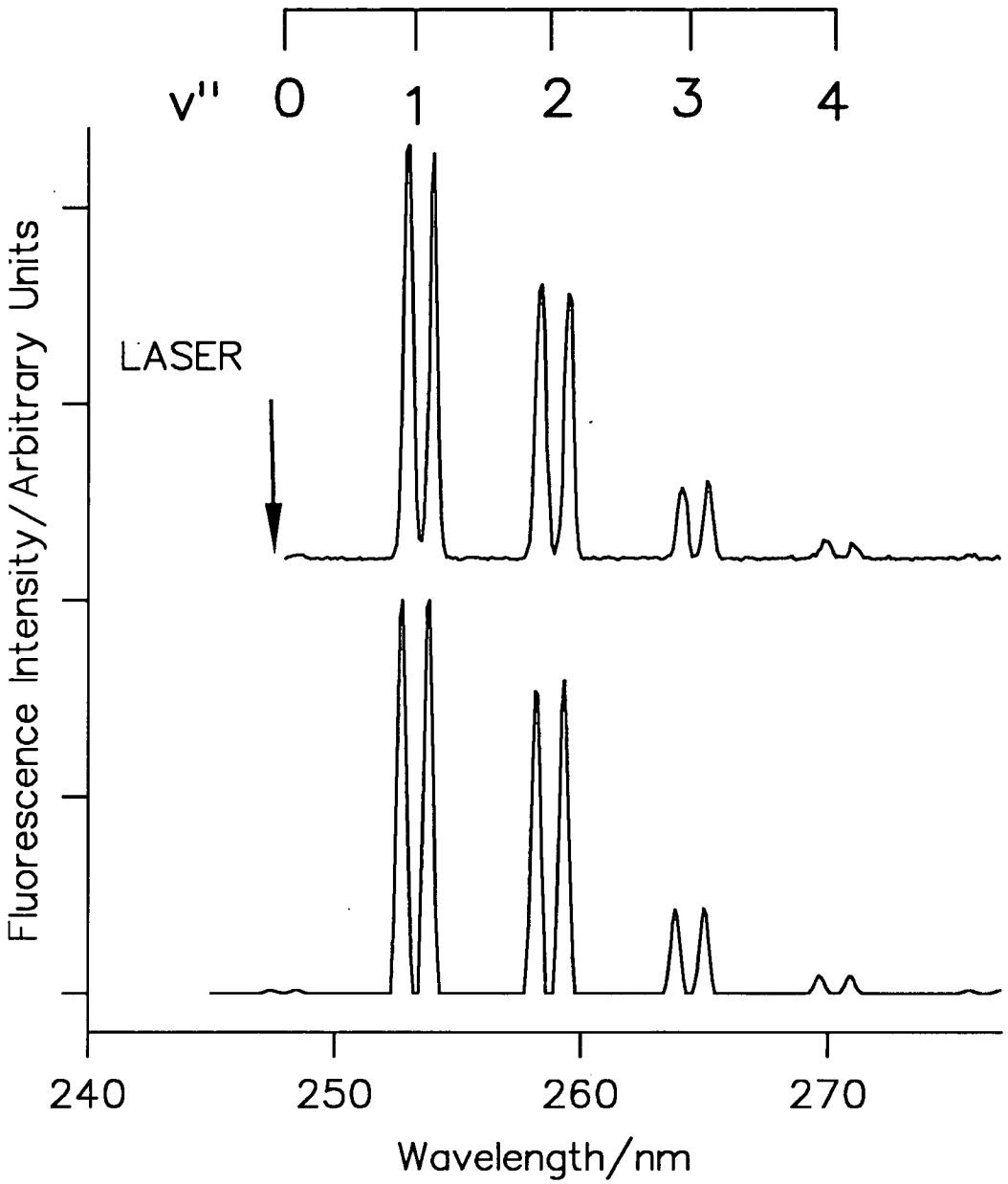

Figure 3–21: Dispersed fluorescence spectrum of the $C^2\Delta(v' = 1) - X^2\Pi(v'')$ transition

The simulation was performed under the same conditions as described in figure 3–20. The laser excitation point is indicated by the vertical arrow; signal was not collected over this region to avoid the detection of scattered light.

utilised in these calculations, hence perhaps indicating that the new values are the more reliable of the two.

The most obvious conclusion to draw from the agreement between the measured $p_{v'v''}$ values and the calculated Franck-Condon factors is that $R_e(r)$, the electronic transition dipole moment function is invariant over this region of r ($\sim 1.40-1.75\mathring{A}$) where the vibrational wavefunction overlap is significant. This was confirmed as any change in the functional form of $R_e(r)$ failed to significantly improve the match between the observed and calculated $p_{v'v''}$ values.

The intensity of the unobserved bands from any hypothetical $B^2\Sigma^+(v' = 3) - X^2\Pi$ emission can therefore be predicted with a large degree of confidence due to the close agreement between the Franck-Condon factors and the measured transition probabilities for the other $B^2\Sigma^+(v')$ emission bands.

The form of the electronic transition dipole moment can be justified in this case by invoking the simple linear combination of atomic orbitals (LCAO) approximation [37]. The LCAO approach describes the electron density probability through the approximation that the molecular wavefunctions ψ can be obtained from a linear combination of the simple well defined atomic orbitals, ψ_A and ψ_B:

$$\psi = C_A\psi_A + C_B\psi_B \tag{3.25}$$

where C_A and C_B are the proportion of ψ_A and ψ_B in the molecular wavefunction.

An LCAO diagram can be constructed for SiF by considering the atomic orbital occupancy of the two atoms;

- Si= $1s^2 2s^2 2p^6 3s^2 3p^2$
- F= $1s^2 2s^2 2p^5$

The diagram shown in figure 3–22 assumes that the silicon $1s$, $2s$ and $2p$ orbitals and the fluorine $1s$ orbital are essentially core orbitals, and therefore omitted, and that the fluorine $2s$ and $2p$ orbitals are of lower potential energy than the analogous silicon $3s$ and $3p$ orbitals. The valence molecular orbitals can be seen from this diagram to be of types

- π , a bonding orbital seen to be most similar to the F $2p_{x,y}$ orbital, therefore $C_F > C_{Si}$.

- σ , a bonding orbital seen to be most similar to the F $2p_z$ orbital, therefore $C_F > C_{Si}$.

- π^* , an anti-bonding orbital seen to be most similar to the Si $3p_{x,y}$ orbital, therefore $C_F < C_{Si}$.

- σ^*, an anti-bonding orbital seen to be most similar to the Si $3p_z$ orbital, therefore $C_F < C_{Si}$ (unoccupied in the ground state).

The dominant electronic configurations of the $X^2\Pi$ and $B^2\Sigma^+$ states have been well established previously from a combination of experimental and theoretical studies [9,15,25,26,31,36]. These configurations are

- $(1\sigma...7\sigma)^2(1\pi 2\pi)^4(3\pi)^1 - X^2\Pi$

- $(1\sigma...7\sigma)^2(1\pi 2\pi)^4(4s\sigma)^1 - B^2\Sigma^+$

where the $B^2\Sigma^+$ state is the first member of a Rydberg series with the odd electron occupying what is essentially the Si $4s$ orbital (not shown in figure 3–22) [31].

The $B - X$ transition therefore involves the movement of an electron between a $4s\sigma$ and a 3π orbital. The 3π orbital is predicted to be weakly anti-bonding and is primarily associated with the Si $3p_{x,y}$ atomic orbitals [31]. Hence, the orbitals between which the electron must transfer are both centred on the Si atom and therefore the electronic wavefunction overlap would not be expected to be significantly affected by the internuclear separation. As this process is similar to an atomic transition, *ie* Si $4s - 3p$, it would also be expected that it is strongly allowed with a radiative lifetime of the order of 10 ns [45]. Both these predictions are borne out by the experimental results where $R_e(r)$ was shown above to be essentially constant over the range of the intermolecular potentials examined and

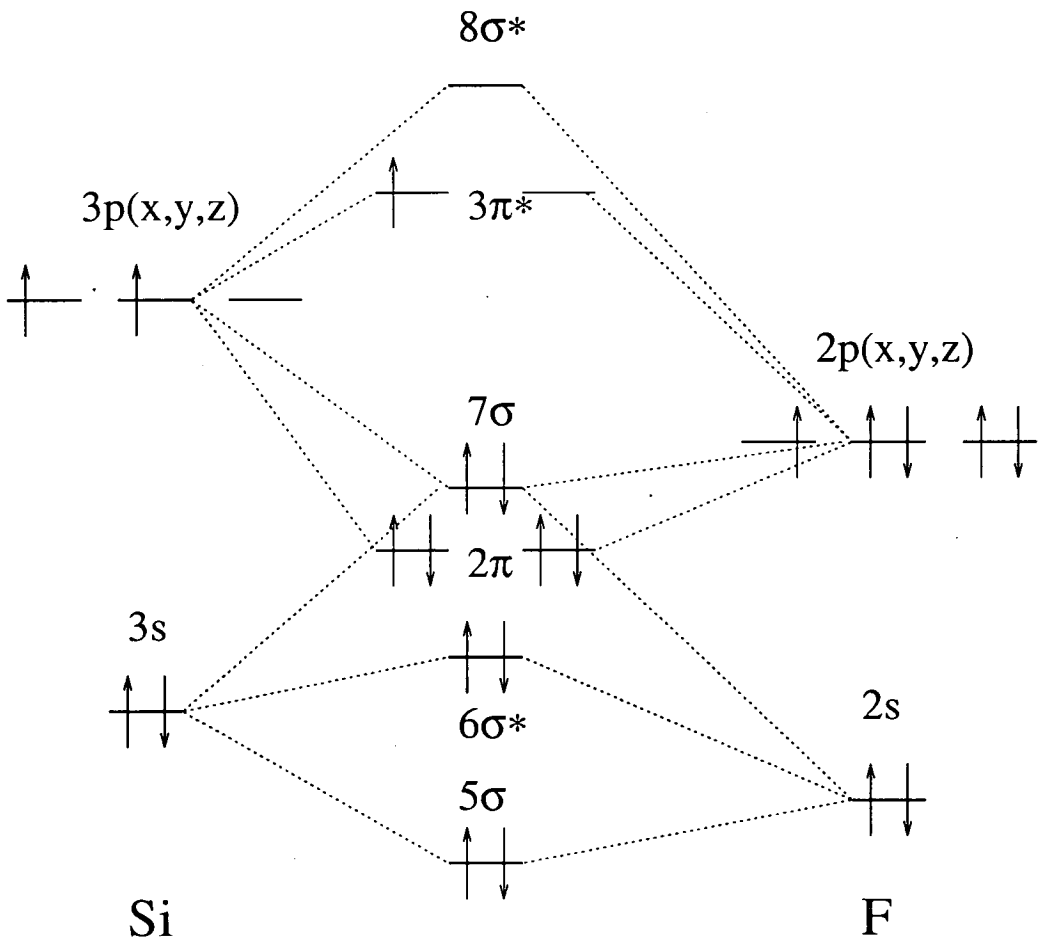

Figure 3–22: Schematic molecular orbital diagram for SiF constructed using the linear combination of atomic orbitals approximation.
This represents the ground state electron configuration. The non-interacting core orbitals not shown.

the radiative lifetime of the $B^2\Sigma^+$ state is shown in this thesis to be of the order of 10ns[6].

3.8.2 $C^2\Delta - X^2\Pi$ System

The measured vibrational transition probabilities for the $C^2\Delta - X^2\Pi$ system, in contrast to those for the $B^2\Sigma^+ - X^2\Pi$ system, do not agree well with the relative Franck-Condon factors. The Franck-Condon factors calculated as part of this study are presented in table 3–3 along with those of the most recently published values [49] which were once again derived using Morse potentials. As the two sets of values are, perhaps surprisingly, in very good agreement with each other but differ significantly from the measured vibrational values it is apparent that the $R_e(r)$ function must vary with internuclear separation.

To find the *best* form of $R_e(r)$, a range of linear functions was first used to calculate new $p_{v'v''}$ values from which, by a process of iteration, the linear function giving best agreement with the experiment was obtained. This resulted in a much improved agreement between the predicted and observed transition probabilities. However, it was found that the match was significantly further improved by replacing the linear form with a quadratic function.

This function was again adjusted iteratively and the resulting $p_{v'v''}$ values can be seen to be in excellent agreement with the experimental values in table 3–3. This agreement is demonstrated in figures 3–20 and 3–21 which show that the experimental spectra are well matched by their corresponding simulations.

The functional form of $R_e(r)$ derived from the experimental $p_{v'v''}$'s can be expressed as

$$R_e(r) = 1 + \alpha(r - r') + \beta(r - r')^2, \tag{3.26}$$

---

[6]The accuracy of this value is limited by the temporal resolution of the detection apparatus. This will be discussed further in chapter 4.

where r' is approximately the mid-point of the range of internuclear separations which contribute to the transition intensities. The iteratively derived optimum values for the parameters were $\alpha = -6.46\mathring{A}^{-1}$ and $\beta = +8.14\mathring{A}^{-2}$. This function results in the transition dipole moment decreasing approximately by a factor of four between the inner and outer classical turning points of the $C^2\Delta(v' = 1)$ state (approximately $1.5\mathring{A}$ to $1.7\mathring{A}$) which would result in it approaching and passing through zero shortly after this point. There are, however, insufficient data to safely predict the form of $R_e(r)$ after the outer turning point.

In a similar way to the $B^2\Sigma^+ - X^2\Pi$ system, the observations made of the $C^2\Delta - X^2\Pi$ system can be rationalised by considering the dominant electronic configurations of the states. The configuration of the SiF $C^2\Delta$ state is given as [21,29,31,36,50];

$$(1\sigma...6\sigma)^2(7\sigma)^1(1\pi 2\pi)^4(3\pi)^2 - C^2\Delta$$

Hence the $C^2\Delta - X^2\Pi$ transition involves the transfer of an electron from a 3π to a 7σ orbital. Employing the same LCAO approximation as applied to the $B^2\Sigma^+ - X^2\Pi$ system, it is apparent that the 7σ orbital is primarily associated with the fluorine $2p_z$ orbital whereas the 3π orbital has been shown to be similar to that of a silicon $3p_{x,y}$ orbital. Therefore the transition involves transfer between orbitals on different atoms so the electronic wavefunction overlap would be expected to decrease with increasing internuclear separation. This might also partially explain the radiative lifetime of the $C^2\Delta$ state, (where the $C^2\Delta$ state can only *fluoresce* to the $^2\Pi$ ground state) measured in the course of this thesis to be approximately 94 ± 2 ns[7], which is considerably longer than a pure atomic transition and is therefore consistent with a less favourable electronic wavefunction overlap.

---

[7]This will be demonstrated and discussed more fully in chapter 4.

3.9 Conclusions

The conclusions that can be drawn from this chapter, where some aspects of the spectroscopy of the SiF $B^2\Sigma^+ - X^2\Pi$ and $C^2\Delta - X^2\Pi$ systems have been studied, are listed below.

1. Laser-induced fluorescence excitation spectra allowed positive identification of excited (ro)vibronic states of SiF and hence indicated the wavelength regions in which selected states could be prepared for subsequent spectroscopic and energy transfer studies. In anticipation of the energy transfer studies it was established that the $C^2\Delta(v' = 0, 1)$ levels were sufficiently spectroscopically isolated from vibronic levels of the $B^2\Sigma^+$ state to allow them to be specifically populated without simultaneous excitation of $B^2\Sigma^+$ levels. The observations were in agreement with the existing literature.

2. Measurements of the vibrational transition probabilities, $p_{v'v''}$, for the $B^2\Sigma^+(v' = 0, 1, 2, 4$ and $5) - X^2\Pi(v'' = 0 - 12)$ and $C^2\Delta(v' = 0, 1) - X^2\Pi(v'' = 0 - 5)$ transitions were reported. and These will be used to deduce relative vibrational populations in the energy transfer experiments involving these states.

3. The values for $p_{v'v''}$, upon comparison with Franck-Condon factors calculated from RKR potentials, indicated that for the $B^2\Sigma^+ - X^2\Pi$ system the transition dipole moment function was essentially invariant with internuclear separation. This was shown to be consistent with the Rydberg-Valence character of the transition between orbitals primarily centred on the Si atom.

4. Conversely, for the $C^2\Delta - X^2\Pi$ system, the transition dipole moment function was found to be strongly decreasing with increasing atomic separation, as would be expected for a transition involving orbitals associated with different atoms.

Bibliography

[1] A.A. Wyller, Astrophys. J. **134** (1961) 805.

[2] A. Schadee, 26th International Astron. Union Symp., Utrecht, Netherlands, 92 (1964).

[3] D.R. Harding and D. Husain, J. Chem. Soc., Chem. Comm. **5** (1986) 419.

[4] H.U. Lee and J.P. Deneufville, Journal of Non-Crystalline Solids **66** (1984) 39.

[5] C. Porlezza, Rend. Acad. Lincei **20** (1911) 486.

[6] C. Porlezza, Rend. Acad. Lincei **33** (1924) 283.

[7] R.K. Asundi and R. Samuel, Proc. Indian Acad. Soc. A **3** (1936) 346.

[8] W.H. Dovell and R.F. Barrow, Proc. Phys. Soc. A **64** (1951) 98.

[9] J.W.C. Johns and R.F. Barrow, Proc. Phys. Soc. A **71** (1958) 476.

[10] R.F. Barrow, D. Butler, J.W.C. Johns and J.L.Powell, Proc. Phys. Soc. A **73** (1959) 317.

[11] Y. Houbrechts, I. Dubois and H.Bredohl, J. Phys. B **15** (1982) 603.

[12] Y. Houbrechts, I. Dubois and H.Bredohl, J. Phys. B **15** (1982) 4551.

[13] C.S. Dulcey and J.W. Hudgens, Chem. Phys. Letts. **118** (1985) 444.

[14] M. Ebben, M. Versluis and J.J. Ter-Mullen, J. Mol. Spec. **149** (1991) 329.

[15] E. Eyster, Phys. Rev. **51** (1937) 1078.

[16] Y. Houbrechts, I. Dubois and H.Bredohl, J. Phys. B **12** (1979) 2137.

[17] H. Bredohl, I. Dubois and Y. Houbrechts, 21st Intern. Astrophys. Symp. (1980) 318.

[18] E.R. Comben and R.F. Barrow, J. Mol. Spec. **109** (1985) 415.

[19] R.D. Verma, Can. J. Phys. **40** (1962) 586.

[20] R.W. Martin and A.J. Merer, Can. J. Phys. **51** (1973) 634.

[21] O. Appelblad, R.F. Barrow and R.D. Verma, **1** (1968) 274.

[22] F. Remy, E. Mahieu, D. Macau-Hercot, I. Dubois, H. Bredohl, J. Breton, F. Launay and M. Benharrous, J. Mol. Spec. **152** (1992) 131.

[23] J.A. Dagata, D.W. Squire, C.S. Dulcey, D.S.Y. Hsu and M.C. Lin, Chem. Phys. Letts.,**134** (1987) 151.

[24] K.H. Wang and V. McKoy, J. Chem. Phys., **97** (1992) 5489.

[25] P.A.G. O'Hare and A.C. Wahl, J. Chem. Phys., **55** (1971) 666.

[26] P.A.G. O'Hare, J. Chem. Phys., **59** (1973) 3842.

[27] K.V. Bozhenko and O.P. Charkin, **18** (1977) 219.

[28] M. Bialski and F. Grein, J. Mol. Spec. **61** (1976) 321.

[29] J.M. Robbe, J. Mol. Spec., **112** (1985) 223.

[30] J.M. Robbe, Y. Houbrechts, I. Dubois and H. Bredohl, J. Mol. Spec., **112** (1985) 228.

[31] S.P. Karna and F. Grein, J. Mol. Spec., **122** (1987) 28.

[32] R. Rydberg, Z. Physik **73** (1931) 376.

[33] O. Klein, Z. Physik **76** (1932) 226.

[34] A.L.G. Rees, Proc. Phys. Soc. (London) **59** (1947) 998.

[35] K.P. Lawley, Dept. of Chemistry, University of Edinburgh, EH9 3JJ, UK.

[36] Y. Houbrechts, I. Dubois and H. Bredohl, J. Phys. B **13** (1980) 3369.

[37] G. Herzberg, Molecular Spectra and Molecular Structure. I. Spectra of Diatomic Molecules, 2nd Edition (Van Nostrand Reinhold, New York, 1950).

[38] E.L. Hill and J.H. Van Vleck, Phys. Rev. **32** (1923) 250.

[39] R.D. Verma, Can. J. Phys., **42** (1964) 2345.

[40] I.E. Ovcharenko, Y.Y. Kuzyakov and V.M. Tatesvkii, Opt. Spec. Mol. Spec. Suppl., **2** (1963) 6.

[41] R.N. Zare, A.L. Schmeltekopf, W.J. Harrop and D.L. Albritton, J. Mol. Spec. **46** (1973) 37.

[42] R.N. Zare, J. Chem. Phys., **40** (1964) 1934.

[43] K.P. Lawley and R. Wheeler, J. Chem. Soc. Far. Trans. II, **77** (1981) 1133.

[44] S. Singleton, Laser Based Studies of Transient Species in a Discharge Flow Apparatus, PhD Thesis, University of Edinburgh, (1990).

[45] W.L. Wiesse, M.W. Smithand B.M. Miles, Atomic Transition Probabilities, Vol. II (National Standard Reference Data Series, USNBS 22, Washington, DC, 1969).

[46] J.B. Jeffries, J. Chem. Phys., **95** (1991) 1628.

[47] S. Singleton and K.G. McKendrick, J. Phys. Chem. **97** (1993) 1389.

[48] R.R.Reddy, T.V.R. Rao and G.T. Naidu, Acta. Phys. Pol. A **64** (1983) 667.

[49] I.D. Singh and R.C. Maheshwari, Indian J. Pure Appl. Phys. **7** (1969) 708.

[50] S.P. Karna and F.Grein, Intern. J. Quantum Chem. **29** (1986) 755.

Chapter 4

$^2\Delta - ^2\Sigma^+$ Vibronic Transfer in SiF and SiCl

4.1 Introduction

The main theme of this thesis is the study of collision-induced energy transfer processes in SiCl and SiF. In this chapter results are reported at the vibronic level for collision-induced transfer between the $C^2\Delta$ and $B^2\Sigma^+$ states of SiF. A more limited set of results is also presented for the analogous $B'^2\Delta$ and $B^2\Sigma^+$ states of SiCl which is in good agreement, though of improved precision, with that of the previous studies of this system [1,2,3].

The potential energy curves and vibrational energy levels of the $^2\Delta$ and $^2\Sigma^+$ electronic states for SiCl and SiF can be seen in figures 4–1 and 4–2, respectively. These curves were constructed using the RKR procedure, as described in Appendix A, using published molecular constants [4,5,6]. The potentials for these two species differ in two immediately obvious ways:

- The SiF $C^2\Delta$ state potential minimum is ~ 5000 cm^{-1} greater than that of the $B^2\Sigma^+$ state compared to a difference of ~ 1500 cm^{-1} for the analogous SiCl electronic states;

- The SiF $C^2\Delta$ state potential is nested inside that of the $B^2\Sigma^+$ state potential whereas in SiCl the potentials intersect in the region of $B'^2\Delta, v = 0$ and $B^2\Sigma^+, v = 2$.

The basis of these experiments was the excitation of the SiX molecules to either the $v' = 0$ or 1 vibrational level of the $^2\Delta$ state in the presence of the collision partner. As a result of a collision some of the molecules may be removed from the relevant $^2\Delta$ state. A variable fraction of these are transferred to lower-lying vibrational levels of the $^2\Sigma^+$ state.

From the study of the resultant time- and wavelength-resolved fluorescence there are three basic quantities that have been measured for these transfer systems;

- the total collisional removal rate of the initially populated $^2\Delta$ state level;
- the fraction of the collisionally removed species transferred to the $B^2\Sigma^+$ state;
- the $B^2\Sigma^+$ state product state (ro)vibronic distribution.

The relatively simple experimental methodology is capable of yielding state-to-state information due to the contrasting radiative lifetimes of the respective electronic states, as discussed in chapter 1. Previous studies have shown the lifetimes of the SiCl $B'^2\Delta$ and $B^2\Sigma^+$ states to be $\sim 1\mu$s and ~ 10 ns, respectively [1, 7] whereas the lifetimes of the analogous SiF states are shown in this chapter to be 94 ± 2 ns and ≤ 10 ns. To reiterate, at an appropriate pressure, $^2\Delta$ state molecules will have a significant chance of a bimolecular collision prior to radiative emission. However, $^2\Sigma^+$ state molecules populated as a result of this collision, will typically have only $\sim 1\%$ chance of a further collision prior to fluorescence. The product state distribution will therefore not be complicated by a series of further collisions and hence transfer can be examined under pseudo-single collision conditions.

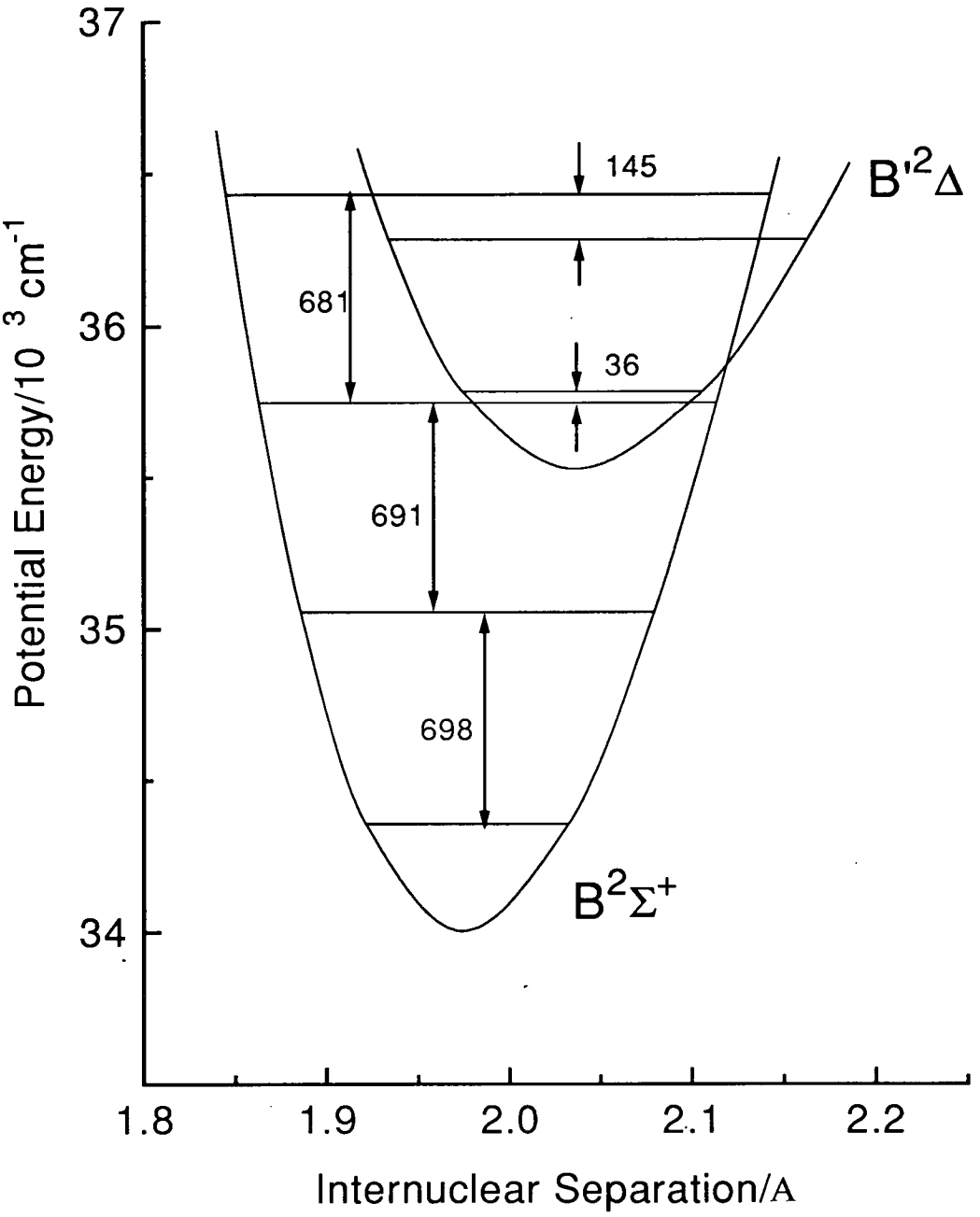

Figure 4–1: Potential energy curves for the SiCl $B'^2\Delta$ and $B^2\Sigma^+$ states. The energy gaps between the vibronic energy levels indicated are in cm^{-1} units. The potentials were calculated using the RKR procedure.

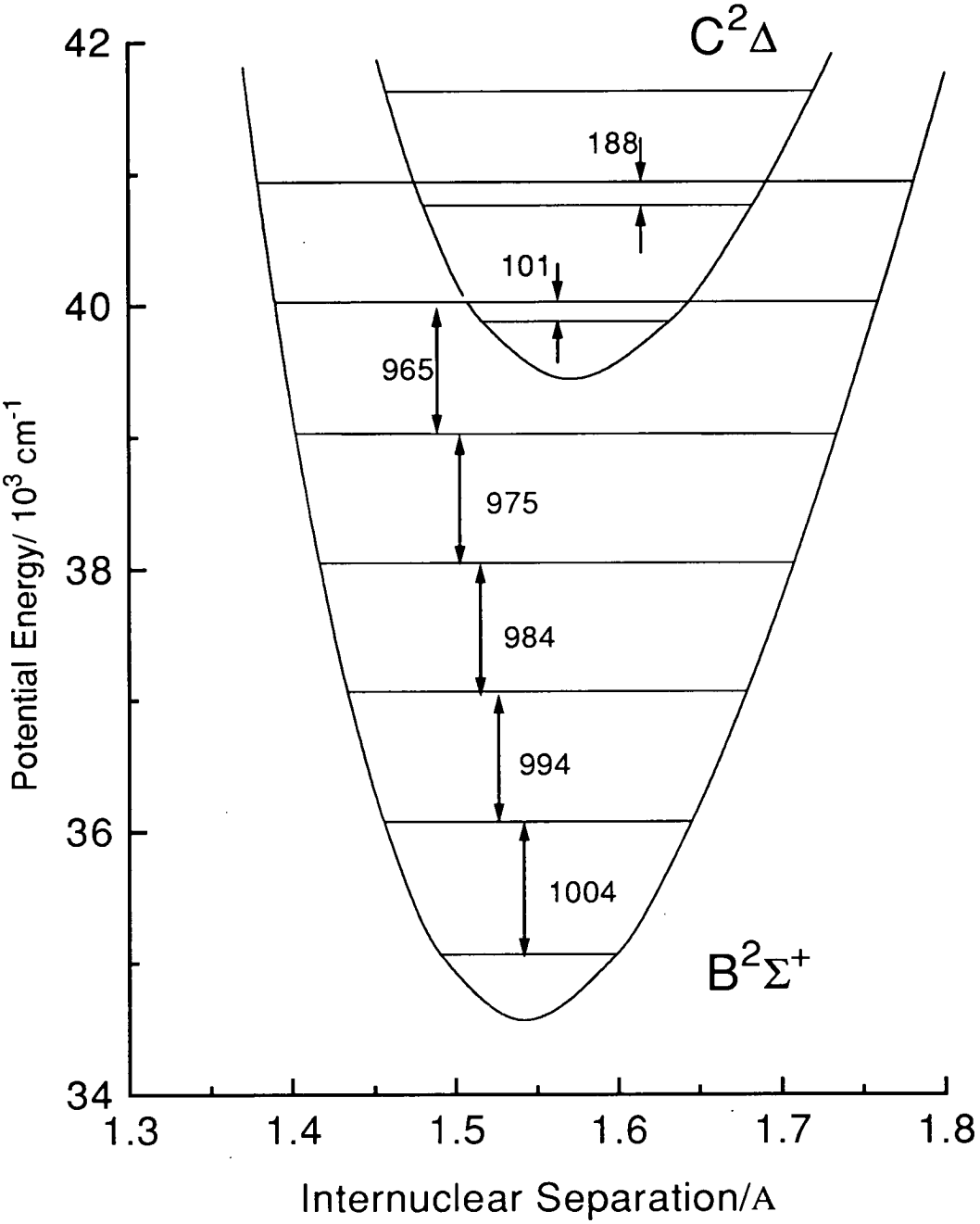

Figure 4–2: Potential energy curves for the SiF $C^2\Delta$ and $B^2\Sigma^+$ states. The energy gaps between the vibronic energy levels indicated are in cm^{-1} units. The potentials were calculated using the RKR procedure.

4.2 Experimental

The time- and wavelength-resolved LIF experiments reported in this chapter were performed using the equipment described in chapter 2. The SiX (X = F or Cl) radicals produced by the microwave discharge of SiX_4, in the presence of argon, were mixed downstream with a second flow of quenching gas. They were then laser excited to the relevant $^2\Delta, v'$ state using the output from the Nd:YAG laser-pumped dye laser system. The resultant fluorescence was dispersed using the monochromator, and the signal waveform captured by the transient digitiser.

This method was a significant improvement on that previously used for the collection of data by Singleton [2,3] for the SiCl $B'^2\Delta - B^2\Sigma^+$ system as in these studies there was no facility for temporal resolution. All these measurements were previously achieved from the examination of the relative $B'^2\Delta - X^2\Pi$ and $B^2\Sigma^+ - X^2\Pi$ band intensities. The considerably smaller series of results obtained by Jeffries [1] were achieved using a similar method to that used in this work.

The gases used in this chapter were Ar (BOC, 99.998%), He (BOC, 99.998%), H_2 (BOC, 99.99%), N_2 (BOC, 99.998%), O_2 (BOC, 99.5%), CO_2 (BOC, 99.8%), CH_4 (Matheson, 99.99%), SiF_4 (Union Carbide, 99.99%). The $SiCl_4$ (Aldrich, 99.99%) was supplied as a liquid.

4.3 Collision Induced $C^2\Delta$ to $B^2\Sigma^+$ Vibronic Energy Transfer in SiF

For the experiments reported in this section, the SiF $C^2\Delta$ state was populated by excitation of the Q_1 head of either the $C^2\Delta - X^2\Pi_{\frac{1}{2}}(0,0)$ or $(1,0)$ transitions. This was ensured by examination of the appropriate LIF excitation spectrum reported in chapter 3 and tuning the laser system to the appropriate wavelength. The laser pulse energies were optimised for each experimental run to maximumise the $C^2\Delta$ state population.

4.3.1 Total Collisional Removal of the SiF $C^2\Delta(v' = 0, 1)$ States

Monitoring the variation in the decay rate of the $C^2\Delta - X^2\Pi$ fluorescence with the system pressure allows a measurement of the bimolecular quenching rate constant, k_Q. This is done on the assumption that there is no transfer from the collisionally populated product vibronic states back to the $C^2\Delta$ state.

The decay rate of the $C^2\Delta$ state fluorescence intensity, I_C, will be determined by the first order decay rate constant, k_1, where

$$\frac{dI_C}{dt} = -k_1 I_C \quad . \tag{4.1}$$

In the presence of a single quencher species, Q, which is assumed to be in infinite excess relative to the SiF species, the first order decay rate constant is given by

$$k_1 = \tau_C^{-1} + k_Q P_Q \tag{4.2}$$

where τ_C is the collisionless radiative lifetime, P_Q is the quencher species pressure and k_Q is the bimolecular quenching rate constant.

In this ideal situation the fluorescence decay would be a single exponential function of time, where the fluorescence intensity can trivially shown to be

$$I_C = I_C^0 exp(-k_1 t) \tag{4.3}$$

where I_C^0 is the fluorescence intensity at $t = 0$.

A typical $C - X$ fluorescence decay plot is shown in figure 4–3 with the *best-fit* single exponential. It is apparent from the quality of this fit that the kinetic model described above is a good approximation over at least three lifetimes. There is a small systematic error at longer times though this is probably due to 'ringing' in the PMT response. The fitting process was performed upon writing a computer program which incorporated a non-linear least squares method[1]. The value of k_1 for any fluorescence decay could therefore be obtained from the *best fit* parameters.

---

[1]For a summary of this method see reference [8].

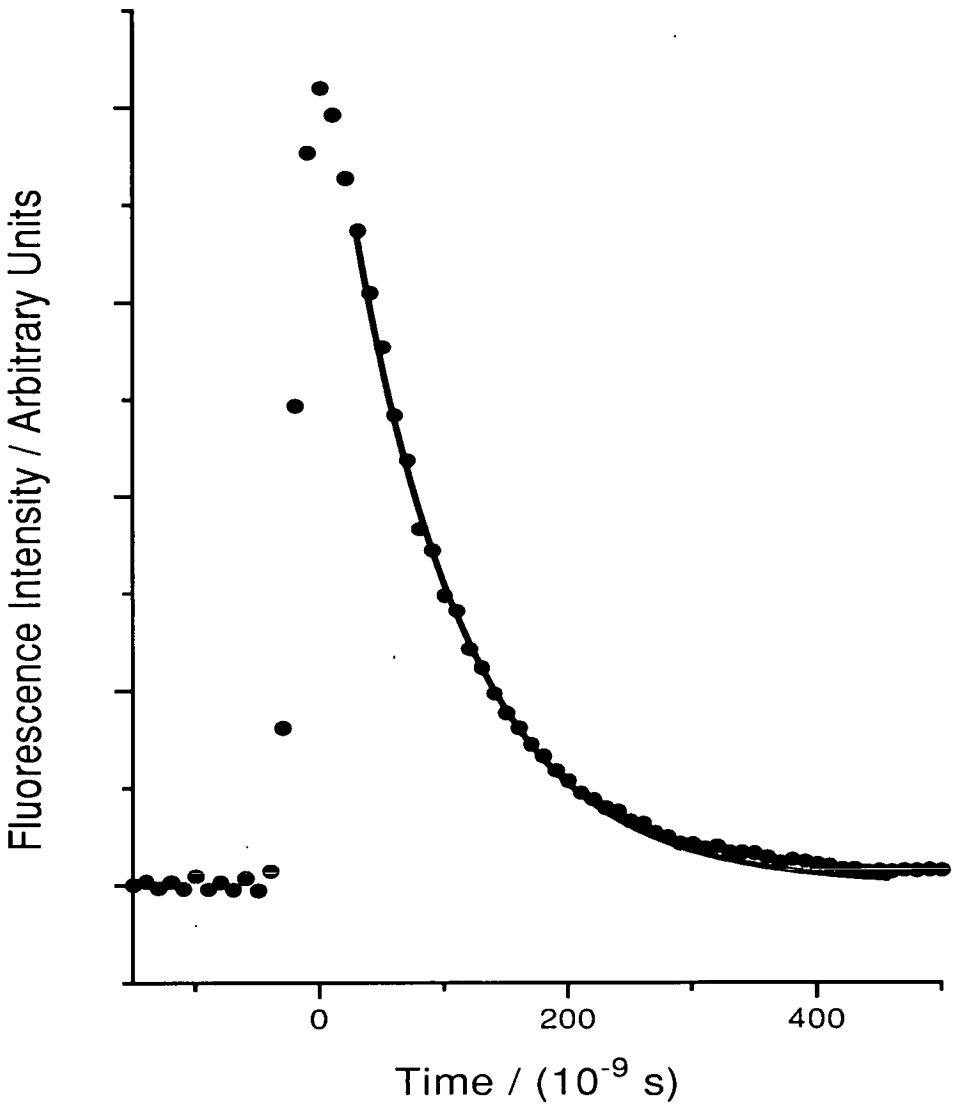

Figure 4–3: Representative radiative decay plot for the SiF $C^2\Delta - X^2\Pi$ transition.

The experimental fluorescence intensities are represented by the circles. The solid line indicates the best single-exponential fit.

The first order decay rates of SiF $C^2\Delta, v' = 0$ were initially measured with argon as the only potential quencher species present over a range of pressures from 1 to 6 Torr. As can be seen from figure 4–4, the first order decay rates are independent of the argon pressure and hence there is no measurable quenching of SiF $C^2\Delta(v' = 0)$ over the range shown. This phenomenon was also observed upon excitation of $C^2\Delta(v' = 1)$.

This happens to be a fortuitous observation from our perspective because, although argon is necessarily present in all vibronic energy transfer experiments, its contribution towards electronic quenching in experiments involving other quenchers can be neglected. This will obviously significantly reduce the degree of uncertainty in all subsequent measured quantities.

The decay rate measurements also yield the collisionless radiative lifetimes, τ_C, for the $C^2\Delta(v' = 0, 1)$ states from the extrapolated zero pressure intercepts. As the lifetimes in these cases are independent of the argon pressure, this will result in all lifetime values being effectively equal to the pure radiative lifetime. The lifetimes for the two vibronic states $C^2\Delta v = 0, 1$ were both determined to be 94 $\pm$ 2 ns, where the uncertainty represents the 2σ statistical variation in the repeated measurements which is probably exceeded by systematic factors. These quantities have not previously been reported in the literature.

Helium was similarly found to be an inefficient quencher of the SiF $C^2\Delta$ state; however, this was not the case for H_2, N_2, CO_2 and CH_4 where the decay rates were found to increase with increasing pressure of these gases. Figures 4–4 and 4–5 show plots of k_1 against P_Q for $C^2\Delta, v' = 0$ and 1, respectively. From equation 4.2 it is apparent that the gradients of these plots are equivalent to k_Q, the bimolecular quenching rate constant. These values were obtained from the best linear least-squares fits which are also shown in figures 4–4 and 4–5.

From these plots it can be seen that the zero pressure intercept varies considerably with quencher. The discrepancy from the 'true' value, derived from the Ar data, is most apparent for H_2. It is believed that this is almost certainly due to inaccuracies in determining the true partial pressure of the argon gas relative to the quencher gas. However the differential pressures are better determined than

Gas[a]	$C^2\Delta(v')$	$k_Q^{(b)}/10^{-11}cm^3s^{-1}$	$\sigma_Q^{(c)}/\AA^2$
H_2	0	116(12)	65(7)
N_2	0	8.2(3)	13.8(5)
CO_2	0	14.0(1.2)	26.8(2.3)
CH_4	0	9.1(1.8)	12.6(2.5)
H_2	1	140(18)	78(10)
N_2	1	14.3(1.2)	24(4)
CO_2	1	9.7(3.0)	19(6)
CH_4	1	14.3(2.4)	20(3)

Table 4–1: Rate constants and thermally averaged cross sections for total removal of SiF $C^2\Delta(v' = 0, 1)$.

Numbers in parentheses represent 2σ uncertainties. a) No measurable quenching by Ar or He. b) Total quenching rate constant. c) Thermally averaged cross section.

the absolute values. Therefore the slopes, and consequently k_Q, can be obtained with reasonable precision.

The bimolecular rate constants are implicitly connected to the relative translational velocity of the collision pair, Q-SiF. This effect can be removed by considering the thermally averaged quenching cross section, σ_Q. This quantity is defined as [9]

$$\sigma_Q = \frac{k_Q}{|v|} \quad . \tag{4.4}$$

The average thermal velocity of the collision pair, $|v|$ is given by

$$|v| = \left\{ \frac{8kT}{\pi\mu} \right\}^{\frac{1}{2}} \quad , \tag{4.5}$$

where k is the Boltzmann constant, T is the temperature and μ is the reduced mass of the collision pair. The bimolecular quenching rate constants are shown collectively in table 4–1 with the related average cross sections. The cross sections for quenching of $C^2\Delta v' = 0$ and 1 can be seen to be to be broadly comparable for N_2, CO_2 and CH_4, however H_2, is significantly more efficient.

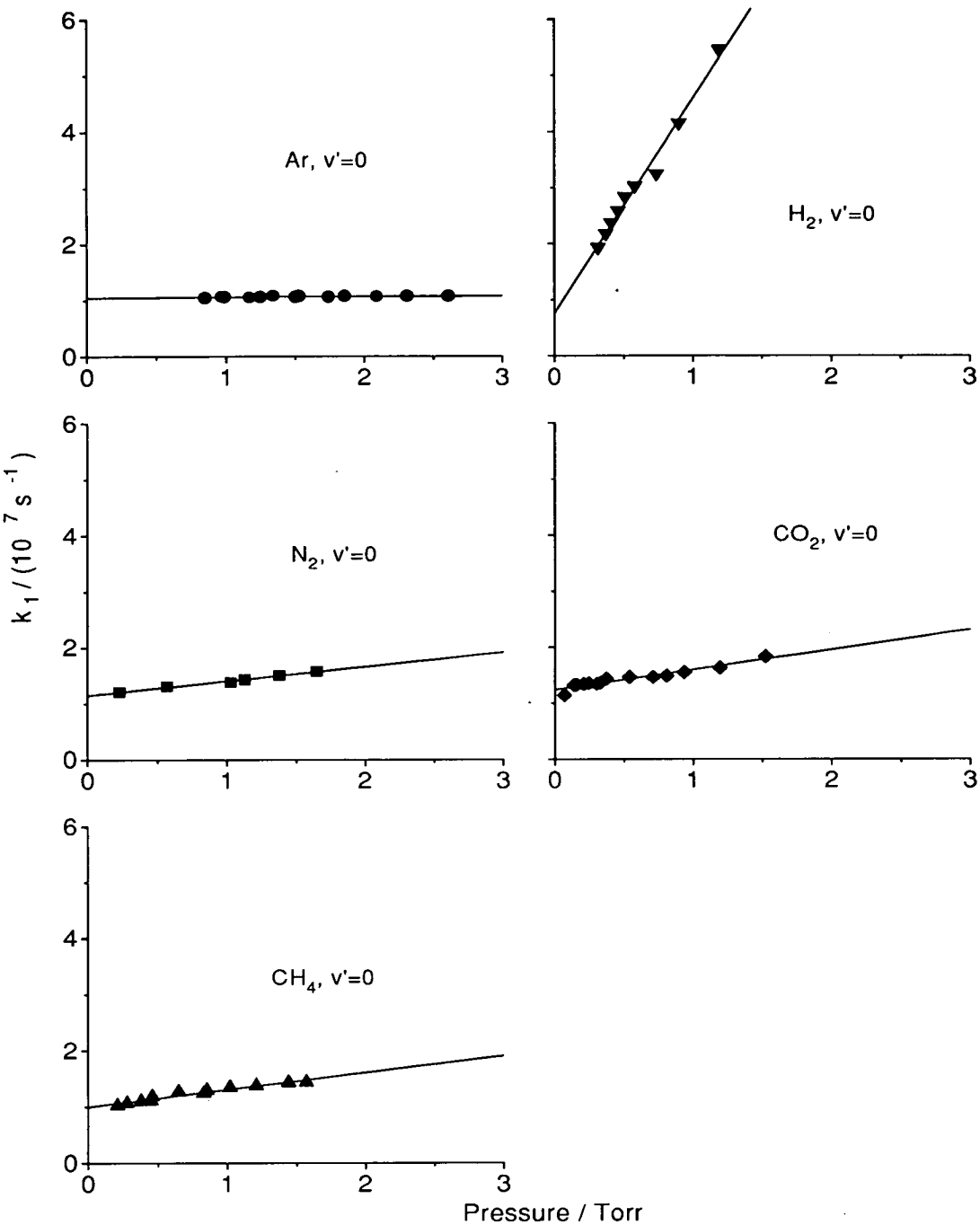

Figure 4–4: Plot of the observed first order decay constants for SiF $C^2\Delta(v' = 0)$ as a function of quencher pressure for Ar, H_2, N_2, CH_4 and CO_2.
Experimentally measured points are represented by the symbols. The solid lines indicate the best-fit straight line. With the exception of the Ar measurements, all experiments were performed with an additional fixed Ar carrier pressure of 1 Torr.

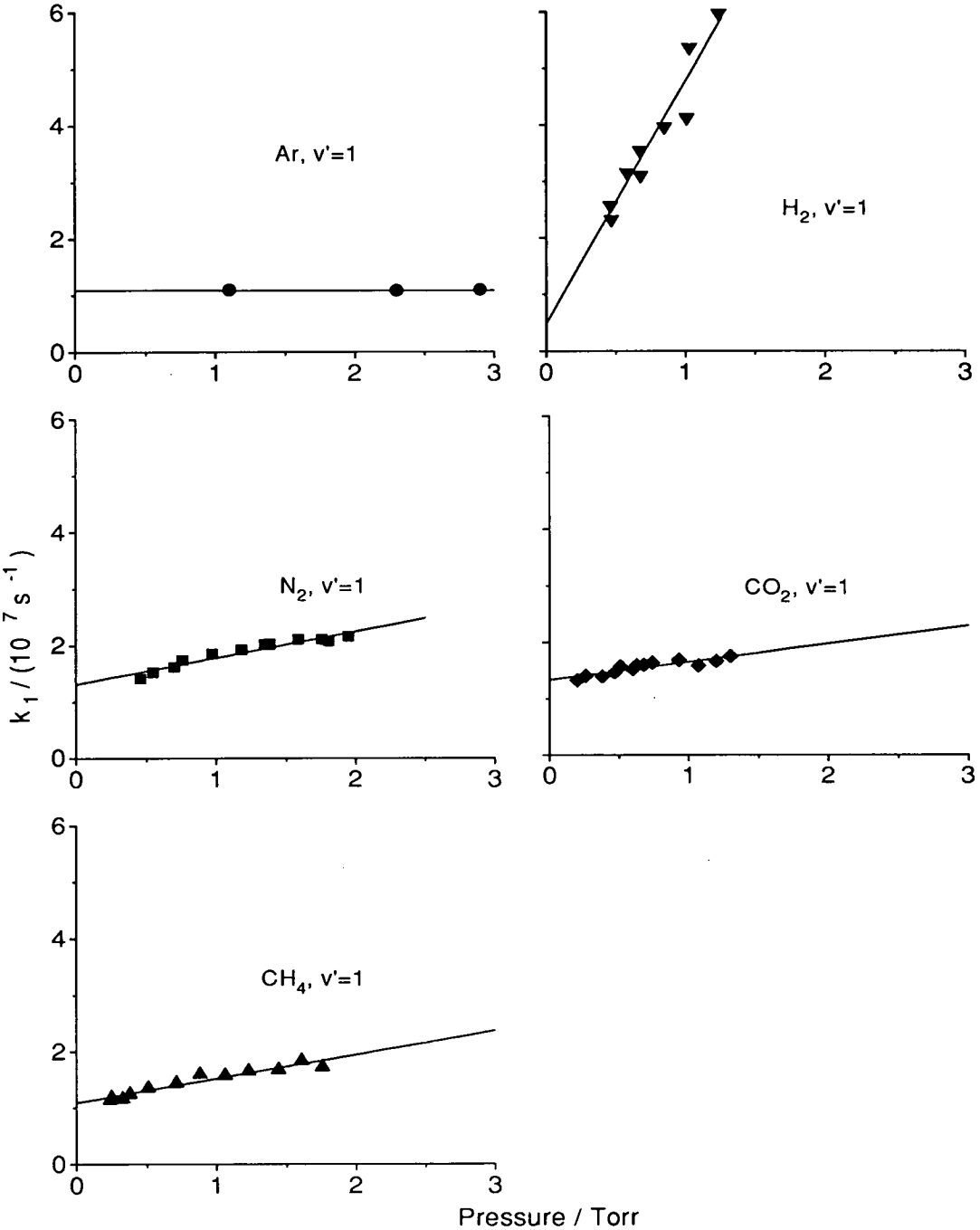

Figure 4–5: Plot of the observed first order decay constants for SiF $C^2\Delta(v' = 1)$ as a function of quencher pressure for Ar, H_2, N_2, CH_4 and CO_2.
Experimentally measured points are represented by the symbols. The solid lines indicate the best fit straight line. With the exception of the Ar measurements, all experiments were performed with an additional fixed Ar carrier pressure of 1 Torr.

Preliminary investigations of oxygen as a quenching gas were unsuccessful because, unfortunately, no SiF LIF signal was observed when it was present. This was considered most likely due to chemical reaction of O_2 with the electronic ground state SiF species prior to excitation.

4.3.2 Specific Collisional Transfer from $C^2\Delta(v' = 0, 1)$ to $B^2\Sigma^+$

To determine the identity of any collisionally populated SiF product states it was necessary to disperse and record the LIF signal. Not surprisingly, in the presence of Ar and He only $C^2\Delta - X^2\Pi$ emission was observed. Unexpectedly this was also the case for CO_2, within the limits of the experimental signal-to-noise, despite the fact that it had proved to be an efficient quencher of the $C^2\Delta$ state. However, for the remaining molecular quenchers H_2, N_2 and CH_4, the resulting fluorescence was found to consist not only of the directly excited $C^2\Delta - X^2\Pi$ bands but also of $B^2\Sigma^+ - X^2\Pi$ emission.

This behaviour is illustrated in figure 4–6a, which shows a representative spectrum of the observed fluorescence in the presence of argon after excitation of SiF $C^2\Delta(v' = 0)$. (This is essentially identical to the spectrum shown previously in figure 3–11.) Presented in figure 4–6b is the spectrum obtained upon the addition of 0.5 Torr H_2. The majority of the fluorescence is still from the directly excited $C^2\Delta(v' = 0)$ state, but it can be seen that there is a significant contribution from $B - X$ emission bands. This can only be the result of collisions between SiF $C^2\Delta$ state molecules and H_2. Similar results are also obtained for the other molecular quenchers with both $C^2\Delta, v' = 0$ and 1 as can be seen in figures 4–7 to 4–11.

Unfortunately the signal-to-noise ratios for the spectra resulting from $C^2\Delta(v' = 1)$ excitation are significantly poorer than those of the analogous spectra for $C^2\Delta(v' = 0)$. This is almost entirely due to the unfavourable Franck-Condon overlap for the $C^2\Delta - X^2\Pi$ (1,0) transition which is approximately two orders of magnitude smaller than that of the $C^2\Delta - X^2\Pi(0,0)$ transition (see table 3–3). Although this is partially offset by optical saturation of the stronger (0,0) band,

it still results in a considerably smaller initial state population for $v' = 1$. In order to increase the signal the monochromator slit width used for recording these spectra was doubled to 0.8 mm though this obviously resulted in a reduction in the experimental resolution. Nevertheless it was still possible to extract reliable information from the relative band intensities following $C^2\Delta$ $v' = 1$ excitation.

It is possible to estimate the fraction of quenched $C^2\Delta$ state molecules which have been transferred to the $B^2\Sigma^+$ state, f_B, by measuring the relative intensities, I_C and I_B, of the respective $C - X$ and $B - X$ emission bands and exploiting the equation

$$f_B = \frac{I_B \tau_C^{-1}}{I_C k_Q P_Q} \quad . \tag{4.6}$$

This relationship is based on two assumptions:

- The $B^2\Sigma^+ - X^2\Pi$ emission occurs effectively instantaneously upon production of the $B^2\Sigma^+$ state by collisional transfer and is therefore not subject to further collisional effects;

- The $B^2\Sigma^+$ state only fluoresces to the $X^2\Pi$ state.

The first assumption can be justified by comparing the waveform of the *directly* excited $B^2\Sigma^+$ emission shown in figure 4–12a with the waveform of the scattered laser radiation in figure 4–12b. These traces are almost identical and are limited by the temporal resolution of the signal detection instrumentation ($\sim 7 - 14$ ns) and the excitation pulse length ($\sim$10 ns). There is no evidence for the lengthening of the tail of the $B^2\Sigma^+$ fluorescence beyond the laser pulse. We therefore estimate that an upper limit on the $B^2\Sigma^+$ state lifetime is $\leq$ 10 ns, which is at least one order of magnitude shorter than that of the $C^2\Delta$ state. At typical experimental system pressures no more than $\sim$ 1% of collisionally populated $B^2\Sigma^+$ molecules will therefore experience further collisions.

Turning to the second assumption, the $B^2\Sigma^+$ state is also optically connected to the $A^2\Sigma^+$ state. Without performing a proper experimental study or detailed theoretical calculations it is impossible to say anything conclusive about the strength of this transition. However, it can be shown to a first approximation

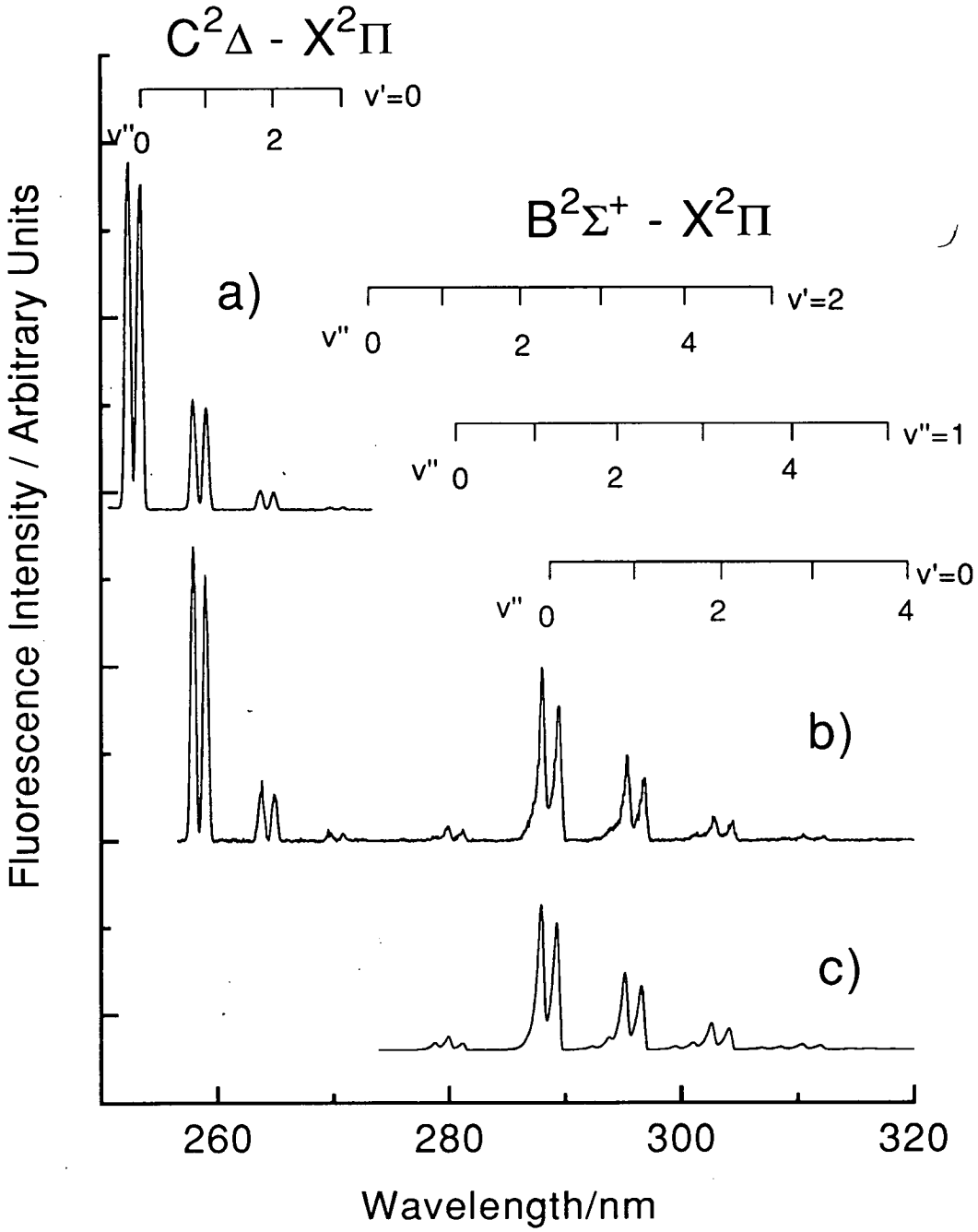

Figure 4–6: Dispersed fluorescence spectra following the initial excitation of SiF $C^2\Delta(v' = 0)$ in the presence of H_2 and Ar.

a) 1 Torr of argon only. The baseline is completely flat to wavelengths longer than shown. b) 1 Torr of argon and 0.5 Torr H_2. c) Least squares fit to the $B^2\Sigma^+ - X^2\Pi$ emission in (b). Fitting procedure performed as described in section 4.3.3.

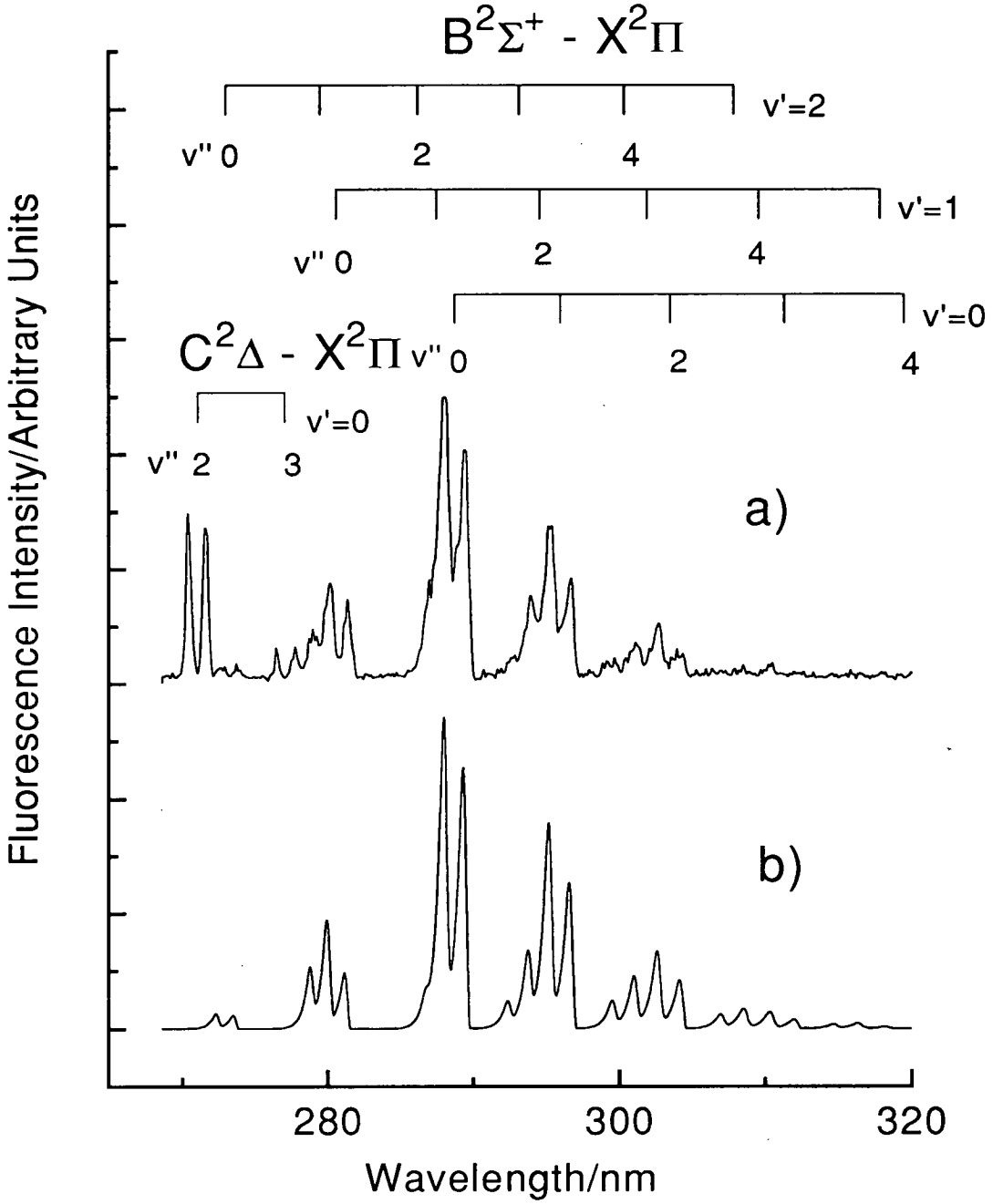

Figure 4–7: Dispersed fluorescence spectrum following the initial excitation of SiF $C^2\Delta(v' = 0)$ in the presence of N_2.

a) 1 Torr of argon and 1.9 Torr N_2. b) Least squares fit to the $B^2\Sigma^+ - X^2\Pi$ emission in (a). Fitting procedure performed as described in section 4.3.3.

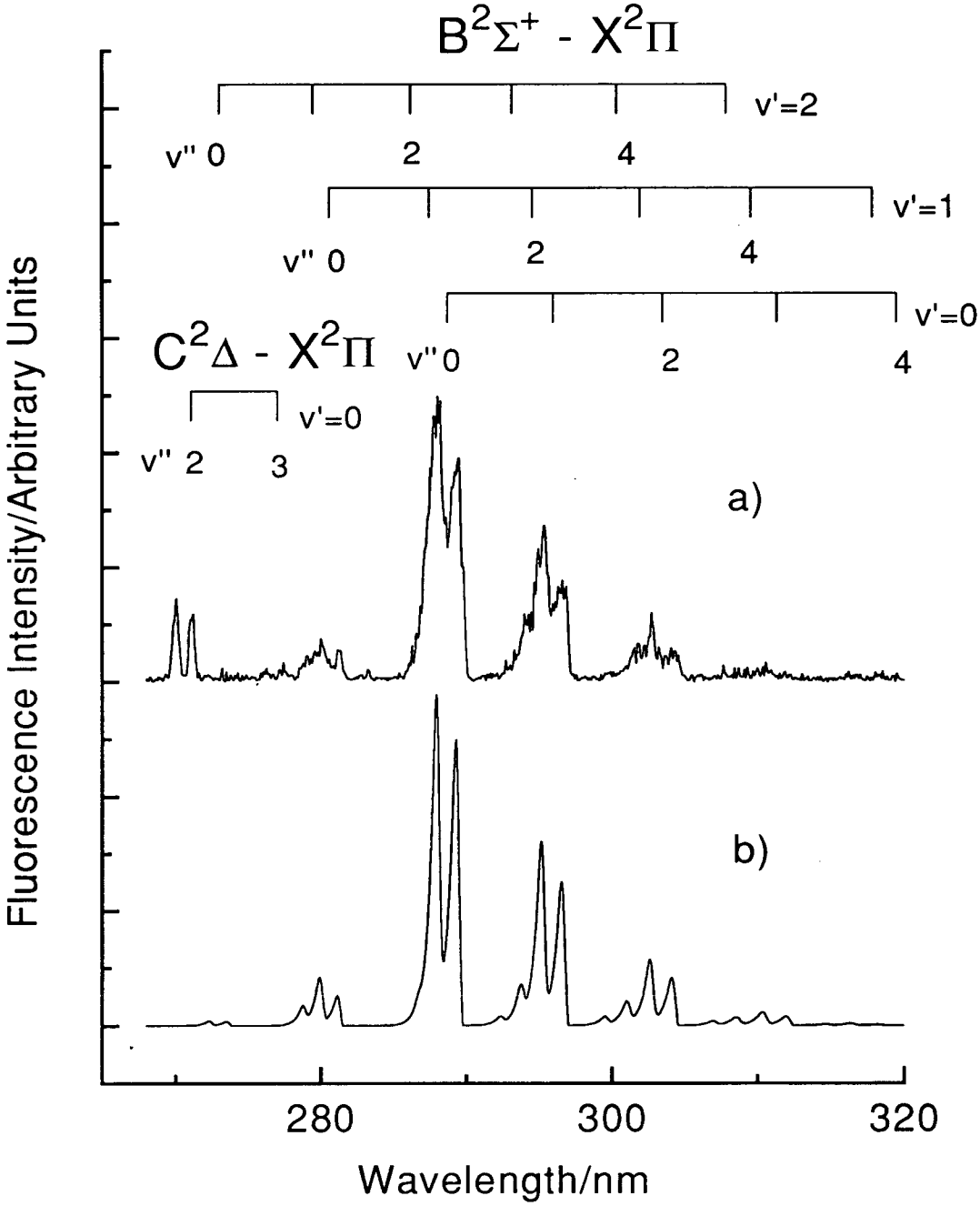

Figure 4–8: Dispersed fluorescence spectrum following the initial excitation of SiF $C^2\Delta(v' = 0)$ in the presence of CH_4.

a) 1 Torr of argon and 1.4 Torr CH_4. b) Least squares fit to the $B^2\Sigma^+ - X^2\Pi$ emission in (a). Fitting procedure performed as described in section 4.3.3.

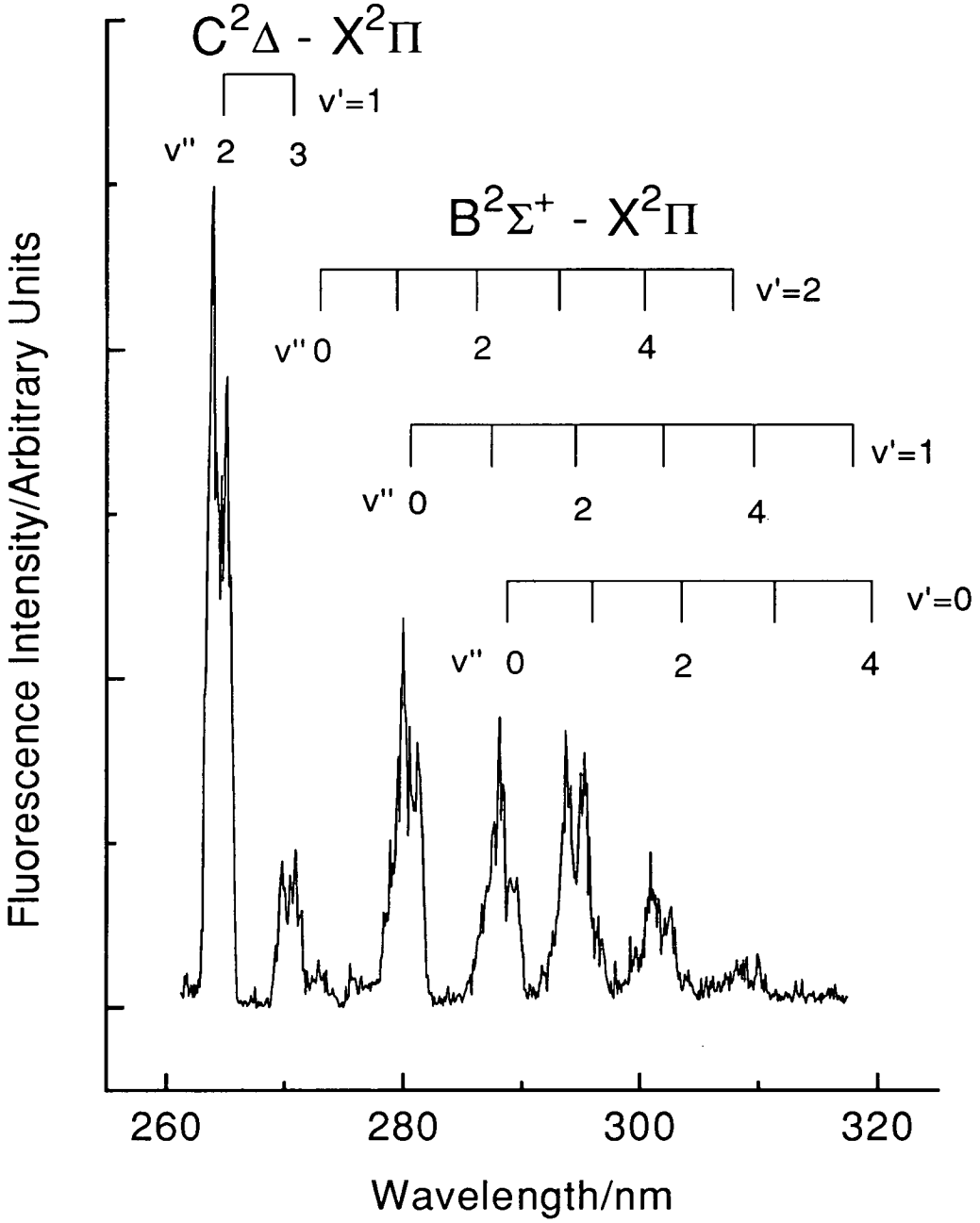

Figure 4–9: Dispersed fluorescence spectrum following the initial excitation of SiF $C^2\Delta(v' = 1)$ in the presence of 1 Torr of argon and 0.6 Torr H_2.

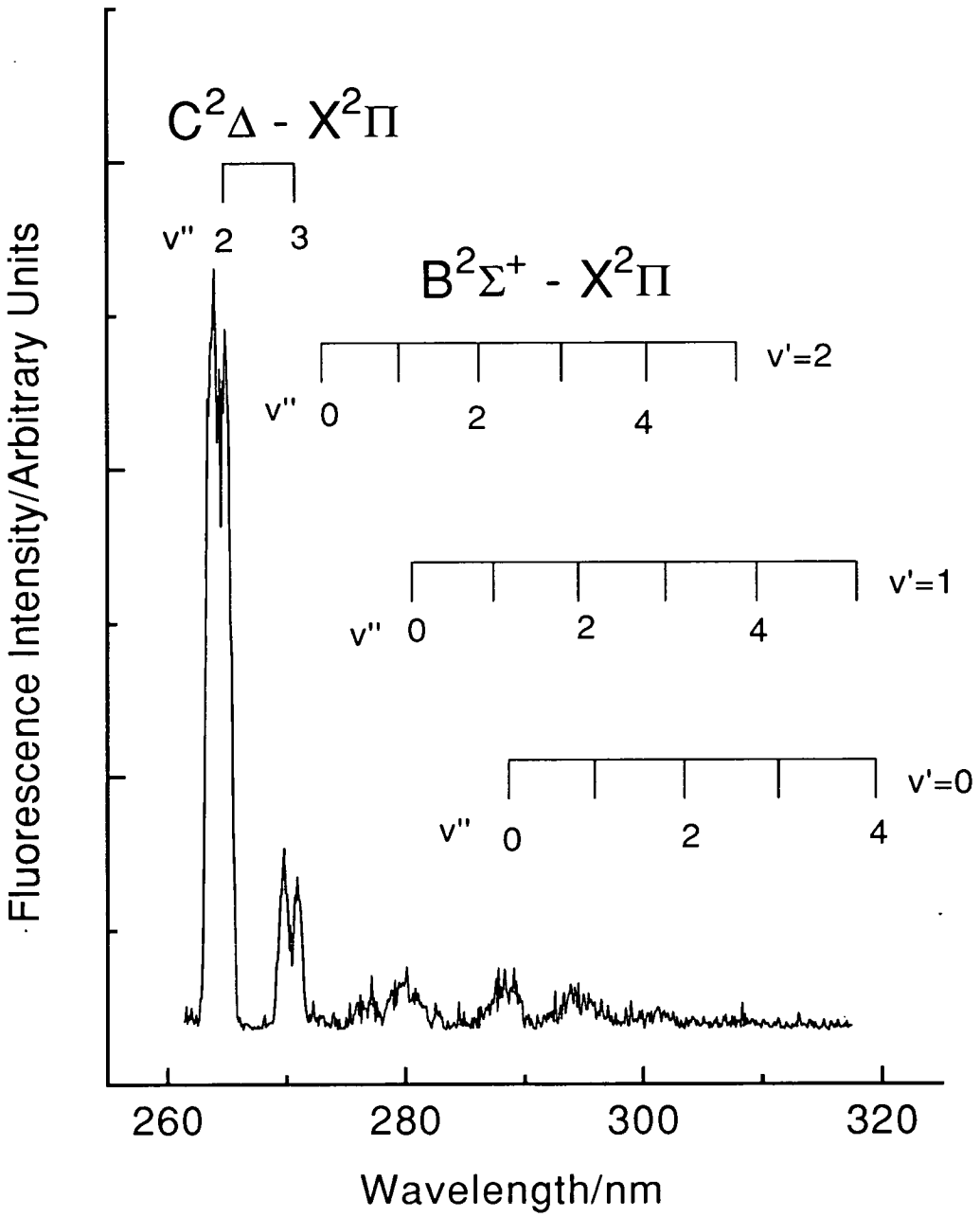

Figure 4–10: Dispersed fluorescence spectrum following the initial excitation of SiF $C^2\Delta(v' = 1)$ in the presence of 1 Torr of argon and 1.3 Torr N_2.

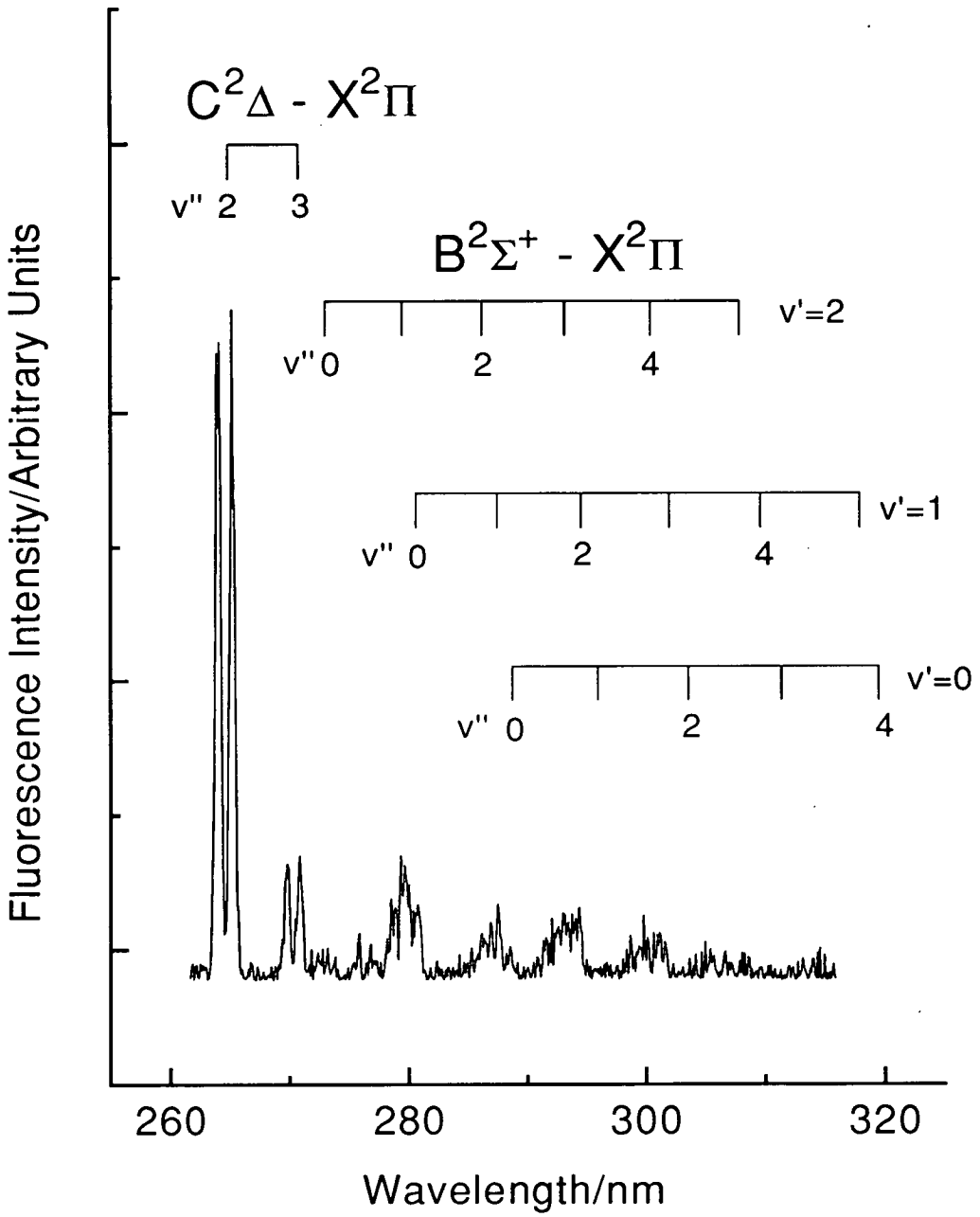

Figure 4–11: Dispersed fluorescence spectrum following the initial excitation of SiF $C^2\Delta(v' = 1)$ in the presence of 1 Torr of argon and 0.9 Torr CH_4.

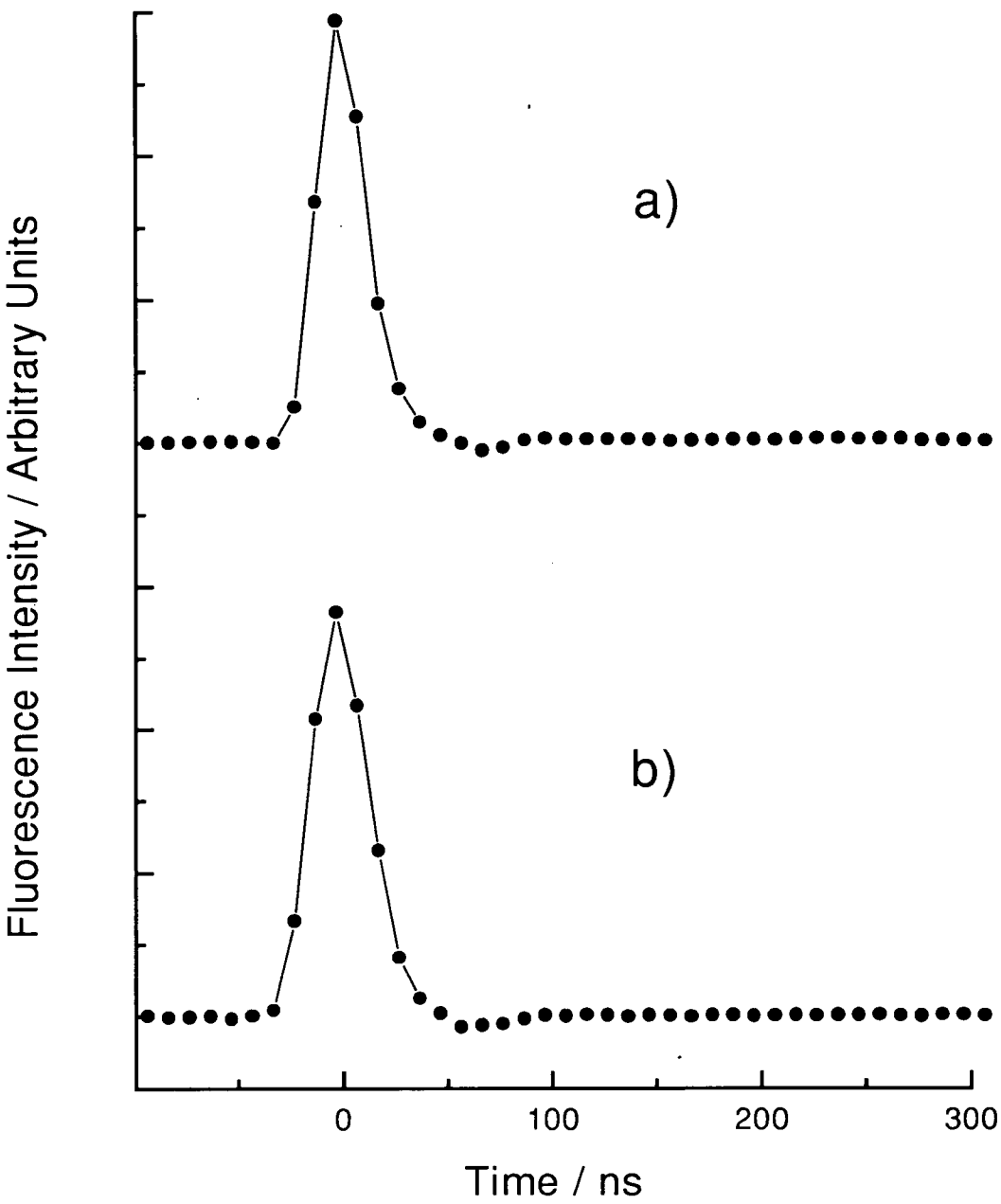

Figure 4–12: a) Time dependent fluorescence profile following excitation of the $B^2\Sigma^+ - X^2\Pi$ (2,0) Q_1 band-head. b) Time dependent profile of the excitation laser pulse intensity.

that $B^2\Sigma^+ - A^2\Sigma^+$ fluorescence is far less likely than $B^2\Sigma^+ - X^2\Pi$ fluorescence by examining equation 3.14. The electronic energy of the SiF $A^2\Sigma^+$ state is 22858 cm^{-1} [11]. Therefore the $B - A$ and $B - X$ origin band transition energies are 11703 cm^{-1} and 34561 cm^{-1} respectively. Hence, purely in terms of the ν^3 factor, $B^2\Sigma^+ - X^2\Pi$ fluorescence is $\sim$ 40 times more likely than $B - A$. Furthermore, the average interatomic separation in the $A^2\Sigma^+$ state is longer than that of the $B^2\Sigma^+$ state and hence the wavefunction overlap would expected to be greater for the off-diagonal transitions which suffer from a further reduction in the ν^3 factor. Therefore, although it is inevitable in principle that some of the collisionally populated $B^2\Sigma^+$ state molecules will fluoresce to the $A^2\Sigma^+$ state and hence escape detection, it seems likely that this will only be the fate of a negligible proportion of the product molecules. Nevertheless, because at this stage the fraction of $B^2\Sigma^+ - A^2\Sigma^+$ emission is not known conclusively, the results reported in this section should be treated as upper limit values.

The spectra shown in figures 4–6 to 4–11 were recorded at the highest quencher pressures that could be achieved whilst maintaining a steady flow rate in the system[2]. Integrating the $B^2\Sigma^+ - X^2\Pi$ and $C^2\Delta - X^2\Pi$ emission intensities allowed estimates of f_B to be obtained which are listed in table 4–2. The values for the fraction of quenched $C^2\Delta$ state molecules transferred to the $B^2\Sigma^+$ state allowed an estimate of the specific rate constants, k_B, and cross sections, σ_B, for this process which are also listed in table 4–2, where

$$k_B = f_B k_Q \tag{4.7}$$

and

$$\sigma_B = f_B \sigma_Q \quad . \tag{4.8}$$

The f_B values range from a maximum of 19% for CH_4 to an immeasurably small fraction for CO_2. Again, the rate constants and cross sections for collisional

---

[2]This pressure was severely limited by the efficiency of the pumping system which had difficulty sustaining a steady state pressure for prolonged periods of time.

Gas[a]	$C^2\Delta(v')$	$k_B^{(b)}/10^{-11}cm^3s^{-1}$	$\sigma_B^{(c)}/\AA^2$	$f_B^{(d)}$
H_2	0	11.4(2.4)	6.4(1.4)	9.8(1.8)
N_2	0	0.6(0.3)	1.1(0.4)	7.7(1.7)
CH_4	0	1.7(0.5)	2.4(0.6)	19(4)
H_2	1	9.0(2.0)	5.0(1.1)	6.4(1.2)
N_2	1	0.7(0.2)	1.1(0.2)	4.8(1)
CH_4	1	2.7(0.7)	3.8(1.0)	19(4)

Table 4–2: Rate constants, thermally averaged cross sections and branching fractions for transfer from SiF $C^2\Delta - B^2\Sigma^+$.
Numbers in parenthesis represent 2σ uncertainties. (a) No transfer observed for He, Ar or CO_2. (b) Specific $C^2\Delta - B^2\Sigma^+$ transfer rate constant. (c) Thermally averaged cross section. (d) Fraction of quenched $C^2\Delta$ molecules transferred to the $B^2\Sigma^+$ state (expressed as a percentage).

transfer for H_2 are significantly greater than those for the other quenching species reflecting the large values for total removal rather than exceptional f_B values. The results indicate that there are no major differences between the $C^2\Delta - B^2\Sigma^+$ transfer rates upon excitation of $C^2\Delta$, $v' = 0$ and 1 for these quenchers.

For the experiments studying transfer from $C^2\Delta$, $v' = 1$ there existed the possibility of collision-induced vibrational relaxation to $C^2\Delta$, $v' = 0$ prior to emission or electronic transfer. This occurrence cannot be ruled out entirely, due to the low resolution conditions employed during these experiments. However, the distinctly different appearance of the collision-induced $B^2\Sigma^+ - X^2\Pi$ spectra after initial preparation of $C^2\Delta, v' = 1$, compared with $v' = 0$, indicates that the vast majority of $B^2\Sigma^+$ molecules are the result of direct transfer from $C^2\Delta$, $v' = 1$. It would therefore appear that vibrational relaxation is not a significant product channel.

4.3.3 $B^2\Sigma^+$ Vibrational Branching Ratios

Perhaps the most interesting information that can be derived from the spectra presented in this chapter is the product $B^2\Sigma^+$ vibrational distributions. As discussed extensively above, these distributions are the direct result of collisional transfer from the $C^2\Delta$ state. From initial examination of the spectra it is apparent that the $B^2\Sigma^+$ vibrational populations are strongly dependent upon the identity of the initially populated $C^2\Delta$ state vibrational level though not strongly collider dependent. It is also obvious, with knowledge of the $B^2\Sigma^+ - X^2\Pi$ transition intensities derived in chapter 3, that only the lower levels of those energetically accessible are significantly populated.

$B^2\Sigma^+$ Vibrational Populations following Excitation of $C^2\Delta(v = 0)$

In the case of the $C^2\Delta$, $v = 0$ spectra, the populations were derived directly by a least-squares fitting procedure. Initially, the collisionally produced $B^2\Sigma^+ - X^2\Pi$ emission spectra were fitted with the emission spectra from individual $B^2\Sigma^+$ state vibrational levels obtained by direct laser excitation from the $X^2\Pi(v'' = 0)$ (as described in chapter 3). However the best-fit simulations of each of these spectra showed that the rotational contours of the collisionally populated spectra differed significantly from those of the directly populated $B^2\Sigma^+$ spectra.

It is clear, however, with knowledge of the vibrational transition probabilities obtained in chapter 3, that the vast majority of the $B^2\Sigma^+$ emission is from the vibrational ground state with a smaller fraction from the $v' = 1$ and 2 states; there is no observable emission $v' = 3, 4$ or 5. From these observations it can be deduced that the major feature in the $B - X$ emission at around 288nm is almost entirely ($\sim 95\%$) due to the $B - X(0,0)$ transition as this coincides only with very weak transitions from $v' = 1$ and 2. The rotational contour was modelled upon this profile using the rotational simulation program described in section 3.5.1. A

Boltzmann temperature of 1200K was found to adequately match the experimental spectrum, at this experimental resolution, as is demonstrated in figure 4–13[3].

The spectral basis sets used for the fitting process were therefore synthesised using this rotational contour and the known vibrational transition probabilities. The simulations are shown with the experimental spectra in figures 4–6 to 4–8. In all cases the simulations can be seen to model the observed $B - X$ emission reasonably well.

Table 4–3 shows the derived vibrational distributions which are also shown graphically in figure 4–14. These confirm that the majority of the $B^2\Sigma^+$ state products are in the vibrational ground state for each quencher with $B^2\Sigma^+ v' = 1, 2$ the only other states receiving significant population. It can be seen that there are only slight differences in the spectra and corresponding distributions resulting from different quenchers although these differences were reproducible.

$B^2\Sigma^+$ Vibrational Populations following Excitation of $C^2\Delta(v' = 1)$.

The collision-induced $B^2\Sigma^+ - X^2\Pi$ spectra presented in figures 4–9 to 4–11, following preparation of $C^2\Delta$, $v' = 1$, again indicate that only the lower vibrational levels have been populated with no evidence of any emission from $v' = 3 - 5$. Unfortunately, due to the poor signal-to-noise ratios it was not possible to perform a direct least-squares fit to the spectra as before.

To obtain an estimate of the relative populations of each $B^2\Sigma^+$ vibrational level, the following expression was used:

$$I_{v'v''} = N_{v'} \nu^3_{v'v''} p_{v'v''} C(\nu) \tag{4.9}$$

where $I_{v'v''}$ is the measured integrated band intensity, $N_{v'}$ is the relative population, $\nu_{v'v''}$ the transition frequency, $p_{v'v''}$ the vibrational transition probability (as

---

[3]A more detailed examination of the product state rotational distribution employing higher resolution observations is presented in chapter 5.

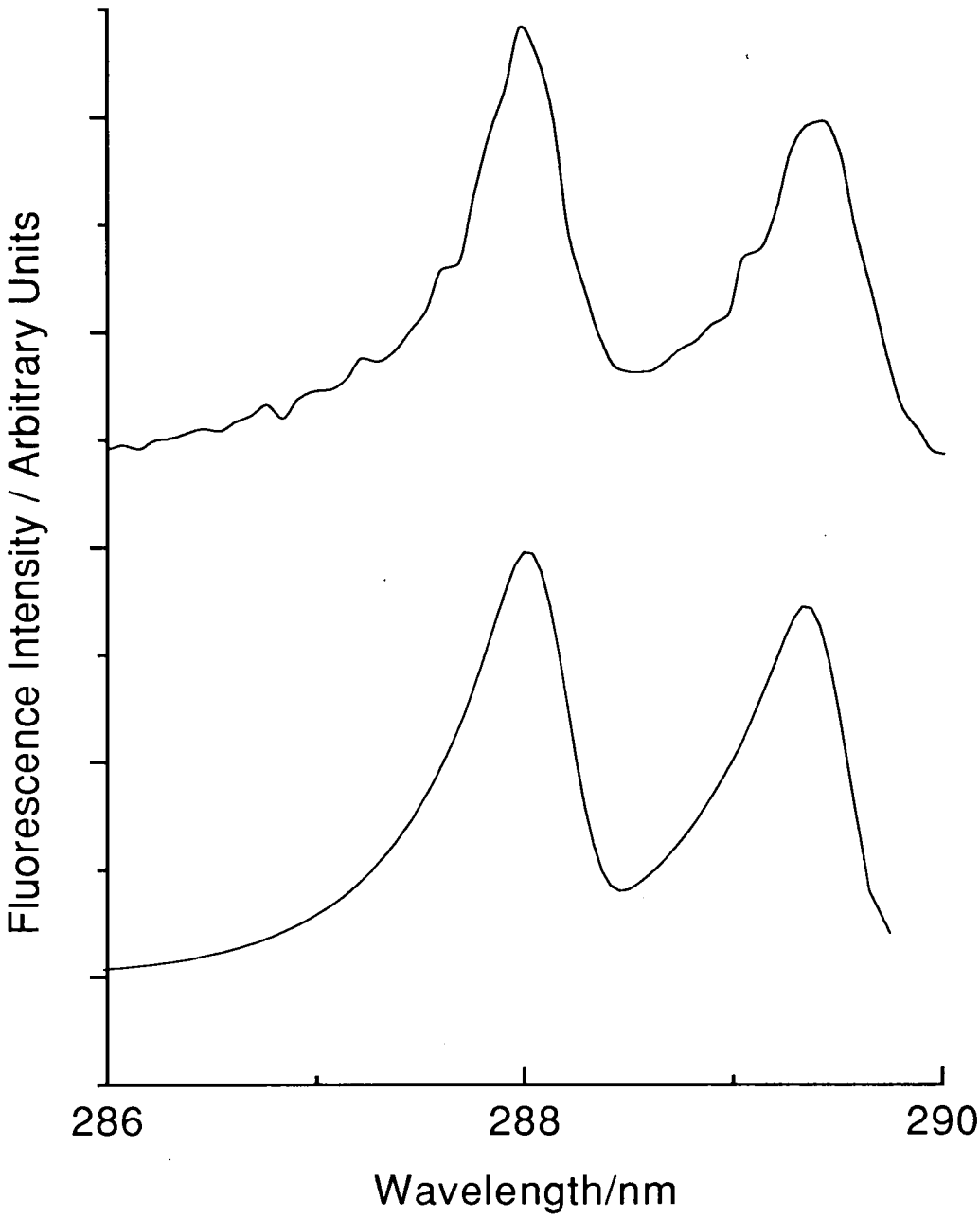

Figure 4–13: Dispersed fluorescence spectrum of the SiF $B^2\Sigma^+ - X^2\Pi(0,0)$ transition obtained after the excitation of the $C^2\Delta(v = 0)$ state in the presence of 0.5 Torr H_2 and 1 Torr Ar.

The lower trace show the rotational simulation of the $B^2\Sigma^+ - X^2\Pi(0,0)$ band obtained using a bandwidth of 35 cm^{-1} and a Boltzmann temperature of 1200K.

Gas[a]	$C^2\Delta(v)$	$v'=0$[b]	$v'=1$[b]	$v'=2$[b]
H_2	0	87(10)	7(6)	6(14)
N_2	0	62(6)	21(9)	16(11)
CH_4	0	80(7)	13(11)	6(10)
$q_{vv'}^{(c)}$	0	88	11	1
H_2	1	24(10)	59(7)	17(15)
N_2	1	33(8)	46(7)	21(12)
CH_4	1	16(14)	53(7)	31(11)
$q_{vv'}^{(c)}$	1	13	65	19

Table 4–3: Nascent vibrational populations in SiF $B^2\Sigma^+$ following transfer from $C^2\Delta(v=0,1)$.

Figures in parenthesis represent 1σ uncertainties as derived from the fits. a) No observable $B^2\Sigma^+$ population for Ar, He and CH_4. b) Relative $B^2\Sigma^+$,v' population, expressed as a percentage, derived from an unconstrained least squares fit. c) Franck-Condon factor for $B^2\Sigma^+ - X^2\Pi$ overlap.

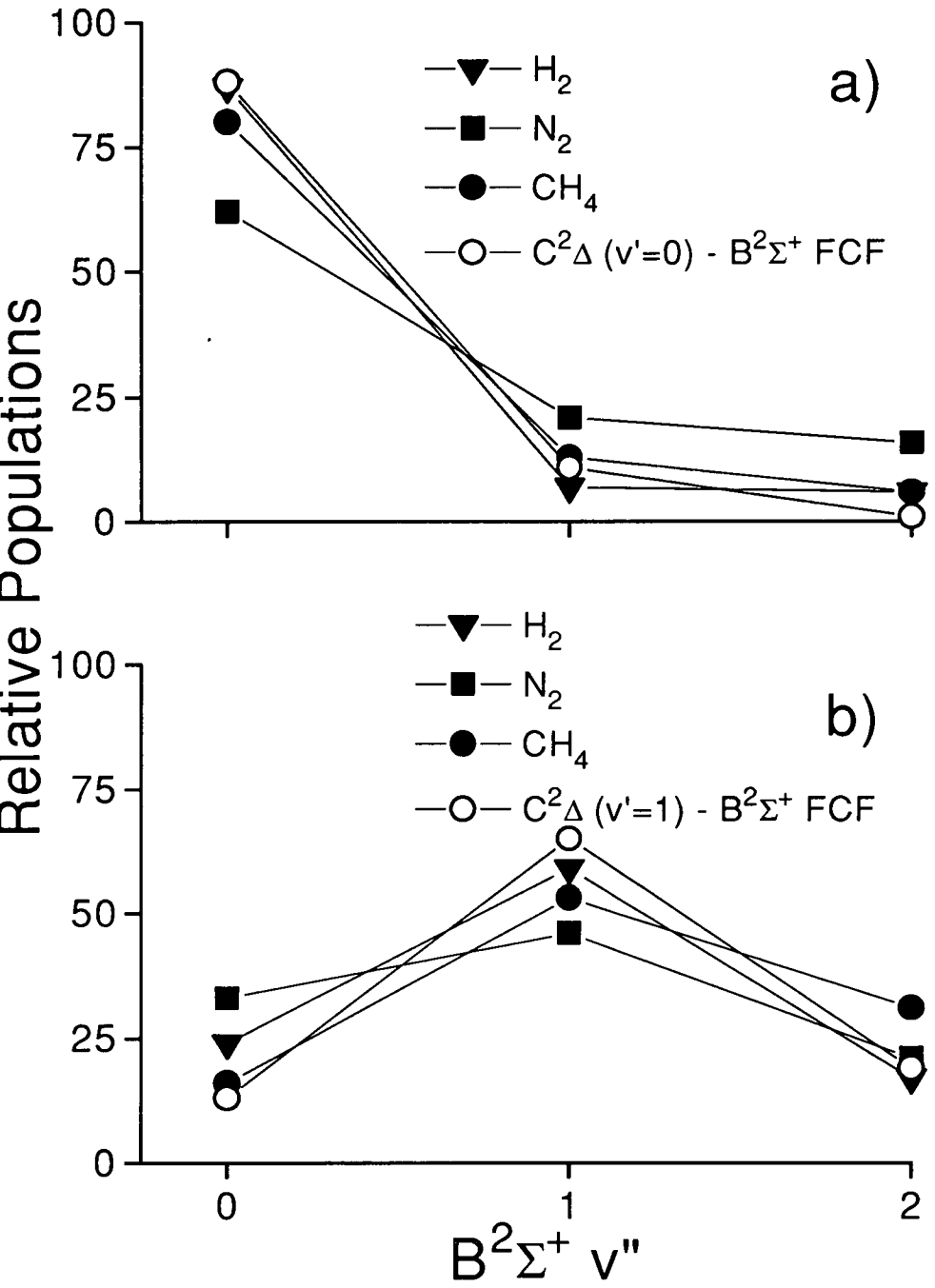

Figure 4–14: Measured SiF $B^2\Sigma^+$ state product vibrational distributions following excitation of $C^2\Delta$ for H_2, N_2 and CH_4.

The corresponding $C^2\Delta - B^2\Sigma^+$ Franck-Condon factors are also shown. a)$v = 0$. b)$v = 1$.

defined in equation 3.21) and $C(\nu)$ is the frequency dependent correction term for the response of the detection apparatus. Therefore, for a spectral region comprising of emission from a number of different vibrational levels, the intensity, I, will be given by

$$I = \sum_{v'}(N_{v'}\nu^3_{v'v''}p_{v'v''}C(\nu)) \quad . \tag{4.10}$$

The collision-induced population of each $B^2\Sigma^+$ vibrational level was obtained by integrating over the prominent regions of emission. These spectral peak areas were fitted, using a non-linear least squares method, with the experimental intensities for the relevant $B^2\Sigma^+ - X^2\Pi(v, v'')$ transitions to obtain the relative values for N_v. The derived distributions are listed in table 4–3 and represented graphically in figure 4–14.

Again, it can be seen from the spectral analysis that there are only slight differences in the product distributions between the quenchers. The majority of the nascent population occurs in $B^2\Sigma^+$, $v' = 1$ with significant population in $v' = 0$ and 1. There was no evidence for any significant population of $v' = 3 - 5$.

4.3.4 Correlation of the Nascent $B^2\Sigma^+$ Vibrational Populations with the $C^2\Delta - B^2\Sigma^+$ Franck-Condon Factors.

The collisionally populated $B^2\Sigma^+$ state vibrational distributions are similar for all the effective quenchers but differ significantly for the two initially populated $C^2\Delta$ state vibrational levels. In both cases the favoured channel occurs over a vibronic energy gap of approximately 5000 cm^{-1} with no observed transfer to the near isoenergetic levels. A calculation of the relevant Franck-Condon factors (as described in section 3.5.2) for overlap of the originally populated $C^2\Delta$ state vibrational level and the $B^2\Sigma^+$ state vibrational levels was carried out using the RKR vibrational wavefunctions. The results are included in table 4–3 and figure 4–14. This reveals a reasonable correlation between the wavefunction overlap and the derived product state distributions. For both initially populated $C^2\Delta$ vibrational levels it can be seen that the product distributions for H_2 as the quencher species most closely match the Franck-Condon factors.

4.4 $B'^2\Delta$ to $B^2\Sigma^+$ Vibronic Energy Transfer in SiCl

The results reported in this section have previously been obtained either using a similar experimental method [1] or, in the case of the significantly larger data set, without a facility for temporally resolved measurements [2,3]. The main motivation for repeating the measurements for the SiCl $B'^2\Delta - B^2\Sigma^+$ system was to confirm that the experimental method, used for all studies described in this thesis, could be used to extract reliable data. It was also hoped that the existing data set could be improved by producing results with smaller uncertainties.

All experiments reported in this section were performed by initial excitation of the Q_1 band head of the appropriate $B'^2\Delta - X^2\Pi_{\frac{1}{2}}(v', 0)$ transition followed by examination of the time- and wavelength-resolved LIF. The laser excitation spectra from the previous SiCl $B'^2\Delta - B^2\Sigma^+$ transfer studies allowed identification of the appropriate wavelengths to selectively prepare the appropriate vibronic levels [2, 10].

The only major experimental difference between the SiCl study and the analogous SiF investigations is caused by the spectroscopic overlap of the $B'^2\Delta - X^2\Pi(0,0)$ and $B^2\Sigma^+ - X^2\Pi(2,0)$ transitions. It can be seen from examination of figure 4–1 that the $B'^2\Delta(v' = 0)$ and $B^2\Sigma^+(v = 2)$ vibronic levels are separated by only 36 cm^{-1}. It was therefore impossible to populate the $B'^2\Delta(v' = 0)$ state without simultaneously exciting a component of the $B^2\Sigma^+ - X^2\Pi(2,0)$ transition. This difficulty was overcome by exploiting the disparity in the radiative lifetimes of the two states. As the lifetime of the $B^2\Sigma^+$ state has been shown to be 10 ns [7], $\sim$ 99% of the directly excited $B^2\Sigma^+$ state molecules would be removed due to spontaneous radiation within approximately 40 ns. Therefore the contribution of directly populated $B^2\Sigma^+$ to any emission spectrum was removed by setting the detection gate to record emission only after this time delay.

4.4.1 Total Collisional Removal of SiCl $B'^2\Delta(v' = 0, 1)$

The total collisional removal rate of the SiCl $B'^2\Delta(v')$ state had proved to be the most difficult quantity to evaluate in the previous study where there was no facility for temporal resolution [2]. In this system, the carrier gas argon also turned out to be an efficient quencher of the $B'^2\Delta$ state and hence its contribution towards the transfer processes had to be taken into account. The devised kinetic model predicted [2] that the integrated intensity of the $B'^2\Delta - X^2\Pi$ emission, $I_{B'}$, would obey the equation

$$\frac{1}{I_{B'}} = \frac{\tau_{B'}}{B'_0}\{k_Q P_Q + k_{Ar} P_{Ar}\} + \frac{1}{B'_0} \tag{4.11}$$

where B'_0 is a proportionality constant to incorporate the dependence of the signal intensity upon the initial $B'^2\Delta$ concentration and the detection sensitivity of the apparatus. With knowledge of the radiative lifetimes, k_Q could be evaluated from a plot of $\frac{1}{I_{B'}}$ against P_Q. This will produce a slope of $\frac{\tau_{B'} k_Q}{B'_0}$ but with an intercept dependent on the argon pressure. Although the quantity $\frac{1}{B'_0}$ could in principle be obtained from the intercept of a plot where argon is the the only quencher species present, this would be difficult in practice because the value of B'_0 will be dependent on the SiCl ground state concentration and upon the excitation laser power. The initial concentration of the $B'^2\Delta$ state was hence estimated from the intensity of the directly excited $B^2\Sigma^+ - X^2\Pi$ LIF excitation signal for each quenching gas pressure. This method, not surprisingly, resulted in large experimental uncertainties as well as being experimentally exhausting. The rate constants and cross sections for total collisional removal derived from the study by Singleton [2] are presented in table 4–4.

In the present study, and the analogous study by Jeffries [1], a similar method to that described in the previous section was applied. However, as it is apparent that argon is an efficient quencher of the $B'^2\Delta$ state, equation 4.2 has to be adapted. The total effective first order removal rate constant, k, is now given by

$$k = k_1 + k_{Ar} P_{Ar} \tag{4.12}$$

and hence

$$k = \tau_{B'}^{-1} + k_Q P_Q + k_{Ar} P_{Ar} \quad . \tag{4.13}$$

Therefore, for any lifetime measurement of the $B'^2\Delta$ state fluorescence, the contribution of the argon carrier, necessarily present, had to be subtracted. The value of k_{Ar} was evaluated from measurements where argon was the only quencher species present. Obviously the accuracy of the calculated values for k_Q is limited by the difficulty in obtaining the true partial pressures of the argon carrier and the quenching gas.

A typical radiative decay plot, following excitation of SiCl $B'^2\Delta$, $v' = 0$, and the best exponential fit are presented in figure 4–15. The derived decay rates are probably more accurate in this respect than for SiF because the lifetime is significantly longer and therefore not so close to the limiting time response of the apparatus.

Figures 4–16 and 4–17 show plots of k_1 against the quencher gas pressure for initial excitation of SiCl $B'^2\Delta, v' = 0$ and 1 respectively. As before, the *best fit* slopes of these plots were evaluated by the method of linear least-squares to produce the bimolecular quenching rate constants, k_Q. These values, along with the quenching cross sections, can also be seen in table 4–4 and can be compared with the values obtained by Jeffries [1] and Singleton [2,3].

These new results presented agree very well with those of Jeffries [1] for the helium and argon quenchers with similar degrees of uncertainty. Comparison with the indirectly measured removal rates of Singleton [2] reveals a reasonably good correspondence for most quenching rate constants although the precision has obviously been much improved.

The magnitudes of the quenching rate constants confirm that this process is efficient, though highly dependent upon the identity of the collision partner. However there are no substantial differences between these quantities for removal of $B'^2\Delta v' = 0$ or $v' = 1$.

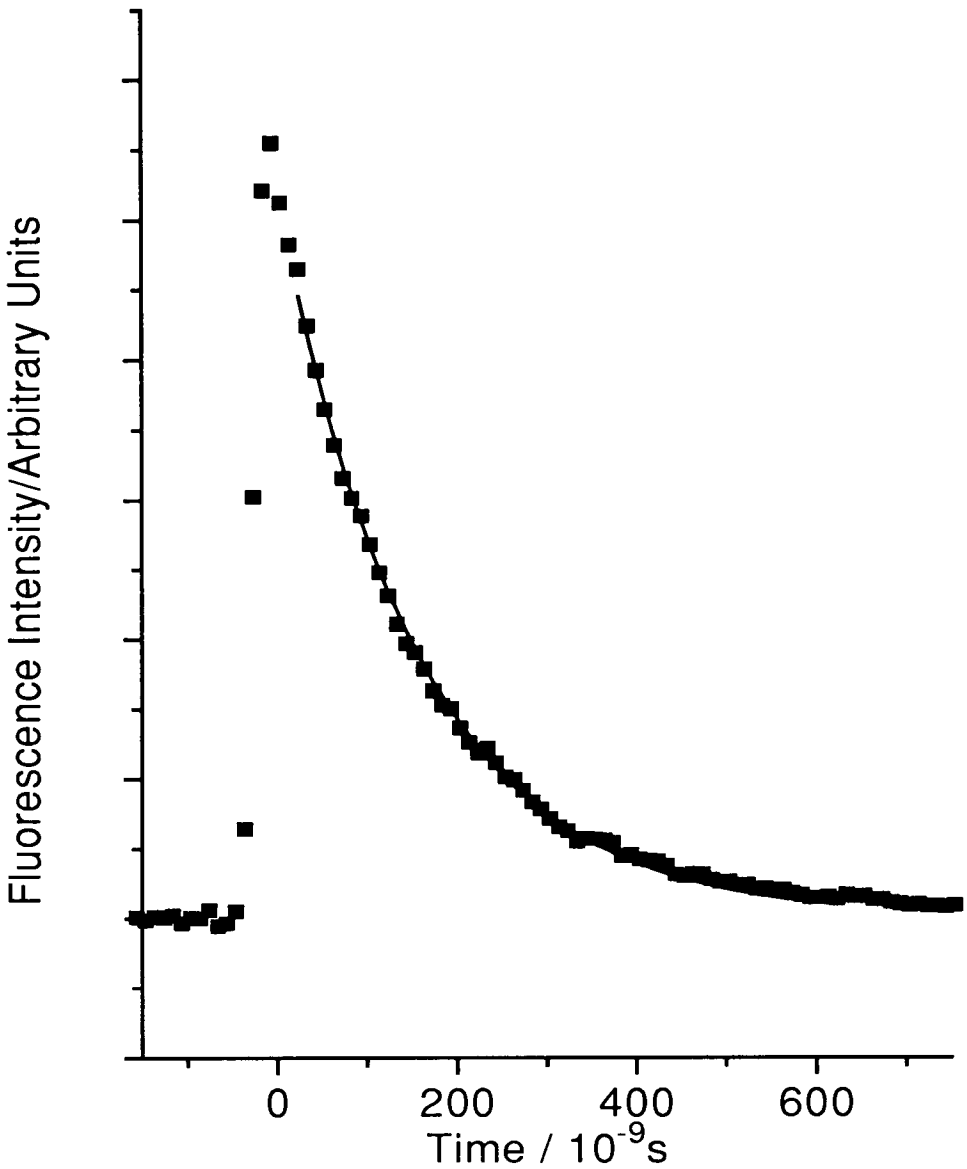

Figure 4–15: Representative radiative decay plot for the SiCl $B'^2\Delta - X^2\Pi$ transition.

The experimental fluorescence intensities are represented by the circles. The solid line indicates the best single-exponential fit.

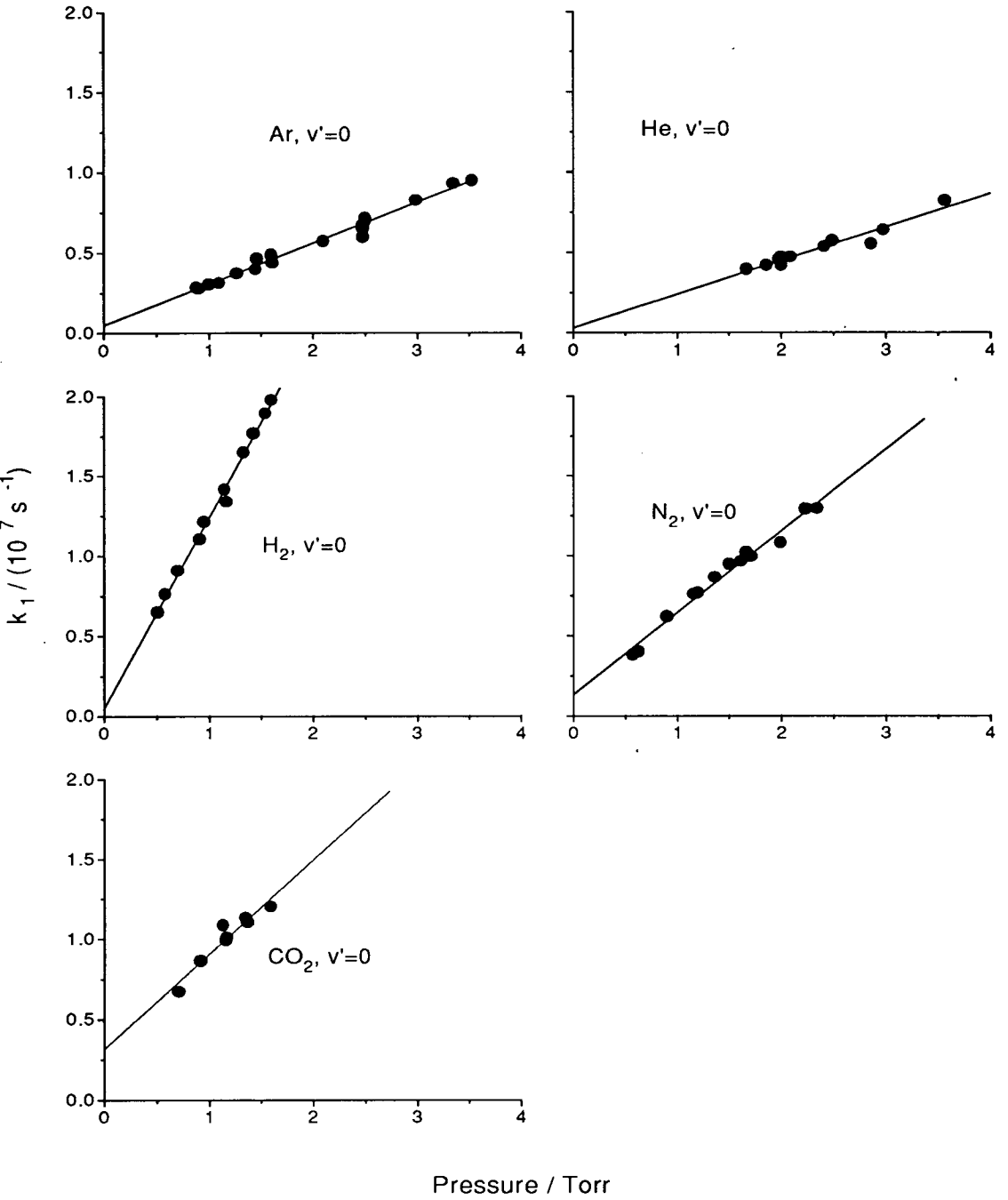

Figure 4–16: Observed first order decay constants for SiCl $B'^2\Delta v' = 0$ as a function of quencher partial pressure.

For the non-argon quenchers, the experiments were performed with an additional fixed argon carrier pressure of ~1 Torr. The contribution of the argon gas to the quenching of the $B'^2\Delta$ state has been subtracted.

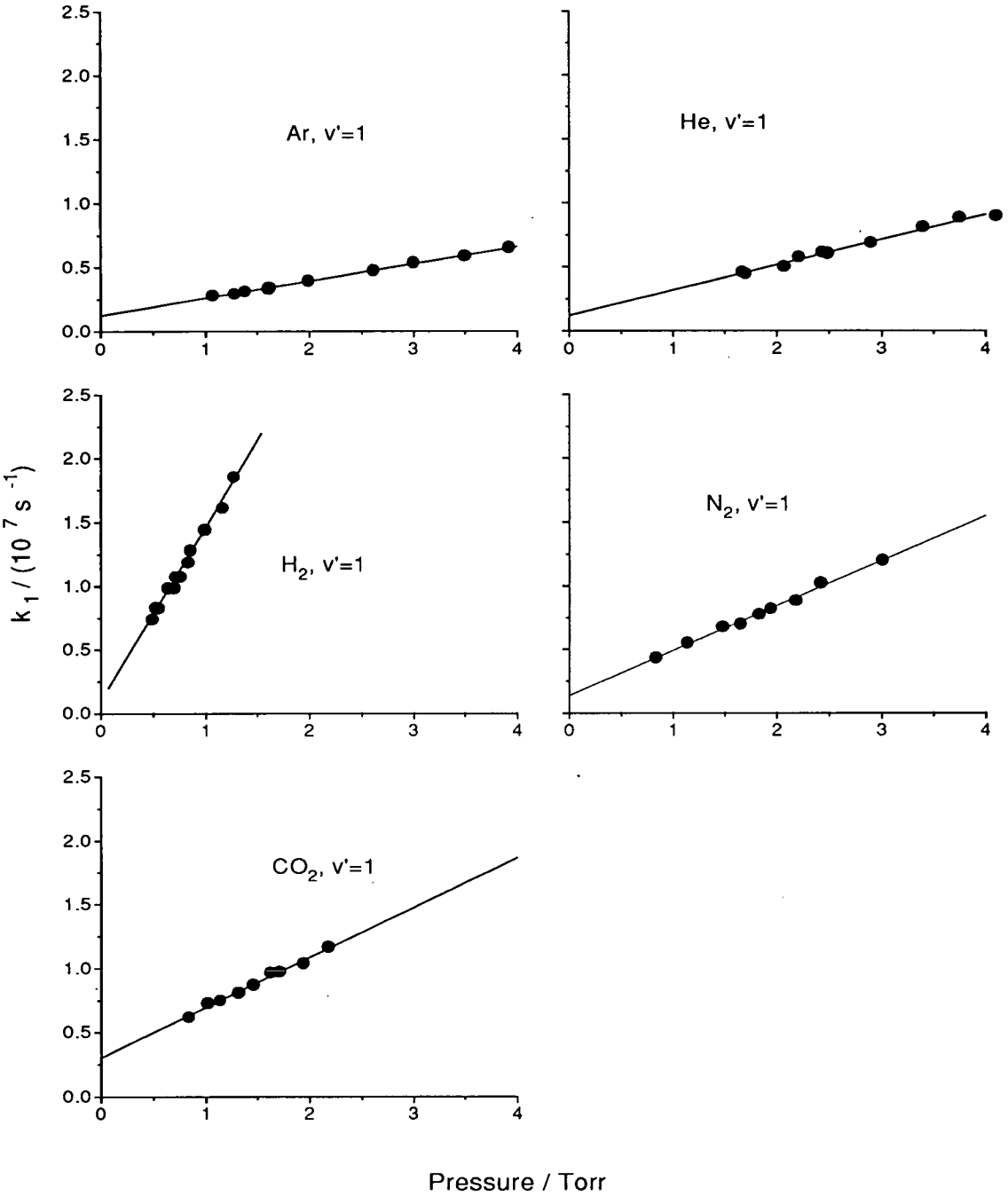

Figure 4–17: Observed first order decay constants for SiCl $B'^2\Delta v' = 1$ as a function of quencher partial pressure.

For the non-argon quenchers, the experiments were performed with an additional fixed argon carrier pressure of ~1 Torr. The contribution of the argon gas to the quenching of the $B'^2\Delta$ state has been subtracted.

gas	$B'^2\Delta(v')$	$k_Q^{(a)}/10^{-11}cm^3s^{-1}$	$\sigma_Q^{(b)}/\AA^2$
He	0	4.1(2.1)[c]	3(1)[c]
		5.6(0.3)[d]	4.3(0.2)[d]
		6.1(0.6)[e]	4.7(0.5)[e]
Ar	0	7.4(3.0)[c]	15(6)[c]
		7.9(0.3)[d]	16(1)[d]
		7.9(0.2)[e]	16(1)[e]
H_2	0	26.6(7.4)[c]	15(6)[c]
		36.1(2.2)[e]	20(1)[e]
N_2	0	7.5(2.4)[c]	14(6)[c]
		15.3(0.8)[e]	27(2)[e]
CO_2	0	17.8(6.7)[c]	36(16)[c]
		17.8(4.2)[e]	36(8)[e]
CH_4	0	17.8(12.6)[c]	26(14)[c]
He	1	4.9(1.5)[c]	3.7(2.6)[c]
		6.6(0.3)[d]	5.1(0.2)[d]
		6.3(0.2)[e]	4.9(0.2)[e]
Ar	1	5.6(2.9)[c]	11(7)[c]
		4.2(0.6)[d]	8.2(1.2)[d]
		4.2(0.1)[e]	8.2(0.2)[e]
H_2	1	36.4(9.0)[c]	20(14)[c]
		41.2(2.8)[e]	23(2)[e]
N_2	1	11.0(4.4)[c]	19(14)[c]
		10.7(0.6)[e]	18(1)[e]
CO_2	1	14.6(5.6)[c]	28(21)[c]
		11.8(0.8)[e]	23(2)[e]
CH_4	1	28.0(13.4)[c]	40(29)[c]

Table 4–4: Rate constants and thermally averaged cross sections for the total collisional removal from SiCl $B'^2\Delta(v' = 0, 1)$.

Numbers in parenthesis represent 2σ uncertainties. a) Bimolecular quenching rate constant for total removal of SiCl $B'^2\Delta(v')$. b)Thermally averaged cross section for removal of SiCl $B'^2\Delta(v')$. c) Values by Singleton [2,3]. d) Values by Jeffries [1]. e) This work.

4.4.2 Specific Collisional Transfer from $B'^2\Delta(v' = 0, 1)$ to $B^2\Sigma^+$

The previous studies [1,2,3] of the specific transfer rates from $B'^2\Delta(v' = 0, 1) - B^2\Sigma^+$ were both performed as described in section 4.3.2. However, as will be demonstrated, the argon carrier also collisionally induces transfer from $B'^2\Delta$ to $B^2\Sigma^+$. Equation 4.6 has therefore to be modified to account for this contribution to yield the fraction , f_B, of quenched $B'^2\Delta$ state molecules transferred to the $B^2\Sigma^+$ state,

$$f_B = \left\{ \frac{I_B}{I_{B'}} \frac{1}{\tau_{B'}} - f_{B,Ar} k_{Ar} P_{Ar} \right\} / k_Q P_Q \quad . \tag{4.14}$$

As the determination of the transfer fraction is dependent upon the ratio of the total integrated intensities of the $B' - X$ and $B - X$ transitions there is no advantage to be gained by having the facility for temporally resolved measurements. The results obtained by Jeffries [1] and Singleton [2,3] have, therefore, a similar degree of precision.

Representative plots of the dispersed fluorescence resulting from the excitation of the $B'^2\Delta v' = 0$ and 1 states in the presence of argon can be seen in figure 4–18 and 4–19, respectively. A brief inspection of these spectra indicates that the majority of the fluorescence in both cases is due to the collision-induced $B^2\Sigma^+ - X^2\Pi$ emission.

As discussed for SiF, complications could have arisen in the experiments on transfer from $B^2\Delta v' = 1$ in that some of the molecules could have become vibrationally relaxed before electronic transfer to the $B^2\Sigma^+$ state. Again there was no evidence in practice of emission from $B'^2\Delta v' = 0$ in these experiments. The distinctly different appearance of $B^2\Sigma^+ - X^2\Pi$ spectra (for all quenchers except argon) indicates that the vast proportion of $B'^2\Delta v' = 1$ molecules must be directly transferred to the $B^2\Sigma^+$ state[4].

---

[4]Higher resolution studies by Singleton [2] had also shown this directly by the absence of $B'^2\Delta$, $v = 0$ emission following $v = 1$ excitation.

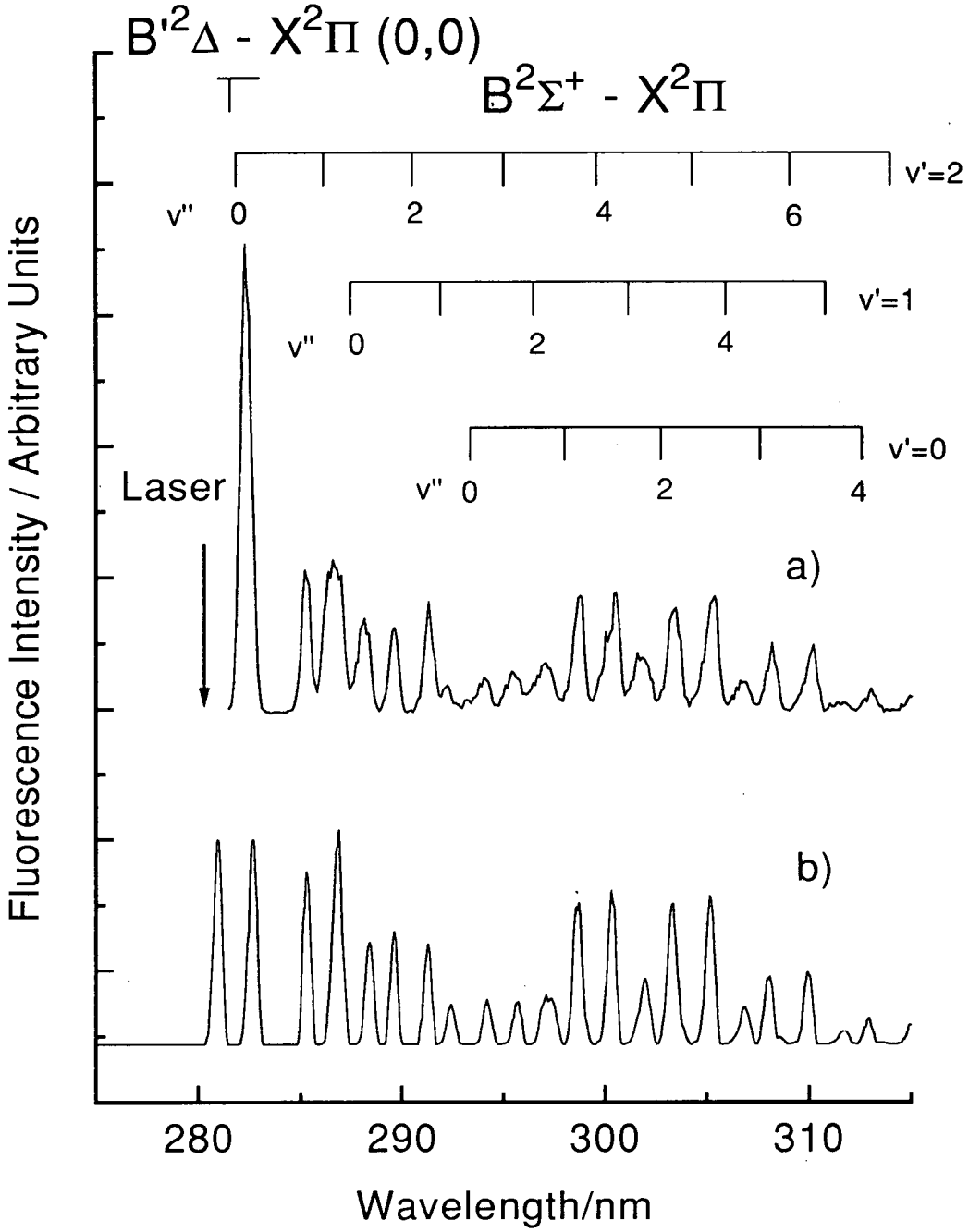

Figure 4–18: Dispersed fluorescence spectrum following excitation to the SiCl $B'^2\Delta v' = 0$ level in the presence of argon.

a) 4 Torr of argon. Laser excitation wavelength indicated by the vertical arrow. b) Least squares fit to the $B^2\Sigma^+ - X^2\Pi$ emission in (a). Fitting procedure performed as described in section 4.4.3.

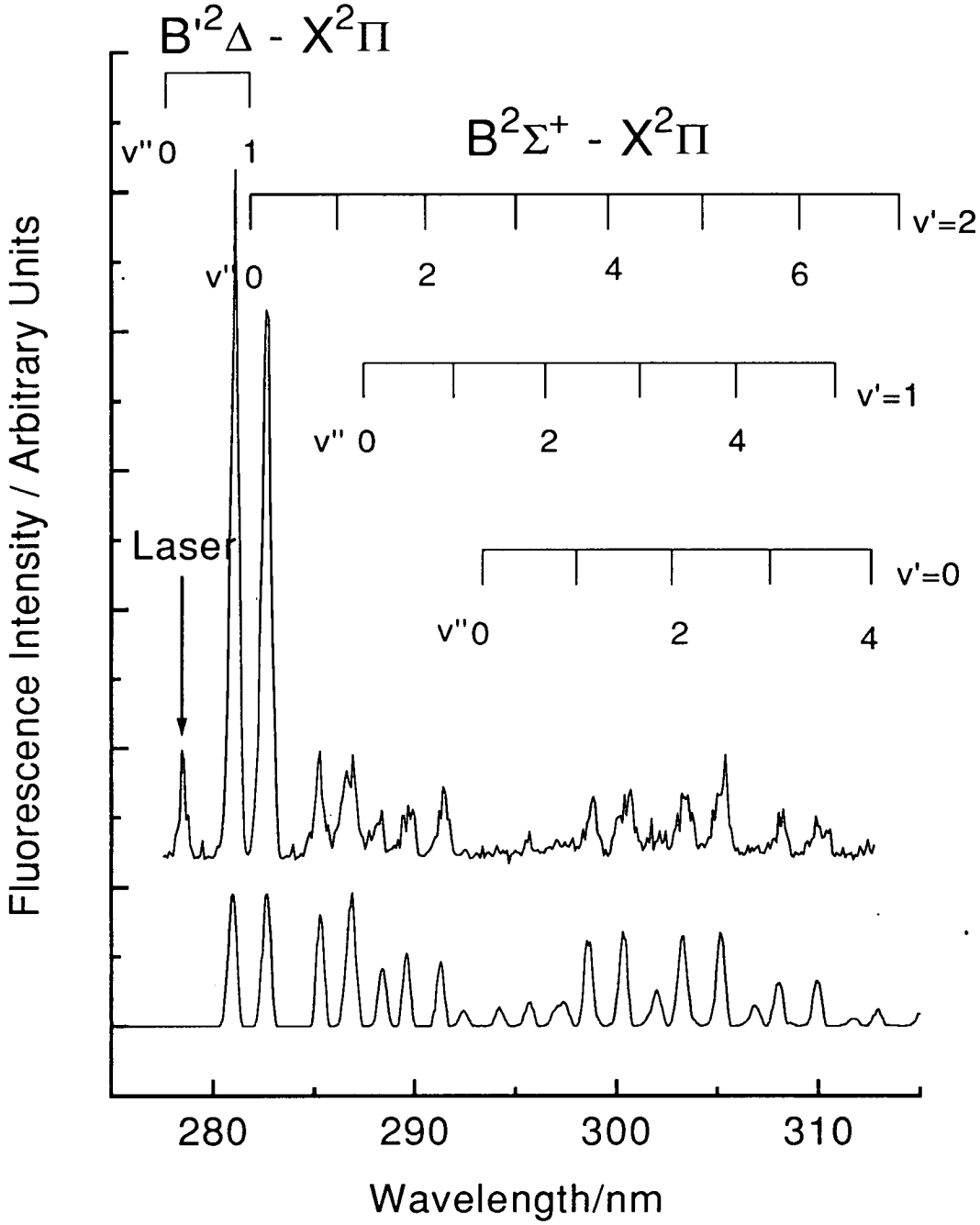

Figure 4–19: Dispersed fluorescence spectrum following excitation to the SiCl $B'^2\Delta v' = 1$ level in the presence of argon.

a) 4 Torr of argon. Laser excitation wavelength indicated by the vertical arrow. b) Least squares fit to the $B^2\Sigma^+ - X^2\Pi$ emission in (a). Fitting procedure performed as described in section 4.4.3.

gas	$B'^2\Delta(v')$	$k_B^{(a)}/10^{-11}cm^3s^{-1}$	$\sigma_B^{(b)}/\AA^2$	$f_B^{(c)}$
Ar	0	$2.7(0.6)^{(d)}$	$5.3(1.2)^{(d)}$	$35(16)^{(d)}$
		$2.4(0.8)^{(e)}$	$4.8(1.6)^{(e)}$	$30(10)^{(e)}$
		$3(0.8)^{(f)}$	$5.9(1.6)^{(f)}$	$38(10)^{(f)}$
He	0	$2.3(0.6)^{(d)}$	$1.8(0.5)^{(d)}$	$60(26)^{(d)}$
		$3.4(0.6)^{(e)}$	$2.6(0.4)^{(e)}$	$60(10)^{(e)}$
		$2.6(1.5)^{(f)}$	$2(1.4)^{(f)}$	$43(24)^{(f)}$
H_2	0	$24(4)^{(d)}$	$13.3(2.2)^{(d)}$	$89(39)^{(d)}$
		$26(16)^{(f)}$	$14.6(9.0)^{(f)}$	$72(22)^{(f)}$
N_2	0	$6.6(1.5)^{(d)}$	$11.6(2.6)^{(d)}$	$83(40)^{(d)}$
		$4(2)^{(f)}$	$7.1(2.8)^{(f)}$	$26(10)^{(f)}$
CO_2	0	$5.0(1.6)^{(d)}$	$9.9(3.2)^{(d)}$	$28(15)^{(d)}$
		$4(3)^{(f)}$	$7.9(6.1)^{(f)}$	$22(16)^{(f)}$
CH_4	0	$23(4)^{(d)}$	$33(6)^{(d)}$	$126(71)^{(d)}$
Ar	1	$0.6(0.2)^{(d)}$	$1.2(0.4)^{(d)}$	$10(7)^{(d)}$
		$1.7(0.5)^{(e)}$	$3.3(1.0)^{(e)}$	$40(10)^{(e)}$
		$0.8(0.4)^{(f)}$	$1.6(0.8)^{(f)}$	$20(10)^{(f)}$
He	1	$1.2(0.3)^{(d)}$	$0.9(0.2)^{(d)}$	$24(18)^{(d)}$
		$2.0(0.7)^{(e)}$	$1.5(0.5)^{(e)}$	$30(10)^{(e)}$
		$1.3(0.7)^{(f)}$	$1.0(0.5)^{(f)}$	$21(12)^{(f)}$
H_2	1	$7.4(1.2)^{(d)}$	$4.1(0.7)^{(d)}$	$21(15)^{(d)}$
		$6.6(1.7)^{(f)}$	$3.7(1.0)^{(f)}$	$16(4)^{(f)}$
N_2	1	$1.8(0.2)^{(d)}$	$3.2(0.4)^{(d)}$	$17(13)^{(d)}$
		$1.4(0.4)^{(f)}$	$2.4(0.7)^{(f)}$	$13(4)^{(f)}$
CO_2	1	$0.7(0.3)^{(d)}$	$1.3(0.6)^{(d)}$	$5(4)^{(d)}$
		$1.2(1.4)^{(f)}$	$2.4(2.8)^{(f)}$	$10(12)^{(f)}$
CH_4	1	$3.5(1.0)^{(d)}$	$5.0(1.4)^{(d)}$	$13(10)^{(d)}$

Table 4–5: Rate constants and thermally averaged cross sections for specific transfer from SiCl $B'^2\Delta(v' = 0, 1)$ to $B^2\Sigma^+$.

Numbers in parenthesis represent 2σ uncertainties. a) Specific $B' - X$ transfer rate constant. b) Thermally averaged cross section. c) Fraction of the quenched $B'^2\Delta(v')$ population transferred to the $B^2\Sigma^+$ state expressed as a percentage. d) Values obtained by Singleton [2,3]. e) Values obtained by Jeffries [1]. f) This work.

As can be seen in equation 4.14, to obtain a good value for f_B the partial pressures of the quencher and carrier gases must be well established. Any uncertainties in these values will result in a high uncertainty in the calculated value of this quantity. Unfortunately this turned out to be a significant problem due to the relative instability of the pumping system employed during the course of this work. As discussed in chapter 2, the pump was unable to sustain steady state pressures above $\sim$ 3 Torr for the periods of time required to record the dispersed spectra (20 - 40 minutes). Consequently this resulted in an undesirably high ration of argon to quencher pressures and hence the component of the $B - X$ spectra due to transfer induced purely by the carrier gas was quite significant. Compounding this problem was the fact that the zero stability of the pressure gauge used at this time was poor with an uncertainty of as high as 0.1 Torr.

Hence, most of the f_B values obtained for all quenchers studied had very large uncertainties so that in most cases they were of little or no improvement upon the previous measurements. The derived values for f_B measured in this work are listed in table 4–5 with the equivalent values for the transfer rate constants, k_B, and thermally averaged cross sections, σ_B, obtained from manipulation of the total removal rate constants and cross sections (as discussed in section 4.3.2). Also included for comparison in table 4–5 are the values obtained by Jeffries [1] and Singleton [2,3]. Generally, the different values for the specific-transfer cross sections obtained in the various studies are within experimental error, although in most cases these limits are quite large. The only serious discrepancy occurs in the conflicting f_B values obtained for transfer from $B'^2\Delta, v' = 0$ with N_2 as the quencher. The origin of this anomaly is thought to be the very large uncertainties for the total quenching cross sections obtained in the previous study. The value obtained in the present work, therefore, is probably the more reliable.

The values obtained in these and the previous studies do show that $B'^2\Delta - B^2\Sigma^+$ transfer is efficient, particularly from $v' = 0$. The magnitude of the transfer cross sections can be seen to be highly dependent upon the identity of the quencher species.

4.4.3 Nascent vibrational populations in $B^2\Sigma^+$ following transfer from $B'^2\Delta(v' = 0, 1)$.

Similarly to the SiF studies, it was also possible to derive the relative vibrational populations of the $B^2\Sigma^+ v'' = 0 - 2$ states upon collision-induced transfer. These are the only $B^2\Sigma^+$ vibrational levels which are energetically accessible in this case as can be seen from figure 4–1. The resulting $B - X$ emission spectra could be simulated using spectra obtained from *direct* excitation of the specific $B^2\Sigma^+$ vibrational levels[5]. These spectra, presented in figure 4–20, were used as the basis sets in a least-squares fitting procedure to obtain the *best-fit* simulation of the collision-induced emission spectra.

Unfortunately, the problems encountered in deducing the specific transfer fractions were also applicable in this case due to the contribution of the carrier gas in inducing $B'^2\Delta$ to $B^2\Sigma^+$ transfer. The uncertainties in the partial pressures propagated into large uncertainties in the contribution of each gas to the resulting spectrum. Hence the nascent vibrational populations for the product $B^2\Sigma^+$ state following initial excitation of $B'^2\Delta v' = 0, 1$ in the presence of argon were all that could be evaluated with an acceptable degree of uncertainty. No attempt was therefore made to repeat Singleton's measurements [2] of the vibrational branching ratios for the remaining quencher species as there was no prospect of improved precision.

The *best-fit* simulations can be seen in figures 4–18 and 4–19 respectively. Again the simulations can be seen to match the experimental spectra reasonably well. These distributions are given in table 4–6 and represented graphically in figure 4–21 along with the values obtained by Jeffries [1] and Singleton [2].

Agreement between the three data sets is very good for transfer from $B'^2\Delta v' = 0$ by Ar. For $B'^2\Delta v' = 1$, the new results are in much better agreement with those

---

[5]The $B^2\Sigma^+$ $v' = 0 - 2$ vibrational levels were excited via the $B^2\Sigma^+ - X^2\Pi$, $(v', 0)$ Q_1 band head. The laser excitation spectra from the $B^2\Sigma^+ - X^2\Pi$ spectroscopic study by Singleton [2] allowed identification of the appropriate wavelengths required.

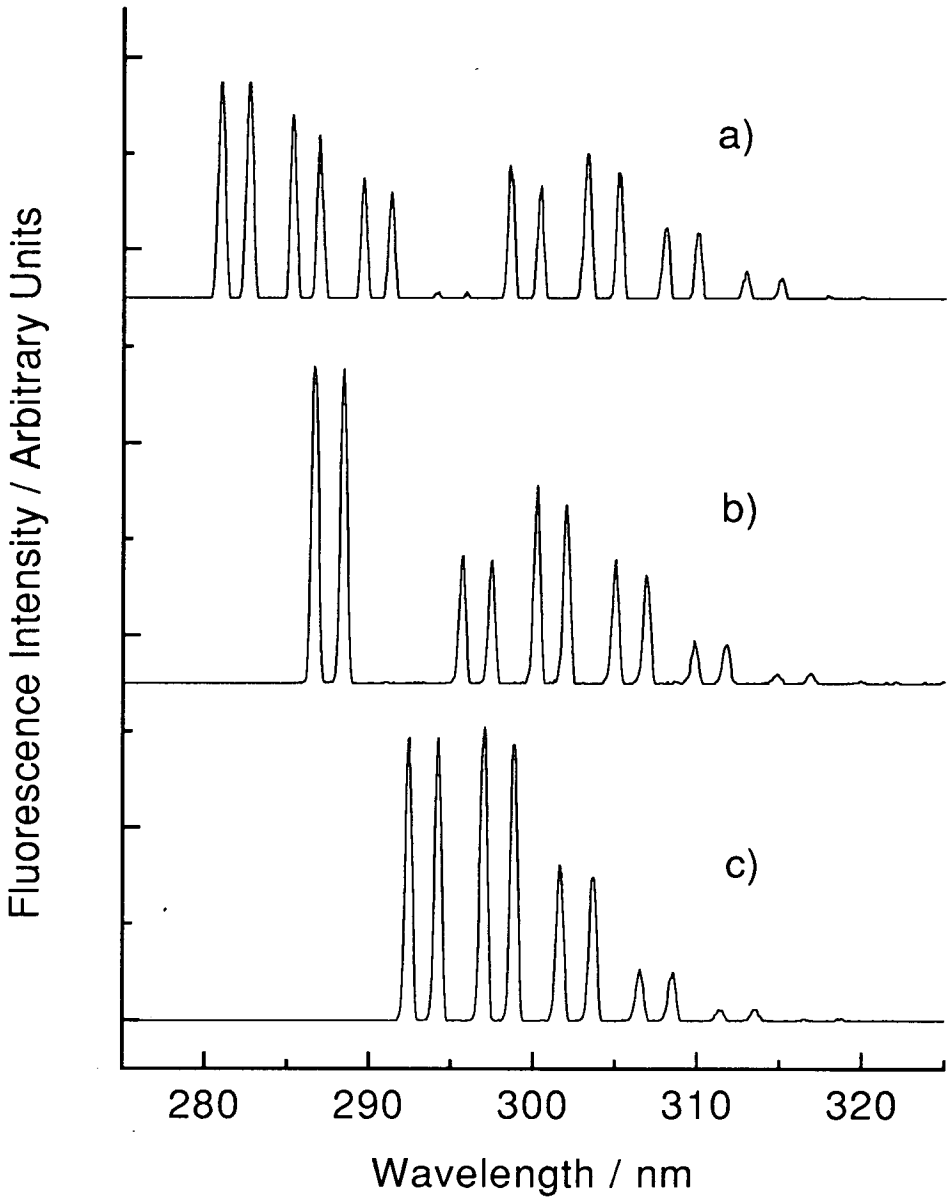

Figure 4–20: Dispersed fluorescence spectra following direct initial excitation of SiCl $B^2\Sigma^+ - X^2\Pi$, $(v', 0)$ Q_1 band heads.

a) v'=2 b) v'=1 c) v'=0.

Gas	$B'^2\Delta(v')$	$v''=0^a$	$v''=1^a$	$v''=2^a$
Ar	0	$9(3)^b$	$27(3)^b$	$64(6)^b$
		13^c	26^c	61^c
		$10(2)^d$	$23(3)^d$	$67(5)^d$
He	0	$9(2)^b$	$60(5)^b$	$31(3)^b$
		11^c	61^c	28^c
H_2	0	$27(2)^b$	$65(4)^b$	$8(1)^b$
N_2	0	$11(1)^b$	$52(5)^b$	$37(4)^b$
CO_2	0	$11(2)^b$	$34(3)^b$	$56(5)^b$
CH_4	0	$71(5)^b$	$12(3)^b$	$17(3)^b$
CF_4	0	$76(4)^b$	$13(2)^b$	$11(1)^b$
Ar	1	$1(1)^b$	$12(3)^b$	$87(12)^b$
		13^c	24^c	63^c
		$6(3)^d$	$22(4)^d$	$72(7)^d$
He	1	$6(2)^b$	$23(4)^b$	$71(9)^b$
		1^c	14^c	85^c
H_2	1	$22(3)^b$	$54(5)^b$	$25(2)^b$
N_2	1	$9(3)^b$	$30(3)^b$	$61(8)^b$
CO_2	1	$21(5)^b$	$49(8)^b$	$30(6)^b$
CH_4	1	$52(5)^b$	$28(3)^b$	$20(4)^b$
CF_4	1	$33(4)^b$	$42(4)^b$	$25(3)^b$

Table 4–6: Nascent vibrational populations in SiCl $B^2\Sigma^+$ following transfer from $B'^2\Delta(v'=0,1)$.

Figures in parenthesis represent 1σ uncertainties as derived from fit. a) Relative $B^2\Sigma^+ v''$ population. b) Results of Singleton [2,3]. c) Results of Jeffries [1]. d) Results from this study. Unconstrained least squares fit.

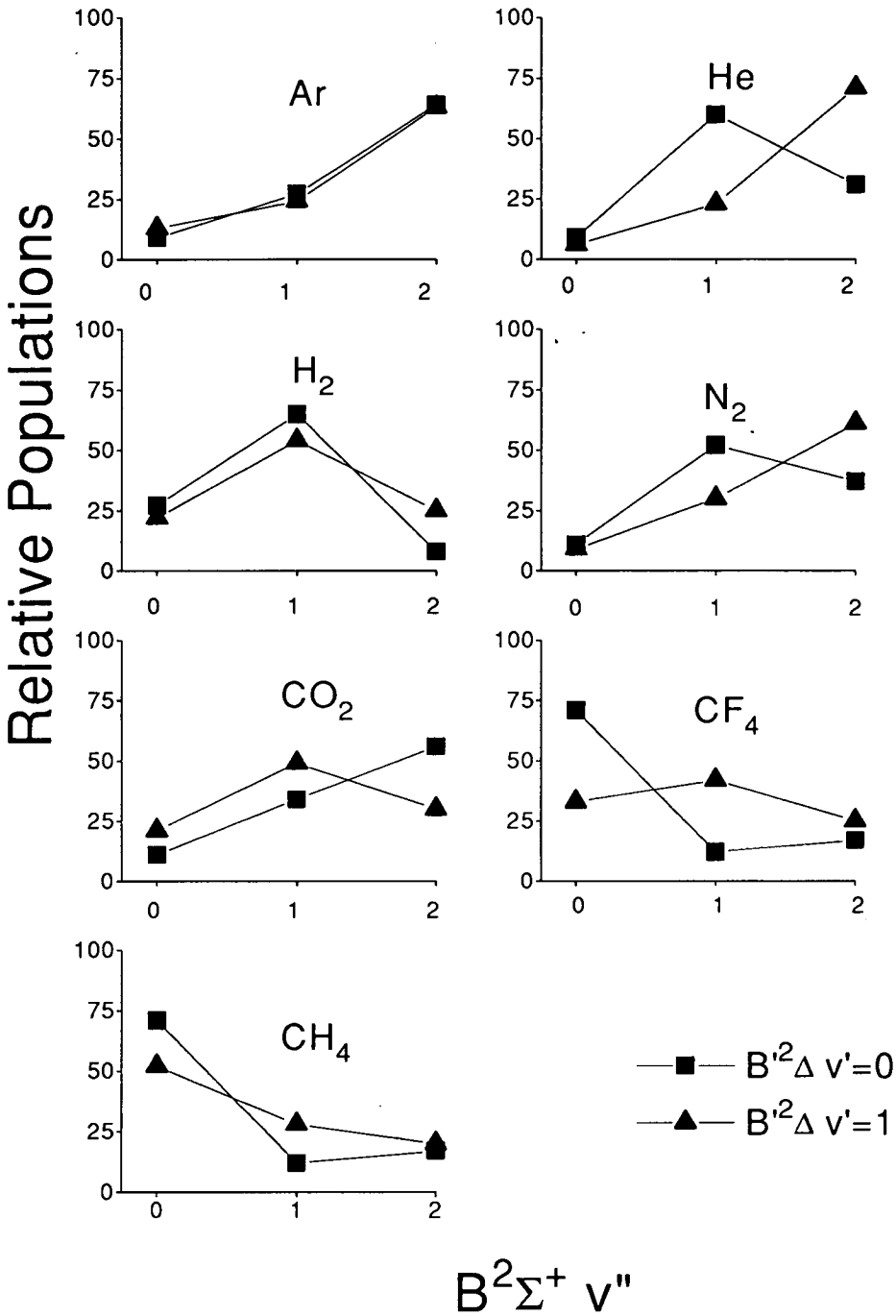

Figure 4–21: Graphic representation of the SiCl $B^2\Sigma^+$ vibrational populations resulting from collisional transfer by each quenching gas from $B'^2\Delta v' = 0$ and 1 as indicated in figure.

Results presented are from Singleton [2] with the exception of the present data for argon.

of Jeffries [1] than of Singleton [2]. The distributions reported in the previous work can be seen to be highly quencher dependent with no obvious correlation between them and any molecular parameter. Obviously, as the distributions are dependent upon the identity of the quencher, there can be no correlation between them and the $B'^2\Delta - B^2\Sigma^+$ Franck-Condon factors.

There does appear to be a rough correlation between the average vibronic energy removed ΔE and the complexity of the collision partner in that the polyatomic species CH_4 and CF_4 remove more energy than the other species, particularly the noble gases. The average amount of energy removed during transfer from $B'^2\Delta$, $v' = 0$ ranges from roughly 300 cm^{-1} to around 1200 cm^{-1}. From $B'^2\Delta$, $v' = 1$, ΔE varies from 600 cm^{-1} to over 1400 cm^{-1}. However the difference between the average energies removed from $v' = 0$ and 1 depends on the quencher and spans a range from 200 cm^{-1} to over 700 cm^{-1} which is comparable to the extra 500 cm^{-1} vibrational energy in $v = 1$.

4.5 Conclusions

The conclusions that can be drawn directly from the results reported in this chapter are:

1. The radiative lifetimes of the SiF $C^2\Delta v' = 0, 1$ states have both been shown to be 94 ± 2 ns whereas the lifetime of the SiF $B^2\Sigma^+$ state has been estimated to be $\leq$ 10 ns.

2. Collisional removal of SiF $C^2\Delta v' = 0, 1$ is efficient for the molecular quenchers H_2, N_2, CO_2 and CH_4 but is negligible for Ar and He. Thermally averaged cross sections are comparable for N_2, CO_2 and CH_4, but H_2 is significantly more efficient for quenching both $C^2\Delta, v' = 0$ and 1.

3. A small but variable fraction of the collisionally removed SiF $C^2\Delta$ molecules are transferred to the nearby $B^2\Sigma^+$ state as a result of collisions with H_2, N_2

and CH_4. No $B^2\Sigma^+ - X^2\Pi$ emission was observed in the presence of CO_2 or, unsurprisingly, Ar and He.

4. The SiF $B^2\Sigma^+$ product vibrational distributions are largely independent of the identity of the quencher species, although small reproducible differences were found. Collision-induced transfer occurs mostly over vibronic energy gaps of $\sim$ 5000 cm^{-1}. These distributions correlate well with the Franck-Condon overlap between the initial and final vibronic levels.

5. The SiCl $B'^2\Delta v' = 0, 1$ states are removed efficiently by all collision partners studied. Remeasured quenching cross sections compared well with previously reported results and are of the same order of magnitude as the equivalent values for the SiF $C^2\Delta$ state quenchers.

6. A large, but quencher dependent, fraction of the SiCl $B'^2\Delta$ state molecules are transferred to the $B^2\Sigma^+$ state. Transfer is generally more efficient from $B'^2\Delta v' = 0$ than $v' = 1$.

7. The vibrational distributions in the SiCl $B^2\Sigma^+$ product states, as shown by Singleton [2], are highly dependent upon the identity of the quenching species and the initial vibrational level. These do not correlate with any obvious molecular parameter.

The mechanistic implications of the observations reported in this chapter for the $^2\Delta - ^2\Sigma^+$ transfer processes will be discussed in chapter 6.

Bibliography

[1] J.B. Jeffries, J. Chem. Phys. **95** (1991) 1628.

[2] S. Singleton, Laser Based Studies of Transient Species in a Discharge Flow Apparatus, PhD Thesis, University of Edinburgh, (1990).

[3] S. Singleton and K.G. McKendrick, J. Phys. Chem. **97** (1993) 1389.

[4] H. Bredohl, P. Demoulin, Y. Houbrechts and F. Mélen, J. Phys. B. **14** (1981) 1771.

[5] G. Meijer, B. Jansen, J.J. Ter Mullen and A. Dynamus, Chem. Phys. Lett., **136** (1987) 519.

[6] Y. Houbrechts, I. Dubois and H. Bredohl, J. Phys. B. **13** (1980) 3369.

[7] G. Meijer, W. Ubachs, J.J. Ter Mullen and A. Dynamus, Chem. Phys. Lett., **139** (1987) 603.

[8] P.R. Bevington, Data Reduction and Error Analysis for the Physical Sciences (McGraw-Hill, New York, 1969) 204.

[9] J.T. Yardley, Introduction to Molecular Energy Transfer (Academic Press, New York 1980).

[10] S. Singleton, K.G. McKendrick, R.A. Copeland and J.B. Jeffries, **96** (1992) 9703.

[11] K.P. Huber and G. Herzberg, Molecular Spectra and Molecular Structure: Constants of Diatomic Molecules (Van Nostrand, London, 1979)

Chapter 5

Rotational Effects in SiF $C^2\Delta - B^2\Sigma^+$ Collisional Transfer

5.1 Introduction

The previous chapter dealt with collision-induced $^2\Delta - ^2\Sigma^+$ transfer where the only experimental variables were the initial $^2\Delta$ state vibrational level and the identity of the collision partner. It is possible to extract more information about the transfer event by examining any differential behaviour which occurs as a result of varying the initial rotational energy of the $^2\Delta$ state molecules.

The study by Singleton [1,2] included a preliminary experimental study of the rotational effects of the SiCl $B'^2\Delta - B^2\Sigma^+$ transfer system. The main conclusions of this study were:

1. Excitation of the $B'^2\Delta - X^2\Pi$ Q_1 bandhead results in the observation of a near-thermal rotational distribution of the $B'^2\Delta$ state within its radiative lifetime, as judged from dispersing the directly excited $B'^2\Delta - X^2\Pi$ fluorescence.

2. Transfer from the $B'^2\Delta$ state results in a near thermal rotational distribution of approximately 300K in the $B^2\Sigma^+$ product state, determined from dispersion of the corresponding indirectly produced $B^2\Sigma^+ - X^2\Pi$ emission.

3. Direct laser excitation of the $B^2\Sigma^+$ state resulted in a rotationally unrelaxed distribution equivalent to that of the initially populated levels, again determined from observation of the dispersed $B^2\Sigma^+ - X^2\Pi$ fluorescence.

The results reported in this chapter are perhaps of a more preliminary nature than those described previously in chapters 3 and 4. This is mainly the result of the limited time available in which the experiments could be performed. However, this study did provide some very interesting provisional results, several of which warrant further, more detailed future investigations. Of perhaps the greatest significance, results are reported of the propensities in the change in J as a result of collision-induced rovibronic transfer. The total quenching rates, the electronic branching fraction and the $B^2\Sigma^+$ vibrational product distributions have been also examined as a function of the initial rotational energy, J', of the SiF $C^2\Delta, v' = 0$ state.

In the preceding chapters all energy transfer experiments had been performed following the initial laser excitation of the intense Q head feature of the SiF $C^2\Delta - X^2\Pi_{\frac{1}{2}}(v', 0)$ transition. This corresponds to the excitation of two different branches, the Q_1 and ${}^QP_{21}$. For reasons discussed in chapter two, these branches are virtually coincident in energy where $Q_1(J') = {}^QP_{21}(J' - 1)$ [3]. This is illustrated in figure 3–4. Consequently, excitation of this feature results in the initial population of $C^2\Delta_{\frac{3}{2}}(J' \approx 10.5 - 15.5)$ and $C^2\Delta_{\frac{5}{2}}(J' \approx 9.5 - 14.5)$ states. The rotational line-strength calculations, performed as described in section 3.5.1, predicted that the population ratio of the spin-orbit states, $\frac{\Omega=3/2}{\Omega=5/2}$ will be about 3:1. However, in these experiments the laser output was optimised to ensure maximum upper state population and therefore this ratio is likely to be reduced due to the effects of optical saturation.

The ideal experiment from which to obtain unambiguous information about the rotational effects in the transfer system would require the population of single J''s in the $C^2\Delta$ state prior to collision. Unfortunately, due to the congestion of spectral lines, this was not possible for a large number of rotational levels. This problem is illustrated in figure 5–1 which shows a simulation of the $C^2\Delta - X^2\Pi_{\frac{1}{2}}(0, 0)$ excitation spectrum. The simulation was performed with a band-width equivalent

to that of the experiment with the result that the majority of the spectral peaks can be seen to be combinations of two or more transitions types. Thus laser excitation at these wavelengths will lead to population of a range of different J''s.

It can, however, be seen that the P_1 branch, shown in more detail in figure 5–2, is spectroscopically isolated from the other transitions. The spectral lines to low wavelength are effectively the result of one specific (J', J'') transition, ignoring the unresolved splitting into two lines caused by the *Lambda*-doubling of both the $X^2\Pi$ and $C^2\Delta$ states. Hence they may be utilised to produce a well defined initial $C^2\Delta_{\frac{3}{2}}$ state rovibrational population. The P_1 bandhead, which forms at approximately $J' = 34$, could also be exploited as a route to producing an initial J' distribution ranging approximately between 32.5 and 38.5.

To populate higher rotational levels in the $C^2\Delta, v' = 0$ state, it was necessary to examine the blue extreme of the excitation spectrum. In figure 5–3 it is apparent that in this region, the ${}^SR_{21}$ transitions become sufficiently isolated to allow population of specific rotational levels. Unfortunately, it can also be seen that these transitions are very weak, simply due to the low population of the high rotational levels in the $X^2\Pi$ state.

5.2 Rotational energy transfer within the SiF $C^2\Delta$, $v' = 0$ state

Although excitation on specific rovibronic transitions would initially produce a well defined rotational distribution in the $C^2\Delta$ state, there remained the possibility that this distribution would be distorted by intermolecular collisions prior to the transfer event. If this redistribution resulted in a thermal distribution regardless of which initial levels were populated, it would be impossible to determine any differential rotational effects using the existing experimental procedure.

To determine whether the proposed experiments were valid, it was necessary to examine any collision-induced rotational relaxation within the $C^2\Delta$ state. This

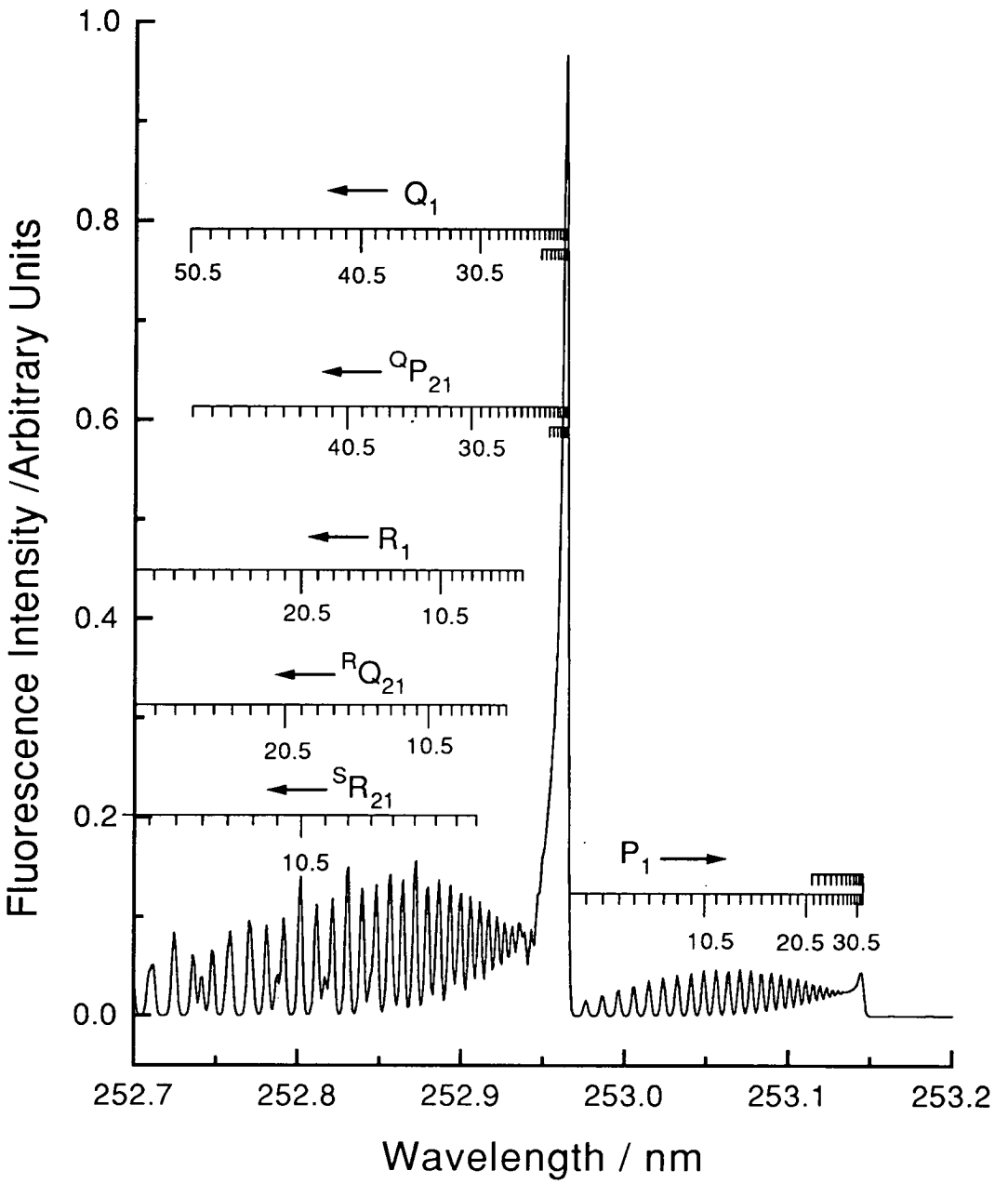

Figure 5–1: Simulation of the $C^2\Delta - X^2\Pi_{\frac{1}{2}}$ $(0,0)$ excitation spectrum. Simulation performed with a band-width of 0.4 cm^{-1}. The spin-orbit splitting constant is equivalent to 4B (as discussed in section 3–4). Excited J' values as indicated on the plot.

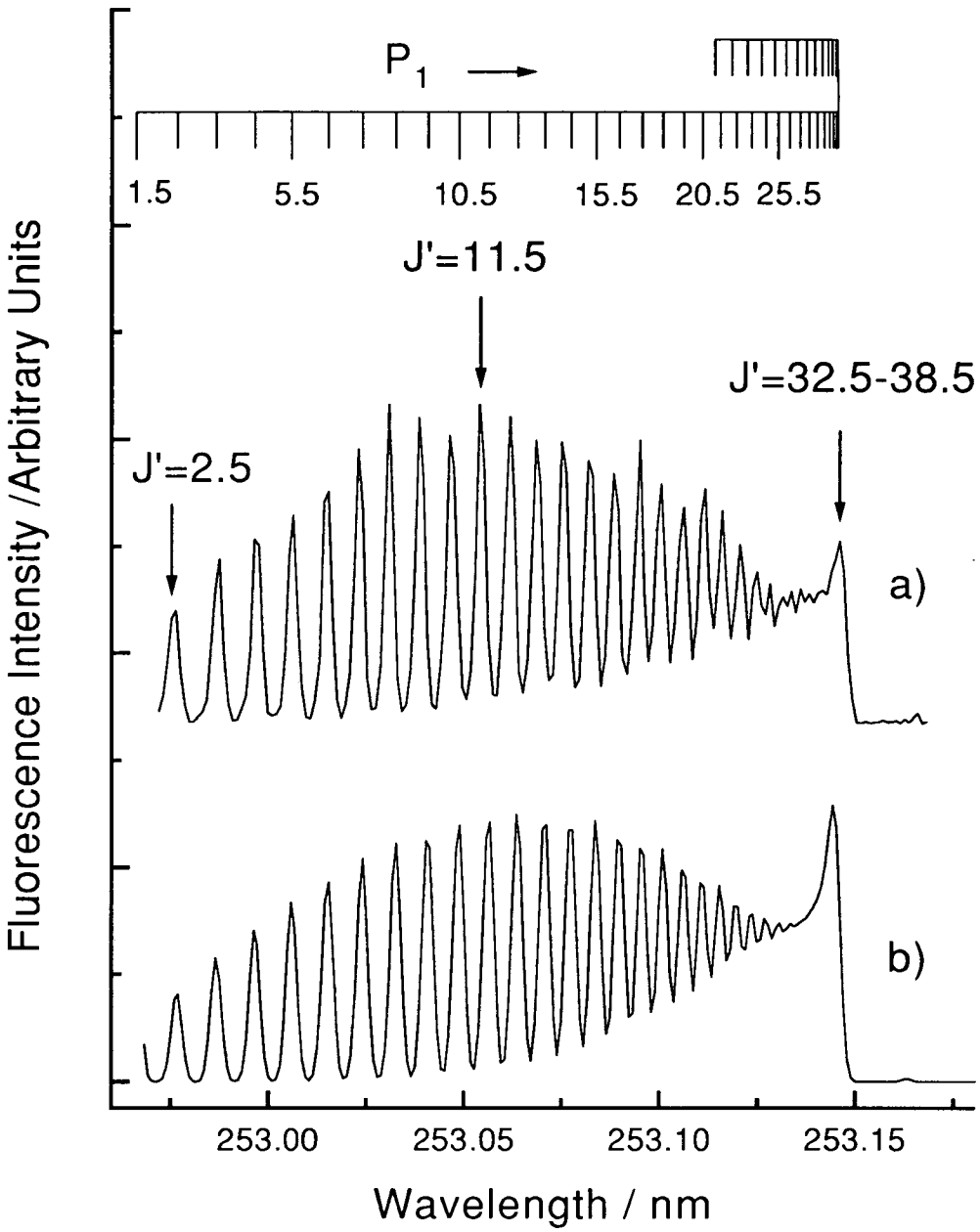

Figure 5–2: Excitation spectrum of the $C^2\Delta - X^2\Pi_{\frac{1}{2}}$ P_1 branch.
a) Experimental. b) Simulation.
Vertical arrows indicate laser wavelengths used in section 5.4.1. Excited J' values as indicated on the plot.

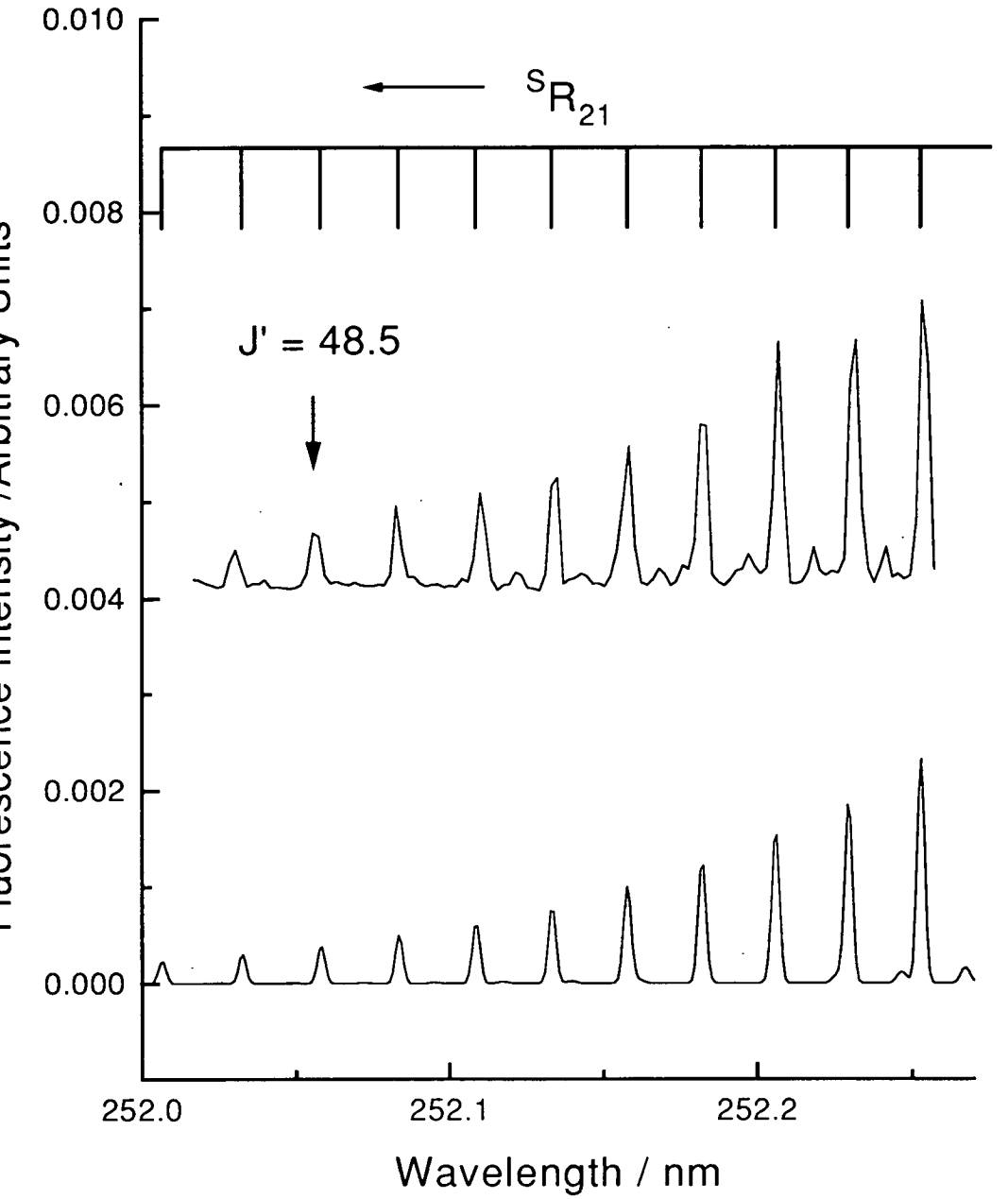

Figure 5–3: 'Blue' region of the $C^2\Delta - X^2\Pi_{\frac{1}{2}}$ $(0,0)$ excitation spectrum. a) Experimental b) Simulation. The majority of fluorescence is the result of excitation of $^SR_{21}$ transitions as indicated on the plot. The vertical arrow indicates the laser excitation wavelength for the experiment performed in section 5.4.1.

was achieved by tuning the excitation laser wavelength in turn to the Q_1 and P_1 bandheads of the $C^2\Delta - X^2\Pi_{\frac{1}{2}}(0,0)$ transition while recording the resultant fluorescence of the $C^2\Delta - X^2\Pi_{\frac{3}{2}}(0,0)$ transition. Hence, the detection of directly scattered laser radiation could thus be avoided. These particular features were chosen not only because they were relatively strong but, more importantly, they result in very different initial $C^2\Delta$ state rotational distributions as discussed above.

Higher resolution measurements than those previously performed were required to extract maximum information about the relative rotational populations from the fluorescence spectra. The monochromator slit widths were thus reduced to a minimum while still allowing an appreciable signal size. The monochromator was operated at the lowest possible scanning speed to allow the maximum number of laser shots per spectrum and the signal was collected by gating over the entire decay profile. The signal-to-noise ratio was further increased by taking the average spectrum of at least five different spectra recorded under essentially identical conditions.

The spectra resulting from Q_1 and P_1 bandhead excitation in the presence of argon are presented in figures 5–4a and 5–5a, respectively. It is immediately apparent from the distinct contrast between the two spectra that the rotational energy distributions must differ significantly. Thus, to a first approximation, it has been demonstrated that there is substantial retention of the initially excited rotational distribution prior to fluorescence.

To obtain a more quantitative picture of the emitting rotational distributions it was necessary to simulate these fluorescence spectra. A computer program was therefore written to synthesise a spectrum for any given rotational distribution: this incorporated the spectroscopic linestrengths, $S_{J'J''}$, calculated as described in section 3.5.1. The simulations were performed by firstly calculating the distribution of the initially excited rotational levels and using this as the program input. The relative population of the upper state, $N_{J'}$, was approximated by a simplification of the Einstein equation for stimulated absorption

$$N_{J'} \propto N_{J''} S_{J'J''} \rho(\nu) \quad . \tag{5.1}$$

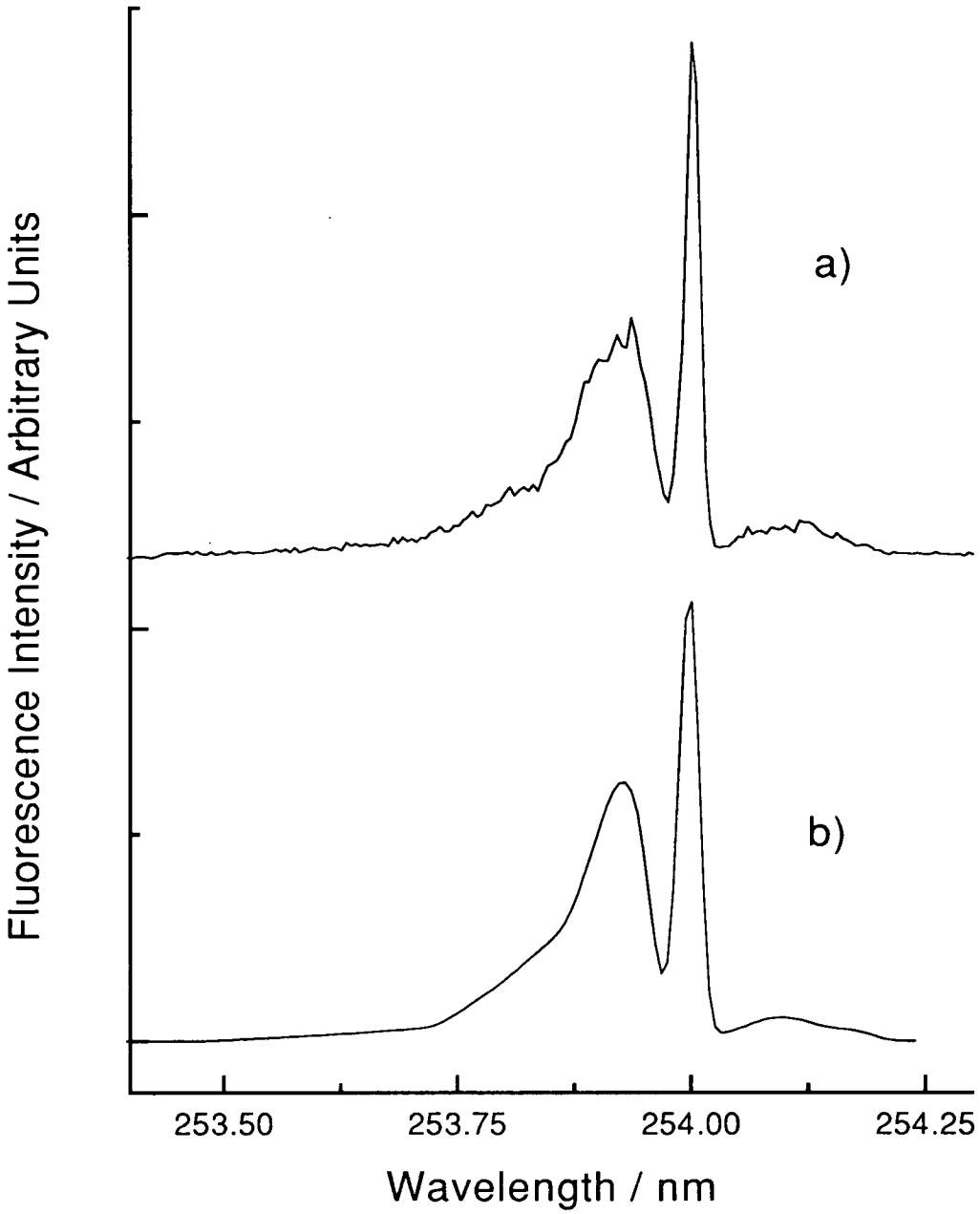

Figure 5–4: High resolution spectrum of the $C^2\Delta - X^2\Pi_{\frac{3}{2}}$ $(0,0)$ transition recorded after excitation of the $C^2\Delta - X^2\Pi_{\frac{1}{2}}$ $(0,0)$ Q_1 bandhead.

a) Average of five experimental spectra recorded with 2.5 Torr of Ar.

b) Simulation performed as described in section 5.2, assuming equal populations of $^2\Delta_{\frac{3}{2}}$ and $^2\Delta_{\frac{5}{2}}$ spin-orbit states.

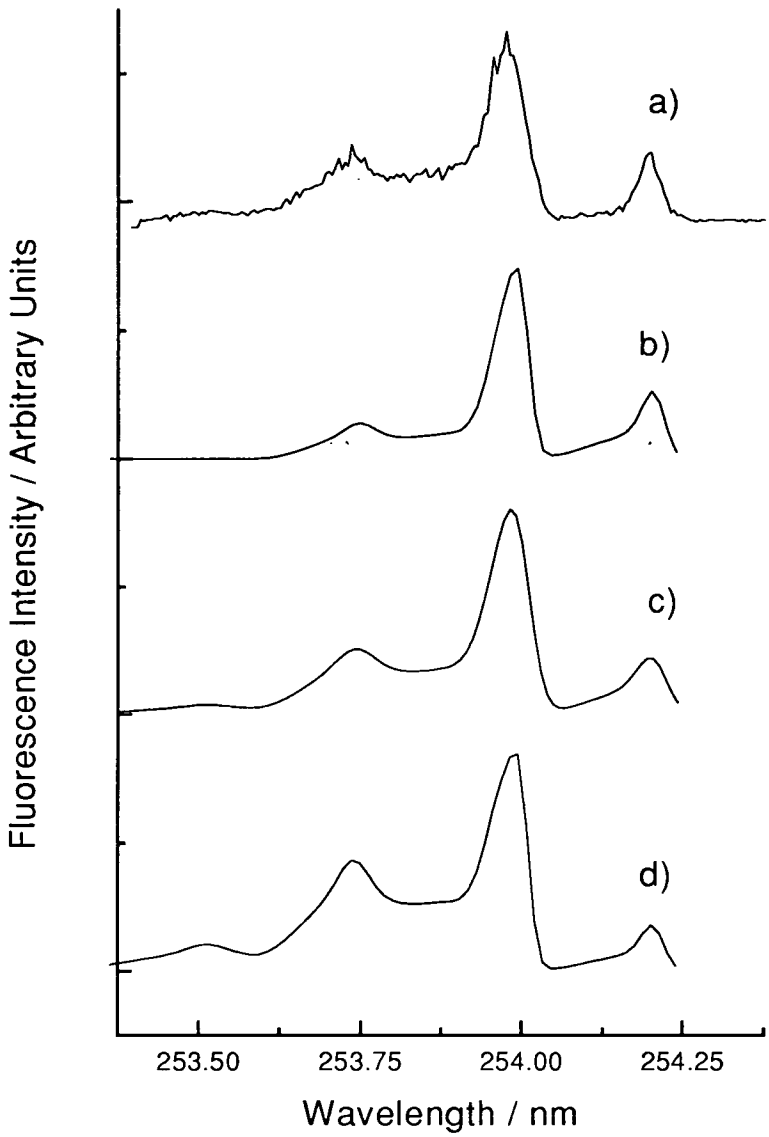

Figure 5–5: High resolution spectrum of the $C^2\Delta - X^2\Pi_{\frac{3}{2}}$ $(0,0)$ recorded after excitation of the $C^2\Delta - X^2\Pi_{\frac{1}{2}}$ $(0,0)$ P_1 bandhead.

a) Average of five experimental spectra recorded with 2.5 Torr of Ar.

b) Simulation performed as described in section 5.2, including unequal contributions from $^2\Delta_{\frac{3}{2}}$ and $^2\Delta_{\frac{5}{2}}$ spin-orbit states.

c) Simulation assuming all molecules in the $C^2\Delta_{\frac{3}{2}}$ state and the same J' distribution as derived for (b).

d) Simulation assuming equal population in the the $C^2\Delta_{\frac{3}{2},\frac{5}{2}}$ spin-orbit states.

The laser intensity profile, $\rho(\nu)$, was assumed to be approximately gaussian and the rotational distribution in the $X^2\Pi$ state was assumed to follow the Boltzmann distribution, with a sample temperature of 300 K, where

$$\frac{N_{J''}}{N_0} = \frac{g_{J''}}{g_0} exp \frac{-(E_{J''} - E_0)}{kT} \tag{5.2}$$

and $g_{J''}$ is the degeneracy of the J''th level. This approximation obviously ignores the possibility of optical saturation.

Unfortunately, it was immediately apparent that the calculated J' distributions, shown in figure 5–6, did not adequately model the experimental spectra. The obviously broader range of J' in the experimental spectra, indicated by fluorescence from J''s definitely not initially populated, implies that a significant degree of rotational relaxation was occurring. It was therefore necessary to adopt an alternative procedure of manually varying the J' rotational distribution iteratively until a satisfactory match, by eye, was achieved. This was fairly straightforward procedure simulating the fluorescence produced after excitation of the Q_1 bandhead as can be seen from the quality of the accompanying simulation, also shown in figure 5–4b.

Laser excitation of the Q_1 bandhead results in simultaneous excitation of the ${}^QP_{21}$ bandhead. In figure 3–6 it can be seen that the Q_1 transition results in population of the $C^2\Delta_{\frac{3}{2}}$ spin-orbit state whereas the ${}^QP_{21}$ transition results in population of $C^2\Delta_{\frac{5}{2}}$. Although the majority of the initially excited molecules will be in the $C^2\Delta_{\frac{3}{2}}$ state, due to the relative line-strengths, a significant fraction will reside in the $C^2\Delta_{\frac{5}{2}}$. The disparity between the relative initial populations of the spin-orbit states will, however, be reduced due to saturation effects caused by the high excitation laser powers used in this experiment. In fact, the simulation in figure 5–4 assumed equal population of the two spin-orbit states and was shown to adequately match the experimental spectrum. The relative rotational populations used for the simulation are illustrated in figure 5–6a which can compared to the predicted initial J' populations in figure 5–6b.

Initially it proved impossible to reproduce the analogous spectrum produced by P_1 bandhead excitation by assuming equal population of the $C^2\Delta$ spin-orbit

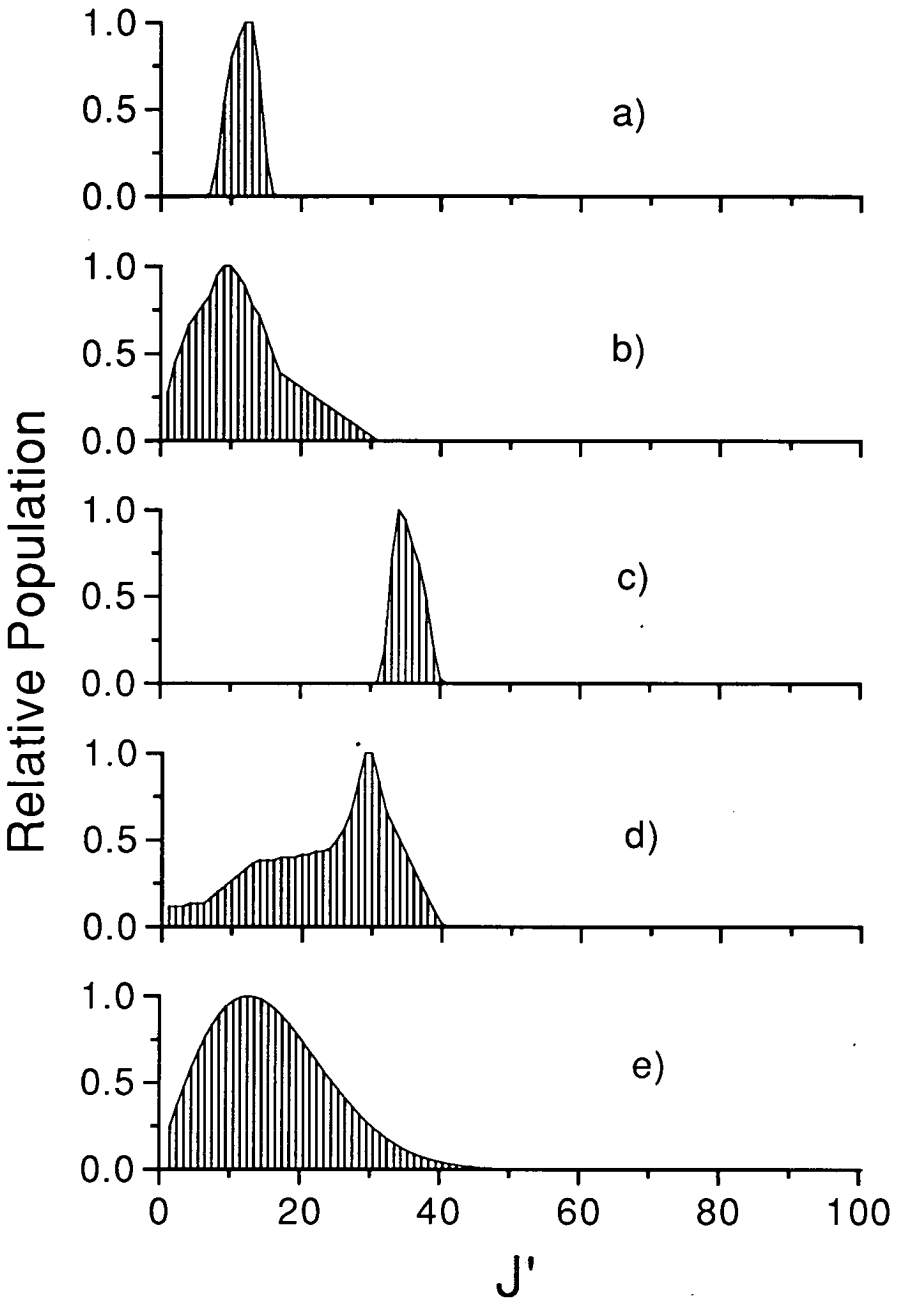

Figure 5–6: Rotational distributions in the $C^2\Delta$ state used to simulate the $C^2\Delta - X^2\Pi_{\frac{3}{2}}$ fluorescence after excitation of the of relevant bandheads:

(a) Predicted population following excitation of $Q_1 + {}^QP_{21}$

(b) Fit to experiment following excitation of $Q_1 + {}^QP_{21}$

(c) Predicted population following excitation of P_1

(d) Fit to experiment following excitation of P_1

(e) Predicted 300 K thermal distribution.

states. The origin of this problem is because excitation of the P_1 bandhead results *exclusively* in initial population of the $C^2\Delta_{\frac{3}{2}}$ state. It was therefore necessary to introduce a further variable, the population ratio of the $C^2\Delta_{\frac{3}{2}}/C^2\Delta_{\frac{5}{2}}$ spin-orbit states, to obtain a simulation which satisfactorily reproduced the spectrum following the P_1 bandhead excitation. The program was therefore adjusted to allow for differential population of the two spin-orbit states although it was still assumed that their rotational distributions were the same. In the event, a $C^2\Delta_{\frac{5}{2}}$ contribution of approximately 20% was required in order to achieve a reasonable simulation of the experiment as can be seen in figure 5–5b. This simulation can be compared to the predicted spectra for the hypothetical cases where either all molecules were in the $C^2\Delta_{\frac{3}{2}}$ state (figure 5–5c) or there is equal population in the $\Omega = \frac{3}{2}, \frac{5}{2}$ spin-orbit states (figure 5–5d). It is thus apparent that spin-orbit, (Ω), changing collisions are efficient and must be taken into consideration. The derived rotational distribution is also shown in figure 5–6b.

A further preliminary experiment was performed to indicate whether the species which are efficient at electronic quenching may result in greater thermalisation of the $C^2\Delta$ state rotational distribution than the Ar carrier. The Q_1 bandhead was excited as before but with the introduction of a large partial pressure of H_2 gas. As can be seen in figure 5–7, the resulting spectrum is almost identical to that produced when only the carrier gas was present, thus indicating a similar rotational distribution to that shown in figure 5–6a.

Due to the resolution of the spectra, the derived $C^2\Delta, J'$ populations presented in figure 5–6 should be treated on a semi-quantitative basis. However, it can be stated that although there are significant modifications of the J' distributions due to rotationally inelastic collisions prior to fluorescence, to a reasonable extent the majority of molecules are in approximately the same rotational levels as those initially populated. Thus population of specific rotational levels would appear to result in a distribution characteristic of the initially populated levels. It is therefore possible to extract meaningful information about any J' dependence in the SiF $C^2\Delta$ to $B^2\Sigma^+$ transfer system using the existing experimental procedure.

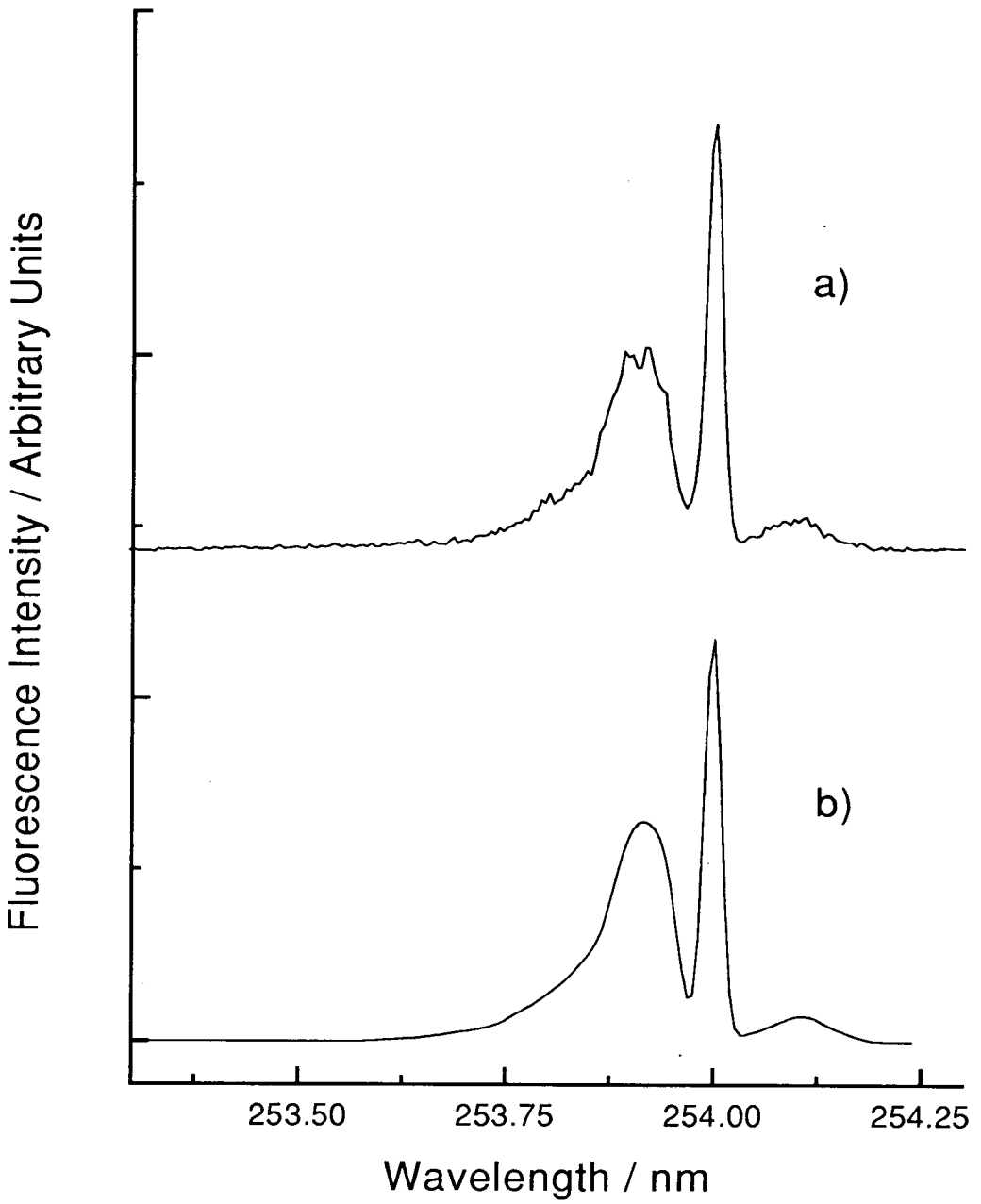

Figure 5–7: High resolution spectrum of the $C^2\Delta - X^2\Pi_{\frac{3}{2}}$ $(0,0)$ transition recorded after excitation of the $C^2\Delta - X^2\Pi_{\frac{1}{2}}$ $(0,0)$ Q_1 bandhead in the presence of H_2.

a) Average of five experimental spectra recorded with 1.5 Torr Ar + 1 Torr H_2.

b) Simulation performed as described in section 5.2.

5.3 ΔJ Propensities upon SiF $C^2\Delta$,$v' = 0$ to $B^2\Sigma^+$, v'' Interstate Transfer.

In section 4.3.3, the low resolution study of the collision induced $B^2\Sigma^+ - X^2\Pi(0,0)$ fluorescence band revealed that the intensity profile could only be simulated by using a high temperature Boltzmann rotational distribution in the $B^2\Sigma^+$ state. It was this intriguing preliminary result that prompted the more detailed investigation described below.

To obtain more quantitative information on the $B^2\Sigma^+$ product state distribution a similar experiment to that described in the previous section was performed with the exception that fluorescence was recorded over the $B^2\Sigma^+ - X^2\Pi_{\frac{1}{2},\frac{3}{2}}(0,0)$ transitions. The $C^2\Delta - X^2\Pi_{\frac{1}{2}}(0,0)$ Q_1 and P_1 bandheads were excited respectively in the presence of H_2 or N_2. The resultant averaged spectra are presented in figures 5–8 to 5–11 with the *best-fit* simulations which were obtained in the same manner as those in the previous section. The derived $B^2\Sigma^+$ J' distributions, used to produce the simulated spectra, are presented in figure 5–12 in comparison with the relevant approximate $C^2\Delta$ state rotational distributions, derived from the total integrated $C - X$ emission.

Due to the poor signal-to-noise ratios of the spectra it is again difficult to make more than qualitative statements concerning the ΔJ propensities upon transfer. The relatively low resolution of the experimental spectra resulted in the appearance of the simulated spectra being fairly insensitive to the details of the input J' distribution. Different distributions which showed the same basic form resulted in the simulations which were difficult to differentiate between by eye. It can be seen, however that the resultant $B^2\Sigma^+$ distributions undoubtedly differ dramatically from those of the $C^2\Delta$ state rotational distributions, derived from the total integrated $C - X$ emission. Unlike the low resolution spectra, no Boltzmann distribution with a single rotational temperature was found to produce a reasonable simulation of these *high resolution* collision-induced spectra. This is further indicative of a dynamically controlled single collision process.

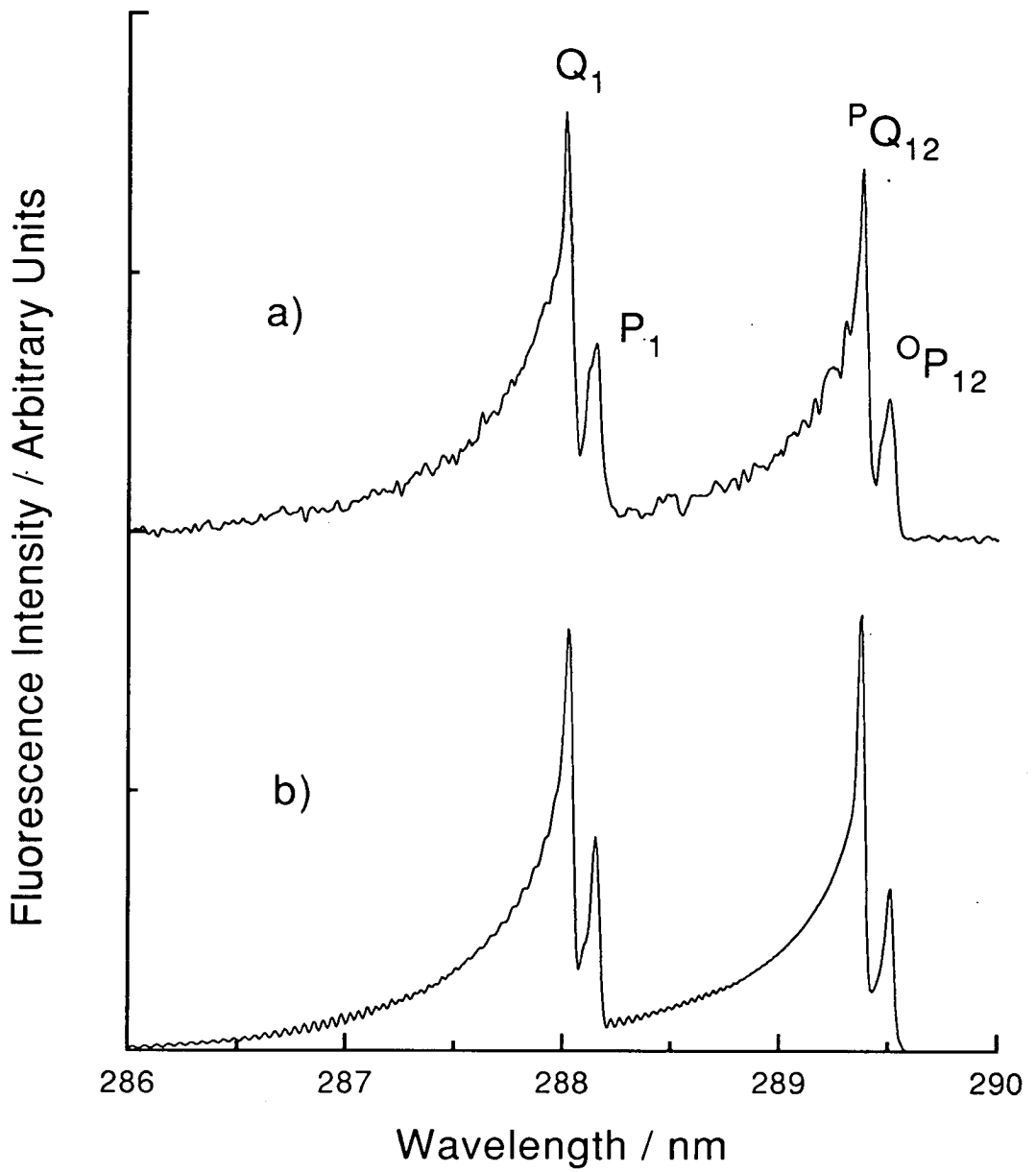

Figure 5–8: High resolution spectrum of the collision-induced $B^2\Sigma^+ - X^2\Pi$ (0,0) band recorded after excitation of the $C^2\Delta - X^2\Pi_{\frac{1}{2}}$ (0,0) Q_1 bandhead.

a) Average of five experimental spectra recorded with 1.5 Torr Ar + 1 Torr H_2.

b) Simulation performed as described in section 5.2, assuming a resolution of 0.04 nm, chosen to match that of the experiment.

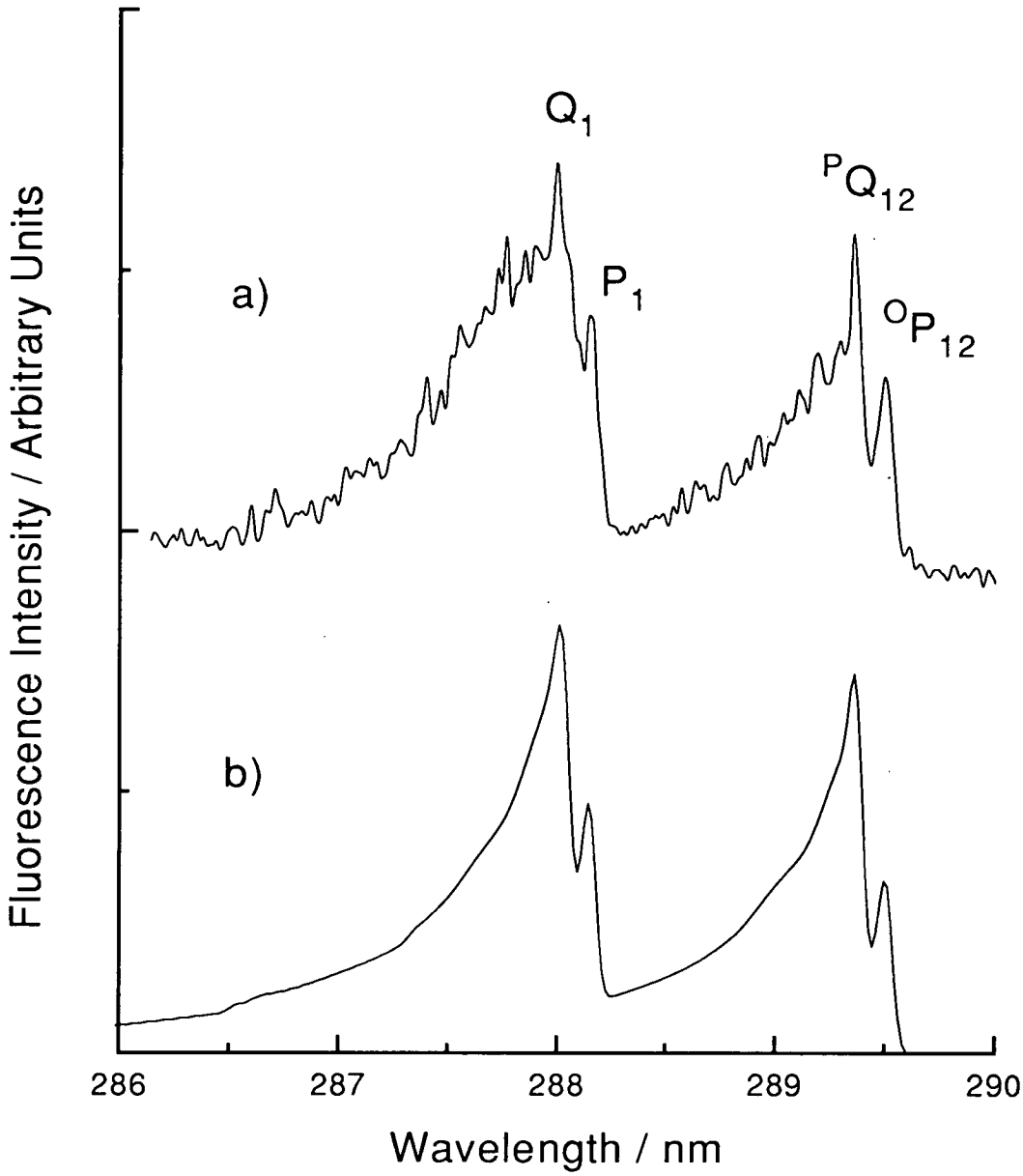

Figure 5–9: High resolution spectrum of the collision-induced $B^2\Sigma^+ - X^2\Pi$ (0,0) band recorded after excitation of the $C^2\Delta - X^2\Pi_{\frac{1}{2}}$ (0,0) P_1 bandhead.

a) Average of five experimental spectra recorded in 1.5 Torr Ar + 1 Torr H_2.

b) Simulation performed as described in section 5.2, assuming a resolution of 0.08 nm, chosen to match that of the experiment.

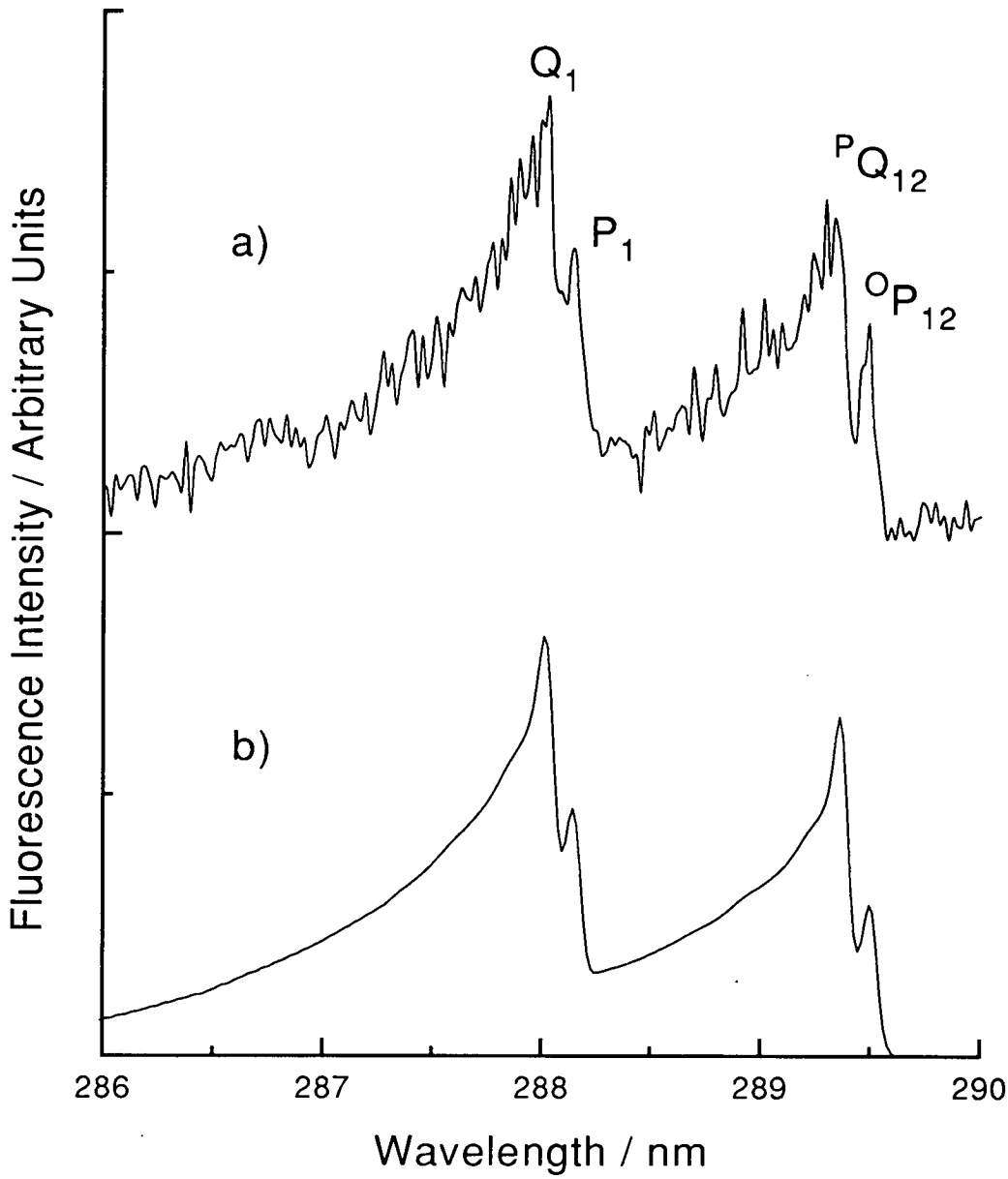

Figure 5–10: High resolution spectrum of the collision-induced $B^2\Sigma^+ - X^2\Pi$ $(0,0)$ band recorded after excitation of the $C^2\Delta - X^2\Pi_{\frac{1}{2}}$ $(0,0)$ Q_1 bandhead.

a) Average of five experimental spectra recorded in 1.5 Torr Ar + 1.5 Torr N_2.

b) Simulation performed as described in section 5.2, assuming a resolution of 0.08 nm, chosen to match that of the experiment.

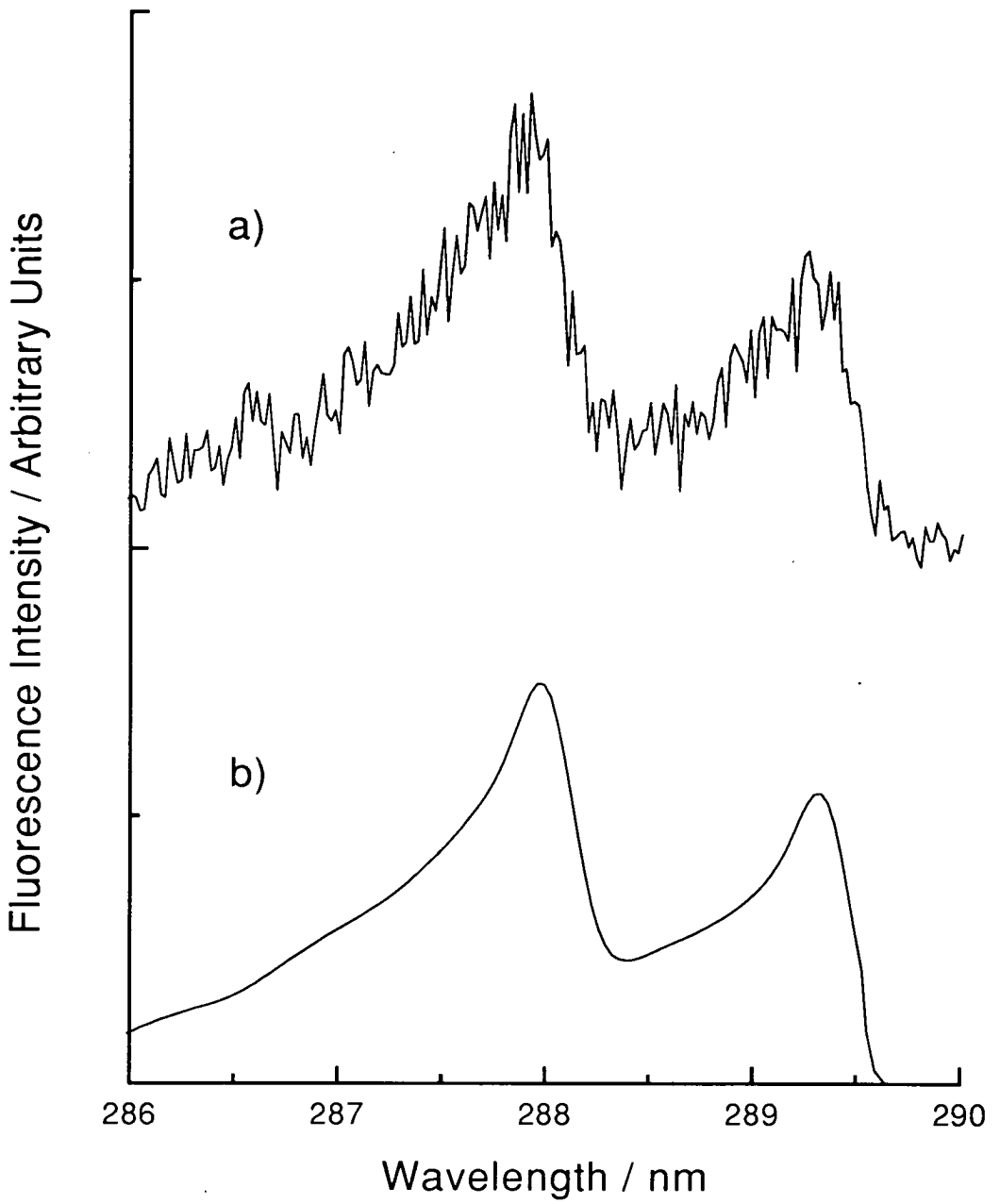

Figure 5–11: High resolution spectrum of the collision-induced $B^2\Sigma^+ - X^2\Pi$ $(0,0)$ band recorded after excitation of the $C^2\Delta - X^2\Pi_{\frac{1}{2}}$ $(0,0)$ P_1 bandhead.

a) Average of five experimental spectra recorded in 1.5 Torr Ar + 1.5 Torr Torr N_2.

b) Simulation performed as described in section 5.2, assuming a resolution of 0.25 nm, chosen to match that of the experiment.

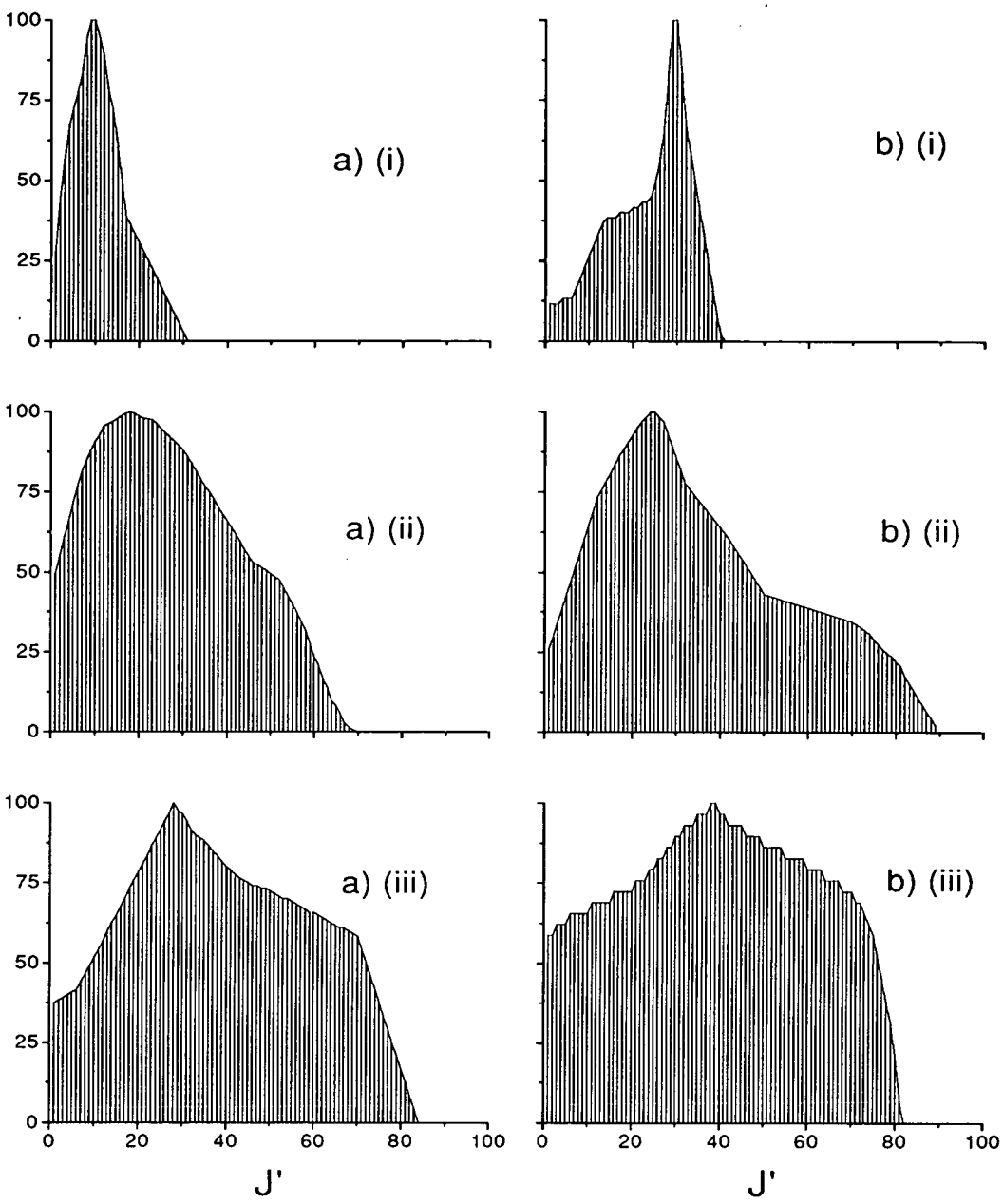

Figure 5–12: Rotational distributions used to simulate the $C^2\Delta - X^2\Pi_{\frac{3}{2}}$ and $B^2\Sigma^+ - X^2\Pi_{\frac{1}{2},\frac{3}{2}}$ fluorescence after excitation of the $C^2\Delta - X^2\Pi_{\frac{1}{2}}$ bandheads:
a) Q_1 and b) P_1 excitation followed by observation of:
(i) $C^2\Delta - X^2\Pi_{\frac{3}{2}}$ in 2.5 Torr Ar
(ii) $B^2\Sigma^+ - X^2\Pi_{\frac{1}{2},\frac{3}{2}}$ with 1 Torr H_2
(iii) $B^2\Sigma^+ - X^2\Pi_{\frac{1}{2},\frac{3}{2}}$ with 1.5 Torr N_2

The distributions derived from the spectra where H_2 was the quencher species represent perhaps the more reliable data set. This was due to both the greater $B^2\Sigma^+$ to $X^2\Pi$ signal obtained and because the component of transitions from $v' = 1,2$ which overlap $B^2\Sigma^+ - X^2\Pi,(0,0)$ band, when N_2 is the quencher, is approximately 5% as opposed to approximately 1% for H_2.

In each case it is apparent that not only is the rotational distribution much broader than that of the $C^2\Delta$ state but the mean value of J has increased by approximately 15 quanta in each case. Most significantly, the maximum J populated in the $B^2\Sigma^+$ state is approximately 40-50 quanta greater than that of the analogous $C^2\Delta$ state distribution. The spectrum produced by the P_1 bandhead excitation clearly resulted in a 'hotter' distribution thus showing that to some extent the additional initial rotational motion is retained upon transfer.

Similar observations were made for the N_2 quencher though the results were unfortunately of an even more qualitative nature. If anything, collisions with N_2 produced even larger changes in J upon transfer, with P_1 excitation again producing the hotter $B^2\Sigma^+ J$ distribution.

No experiment was performed to conclusively show that the $B^2\Sigma^+$ rotational distribution could not be distorted prior to fluorescence in analogy to the rotational relaxation within the $C^2\Delta$ state. However, due to the short radiative lifetime of the product state, which was shown in the previous chapter to be ≤ 10 ns, it seems highly unlikely that there will be any significant change in the product state within this time scale where there exists approximately a 1% probability of a hard sphere collision. The observation of the high J levels is itself an indication that little or no thermalisation has occurred.

5.4 Rotational Dependence of SiF $C^2\Delta,(v' = 0)$ Quenching and Transfer to $B^2\Sigma^+$, (v'') Rates.

5.4.1 Introduction

This section of work deals with preliminary studies into the J' dependence of SiF $C^2\Delta$ collision-induced quenching and transfer to rovibronic levels of the $B^2\Sigma^+$ state. The experiments were performed using the same methodology as the analogous experiments in the previous chapter with the exception that different excitations wavelengths were utilised to populate specific $C^2\Delta$ state rotational levels.

In chapter 4 it was successfully shown that after excitation of the SiF $C^2\Delta - X^2\Pi$ Q_1 head there was no subsequent electronic quenching when only argon was present. However, in this section of work the studies involve differing initial rotational levels, which may not exhibit the same behaviour as those populated upon excitation of the Q_1 band-head. There existed the, admittedly unlikely, possibility that the carrier gas could have a more significant effect upon the $C^2\Delta$ state depending upon the SiF rotational energy. This therefore formed the basis of the initial investigation.

The $C^2\Delta$ state was populated using the wavelengths indicated in figures 5–2 and 5–3. This resulted in excitation of the following transitions respectively:

1. $C^2\Delta_{\frac{3}{2}}(v' = 0, J' = 2.5) - X^2\Pi_{\frac{1}{2}}(v'' = 0, J'' = 3.5)$
2. $C^2\Delta_{\frac{3}{2}}(v' = 0, J' = 11.5) - X^2\Pi_{\frac{1}{2}}(v'' = 0, J'' = 12.5)$
3. $C^2\Delta_{\frac{3}{2}}(v' = 0, J' \approx 32.5 - 38.5) - X^2\Pi_{\frac{1}{2}}(v'' = 0, J'' \approx 33.5 - 39.5)$
4. $C^2\Delta_{\frac{5}{2}}(v' = 0, J' = 48.5) - X^2\Pi_{\frac{1}{2}}(v'' = 0, J'' = 47.5)$

Excitation of the ${}^SR_{21}$ transition, indicated in figure 5–3, results in population of the $\Omega = \frac{5}{2}$ spin-orbit state and not $\Omega = \frac{3}{2}$ which is the result of the P_1 transition excitation.

Lifetimes were recorded at various carrier gas pressures using the same procedure as described in section 4.3.1. The slitwidth of the monochromator was chosen so that signal was collected over the entire SiF $C^2\Delta - X^2\Pi_{\frac{3}{2}}$, (0,0) sub-band. This was fairly straightforward for excitation of the P_1 transitions where there was a relatively strong LIF signal. Unfortunately, the ${}^SR_{21}$ transition was particularly weak, due to the low population of the initial J'' level. Therefore, to obtain a reasonable temporal profile of the waveform decays, the signal was averaged over 8192 laser shots compared with 512 for all previous lifetime measurements. Even with this substantial averaging, the recorded decays were significantly noisier and hence resulted in greater uncertainty in the calculated *best-fit* exponential decays.

Plots of the first order decay rates for each excitation wavelength against argon pressure are presented in figure 5–13.

The $C^2\Delta, v' = 0$ state lifetimes, recorded after excitation of the $C^2\Delta_{\frac{3}{2}} v' = 0, J' = 2.5$ and $J' = 11.5$ states and the P_1 bandhead show little variation with carrier gas pressure. Any apparent pressure dependence is most probably a combination of uncertainties in the *best-fit* decay constants and the small data set. In any event, the uncertainties in the gradients and the gradients themselves were of a similar magnitude.

Not surprisingly the lifetimes recorded after excitation of $C^2\Delta_{\frac{5}{2}} v' = 0, J' = 48.5$ exhibited a greater degree of uncertainty. This resulted in the best straight-line fit indicating an apparent increase in the radiative lifetimes with increasing argon pressure. Although at very low pressures the effects of diffusion could result in a similar observation, this phenomenon is certainly not responsible in this case due to the relatively high experimental pressures used in this study and the fact that such an effect should affect all J''s equally. The more likely explanation is, once more, that of the high degree of uncertainty in the lifetime measurements and the small number of data points in the plot.

It is therefore most likely that there is no significant quenching of the $C^2\Delta$ state by argon regardless of the rotational energy or spin-orbit state of the SiF molecule. Although a more extensive study would be required to prove this beyond

any doubt, it was concluded that, as before, there was no need to account for electronic quenching by argon in the subsequent experiments.

5.4.2 J'-Dependent Radiative Lifetimes of the $C^2\Delta$, $v' = 0$ State

An interesting by-product of this investigation was the observation that although the radiative lifetimes of the $C^2\Delta v' = 0$ state did not appear to be significantly affected by increasing the pressure of the carrier gas, there did appear to be a correlation between the lifetime and the initially excited J' level. Figure 5–14 gives an example of two extremes where the radiative decay profiles can be compared after excitation of the $C^2\Delta_{\frac{3}{2}}$ $J' = 2.5$ and the $C^2\Delta_{\frac{5}{2}}$ $J' = 48.5$ levels, respectively. The 'true' radiative lifetimes will be somewhat masked because only the resultant $C^2\Delta - X^2\Pi_{\frac{3}{2}}$ (0,0) fluorescence was monitored. In the case of the $C^2\Delta_{\frac{5}{2}}$ excitation this will result in a slight decrease in the apparent lifetime due to collisional transfer to the $C^2\Delta_{\frac{3}{2}}$ state, as inferred in section 5.2. According to the rotational line strength calculations, performed as described in section 3.5, approximately only 30% of the product $C^2\Delta_{\frac{3}{2}}$ state molecules will radiate to the $X^2\Pi_{\frac{3}{2}}$ state compared to 70% of the $C^2\Delta_{\frac{5}{2}}$ state molecules. Therefore the time dependent loss of intensity will not be entirely due to the pure radiative process. Similarly, excitation of the P_1 transitions will result in an apparent increase in the lifetimes as the $C^2\Delta - X^2\Pi_{\frac{3}{2}}$ intensity will increase following any transfer to the $C^2\Delta_{\frac{5}{2}}$ state. However, because it was estimated that only about 20% of the population radiated while in the collisionally produced spin-orbit state, as deduced in section 5.2, this is unlikely to significantly affect the qualitative nature of the results. It is therefore quite apparent that there is a significant increase in the lifetime with increasing rotational quantum number. This trend was also consistently observed for lifetimes recorded for excitation of the other rotational levels. Table 5–1 shows the average radiative lifetimes recorded after each specific J' excitation.

These observations can perhaps be justified by considering the change in the average internuclear separation with increasing rotational energy. Due to the

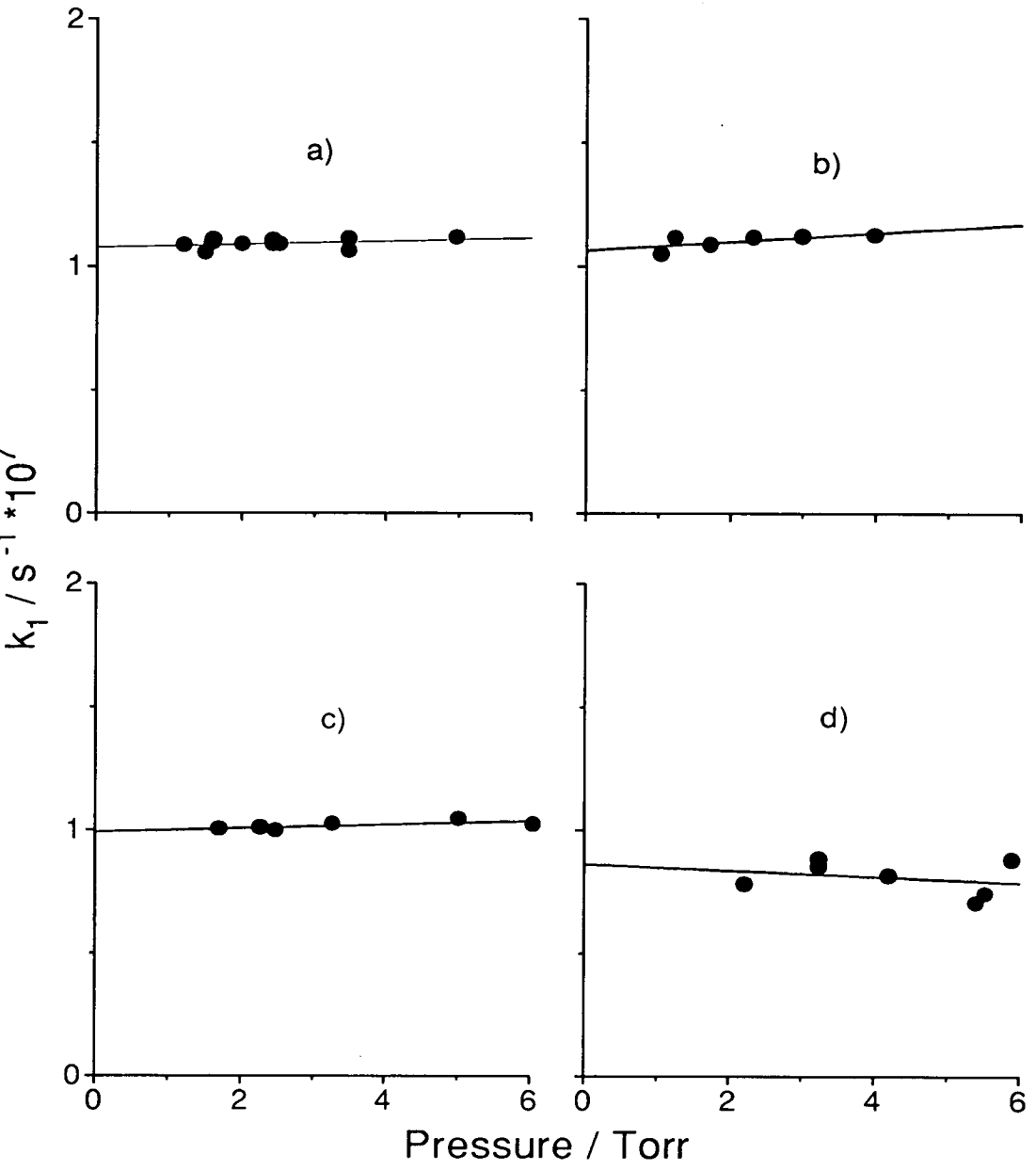

Figure 5–13: Plot of the observed first order decay constants after excitation of SiF $C^2\Delta_\Omega, v' = 0, J'$ as a function of argon pressure.

Initially populated levels

a) $\Omega = \frac{3}{2}$ $J' = 3.5$

b) $\Omega = \frac{3}{2}$ $J' = 12.5$

c) $\Omega = \frac{3}{2}$ $J' \approx 33.5 - 39.5$

d) $\Omega = \frac{5}{2}$ $J' = 48.5$.

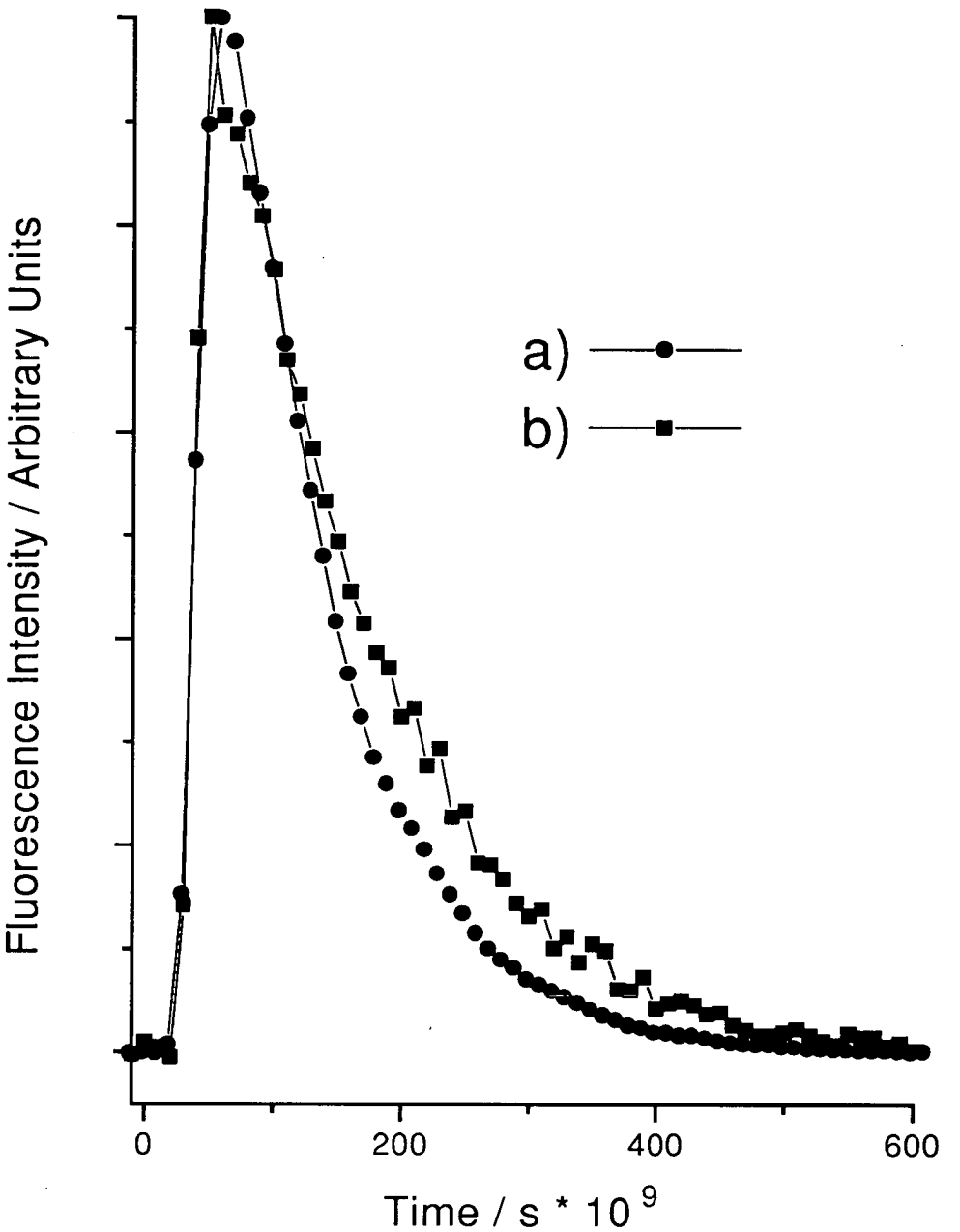

Figure 5–14: Comparison of the temporal profiles of the LIF signal after excitation of (a) $C^2\Delta_{\frac{3}{2}}$ $v' = 0$, $J' = 2.5$ and (b) $C^2\Delta_{\frac{5}{2}}$ $v' = 0$, $J' = 48.5$ states as indicated on the plot.

Initially Excited Level	$\tau_{rad}(10^9 s)^{(a)}$	$k^{(b)}_{rad(rel)}$	$\lvert R\rvert^{2(c)}_{(rel)}$
$C^2\Delta_{\frac{3}{2}} J' = 2.5$	92(3)	1.0(0.05)	1
$C^2\Delta_{\frac{3}{2}} J' = 11.5$	91(5)	1.01(0.06)	0.99
$C^2\Delta_{\frac{3}{2}} J' = 33.5 - 39.5$	98(3)	0.94(0.04)	0.95
$C^2\Delta_{\frac{5}{2}} J' = 48.5$	124(21)	0.74(0.13)	0.91

Table 5–1: Radiative lifetimes for SiF $C^2\Delta v' = 0, J'$.
Numbers in parenthesis represent 2σ uncertainties calculated from the statistical variation in the measurements. a) Radiative lifetime. b) Relative radiative decay rate. c) Relative transition moment.

effects of the centrifugal forces, the equilibrium bond length will increase with J [4]. The transition dipole moment function for the $C^2\Delta - X^2\Pi$ system has been shown, in section 3.8.2, to decrease with increasing internuclear separation as it involves an electronic transition between orbitals centered on different atoms. The rate of emission is directly proportional to the square of this orbital overlap, as shown in equation 3.14, therefore it follows that the lifetime of the $C^2\Delta$ state will increase as the degree of overlap decreases with J.

This effect can be quantified by calculation of the total J dependent relative transition moment for the $C^2\Delta - X^2\Pi$, $(0, v'')$ transitions. The calculations were performed as described in section 3.5.2 and the results are presented in table 5–1 where they can be compared with the analogous relative radiative decay rates.

It is also apparent from the relative decay rates are similar to the relative total rovibronic wavefunction overlap with the exception of that following excitation of the $C^2\Delta_{\frac{5}{2}}$, $J' = 48.5$ level. In this case it appears that the radiative decay is significantly smaller than anticipated, according to the relative transition moment calculations, although the measured lifetimes for this level were subject to a large degree of uncertainty. This discrepancy could also be partly due to the transition dipole moment function, as inferred from the vibronic transition probabilities in section 3.8.2, being not so well defined at the larger interatomic separations. It should be emphasised that the measured lifetimes are not those of a pure rovibronic

Gas[a]	J'[b]	$k_Q/10^{11}cm^3s^{-1}$[c]	$\sigma_Q/\AA^2$[d]
H_2	2.5	67(22)	38(12)
	11.5	83(22)	47(12)
	33.5-39.5	128(36)	72(21)
N_2	2.5	11.6(3.5)	19(6)
	11.5	9.7(2.1)	16(3)
	33.5-39.5	6.9(1.9)	12(3)

Table 5–2: Rate constants and thermally averaged cross sections for total removal after excitation of SiF $C^2\Delta_{\frac{3}{2}}$ $v' = 0, J'$.
Numbers in parenthesis represent 2σ statistical uncertainties. a) No measurable quenching for Ar. b) Initially excited rotational level. c) Total quenching rate constant. d) Thermally averaged cross section.

state but are convoluted with with those of other, collisionally produced rovibronic and spin-orbit states.

5.4.3 Total collisional removal of SiF $C^2\Delta v' = 0$: J' Dependence

A further series of experiments was performed where controlled pressures of H_2 and N_2 were introduced into the flow system to examine any J' dependent quenching behaviour. Lifetimes were recorded as a function of quencher gas pressure after excitation of the three P_1 transitions indicated in figure 5–2. The two quenchers were, not surprisingly, found to collisionally remove the $C^2\Delta$ state species as already established for Q_1 excitation in section 4.3.1. The bimolecular quenching rate constants and thermally averaged cross sections are listed in table 5–2 and represented graphically in figure 5–15.

Taken at face value there does appear to be some correlation between the bimolecular quenching rate constants and the initially populated rotational level. The results show that the $C^2\Delta$ state quenching cross sections increase with J'

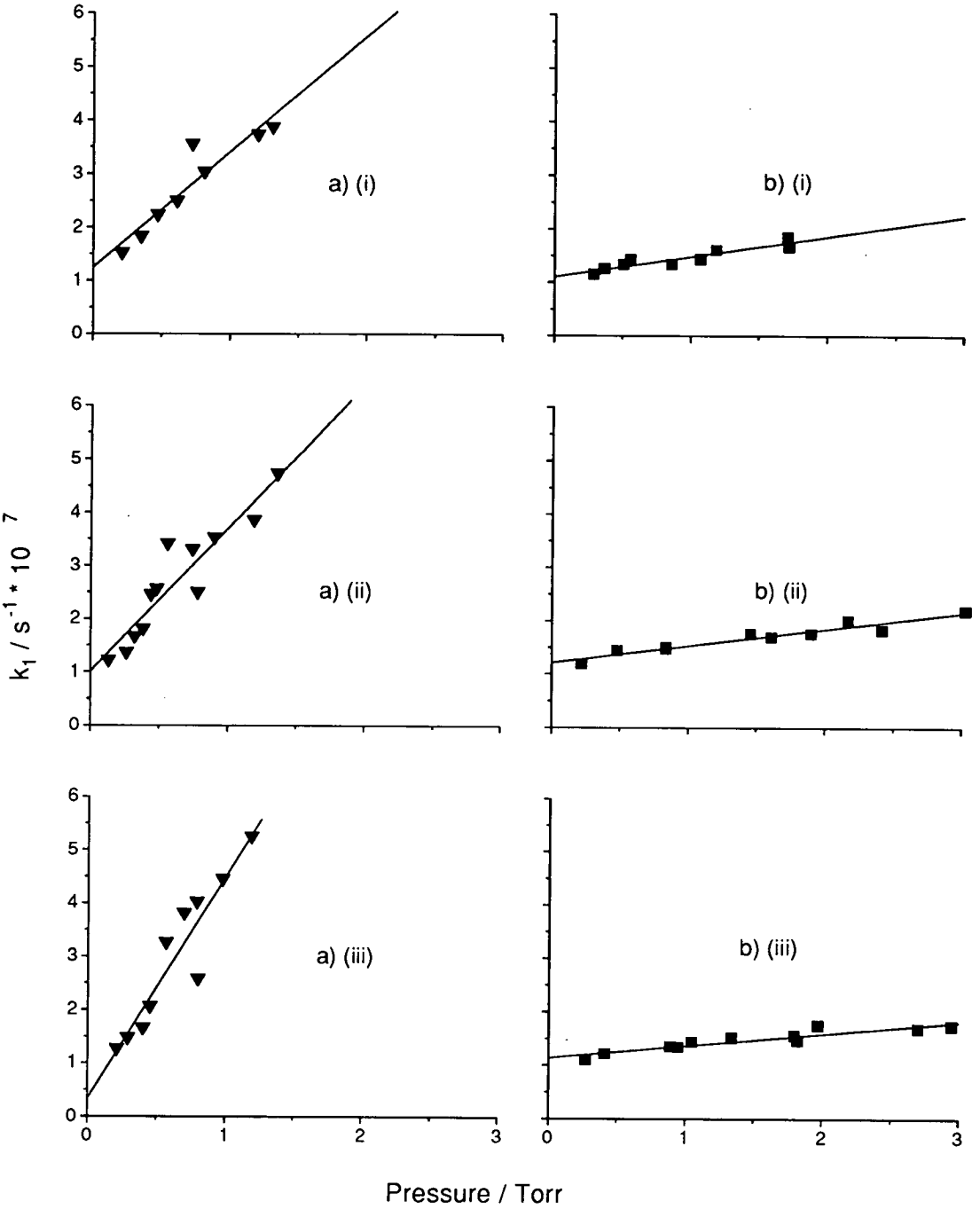

Figure 5–15: Observed first order decay rate constants for SiF $C^2\Delta, v' = 0, J'$ as a function of quencher partial pressure.

All experiments were performed with an additional fixed argon pressure of 1 Torr.

(a) H_2 (b) N_2

(i) $J' = 2.5$ (ii) $J' = 11.5$ (iii) $J' \approx 33.5 - 38.5$

for the H_2 quencher but decrease with J' for N_2! However, the uncertainties are so large that for both quenchers there is a degree of overlap between virtually all the quenching cross section 2σ error limits for each collision partner. With the exception of the data produced by excitation of $J' = 2.5$ in H_2, all cross sections were within experimental error of those obtained after excitation of the Q_1 band-head.

The quality of the results has suffered both due to the difficulty in obtaining consistently reliable pressure measurements and to the reduced LIF signal produced by excitation of the weaker $C^2\Delta - X^2\Pi$ P_1 transitions. The most that can be stated with conviction is that if the quenching rate is dependent upon J' then the effect is within the relatively large experimental uncertainty of the current method. Obviously if this effect is to be properly investigated in future the experimental quencher pressure must be more accurately controlled.

5.4.4 Specific collisional transfer SiF $C^2\Delta$, $v' = 0 - B^2\Sigma^+ v''$: J' Dependence

To quickly determine if the $C^2\Delta - B^2\Sigma^+$ electronic branching fraction was dependent upon the SiF rotational energy, the P_1 bandhead was excited in the presence of H_2 and N_2 respectively whilst recording the dispersed fluorescence. The resulting spectra are presented in figures 5–16 and 5–17, respectively where they can be compared to the analogous spectra recorded, under the same conditions, after excitation of the Q_1 bandhead (previously shown as figures 4–6 and 4–7).

It is apparent from a visual examination of the H_2 quencher spectra that the ratio of the integrated $C^2\Delta - X^2\Pi$ to $B^2\Sigma^+ - X^2\Pi$ fluorescence is essentially the same following excitation of either the Q_1 or P_1 bandhead. This is confirmed upon calculation of the peak areas where the electronic branching fraction of $C^2\Delta$ to $B^2\Sigma^+$ transfer for each excitation wavelength was shown to be virtually identical.

In the case of the N_2 quencher spectra, the relative specific transfer rates were more difficult to obtain accurately due to the poor signal-to-noise in the spectrum produced by excitation of the P_1 band head. Integration of the fluorescence peaks

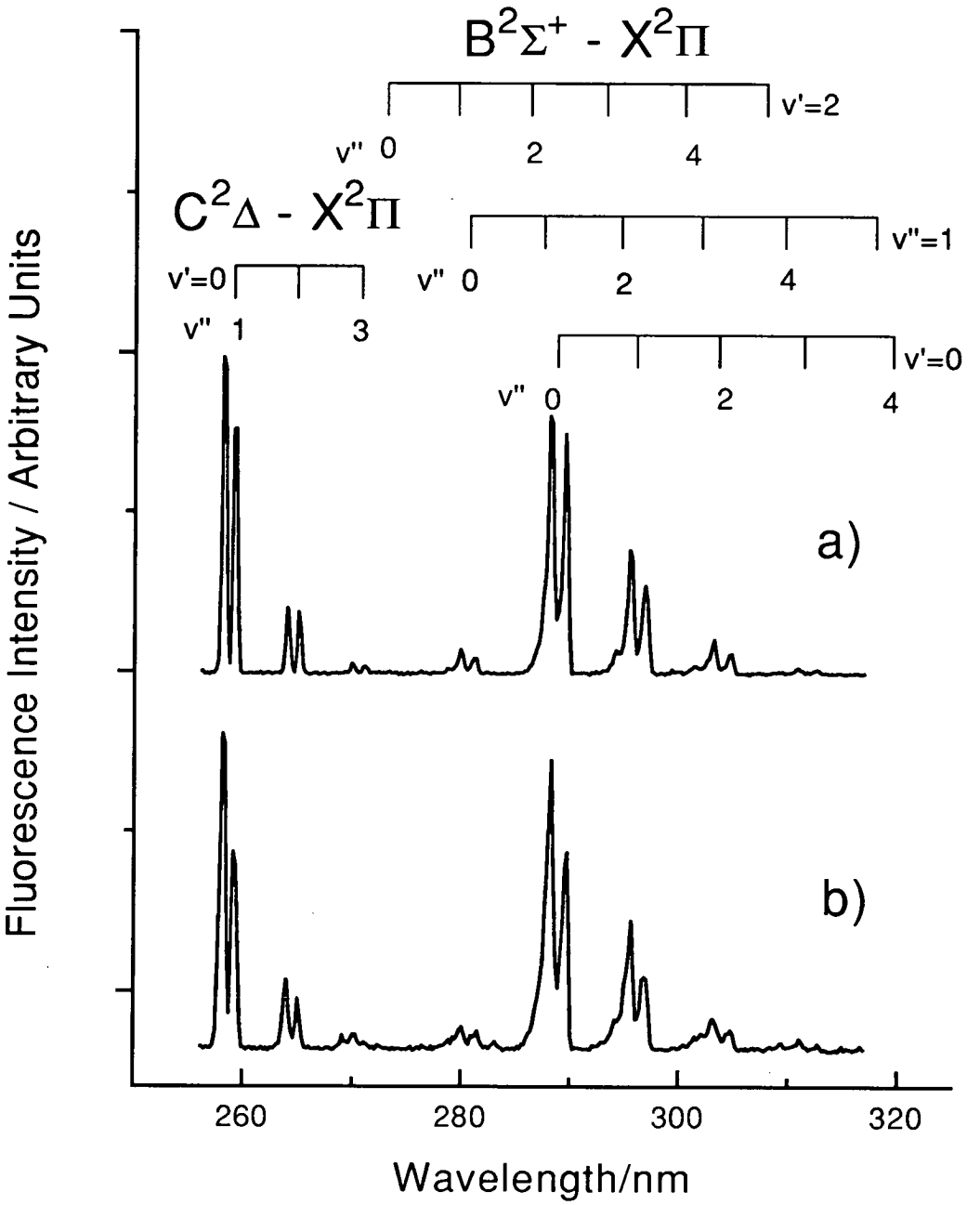

Figure 5–16: Dispersed fluorescence spectra following the initial excitation of the $C^2\Delta - X^2\Pi_{\frac{1}{2}}$, $(0,0)$ transition in the presence of 3 Torr H_2 and 1 Torr Ar.

(a) Q_1 bandhead (cf. figure 4–6).

(b) P_1 bandhead.

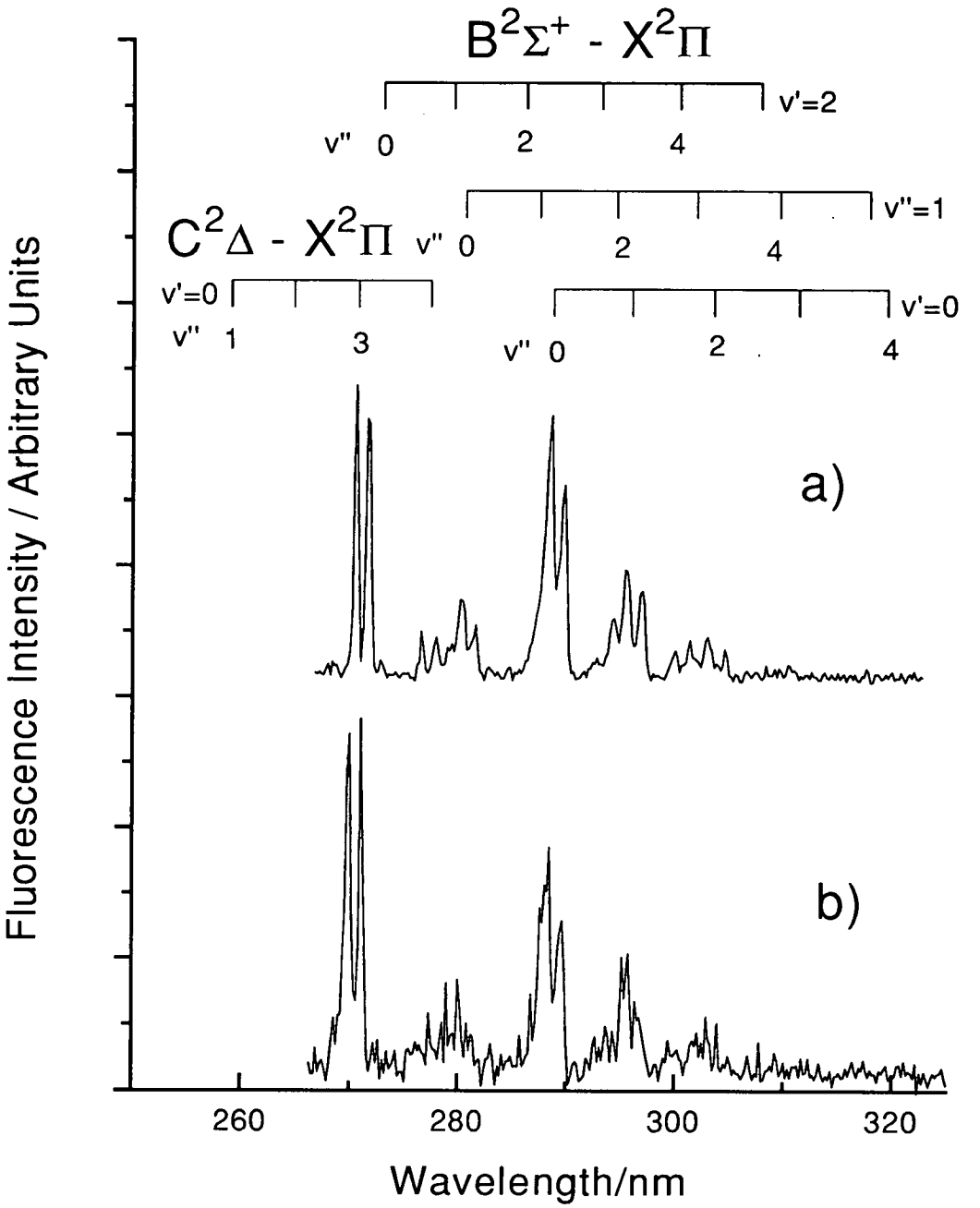

Figure 5–17: Dispersed fluorescence spectra following the initial excitation of the $C^2\Delta - X^2\Pi$ (0, 0) transition in the presence of 3 Torr N_2 and 1 Torr Ar.

(a) Q_1 bandhead (cf. figure 4–7).

(b) the P_1 bandhead.

showed that the $C^2\Delta - B^2\Sigma^+$ transfer rate was about 1.3 times larger following excitation of the Q_1 head. However, the uncertainty in the quencher pressures and the spectral noise means that it is impossible to say whether the rate of $C^2\Delta - B^2\Sigma^+$ transfer rate is truly dependent upon the rotational energy of the $C^2\Delta$ state. To conclusively prove that there is a weak rotational effect on the electronic branching fraction in the N_2 collision-induced transfer system would require further investigation.

5.4.5 J' dependence of the $B^2\Sigma^+$ Vibrational Branching Ratios

The spectra in figures 5–16 and 5–17 which also indicate any variation in the product $B^2\Sigma^+$ vibrational populations with initial $C^2\Delta$ rotational level. However, integration of the obvious $B^2\Sigma^+ - X^2\Pi$ spectral bands revealed no significant differences in the relative peak areas which is apparent purely from a visual examination of the spectra. The $C^2\Delta - X^2\Pi$ and $B^2\Sigma^+ - X^2\Pi$ band profiles can be seen to change with the different excitation wavelengths though this is consistent with the observations made in sections 5.2 and 5.3 in that excitation of the P_1 bandhead produced a rotationally hotter distribution in the $C^2\Delta$ and product $B^2\Sigma^+$ states than Q_1 bandhead excitation.

5.5 Conclusions

The conclusions that can be drawn directly from the results reported in this chapter are as follows:

1. LIF excitation spectra indicated that it was possible to selectively populate specific rotational levels of the SiF $C^2\Delta, v' = 0$ state by exploiting the $C^2\Delta - X^2\Pi$ P_1 and R_{21} branches.

2. Population of specific rotational levels of the $C^2\Delta$ state in the presence of Ar results in a degree of collision-induced rotational relaxation within

the radiative lifetime. This does not result in a thermalised distribution. Collisional transfer from $C^2\Delta_{\frac{3}{2}} - C^2\Delta_{\frac{5}{2}}$ was also observed.

3. The SiF $C^2\Delta, v' = 0$ state collisionless radiative lifetime increases moderately but significantly with increasing J'.

4. Collision-induced transfer from the $C^2\Delta$ to $B^2\Sigma^+$ states results in a 'hot', non-Boltzmann rotational distribution in the $B^2\Sigma^+$ state for the molecular quenchers H_2 and N_2. N_2 appeared to show a propensity for even larger changes in J' than H_2. Excitation of higher initial $C^2\Delta$ state rotational levels results in a larger mean value for J' in the product state. The change in rotational quantum number upon transfer was shown to range up to ΔJ=50.

5. Neither the electronic branching fraction for $C^2\Delta$ to $B^2\Sigma^+$ transfer in the presence of H_2 nor the $B^2\Sigma^+$ product state vibrational populations appear to be significantly affected by the identity of the initially excited rotational level. Studies of the dependence of the total quenching rate constants upon the initially populated rotational level proved inconclusive.

Bibliography

[1] S. Singleton, Laser Based Studies of Transient Species in a Discharge Flow Apparatus, PhD Thesis, University of Edinburgh, (1990).

[2] S. Singleton and K.G. McKendrick, J. Phys. Chem. **97** (1993) 1389.

[3] O. Appelblad, R.F. Barrow and R.D. Verma, J. Phys. B **2** (1968) 274.

[4] G. Herzberg, Molecular Spectra and Molecular Structure. I. Spectra of Diatomic Molecules, 2nd Edition (Van Nostrand Reinhold, New York, 1950).

Chapter 6

The Mechanism of Collision-Induced Energy Transfer between the $^2\Delta$ and $^2\Sigma^+$ States of the Silicon Halides

In this chapter, an attempt is made to rationalise the findings from the study of the collision-induced SiF $C^2\Delta$ to $B^2\Sigma^+$ and, electronically analogous, SiCl $B'^2\Delta$ to $B^2\Sigma^+$ energy transfer systems. The extent to which these results are consistent with existing energy transfer models is also discussed.

6.1 Total Collision-Induced Electronic Quenching Rates

6.1.1 SiCl $B'^2\Delta$,$v' = 0, 1$ Removal

The total collisional removal rates of the SiCl $B'^2\Delta, v' = 0$ and 1 levels measured in this thesis were generally found to be in good agreement with those previously reported by Singleton [1,2] and Jeffries [3]. The cross sections showed quenching to be very efficient for the series of non-polar quenchers Ar, He, H_2, N_2, CO_2 and CH_4. The efficiency of removal is dependent upon the identity of the collision partner and, to a lesser extent, the vibrational level of the $B'^2\Delta$ state.

The magnitudes of the total removal cross sections are comparable to those reported for the quenching of, for example, CN $A^2\Pi$ [4,5,6,7], N_2^+ $A^2\Pi_u$ [8,9,10, 11,12,13], NS $B^2\Pi$[14], *etc.* The quenching efficiency was originally shown by Singleton [1,2] to correlate with long range, attractive interactions between SiCl $B'^2\Delta$ and the collision partner. The model which was successfully applied to this case was that developed by Parmenter and Seaver [15] which has already been discussed in some detail in section 1.2.1. The correlation plots of the cross sections for total removal from the $v' = 0$ and 1 vibrational levels of SiCl $B'^2\Delta$ are shown in figure 6–1. The values for the intermolecular well depths, ϵ_{MM}, were those determined by the originators of this model [15]. The correlation is seen to be fairly successful for quenching of $B'^2\Delta$ $v' = 0$ thus indicating that this quenching process is controlled by attractive interactions. The correlation was less successful for quenching of $v' = 1$ where there can be seen to be a considerable degree of scatter, outwith the experimental uncertainties. For both cases it might be argued that the quenching cross sections for H_2 are anomalously high: therefore, these data points were excluded when calculating the best-fit straight lines through the remaining points shown in figure 6–1. This correlation has previously been successfully applied to the quenching of the predissociative higher vibrational levels of NO $B^2\Pi$ [17] and, in a more qualitative way for a limited number of partners, to the quenching of N_2 $B^3\Pi_g$ [18,19,20].

As noted in section 1.2.1, cross sections for quenching should be dependent upon the rotational angular momentum when the process is controlled by long range interactions. The quenching efficiency would therefore be expected to decrease with increasing J. This might then appear at odds with the observations of Singleton [1,2] where the quenching cross sections were shown to be constant upon variation of the excitation wavelength. However, the high degree of rotational relaxation which occurs in the $B'^2\Delta$ state coupled with the large uncertainties involved in evaluating the total quenching cross sections indicate that this result requires a more cautious interpretation. Further work would be necessary to establish the true extent of any J dependence of the quenching.

The opposite extreme alternative to that of a long-range, attractive interaction

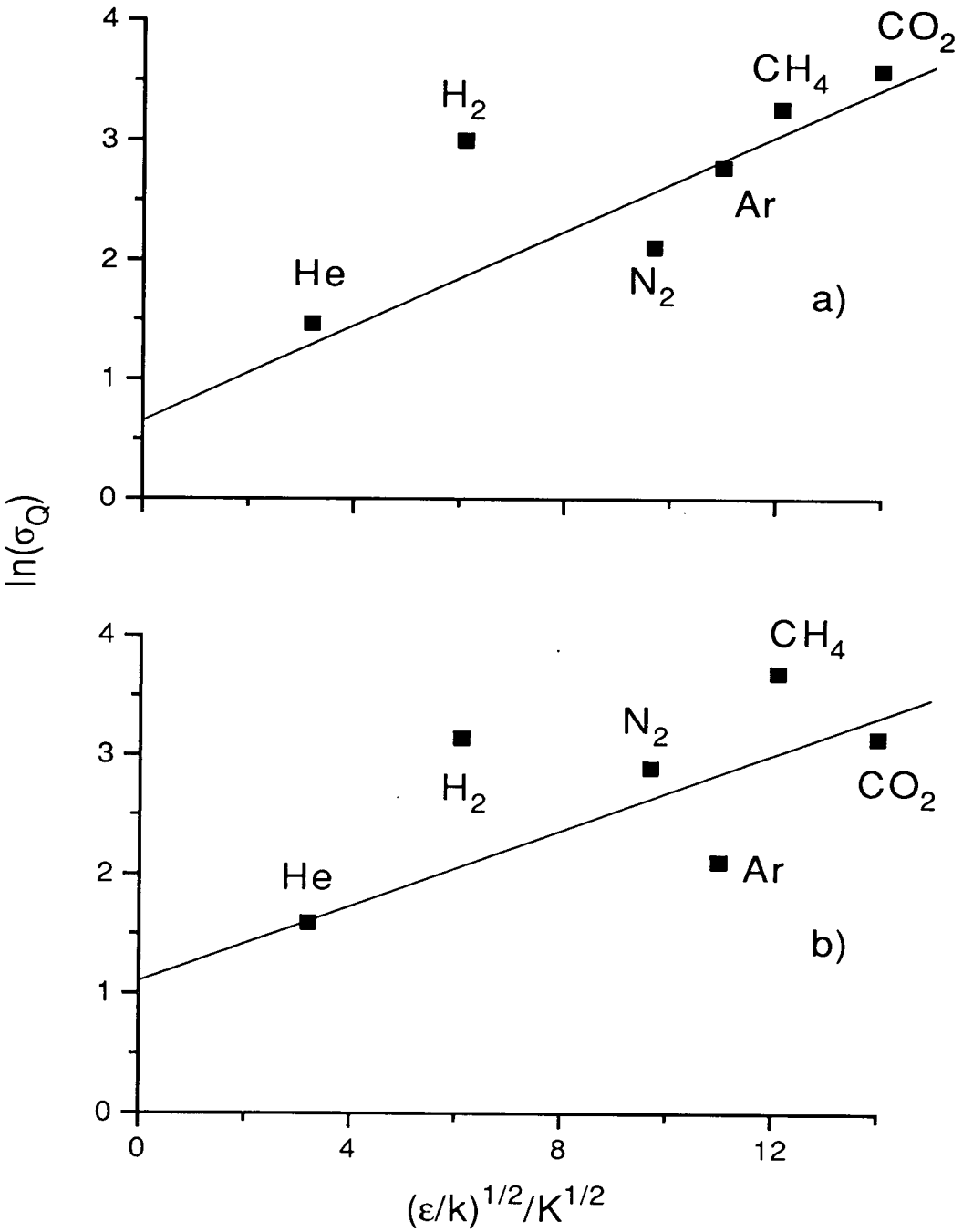

Figure 6–1: Parmenter-Seaver attractive well depth correlation plots of the cross sections for total collisional removal of SiCl $B'^2\Delta$ (a) $v' = 0$ and (b) $v' = 1$. The results for H_2 were excluded from the calculation of the best-fit straight lines through the remaining points.

is that the quenching rate is controlled by hard sphere, impulsive collisions. Not only are the magnitudes of the quenching cross sections significantly larger than those expected for a typical hard sphere collision but the anticipated correlation predicts a decrease in efficiency with increasing reduced mass of the collision pair [21] (as discussed in section 1.2.3). If anything, there is a systematic increase in the quenching cross section with reduced mass. It was thus concluded that a repulsive interaction is not of prime importance in the quenching of the SiCl $B'^2\Delta$ state.

6.1.2 SiF $C^2\Delta$,$v' = 0, 1$ Removal

The results in chapter 4 show that collisional removal of SiF, $C^2\Delta$, $v' = 0$ or 1, is efficient for the molecular collision partners H_2, N_2, CO_2 and CH_4. In contrast, quenching was *negligible* for the inert gases Ar and He. The cross section magnitudes are comparable for N_2, CO_2 and CH_4, but H_2 is significantly more efficient for quenching of both vibronic levels.

Obviously, the attractive force model, which was relatively successful for SiCl $B'^2\Delta$ quenching, will fail in the SiF case, quite disastrously for the He and Ar results [15], but also because of the trends among the other gases. The predictions of the simple repulsive model also fail to correlate with the experimental results for similar reasons.

In contrast to SiCl $B'^2\Delta$ state quenching Ar and He fail to quench the SiF $C^2\Delta$ state. This could conceivably suggest that the quenching mechanism involves energy transfer to the rotational and vibrational modes of the molecular collision partners. However, there is no direct evidence for this proposal. This point will be considered further in section 6.4.1.

Quenching by H_2 is significantly more efficient than by the other molecular quenchers. This may be explained due to the H_2 chemically reacting with the SiF $C^2\Delta$ state molecules. On purely thermodynamic grounds there are a number of reactive channels available which are listed in table 6–1. However, this explanation is not complete because there are also a number of reactions thermodynamically

possible for quenching by CH_4 and CO_2, also shown in table 6–1, but there are none for N_2 (which was of comparable quenching efficiency to CH_4 and CO_2). Obviously this point requires further experimental investigation before any definite conclusions can be drawn.

6.2 Specific Collisional Transfer from $^2\Delta$ to $^2\Sigma^+$

6.2.1 SiCl $B'^2\Delta$ to $B^2\Sigma^+$ Transfer

For all quenching gases investigated, a significant fraction of the collisionally removed SiCl $B'^2\Delta$ state molecules are transferred to the $B^2\Sigma^+$ state. This fraction has been shown to be highly sensitive to the identity of the quencher and the initial $B'^2\Delta$ vibrational level. Transfer is generally more efficient for the polyatomic species with the exception of CO_2.

The role of the attractive forces for this particular channel was also examined [1] using the Parmenter and Seaver correlation [15]. In this case the plots of the specific $B'^2\Delta$ to $B^2\Sigma^+$ cross sections exhibited a considerable degree of scatter. No obvious molecular property could be identified to explain the sensitivity of the propensities for $B'^2\Delta$ to $B^2\Sigma^+$ transfer upon the identity of the quencher.

The accepted electronic configurations for the SiCl $B'^2\Delta$ and $B^2\Sigma^+$ states, analogous to those for the SiF $C^2\Delta$ and $B^2\Sigma^+$ states (discussed in section 3.8), are:

- $B'^2\Delta$ ... $(7\sigma)^2(8\sigma)^2(5\pi)^2(6\pi)^2(9\sigma)^1(7\pi)^2$ [22]
- $B^2\Sigma^+$ ... $(7\sigma)^2(8\sigma)^2(5\pi)^2(6\pi)^2(9\sigma)^2(4s\sigma)^1$ [22,23]

Thus collision-induced transfer between these two states will involve the movement of *two* electrons between molecular orbitals. It is known that interactions between Rydberg and valence states, where the electronic configurations differ by two orbitals, can occur [24]. For example the O_2 valence $B^3\Sigma_u^-$ and the Rydberg

Reaction		ΔH^{θ}_{298}/kJmol^{-1}
SiF ($C^2\Delta$,$v' = 0$) + H_2 $\longrightarrow$	HF + SiH	-362
	HF + Si + H	-44
	HSiF + H	~-349[a]
	H_2SiF[b]	~-667[a]
	SiH_2 + F	~-103[a]
SiF ($C^2\Delta$,$v' = 0$) + CH_4 $\longrightarrow$	HF + Si + CH_3	-42
	HF + Si(CH_3)	~-493[a]
	SiH + CH_3F	-267
	HSiF + CH_3	~-347[a]
	H_2SiF + CH_2	~-200[a]
	HSiF(CH_3)[b]	~-798[a]
	SiF(CH_3) + H	~-480[a]
SiF ($C^2\Delta$,$v' = 0$) + CO_2 $\longrightarrow$	SiO + CO + F	-183
	SiO_2 + CF	~-800[a]
	SiFO + CO	~-735[a]
	SiFO(CO)[b]	~-1186[a]
	SiF(CO) + O	~-386[a]

Table 6–1: Potential reactive channels available for the quenching of SiF $C^2\Delta$,$v' = 0$ by H_2, CH_4 and CO_2.

ΔH values estimated using bond enthalpies listed in ref. [16].

a) The dissociation energy for some of the bonds formed in this reaction have not previously been measured and have therefore been estimated relative to the formation of the appropriate diatomic bond.

b) Note that these involving a single produce would require 3rd body stabilisation.

$B'^3\Sigma_u^+$ states can be described as a mixture of the $\pi_u^3\pi_g^3$ and $\pi_u^4\pi_g 3p\pi_u$ configurations [26]. This state mixing is made possible by to the electrostatic interaction operator, e^2/r_{ij}, which represents the Coulombic interelectronic repulsion. Coupling can occur only between states of the same electronic symmetry, therefore perturbation between the SiX $^2\Delta$ and $^2\Sigma^+$ states is forbidden. However, with the approach of the collision partner the symmetry is broken. The doubly degenerate $^2\Delta$ state will be split into states of A' and A'' symmetry and the $^2\Sigma^+$ state will have A' symmetry. Thus perturbation between the $^2\Delta$ and $^2\Sigma^+$ states may be allowed by interaction of the two A' states, in this case, induced by the presence of the quencher.

The fate of the quenched SiCl $B'^2\Delta$ state molecules which are not transferred to the $B^2\Sigma^+$ state has not been established. The dissociation limit of the $X^2\Pi$ state is not known with sufficient certainty to determine whether collision-induced dissociation to Si and Cl atoms is energetically feasible. The heat of formation of SiCl has been estimated as approximately 390 $\pm$20 kJmol^{-1} [27] ($\sim$ 32500 cm^{-1}) and therefore it is more probable, on balance, that the $B^2\Delta$, $v' = 0$ and 1 levels lie above the limit (see figure 4–1). Therefore in purely thermodynamic terms, the SiCl $B'^2\Delta$ state molecules contain sufficient energy to dissociate to gound state Si and Cl atoms.

There also exists the possibility of collisional transfer to the $A^2\Sigma^+$ state, the predicted (but as yet not observed) $a^4\Sigma^+$ state [28] or to the ground $X^2\Pi$ state. Transfer to the $A^2\Sigma^+$ state would result in $A^2\Sigma^+ - X^2\Pi$ fluorescence though none has yet been observed. Preliminary calculations have shown that, due to the Franck-Condon principle and the electronic energy of the $A^2\Sigma^+$ state ($\sim$ 23010cm^{-1}[29]), any $A^2\Sigma^+ - X^2\Pi$ fluorescence is likely to be at wavelength greater than 600 nm. Any such fluorescence would not be detected in our current experiments due to the low response of the photomultiplier tube in this region. Obviously, any $a^4\Sigma^+$ or $X^2\Pi$ products would be impossible to detect using the existing experimental procedure.

6.2.2 SiF $C^2\Delta$ to $B^2\Sigma^+$ Transfer

The efficiency of SiF $C^2\Delta$ to $B^2\Sigma^+$ transfer was shown to be significantly smaller than for the equivalent SiCl process. No more than 20% of the removed $C^2\Delta$ state population was transferred to the $B^2\Sigma^+$ system for any quencher species. Surprisingly, CO_2 showed no propensity for $C^2\Delta$ to $B^2\Sigma^+$ transfer despite being an efficient quencher. The relatively low transfer efficiency, when compared with SiCl, may conceivably be partially explained by considering the possibility of a chemical reaction between the collision partners. As discussed in section 6.1.2, from a purely thermodynamic perspective, there are a number of channels available for the reaction of SiF $C^2\Delta$ with H_2, CH_4 and CO_2, though there are none for N_2. In contrast to SiCl, there is no possibility of collision-induced dissociation as the SiF ground state dissociation limit has been estimated to be approximately 550 kJmol^{-1} [31] ($\sim$46000 cm^{-1}) and is therefore significantly greater than the energies of the lower vibrational levels of the $C^2\Delta$ state (as shown in figure 4–2). Similarly to SiCl, the only remaining channels are those of transfer to the $A^2\Sigma^+$, $a^4\Sigma^+$ and $X^2\Pi$ states.

Obviously the attractive and repulsive force models will not show a complete correlation with the transfer cross sections for all collision partners because of the unobservably slow quenching by He and Ar and the lack of transfer by CO_2. However, the cross sections for the very limited number of quenching gases so far examined which result in $C^2\Delta$ to $B^2\Sigma^+$ transfer admittedly do show some correlation with the reduced mass of the collision pair. The model devised by Schwartz, Slawsky and Herzfeld (SSH) [51] (discussed in more detail in section 1.2.3) predicts that the collision-induced probability scales as

$$ln(\sigma) \propto A - \mu^{\frac{1}{3}} \quad . \tag{6.1}$$

Figure 6–2 shows a SSH correlation plot of the cross sections for SiF $C^2\Delta - B^2\Sigma^+$ transfer. The measurements for transfer from $C^2\Delta$,$v' = 0$ with H_2, N_2 and CH_4 fit the model reasonably well but are more scattered for $C^2\Delta$,$v' = 1$. There is, however, a considerable degree of experimental uncertainty in these results. Although the data set is too small to draw any real conclusions there does appear

to be an increase in the transfer cross section with decreasing reduced mass of the collision pair. Unfortunately, the absence of any observed transfer for He, Ar and CO_2 does not fit the SSH model. In fact He is predicted by this model to have the second largest transfer cross section of all the tested collision partners! Therefore the most that can be drawn from these observations is that the reduced mass *may* be a partially contributing factor in determining the transfer probabilities. The model does not consider the structure of the collision partner which is obviously of considerable importance in this case. This aspect obviously needs further investigation of a greater range of quenchers before any firm conclusions can be drawn.

6.3 Vibrational Populations in the Product States

6.3.1 Vibrational Populations in the SiCl $B^2\Sigma^+$ State

The relative vibrational populations of the collisionally transferred SiCl $B^2\Sigma^+$ products showed a remarkable dependence on the identity of the quenching gas. This is the only known system which shows such a dramatic variation in the propensities for differing collision-induced vibronic channels[1].

It proved impossible to identify any obvious molecular parameter to justify the different transfer propensities which are summarised in figure 4–21 and table 4–6. There were some surprising coincidences and variations in the population ratios for quenchers which might have been expected to behave differently or to be more similar, respectively. For example, He and N_2 quenching result in similar $B^2\Sigma^+$ vibrational populations after excitation of both $B'^2\Delta$, $v' = 0$ and 1. H_2 quenching results in a comparable distribution only for excitation of $v' = 0$, though conversely Ar behaves like He and N_2 only for $v' = 1$!

---

[1] As discussed in section 1.1.2, collision-induced transfer from NH $c^1\Pi$ to $a^1\Delta$ showed slightly different transfer propensities for O_2 and NO as quenchers [32].

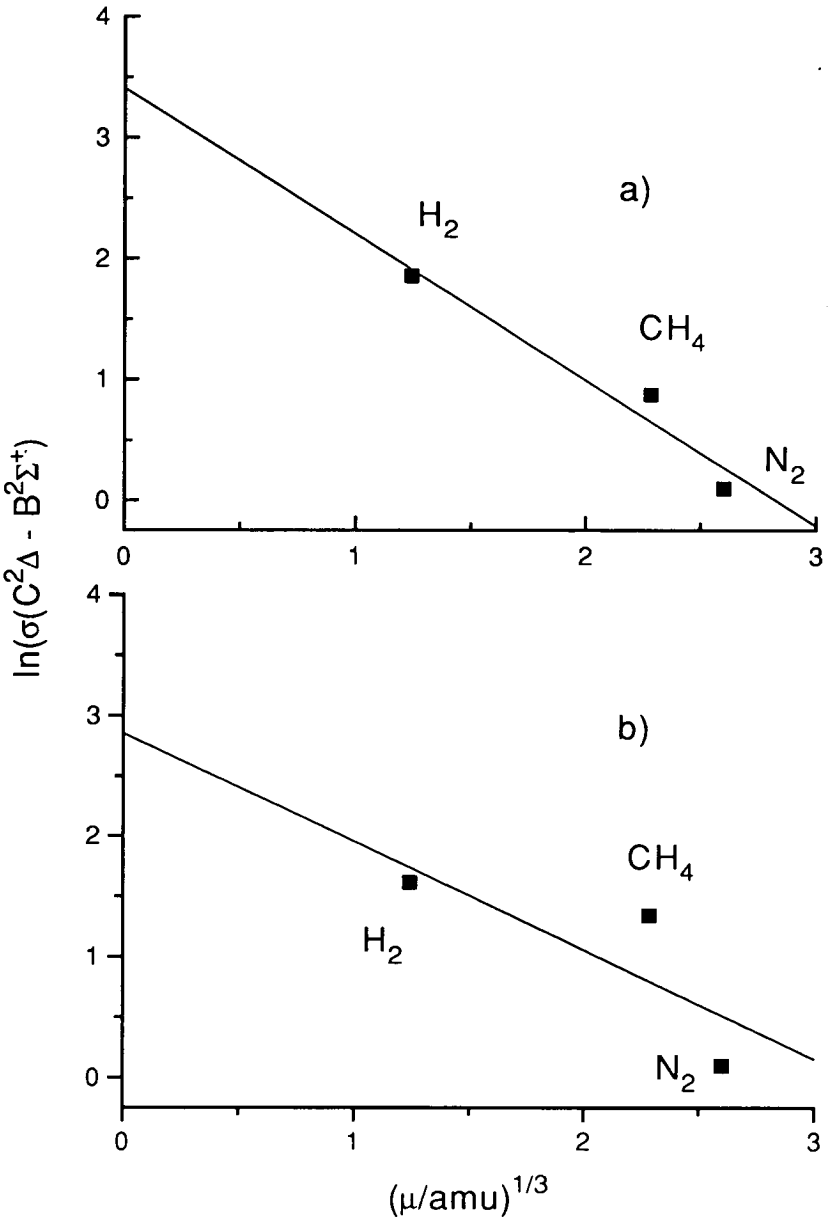

Figure 6–2: Plots of the SiF $C^2\Delta - B^2\Sigma^+$ transfer cross section against the collision reduced mass term according to SSH theory.

a) $v' = 0$ b) $v' = 1$

The straight lines are least-squares straight line fits through the experimental points.

It was demonstrated by Singleton[1,2] that the cross sections for the specific transfer channel $B'^2\Delta$, $v' = 0$ to $B^2\Sigma^+$, $v' = 2$ were clearly correlated with the intermolecular attractive forces as shown on the Parmenter-Seaver plot in figure 6–3. The explanation given for this behaviour was that this near-isoenergetic process (with $\Delta E \sim 36$ cm^{-1}) will be induced by the 'softest' large impact parameter collisions in which there is little exchange of energy to the vibrational and translational degrees of freedom. There is no equivalent behaviour for $B'^2\Delta$, $v' = 1$ because the nearest $B^2\Sigma^+$ state vibrational level ($v' = 3$) lies approximately 150 cm^{-1} higher and to which no population was observed to be transferred. This may be a partial explanation of why transfer is generally more efficient from $B'^2\Delta$, $v' = 0$ because the $v' = 1$ level has no isoenergetic $B^2\Sigma^+$ level which can be populated via long range collisions. On the other hand, this may be due to the classical curve crossing being located very near to the $B^2\Sigma^+$,$v' = 2/B'^2\Delta$,$v' = 0$ energy levels. Therefore, since this pair of levels require the minimum perturbation by the quencher to induce transfer between the two potential curves it may be expected that the $B'^2\Delta$,$v' = 0$ to $B^2\Sigma^+$,$v' = 0$ channel gives the best correlation with long range forces (this point will be dealt with in greater detail in section 6.4).

It is apparent from the vibrational populations that the SiCl molecules are losing significant amounts (up to $\sim$ 1900 cm^{-1}) of their total vibronic energy as a result of collision-induced transfer. It is possible that some of this energy is transferred to the internal modes of the quencher. Perhaps some evidence for this is that the polyatomic species CH_4 and CF_4 were shown to remove, on average, considerably more energy than the other species, particularly the noble gases. However, the results for the polyatomic CO_2 are not explained by this premise. It is probably more likely that the energy is coupled to the mechanical recoil energy of the collision pair, but again a firm conclusion would require further direct experimental observations.

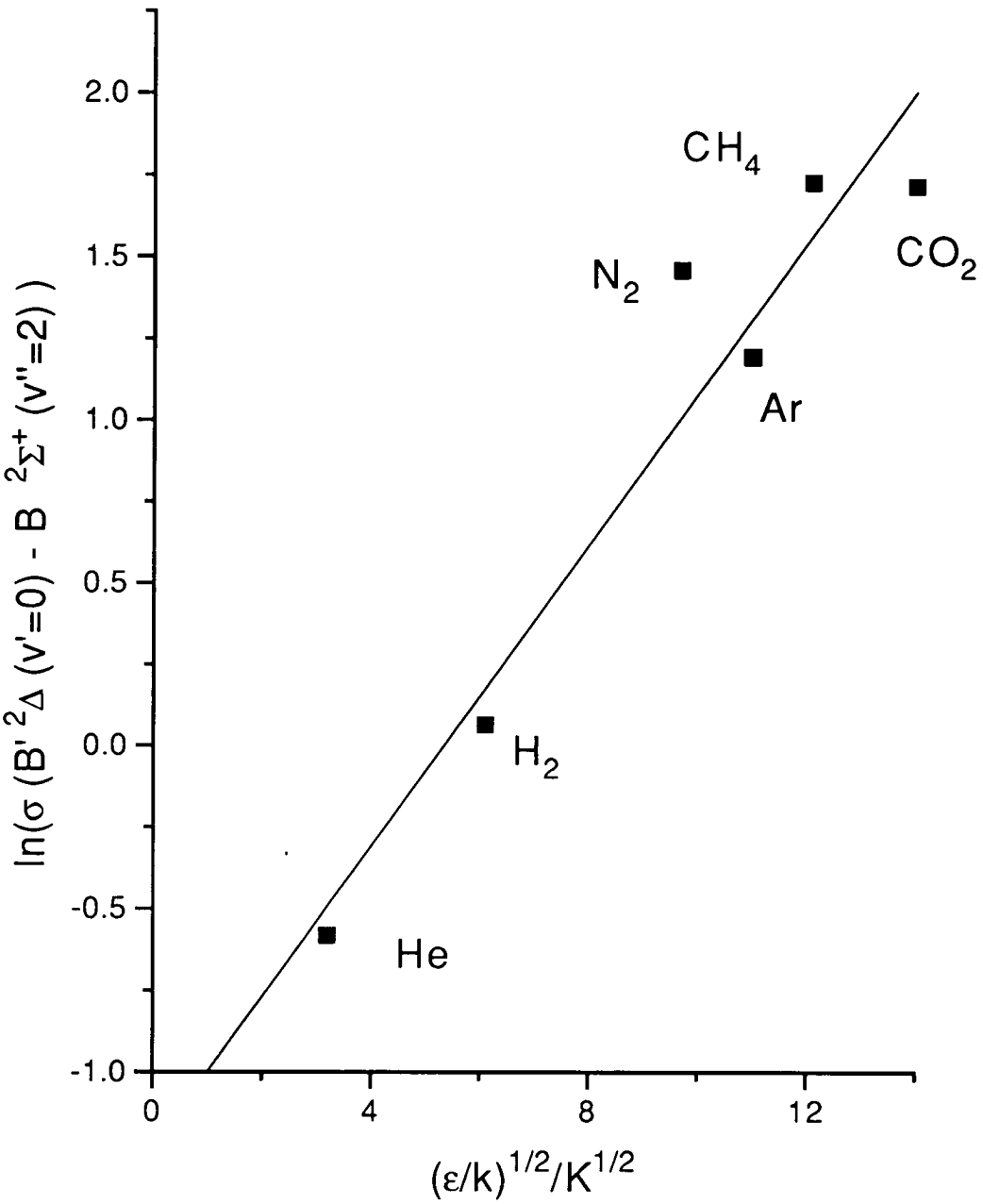

Figure 6–3: Parmenter-Seaver correlation plot of specific state-to-state cross sections for the near-resonant collisional collisional transfer from SiCl $B'^2\Delta$, $v' = 0$ to $B^2\Sigma^+$, $v' = 2$.

The cross sections were obtained by multipling the $B'^2\Delta$, $v' = 0$ to $B^2\Sigma^+$ transfer cross section by the appropriate fractional population deposited in $B^2\Sigma^+$, $v' = 2$. The straight line is the linear least-squares fit through the experimental points.

6.3.2 Vibrational Populations in the SiF $B^2\Sigma^+$ State

The collisionally transferred SiF $B^2\Sigma^+$ vibrational populations were shown (see figure 4–14 and table 4–3) to correlate reasonably well with the Franck-Condon overlap between the initial and product vibronic states. The transfer propensities are therefore largely independent of the identity of the quencher, although the small differences observed were found to be reproducible. In each case the wave-function overlap was matched best by the H_2 results and worst by the N_2 results. Vibronic transfer to the $B^2\Sigma^+$ state is therefore accompanied by the removal of an average of $\sim$ 5000 cm^{-1} to other degrees of freedom. Consequently, it was possible to propose a qualitative model to justify this large energy loss which will be discussed in section 6.4.

6.3.3 Comparison of the Vibrational Populations with Existing Energy Transfer Models

The exponential energy gap model proposed as a general description for electronic energy transfer [33,34] (as discussed in section 1.1.1) does not successfully predict the vibronic transfer channels for either the SiF or SiCl systems. In SiCl, for many of the collider specific distributions, the isoenergetic channel was not the most (and in some cases was the least!) favoured. It is apparent that any model which does not take into account the properties of the collision partner will not have universal success. SiF $C^2\Delta$ to $B^2\Sigma^+$ transfer *completely contradicts* the energy gap model as no transfer was observed over the near-isoenergetic channels. The model proposed by Katayama [35] in which the relative transfer cross section should be proportional to a function of the energy gap and the Franck-Condon overlap is also similarly not applicable to the SiCl transfer system. The SiF results have shown that the Franck-Condon overlap *is* a factor in specific cases.

The 'cascade' mechanism for electronic quenching as promoted by Bondybey *et al* [37,38,39] where a sequence of single-collision transfers only occur via adjacent vibronic levels has also clearly been shown, for similar reasons, to be far from a universally successful model. This model also involves (at least) *two* sequential

collision transfers: however, for the SiF and SiCl cases only the *first step* of a 'cascade' could be observed because of the very short $B^2\Sigma^+$ states lifetimes. There are two pieces of direct evidence for this:-

- Laser excitation of the $B^2\Sigma^+$, v' levels resulted in emission from *only* that initially populated vibronic level.

- Following excitation of $^2\Delta$, $v' = 1$ levels, no emission was observed from $^2\Delta$,$v' = 0$ (which would be the 'cascade' $^2\Delta - ^2\Sigma^+ - ^2\Delta$ product).

The 'gateway' model proposed by Gelbert and Freed [40] (as discussed in section 1.1.2) is obviously not applicable to the SiCl and SiF $^2\Delta$ to $B^2\Sigma^+$ transfer systems as first order perturbation is forbidden because of the $\Delta\Lambda = 0, \pm 1$ selection rule [41]. In any case, there was no experimental evidence for the preferred removal or production of a few selective $^2\Delta$ or $^2\Sigma^+$ state rovibronic levels, respectively. Previous experimental studies of other CIEET processes have also indicated that this model is only applicable to a very small subset of transfer systems, for example, CO^+, $A^2\Pi$ to $X^2\Sigma^+$ [42] and CN $B^2\Sigma^+$ to $A^2\Pi$ [43].

6.4 Proposed Mechanism for SiCl and SiF $B', C^2\Delta - B^2\Sigma^+$ Collision-induced Transfer

In this section a simple qualitative model is proposed to account for transfer across the relatively large *vibronic* energy gaps and for the distinct propensities for specific channels observed for the SiCl and SiF $B', C^2\Delta$ to $B^2\Sigma^+$ processes. We believe that the radically different results obtained from the SiCl and SiF studies can be partially explained by the electronic character of the respective states and by the contrasting nature of the relative interatomic potentials.

The SiCl and SiF $B', C^2\Delta$ states are thought to be predominantly excited valence states [1,44] whereas the $B^2\Sigma^+$ states are attributed to have a large degree of Rydberg character [22,45] (as discussed in section 3.8). Thus because the $B^2\Sigma^+$

states have an electron which is essentially occupying an orbital of a higher principle quantum number it might be expected that their electron density occupies a greater volume than that of the $^2\Delta$ valence states.

The 'size' of the valence molecular orbitals can be estimated using Slater's rules [46]. The atomic radius, ρ, is equal to the distance from the nucleus where there is a maximum in the radial probability density associated with the outermost electron. The approximate value for the radius of an atomic orbital in a many electron atom is given by

$$\rho = n^2 a_0 / Z^* \quad . \tag{6.2}$$

n is the principle quantum number of the highest occupied atomic orbital, a_0 is the Bohr radius ($\sim$ 52.9 pm) and Z^* is the *effective* nuclear charge. Z^* will be smaller than the *real* nuclear charge, Z, due to the screening effect of the inner electrons. The effective nuclear charge is given by

$$Z^* = Z - \sigma \tag{6.3}$$

where σ is the screening constant which represents the mean repulsive effect of the inner electrons. The rules for estimating the effective charge are summarised in reference [46]. For an electron in the Si $3p$ atomic orbital (equivalent to the SiF 3π and SiCl 7π orbitals) the screening constant was calculated to be 9.85 which results in an effective charge of 4.15 and hence an atomic radius of 115 pm. This can be taken as a rough measure of the size of the valence SiF 3π and SiCl 7π molecular orbitals.

The atomic radius of the Rydberg SiF $4s$ orbital can be calculated from the *effective* principle quantum number, n^*, of the $B^2\Sigma^+$ state [24]. The value of n^* is given by [24]

$$n^* = n - \delta \tag{6.4}$$

where n is the 'real' principle quantum number of the orbital and δ is the quantum defect. An estimate of δ can be obtained from the electronic energy of the Rydberg state, E_R, and that of the ion to which the Rydberg series converges , E_{ion}. The relationship is given by

$$E_R = E_{ion} - \frac{\Re}{(n-\delta)^2} \tag{6.5}$$

where $\Re$ is the Rydberg constant (109,737.318 cm^{-1}). The Rydberg Bohr radius is given by [25]

$$\rho = a_0 n^* \quad . \tag{6.6}$$

Hence, the radius of the SiF ($\delta = 1.88$ [23]) and SiCl ($\delta = 1.715$ [22] $4s$ orbitals can be shown to be approximately 239 pm and 276 pm, respectively, more than a factor of two larger than the pure Si $3p$ orbital.

The simple model of the transfer process was developed by first considering only the pure electronic energies of the states with respect to the SiX - quencher separation. Due to the dispersive forces caused by the induced dipole interactions, etc., there will be an initial attraction between the quencher and the SiX $^2\Delta$ state molecule at long range. With the approach of the collision partner towards the $^2\Delta$ state molecule, the electronic repulsions due to overlap of the outer filled orbitals will begin to dominate the interaction. By analogy with the quenching of excited atomic states (discussed previously in section 1.2.2) the collision-induced transfer between the $^2\Delta$ states and the $B^2\Sigma^+$ states is most likely to occur in the region of a curve crossing between the two SiX/quencher diabatic potentials. This crossing is possible because the net repulsive interaction between the physically larger Rydberg $B^2\Sigma^+$ state will be much greater at a given range than that of the relevant $^2\Delta$ valence state. The phenomenon of the strong blue shift of the lower-lying Rydberg states relative to valence states is well known from spectroscopic studies of simple molecules in low temperature condensed phases [47,48,49]. For higher Rydbergs the interaction can become attractive because the quencher is bound within the average radius of the outermost electron and hence is effectively complexed with the molecular ion. This is illustrated by the increasing spectral red-shift with principle quantum number of the gerade Rydberg states of I_2-Ar observed between 53,000 cm^{-1} and 69,000 cm^{-1} relative to the free I_2 molecule [50].

The one-dimensional crossing of the *diabatic* curves is demonstrated qualitatively in figure 6–4. As discussed previously in section 6.3.3, interaction between pure $^2\Delta$ and $^2\Sigma^+$ states is 'forbidden'. However, the cylindrical symmetry of the

$^2\Delta$ ($C_{\infty v}$) will reduced to a pair of A' and A'' (C_s) surfaces by the presence of the collision partner. These surfaces will be split energetically. The A' surface can couple to the $A'(C_s)$ surface arising from the $^2\Sigma^+$ state on approach of the quencher, as discussed in section 1.2.4. In the adiabatic scheme this will result in an avoided crossing of the of the two A' surfaces. Thus if the collision partner induces the electronic transition it would be expected that the SiX-Q species would be transferred onto the repulsive Rydberg A' surface. Using the primitive 1-dimensional picture described above, the strong Rydberg SiX-Q repulsion will go into relative translation of the collision partners.

Obviously the model just described is an over simplification of the actual transfer process as it fails to consider the motion in the Si-X coordinate on approach of the quencher, and variations in the angular coordinate. These aspects are now considered more carefully in turn for each of the SiX systems.

6.4.1 SiF $C^2\Delta$ to $B^2\Sigma^+$ Transfer

In the SiF case it is apparent upon inspection of figure 4–2 that the $C^2\Delta$ state potential is 'nested' inside the $B^2\Sigma^+$ state in the isolated molecule. For transfer to occur, the quencher must sufficiently repel the $B^2\Sigma^+$ state to induce a classical potential crossing. Furthermore, for the successful quenchers, this intersection must happen at a point where the $C^2\Delta$ - quencher interaction is not substantially repulsive. Otherwise, the crossing point will not be reached during the course of a collision because the reagents will have only ambient thermal kinetic energies.

The explanation for the failure of Ar, He and CO_2 to promote transfer from the SiF $C^2\Delta$ to $B^2\Sigma^+$ states could be that these species are unable to induce the relative potential surfaces to intersect within a region accessible at thermal energies. Another possible reason may be that these species do not induce a sufficiently strong coupling between the two states even in the vicinity of such a crossing.

For the SiF product vibrational populations to be truly correlated with the

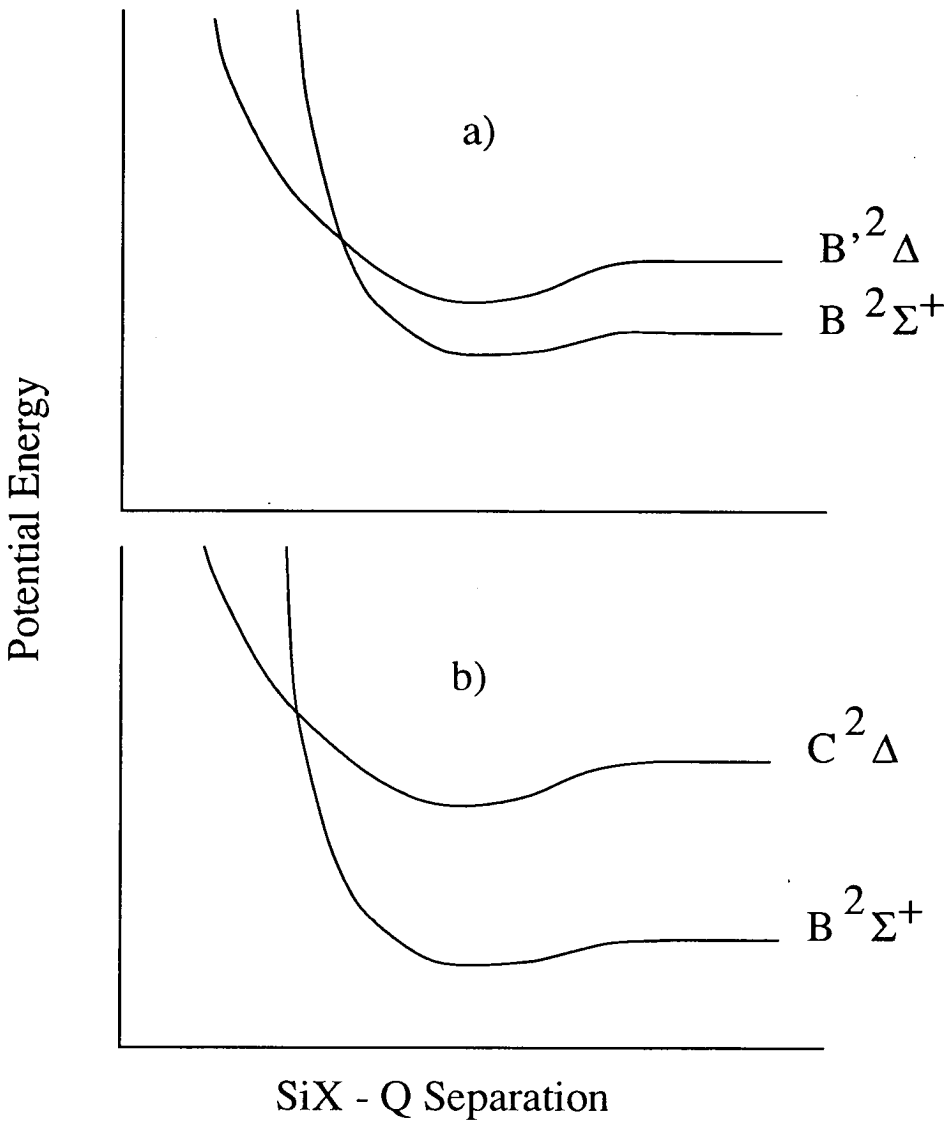

Figure 6–4: Schematic representation of the diabatic potential surfaces for the SiX-quencher $C, B'^2\Delta$ and $B^2\Sigma^+$ states.

a) SiCl

b) SiF

Franck-Condon overlap between the $C^2\Delta$ and $B^2\Sigma^+$ states the following conditions must hold:

- The transfer event must be very 'sudden' such that the Born-Oppenheimer approximation will hold [41];
- The transfer probability must be otherwise unaffected by the Si - F coordinate;
- The potential crossing must occur at a point where the Si - F motion has not been significantly affected by the quencher relative to that in the isolated molecule.

The disparity in the electronic energies of the states ($\sim$5000 cm^{-1}) requires that, at the crossing point of the valence/Rydberg surfaces, the $B^2\Sigma^+$-quencher interaction will be substantially repulsive as already indicated in figure 6–4. Thus the electronic transition will occur only at an essentially localised SiF-Q distance over all relevant Si-F separations. The factors which will govern the transition probabilities are:

- the strength of the quencher-induced coupling between the surfaces;
- the time spent in the region of the crossing (proportional to the collision velocity through the crossing region);
- the difference in the gradients of the potentials at the crossing (see section 1.2.2);
- the chance of the system reaching the crossing point with a thermal velocity.

The perturbation induced by the quencher will likely be a function of the SiF - quencher separation. However, because the point at which the potentials cross is over a very limited region in the SiF-Q coordinate, the perturbation will probably not differ much for coupling between the $C^2\Delta$ and $B^2\Sigma^+$ levels. The probabilities

of the system reaching the crossing point for the three vibronic channels will not be equal.

Obviously, a smaller SiF-quencher interaction is required to induce a crossing between, for example, the $C^2\Delta$, $v' = 0$ level and the $B^2\Sigma^+$,$v' = 2$ than for example $B^2\Sigma^+$,$v' = 0$. This might explain why this channel is more strongly preferred, for all quenchers, relative to the Franck-Condon factor as there will be more collisions which reach this point.

It is therefore difficult to see how the Si-F separation might otherwise affect the transfer event. The better correlation of the H_2 data with the Franck-Condon overlap is perhaps also consistent with transfer to this steeply repulsive surface as the lighter H_2 molecule can be repelled more quickly away from the crossing point than the other quencher species.

The studies of the collision-induced NH $a^1\Delta$ to $X^3\Sigma^-$ transfer [36,52,53] have shown a similar propensity for vibronic transfer over large energy gaps. Quenching of NH $a^1\Delta$, $v' = 0$ by Xe has been shown to result in population of only $v = 0$ in the $X^3\Sigma^-$ state. The two states have a very similar equilibrium separation and therefore this process is equivalent to transfer between levels with the optimum wavefunction overlap. The relative state potentials have a similar 'nested' arrangement to that of the SiF case though *both* NH states have essentially valence character [54]. The valence-Rydberg argument proposed for the SiF transfer process cannot therefore be invoked as justification for the large electronic energy loss of the NH to other degrees of freedom. However, the authors of the NH $a^1\Delta$ to $X^3\Sigma^-$ study also failed to advance a mechanism to account for the removal of the excess energy in this process [36,52,53].

The SiF $B^2\Sigma^+$ products were shown to be significantly rotationally hotter than the initial $C^2\Delta$ state molecules (see section 5.3 and figure 5–12). The highest rotational levels observed in the $C^2\Delta$ state following excitation of the Q_1 and P_1 band heads of the $C^2\Delta - X^2\Pi$, (0,0) transition were estimated to be 30.5 and 40.5, respectively. The highest J's observed upon collision-induced transfer to the $B^2\Sigma^+$ state could only be reasonably well defined for Q_1 excitation, where J_{max} was $\sim$ 70.5 for H_2 and 80.5 for N_2. Therefore, the largest changes in J for the quenchers

H_2 and N_2, which could unambiguously be assigned, were equivalent to at least an increase in 40 and 50 quanta or, in energetic terms, $\sim$ 2400 cm^{-1} and 3300 cm^{-1}, respectively. This observation of large changes in J upon electronic transfer was very surprising. Previous studies of other transfer systems, most notably the double resonance investigations of CN [4,5,6,7], N_2^+ [8,9,10,11,12,13] and CO^+ [42] have generally shown a strong propensity for the conservation of J.

Let us consider first the apparent consequences of the simplest kinematic model of a collinear repulsion between SiF and the quencher of mass m_{SiF} and m_Q, respectively. Due to the conservation of momentum, the velocity of the quencher, v_Q, in terms of the velocity of the SiF, v_{SiF}, will be

$$v_Q = v_{SiF} m_{SiF}/m_Q \quad , \tag{6.7}$$

where in this case it is assumed that all recoil energy has gone into relative translation. The total electronic energy removed from the SiF molecule ($\sim$ 5000 cm^{-1}) will be equal to the kinetic energy, E_{kin}, gained by the system where

$$E_{kin} = \frac{1}{2} m_Q v_Q^2 + \frac{1}{2} m_{SiF} v_{SiF}^2 \quad . \tag{6.8}$$

If the quencher is H_2, the SiF fragment would only receive approximately 200 cm $^{-1}$ ($\sim$ 4%) of the excess energy whereas in the N_2 case this would by roughly 1850 cm^{-1} ($\sim$ 37%).

This result may seem to suggest an intuitive contradiction between the large δj's for H_2 and the repulsive prediction. Even if the H_2 is assumed to interact locally with the F end of the SiF (because it is the best case), through a strongly bent geometry, then the fractions of energy carried away by the H_2 are only slightly less (*i.e.* $m_{H_2}/m_{SiF} \sim 0.4\ m_{H_2}/m_F$) than for collinear geometry.

Therefore we need to explore this more thoroughly by treating the collision as interaction of a point mass (or 'hard-sphere') quencher with a 'hard-shape' (non-spherical) SiF molecule before considering;

- the initial rotational motion of the SiF,
- initial relative velocity of the collision,

- release of the electronic potential energy as additional impulsive recoil.

In the simple case of a classical 'hard-shaped' inelastic collision (the intermolecular repulsive barrier is assumed to be infinitely steep), where *no* energy is released, the maximum rotational energy transfer will result when there is back scattering following impact. The torque that is applied to the rotator is proportional to the effective impact parameter, b. This can be found by extrapolating the line of force at the point of impact (perpendicular to the potential contour) to find the shortest distance from this line to the centre of mass (see figure 4.1 in reference [55]). Obviously the maximum torque applied to the system will occur when b is at its largest value ($= b_{max}$).The resultant change in the rotational angular momentum of the rotator can be derived from the conservation of the total angular momentum [55]

$$b_{max}(p_i + p_f) = \hbar(j_f - j_i) \tag{6.9}$$

and the conservation of energy

$$\frac{p_i^2 - p_f^2}{2\mu} = \frac{\hbar^2(j_f^2 - j_i^2)}{2I} \tag{6.10}$$

where p_i and p_f are the initial and final values of the relative momentum in the direction of the initial trajectory, j_i and j_f are the corresponding rotational angular momentum quantum numbers, μ is the reduced mass of the collision pair and I is the moment of inertia of the rotator. By eliminating p_f, it can be shown that the maximum change in j ($=\delta j_{max}$) as a result of a *single* collision will be

$$\delta j_{max} = \frac{2b_{max}}{\hbar}\left(p_i - \frac{\hbar j_i \mu b_{max}}{I}\right)(1+\eta)^{-1} \tag{6.11}$$

where

$$\eta = \frac{\mu b_{max}^2}{I} \tag{6.12}$$

The maximum δj for an SiF quencher collision can be calculated if b_{max} is known. For there to be a hard sphere collision, the upper limit of the maximum impact parameter is unlikely to greatly exceed the bond length of the SiF molecule ($\sim 1.6\mathring{A}$). Explicitly continuing to ignore for the moment the electronic energy

released in the 'real' process, assuming this value for b_{max}, δj_{max} can be calculated for any j_i at any collision velocity. Figure 6–5 shows plots of δj_{max} against j_i for the simple SiF - H_2 hard-shape collision over a range of collision velocities which were taken as one, two and three times that of the average relative velocity, $\overline{v}$, where [56]

$$\overline{v} = \sqrt{(8kT/\pi\mu)} \quad . \tag{6.13}$$

Perhaps not surprisingly, it can be seen from figure 6–5 that δj_{max} increases with the velocity of the collision. However, there is a significant reduction with increasing j_i. Physically, this is due to the increasing radial velocity of the rotator which is therefore moving away more rapidly from the quencher at the point of impact and hence the relative force of the impact is reduced. It has therefore been demonstrated that significant increases in the rotational quantum number can result purely from impulsive conversion of initial orbital angular momentum to final rotational angular momentum. Nevertheless, it would require very high velocity collisions, in the tail of the Boltzmann distribution and a very generous b_{max} to explain the SiF-H_2 results on this basis alone.

However, the approach described above is obviously an over simplification as it ignores the electronic energy release following the transfer event. As discussed above, the SiF $B^2\Sigma^+$ product state vibronic populations indicated that the transfer event was very 'sudden'. Hence, it is reasonable that the transfer event can be modeled as an impulsive process. Therefore the maximum δj for the SiF-quencher collision can again be calculated if b_{max} is known. Obviously without detailed calculation of the intermolecular potentials it is impossible to evaluate b_{max} accurately although the cross section for specific $C^2\Delta$ to $B^2\Sigma^+$ transfer process implies an impact parameter of approximately $\sqrt{(\sigma_{C\rightarrow B}/\pi)} \sim 1.4\mathring{A}$, reasonably consistent with the SiF bond length. In the real event the hard potentials cannot be spherical as the extrapolated line of force would always result in no torque for any collision.

To account for this *extra* energy, ΔE, equation 6.10 has to be modified to

$$\frac{p_i^2 - p_f^2}{2\mu} = \frac{\hbar^2(j_f^2 - j_i^2)}{2I} - \Delta E \quad . \tag{6.14}$$

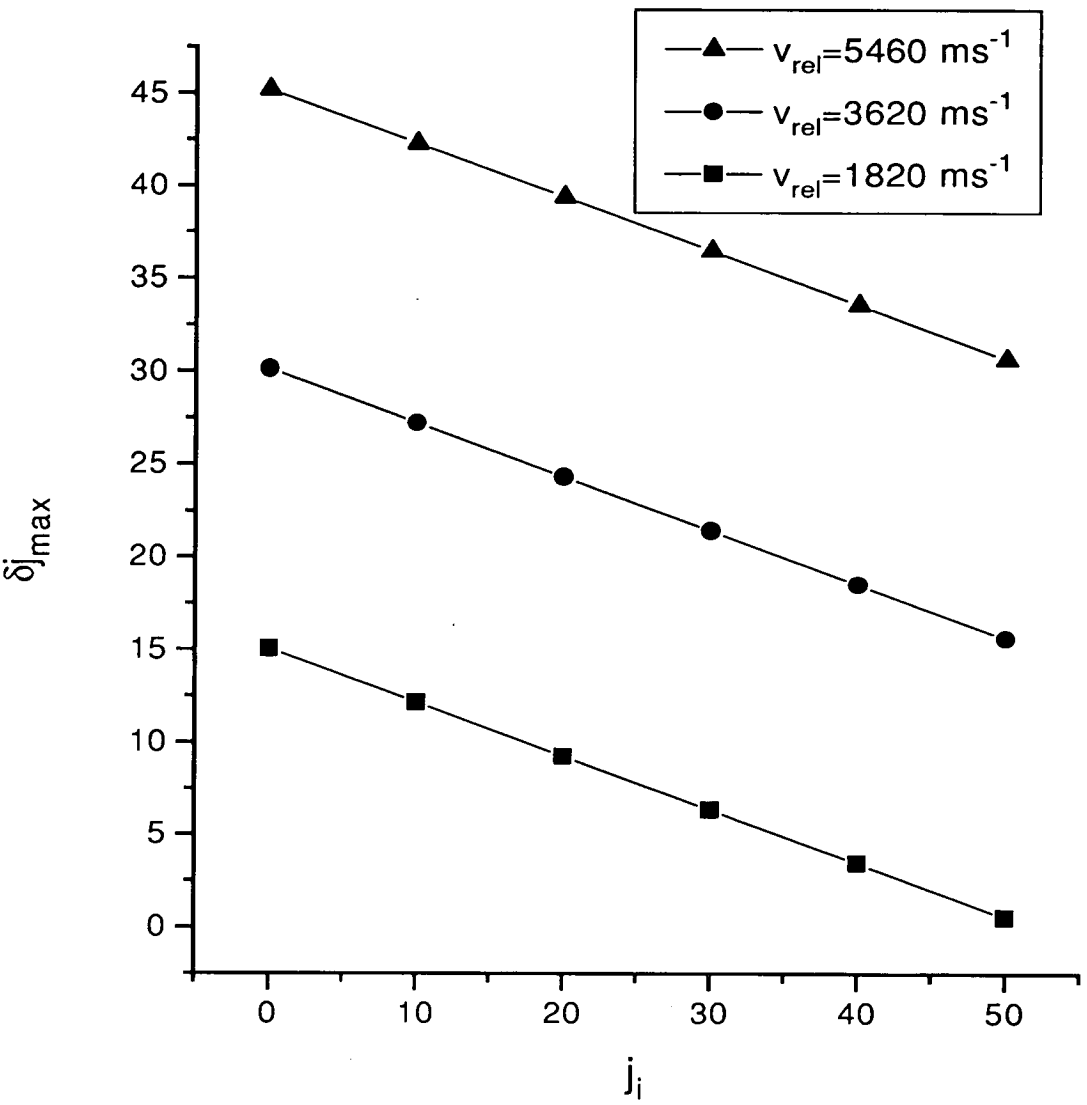

Figure 6–5: Plots of the maximum change in the rotational quantum number in SiF for 'hard shape' SiF and 'hard sphere' H_2 collisions as a function of the initial rotational quantum number assuming *no* electronic energy release.
Impact parameter, b_{max}, = 1.6 $\AA$. Collision velocities as indicated on the plot, which represents integar multiples of the average thermal relative velocities (1820 cm^{-1}).

It can therefore be shown, again by eliminating p_f, that the maximum change in j in this case is given by the relationship

$$\delta j_{max} = \frac{b_{max}}{\hbar(1+\eta)} \left\{ p_i - \frac{\hbar\mu b_{max} j_i}{I} + \sqrt{\left(p_i - \frac{\hbar\mu b_{max} j_i}{I} \right)^2 + 2\mu\Delta E(1+\eta)} \right\} . \tag{6.15}$$

If ΔE is taken as the pure vibronic energy loss following $C^2\Delta$ to $B^2\Sigma^+$ transfer then δj_{max} can again be calculated for any collision velocity and any impact parameter. The effect upon J_{max} of varying b_{max} with a constant collision velocity is illustrated in figure 6–6. Predictably δj_{max} increases with b due to the increase in the applied torque. For similar reasons to the case shown in figure 6–5, δj_{max} decreases with increasing j_i. However, this effect becomes more significant for the larger impact parameters due to the increasing tangential velocity of the rotator. The *relative* decline in δj_{max} with j_i is also significantly less than when ΔE is not taken into consideration.

Although δj_{max} has been shown to decrease moderately with j_i the proportion of energy transferred to rotational *energy* gets significantly larger with the initial rotational quantum number, accompanied by a corresponding reduction in the relative translational energy of the products. This point is illustrated graphically in figure 6–7. This kinematic effect is because, to a first approximation, the orbital and tangential *velocities* are additive, which is non-linear in the energy. The figure also demonstrates, as a check on the calculations, the essential conservation of energy following the transfer event. The sum of the final translational (T_f) and rotational (R_f) energy is shown to be indeed equal to the sum of the initial translational/rotational energy (T_i and R_I, respectively) and the energy release, (ΔE).

Finally, the effect upon δj_{max} of different collision velocities with a fixed impact parameter is shown in figures 6–8 and 6–9 where b_{max} is 0.8 $\mathring{A}$ and 1.6 $\mathring{A}$, respectively. Again it can be seen that there is a considerable change in j , even when the collision velocity approaches zero.

The best defined δj_{max} propensities for collision-induced electronic energy transfer observed experimentally were those following excitation of the $C^2\Delta - X^2\Pi$, Q_1

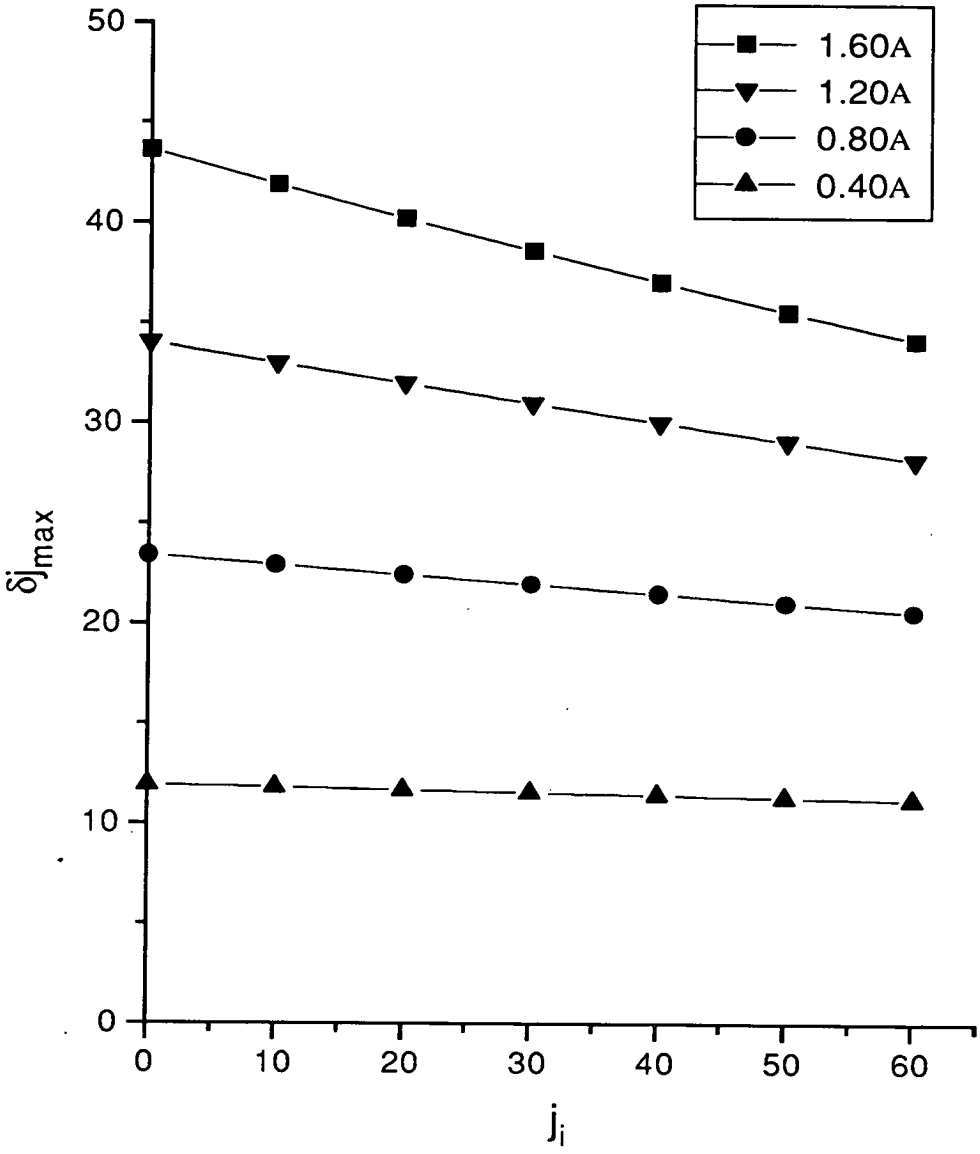

Figure 6–6: Plots of the maximum δj as a function of the initial rotational quantum number following the collision of SiF and H_2 in an impulsive 'hard-shape' - 'hard-sphere' model. There is an assumed additional energy release of 4816 cm^{-1}, at constant collision velocity for different impact parameters.
Collision velocity is the thermal average (1820 ms^{-1}) in all cases. Impact parameters as indicated on the plot.

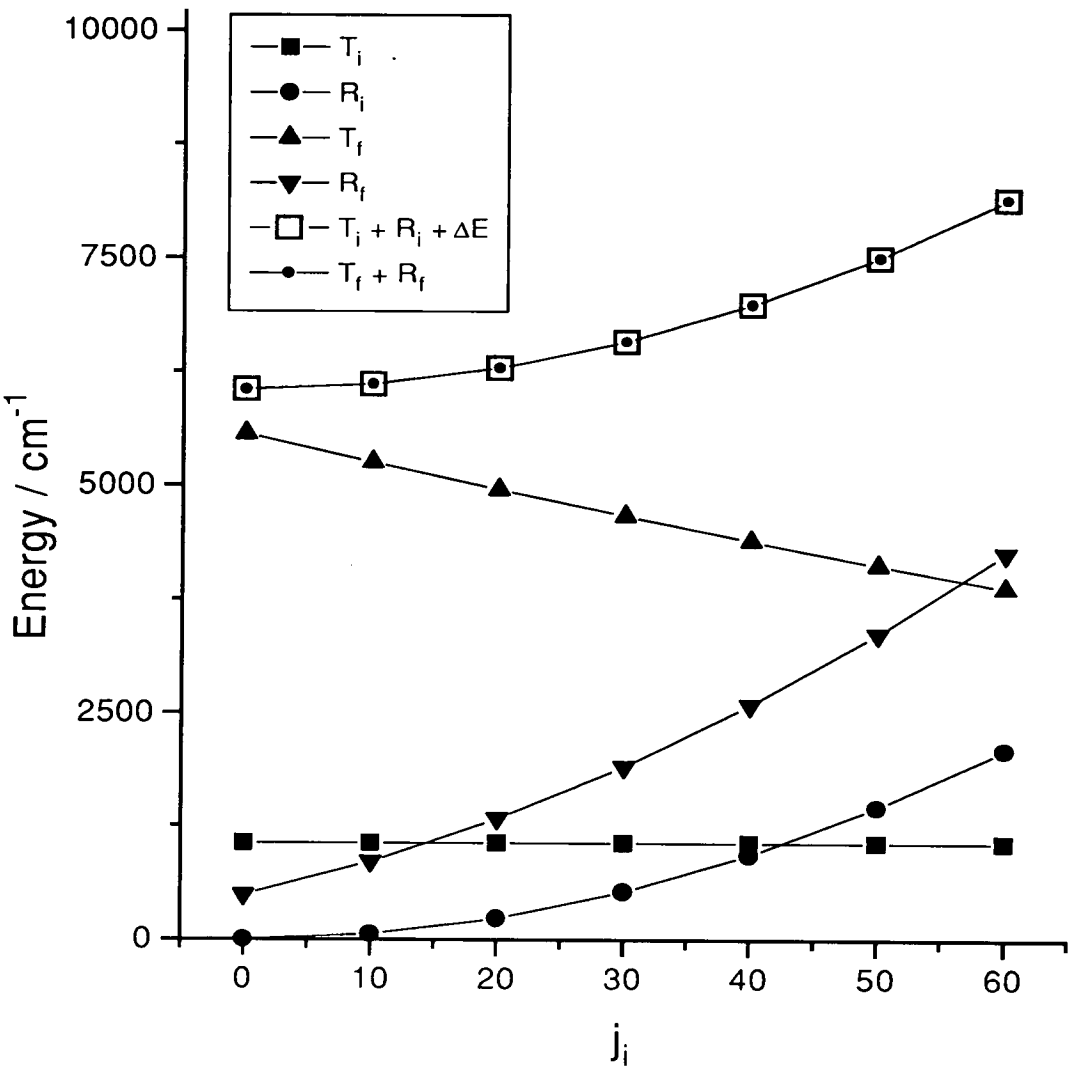

Figure 6–7: Plot of the rotational and translational energy of the SiF - H_2 system before and after a 'hard-shape' - 'hard-sphere' collision accompanied by the additional release of 4816 cm^{-1} energy.

The plot illustrates initial, T_i, R_i, and final T_f, R_f, translational and rotational energy, respectively, the sum of the total initial energy and the energy release, ΔE and the total final energy of the system (as indicated on the plot).

$b_{max} = 0.8$ Å

Collision velocity = 3640 ms $^{-1}$ ($\sim$ twice the mean collision velocity).

transition. In section 5.3 it was observed that the maximum populated j's in the initial and final $C^2\Delta$ and $B^2\Sigma^+$ states were approximately 30.5 and 70.5, respectively. Therefore to populate the maximum j observed in the $C^2\Delta$ state, δj_{max} must be ~ 40 when $j_i = 30.5$. Figure 6–8 shows that a δj of 40 cannot be achieved at any reasonable thermal collision velocity using the model described above if $b_{max} = 0.8\mathring{A}$. However, in figure 6–9, where $b_{max} = 1.6\mathring{A}$, it can be seen that δj_{max} is approximately 40 for the mean collision velocity and significantly greater for collision velocities equal to two and three times this value. Obviously this b_{max} value of 1.6 $\mathring{A}$ may well be a generous estimate of the true maximum impact parameter. The point where maximum torque can be applied to the rotator will probably be adjacent to the fluorine atom, perpendicular to the SiF bond. This impact parameter would therefore be approximately 1 $\mathring{A}$, significantly less than 1.6 $\mathring{A}$. Nevertheless, it is clear that a δj_{max} of 40 is readily accessible with a lower b_{max} within ambient thermal collision velocities. It is worth remembering that the maximum observed δj's are subject to considerable uncertainty and that they occur in only a tiny minority of collisional transfer events. Indeed the average δj's were estimated to be approximately 15 quanta for H_2, as discussed in section 5.3. Therefore it is reasonable to suggest that this model can explain the experimental results if the 'true' maximum impact parameter lies somewhere between 0.8 $\mathring{A}$ and 1.6 $\mathring{A}$ and that the maximum δj observed occurs in a collision with greater than mean collision velocity.

As previously mentioned the N_2 quencher produced rotationally hotter distributions in the $B^2\Sigma^+$ state than H_2. It was shown in section 5.3 that the minimum δj required to populate the highest j in the $B^2\Sigma^+$ state, inferred from the spectra recorded following excitation of the $C^2\Delta - B^2\Sigma^+$, Q_1 band head, was approximately 50. The maximum δj's when the quencher is N_2 were therefore calculated in the same way as for H_2. The cross section for $C^2\Delta$ to $B^2\Sigma^+$ collision-induced transfer was considerably smaller for N_2 than the equivalent value for H_2. Therefore the impact parameter was taken to be 0.6 $\mathring{A}$ $(= \sqrt{(\sigma_{C\rightarrow B}/\pi)})$. The collision velocities were equal to zero, one, two and three times the mean collision velocity. The calculated values are shown graphically in figure 6–10. It can be seen

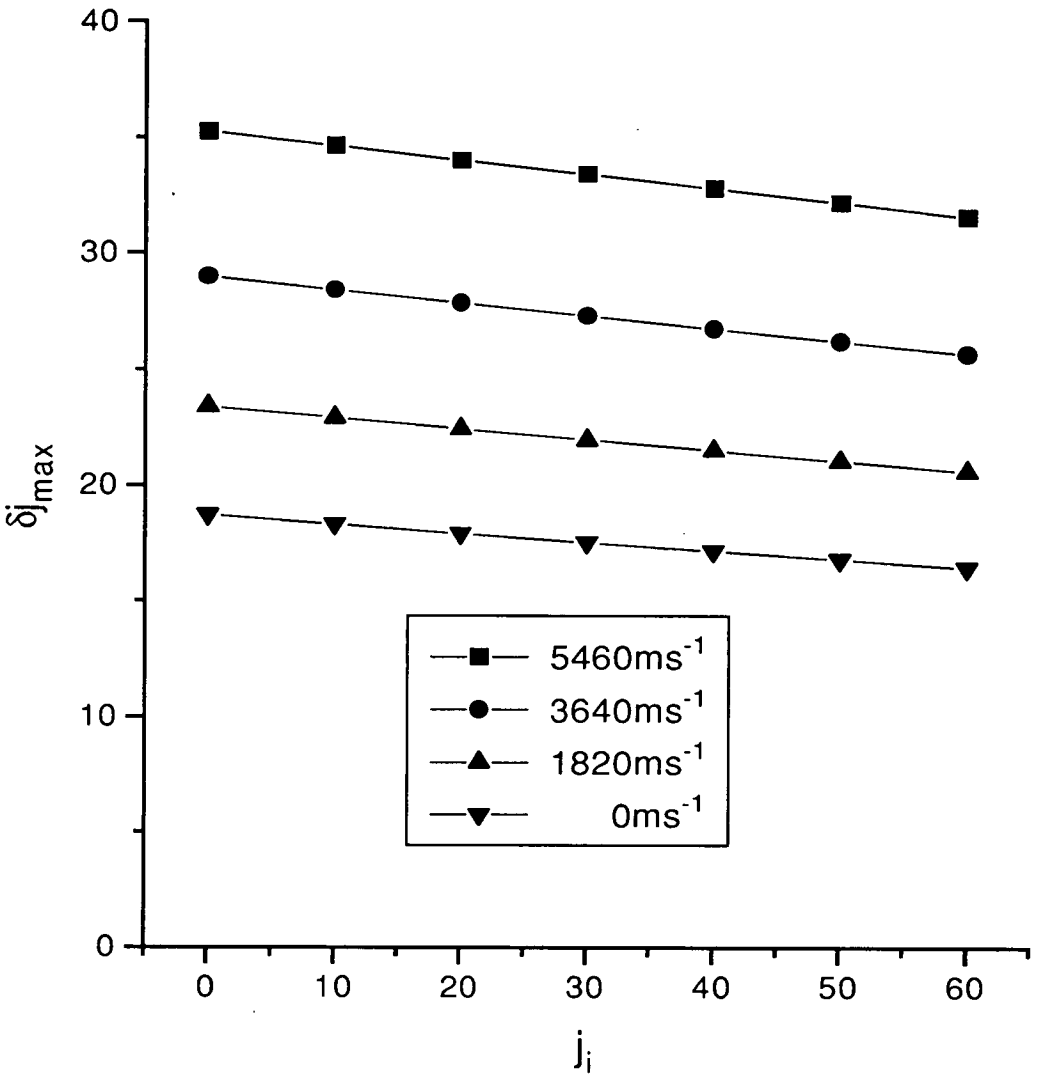

Figure 6–8: Plots of the maximum δj as a function of the initial rotational quantum number following the collision of SiF and H_2 in an impulsive 'hard-shape' - 'hard-sphere' model, where there is an energy release of 4816 cm^{-1}, at constant impact parameter for different collision velocities.

Impact parameter 0.8 $\AA$. Collision velocities as indicated on the plot.

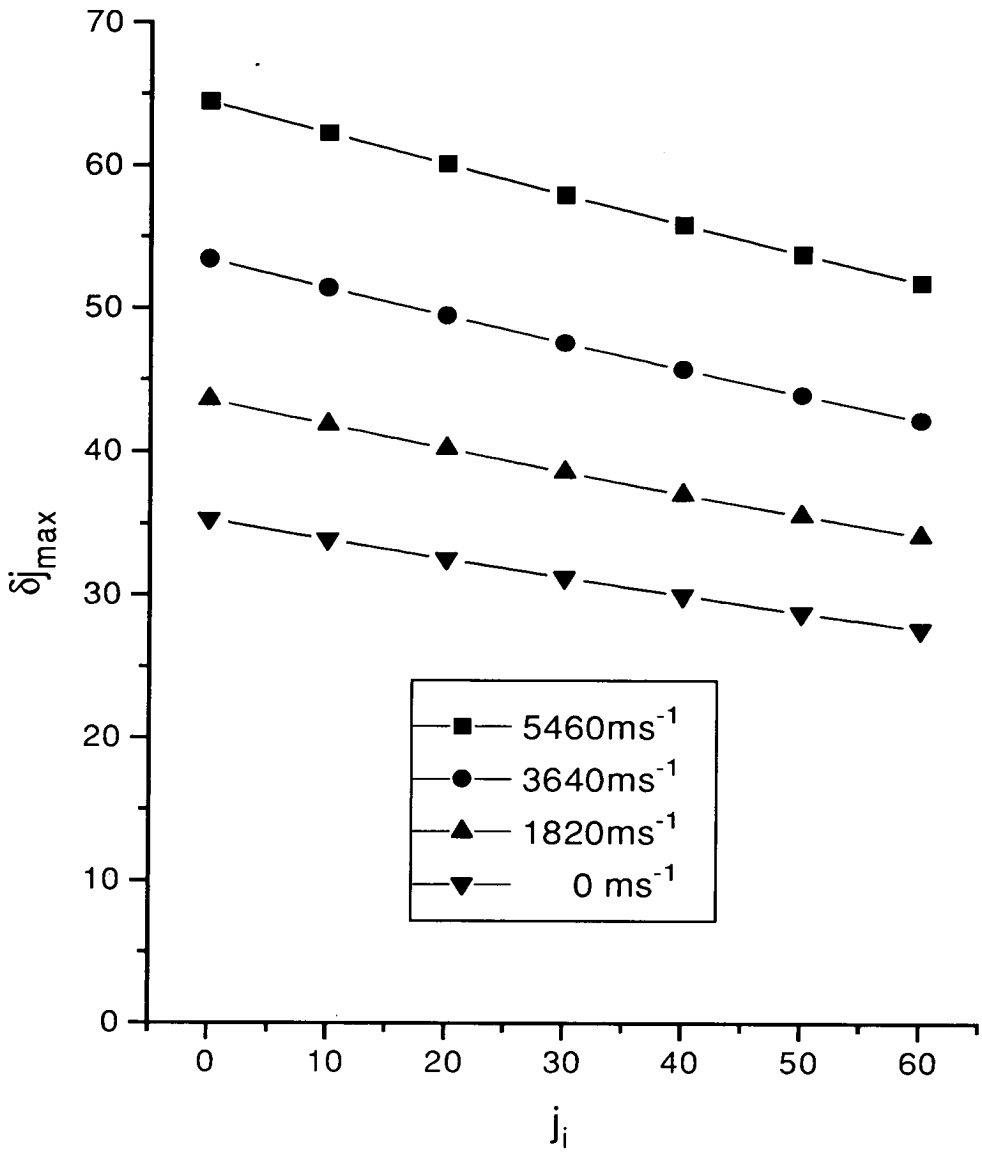

Figure 6–9: Plots of the maximum δj as a function of the initial rotational quantum number following the collision of SiF and H_2 in an impulsive 'hard-shape' - 'hard-sphere' model, where there is an energy release of 4816 cm^{-1}, at constant impact parameter for different collision velocities.

Impact parameter 1.6 $\AA$. Collision velocities as indicated on the plot.

that even at this considerably smaller b_{max} value, δj's larger than 50 are possible for collision velocities not much greater than their mean value. There is obviously no equivalent kinematic problem, as encountered with SiF-H_2, because of the similarity of the N_2 and SiF masses.

It has therefore been demonstrated that the surprisingly large δj's observed following collision-induced SiF $C^2\Delta$ to $B^2\Sigma^+$ transfer with the collision partners H_2 and N_2 can be justified with respect to the conservation of energy and angular momentum within a limiting impulsive model. The basic conclusion that can be drawn is that the SiF-quencher potential is considerably non-spherical at the SiF-Q distances of the *crossing point* at which the electronic transition is induced. Although it might be expected that a Rydberg-Q potential will be fairly spherical at longer range, this is not necessarily the case if the quencher has already penetrated close by approaching in on the valence surface.

A possible alternative to the impulse mechanism is that is that of a short-lived collisional complex where the quencher molecule is 'captured' by the SiF molecule. To account for the increase in the SiF rotational angular momentum *and* rotational energy the result of the complex must be the reduction in the quenchers translational energy upon repulsion. The fact that the vibrational populations of the $B^2\Sigma^+$ correlate with the Franck-Condon overlap indicates that the Rydberg-quencher complex must not have a strong chemical association. A strongly bound intermediate would lead to exchange of energy between the internal and relative degrees of freedom. However such an association would have to be sufficiently persistent to couple the angular momentum within the lifetime of the complex. However, there is no experimental evidence which requires the proposal of such a mechanism. Therefore, the purely repulsive mechanism seems adequate to explain all the current results.

The simplistic repulsive model could be extended by incorporating a more finite *range* for the repulsive interaction, ideally based on a proper theoretical prediction of the SiF-Q intermolecular potential. It would then be interesting to see if this could still explain the observations on a purely impulsive basis.

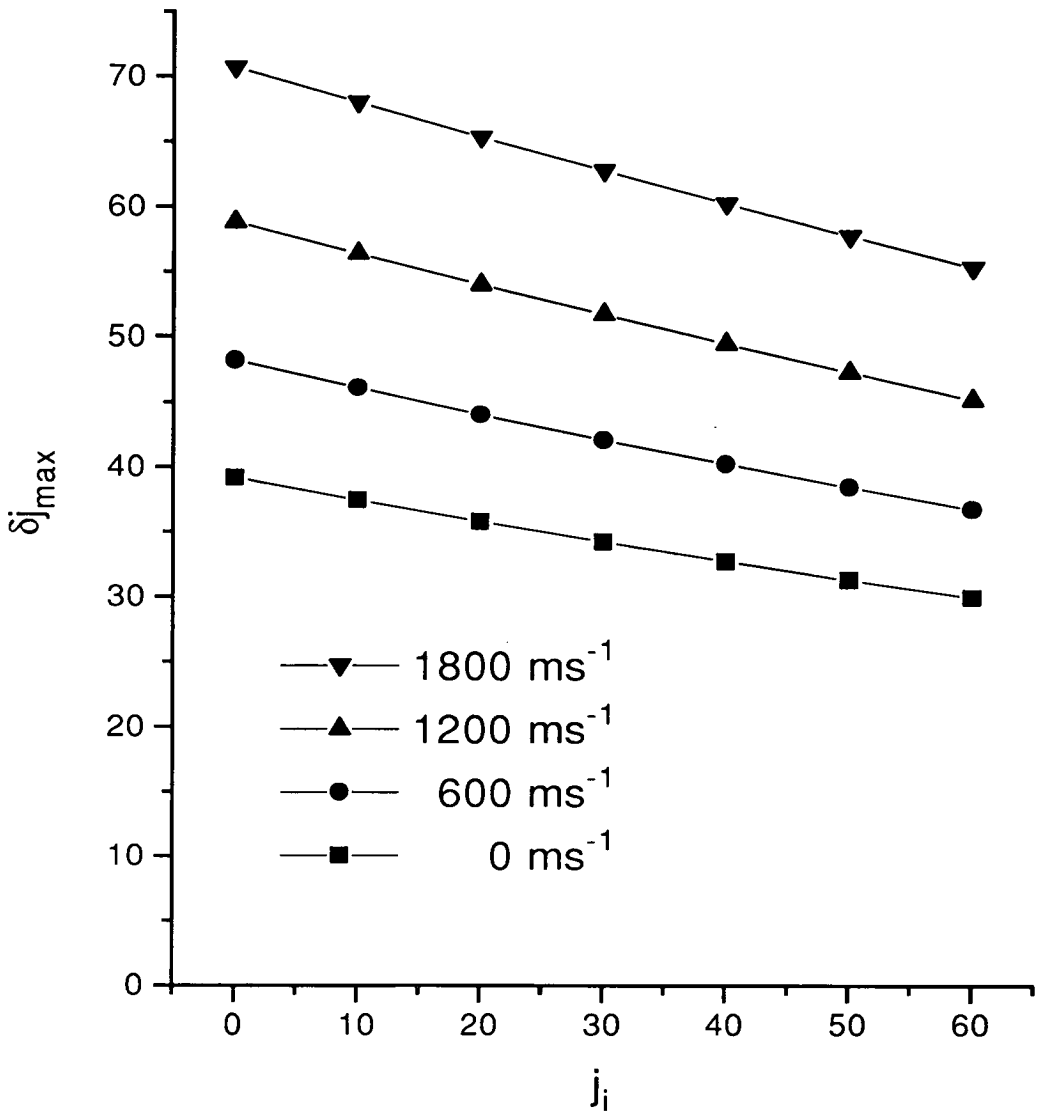

Figure 6–10: Plots of the maximum δj as a function of the initial rotational quantum number following the collision of SiF and N_2 in an impulsive 'hard-shape' - 'hard-sphere' model, where there is an energy release of 4816 cm^{-1}, at constant impact parameter for different collision velocities.

Impact parameter 0.6 $\AA$. Collision velocities as indicated on the plot.

6.4.2 SiCl $B'^2\Delta$ to $B^2\Sigma^+$ Transfer

We believe that the behaviour of the SiCl $B'^2\Delta$ to $B^2\Sigma^+$ transfer process differs so dramatically from that of the SiF analogue due to presence of the classical crossing close to the outer turning points of the near-degenerate $B'^2\Delta$, $v' = 0$ and $B^2\Sigma^+$, $v' = 2$ levels (as indicated in figure 4–1). Due to the differential attractive and repulsive forces of the SiCl $B'^2\Delta$ and $B^2\Sigma^+$ states with the collision partner, the surfaces will therefore have a very complicated seam of intersection in the SiCl - quencher coordinate. Thus it can be envisaged that transfer may be induced over a large range of intermolecular separations consistent with the large cross sections measured for $B'^2\Delta$ to $B^2\Sigma^+$ transfer. The propagation of the seam of intersection is likely to be highly dependent on the identity of the collision partner. In addition to this, the perturbation coupling the two states caused by the quencher at any specific SiCl-Q distance will also be a function of the quencher identity. It is therefore not surprising that the propensities for specific $B^2\Sigma^+$ vibrational transfer channels show so much variation for each quenching gas.

The deviation from a Franck-Condon vibrational distribution is therefore perhaps to be expected considering that transfer is more likely in the region of the classical crossing. In the SiCl case there will be a potential crossing for any quencher - SiCl distance though the surface intersection will occur only at specific Si-Cl separations and not over the entire coordinate. The perturbation induced by the collision partner which couples the states will be dependent upon the SiCl-quencher separation, thus the transfer propensities will not be solely controlled by the wavefunction overlap of the vibronic levels. The effect of this can be thought of as analogous to the fole of the electronic transition dipole moment, $R_e(r)$, in an optical transition. $R_e(r)$ is a function of the diatomic separation (as discussed in section 3.5.2), which can result in significant deviations of the vibronic transition probabilities from the Franck-Condon factors.

The possibility that SiCl transfer occurs over a long range of intermolecular separations is consistent with the high transfer cross sections obtained. The cor-

relation with the attractive nature of the interaction can also be explained by this proposal in that transfer can be induced by long-range, 'soft' collisions.

The SiCl system was not found to exhibit the same changes in rotational energy as observed for SiF [1]. There remains the possibility that this observation could be partly clouded by a greater extent of rotational thermalisation within the $B'^2\Delta$ state because of the order of magnitude longer lifetime relative to the SiF $C^2\Delta$ state. However, we believe that the observation is again consistent with the nature of the intermolecular potentials. The transfer event has been inferred to occur up to a much longer-range, relative to the SiF analogue, which would result in 'softer', less repulsive transfer collisions. Therefore, the model proposed to explain the large δj propensities observed in SiF $C^2\Delta$ to $B^2\Sigma^+$ transfer is not applicable in this case. The smaller amounts of excess electronic energy available for partition into the remaining degrees of freedom may also partially account for the differing observations.

6.5 Final Conclusions

This thesis has demonstrated the dramatically contrasting nature of SiF $C^2\Delta - B^2\Sigma^+$ and SiCl $B'^2\Delta - B^2\Sigma^+$ collision-induced energy transfer. Results were presented at the vibronic and, more qualitatively, the rovibronic level for these state-specific processes. The SiF $B^2\Sigma^+$ product state vibrational *and* rotational populations were shown to be consistent with an 'sudden' impulsive energy release mechanism. This contrasted with the cross sections for total quenching of SiCl $B'^2\Delta$ and the collision-induced $B^2\Sigma^+$ product state which indicated that a long-range attractive interaction dictated the collision outcome. It was proposed that the two main factors governing the transfer process in these cases were the valence-Rydberg character of the analogous potentials and the relative position of the interatomic potentials in the isolated molecules.

Neither of the data sets could be adequately explained by any of the existing empirical laws for energy transfer. It was therefore confirmed that the degree of

understanding of this elementary process is surprisingly poor. It is imperative that any future theoretical calculations or models take account of the identity of the collision partner and the relative positions of the interatomic potentials, the electronic configurations and the rotational and vibrational energy levels of the states involved.

It is hoped that because the transfer propensities observed in this work contrast so much with the existing body of data that they might stimulate renewed fundamental theoretical studies. Hopefully, potential surfaces similar to those developed for the CN $^2\Pi - ^2\Sigma^+$ system [57] may be eventually calculated for this $^2\Delta - ^2\Sigma^+$ process to be followed by the appropriate scattering calculations to model the experimental results.

Bibliography

[1] S. Singleton, Laser Based Studies of Transient Species in a Discharge Flow Apparatus, PhD Thesis, University of Edinburgh, (1990).

[2] S. Singleton and K.G. McKendrick, J. Phys. Chem. **97** (1993) 1389.

[3] J.B. Jeffries, J. Chem. Phys. **95** (1991) 1628.

[4] N. Furio, A. Ali and P.J. Dagdigian, Chem. Phys. Letts. **125** (1986) 561.

[5] N. Furio, A. Ali and P.J. Dagdigian, J. Chem. Phys. **85** (1986) 3860.

[6] G Jihua, A. Ali and P.J. Dagdigian, J. Chem. Phys. **85** (1986) 7098.

[7] P.J. Dagdigian, D. Patel-Misra, A. Berning, H.-J. Werner, M.H. Alexander, J. Chem. Phys. **98** (1993) 8580.

[8] D.H. Katayama, J. Chem. Phys. **81** (1984) 3495.

[9] D.H. Katayama, Phys. Rev. Letts. **54** (1985) 657.

[10] D.H. Katayama and A.V. Dentamaro, J. Chem. Phys. **85** (1986) 2595.

[11] D.H. Katayama, A.V. Dentamaro and J.A. Welsh, J. Chem. Phys. **87** (1987) 6983.

[12] D.H. Katayama and A.V. Dentamaro, J. Chem. Phys. **91** (1989) 4571.

[13] A.V. Dentamaro and D.H. Katayama, Phys. Rev. A **43** (1991) 1306.

[14] I. Wysong, J.B. Jeffries and D.R. Crosley, J. Chem. Phys. **91** (1989) 5343.

[15] H.-M. Lin, M. Seaver, K.Y. Tang, A.E.W. Knight and C.S. Parmenter, J. Chem. Phys. **70** (1979) 5442.

[16] C.R.C. Handbook of Chemistry and Physics, 70th Edition (CRC Press Inc., Florida 1989-90).

[17] K. Shibuya and F. Stuhl, Chem. Phys. **79** (1983) 367.

[18] A. Rotem, I. Nadler and S. Rosenwaks, J. Chem. Phys. **76** (1982) 2109.

[19] A. Rotem and S. Rosenwaks, Opt. Eng. **22** (1983) 564.

[20] N. Sadeghi and D.W. Setser, J. Chem. Phys. **79** (1983) 2710.

[21] J.T. Yardley, Introduction to Molecular Energy Transfer (Academic Press, New York 1980).

[22] R.D. Verma, Can. J. Phys. **42** (1964) 2345.

[23] G. Bosser, H. Bredohl and I. Dubois, J. Mol. Spec. **106** (1984) 72.

[24] H Lefebvre-Brion and R.W. Field, Perturbations in the Spectra of Diatomic Molecules (Academic Press, London, 1986) 206.

[25] L. Pauling and E.B. Wilson, Introduction to Quantum Mechanics (McGraw-Hill, New York, 1935) 144.

[26] D.H. Katayama, S. Ogawa, M. Ogawa and Y. Tanaka, J. Chem. Phys. **67** (1977) 2132.

[27] M.E. Weber and P.B. Armentrout, J. Phys. Chem. **93** (1989) 1596.

[28] R.K. Gosavi and O.P. Strauss, Chem. Phys. Letts. **131** (1986) 243.

[29] H. Bredohl, P. Demoulin, Y. Houbrechts and F. Mélen, J. Phys. B. **11** (1978) 1771.

[30] R.N. Schwartz, Z.I. Slawsky and K.F. Herzfeld, J. Chem. Phys. **20** (1952) 1591.

[31] M. Farber and R.D. Srivastava, J. Chem. Soc. Faraday Trans. I **74** (1978) 1089.

[32] F. Roher and F. Stuhl, J. Chem. Phys. **86** (1987) 226.

[33] D.H. Katayama , T.A. Miller, J. Chem. Phys. **69** (1978) 3597.

[34] D.H. Katayama and J.A. Welsh, Chem. Phys. Letts. **106** (1984) 74.

[35] A.V. Dentamaro and D.H. Katayama, J. Chem. Phys. **101** (1994)

[36] J.S. Adams and L. Pasternack, J. Phys. Chem. **95** (1991) 2975.

[37] V.E. Bondybey, J. Chem. Phys. **63** (1977) 794.

[38] V.E. Bondybey and N. Nitzen, Phys. Rev. Letts. **38** (1977) 889.

[39] H. Dubost and R. Charneau, Chem. Phys. **12** (1976) 407.

[40] W.M. Gelbert and K.F. Freed, Chem. Phys. Letts. **18** (1973) 470.

[41] G. Herzberg, Molecular Spectra and Molecular Structure I. Spectra of Diatomic Molecules 2nd Edition (Van Nostrand, New York, 1950).

[42] A.V. Dentamaro and D.H. Katayama, J. Chem. Phys. **90** (1989) 91.

[43] D.W. Pratt and H.P. Broida, J. Chem. Phys. **50** (1969) 2181.

[44] Y. Houbrechts, I. Dubois and H. Bredohl, J. Phys. B **13** (1980) 3369.

[45] S.P. Karna and F. Grein, J. Mol. Spec. **122** (1987) 28.

[46] Y. Jean and F. Volatron, An Introduction to Molecular Orbitals (Oxford University Press, New York, 1993) 54.

[47] G. Herzberg, A. Lagerqvist and E. Miescher, Can. J. Phys. **34** (1956) 622.

[48] A. Lagerqvist and E. Meischer, Helv. Phys. Acta **31** (1958) 221.

[49] A. Lagerqvist and E. Meischer, Can. J. Phys. **40** (1962) 352.

[50] M.C.R. Cockett, J.G. Goode, R.R.J. Maier, K.P.Lawley and R.J.D. Donovan, J. Chem. Phys. **101** (1994) 126.

[51] R.N. Schwartz, Z.I. Slawsky and K.F. Herzfeld, J. Chem. Phys. **20** (1952) 1591.

[52] W. Hack and K. Rathmann, J. Phys. Chem. **96** (1992) 47.

[53] D. Patel-Misra and P.J. Dagdigian, J. Chem. Phys. **97** (1992) 4871.

[54] T. Fueno, U. Bonacic-Koutecky, J. Am. Chem. Soc. **105** (1983) 5547.

[55] J.N. Murrel and S.D. Bosanac, Introduction to the Theory of Atomic and Molecular Collisions (John Wiley and Sons, West Sussex, 1989) 79.

[56] Physical Chemistry, P.W. Atkins (3rd Edition, Oxford University Press,1987).

[57] M.H. Alexander and G.C. Corey, J. Chem. Phys. **84** (1986) 100.

Appendix A

Rydberg-Klein-Rees Interatomic Potential Curves

Accurate interatomic potential energy curves are essential for the Franck-Condon factor calculations which were performed in the course of this thesis. The well known Rydberg [1] - Klein [2] - Rees [3] (RKR) procedure has proved to be a reliable method of deriving these potential functions using the experimental vibrational and rotational spectroscopic terms. The procedure, first derived by Rydberg [1], equates the classical expressions of the action integral, I, and the rotational energy, E_{rot} to calculate the potential curve.

The action integral for a rotating vibrator is given by

$$I = \int p_r dr = (2\mu)^{\frac{1}{2}} \int (U - V_{eff}(r))^{\frac{1}{2}} dr, \tag{A.1}$$

where p_r is the radial momentum, r the internuclear separation, μ the reduced mass, U the constant total energy,

$$U = p_r^2/(2\mu) + V_{eff}(r) \tag{A.2}$$

and $V_{eff}(r)$ is the effective potential energy equivalent to the sum of the actual potential $V(r)$ and the centrifugal potential. Upon quantisation, I is given by

$$I = h(v + \frac{1}{2}) = (2\mu)^{\frac{1}{2}} \int (U - V_{eff}(r))^{\frac{1}{2}} dr, \tag{A.3}$$

where h is Planck's constant and v is the vibrational quantum number.

The classical rotational energy of a vibrating rotator is

$$E_{rot} = p_\theta^2/(2\mu\tau_v)\int(1/r^2)dt = p_\theta/(2\tau_v)\int(r^2 p_r)^{-1}dr \tag{A.4}$$

where p_θ is the angular momentum and τ_v is the period of vibration. Quantisation of the angular momentum phase integral results in

$$p_\theta^2/(2\mu) = (8\pi\mu/h^2)^{-1}J(J+1) \tag{A.5}$$

where J is the rotational quantum number. Substitution in equation A.4 for p_r and p_θ leads to

$$h^2(2\mu)^{-\frac{1}{2}}(8\pi^2\tau_v)^{-1}\int(U - V_{eff}(r))^{-\frac{1}{2}}dr/r^2 = B_v \tag{A.6}$$

where B_v is the experimental spectroscopic rotational constant. Therefore, using the experimental values of U, τ_v and B_v, the form of the true potential, $V(r)$ could be adjusted to fit equations A.3 and A.6. The integrals were evaluated graphically.

This procedure was modified first by Klein [2] so that the classical turning points, r_+ and r_- , could be calculated directly using the functions f and g. where

$$r_\pm(U) = (f/g + f^2)^{\frac{1}{2}} \pm f \tag{A.7}$$

and f and g are given by

$$f(U) = \frac{h}{2\pi(2\mu)^{\frac{1}{2}}}\int_0^{I'}(U - E(I,\kappa))^{-\frac{1}{2}}dI \tag{A.8}$$

$$gU = \frac{h}{2\pi(2\mu)^{\frac{1}{2}}}\int_0^{I'}\frac{\delta E}{\delta\kappa}(U - E(I,\kappa))^{-\frac{1}{2}}dI. \tag{A.9}$$

$E(I,\kappa)$ is the sum of the rotational and vibrational energies, $I = I'$ when $E = U$ and

$$\kappa = J(J+1)h^2/8\pi^2\mu. \tag{A.10}$$

This semi-classical approach does not restrict the variable I to discrete values. Rees [3] subsequently showed that if $E(I,\kappa)$ is a quadratic function of I and κ then $f(U)$ and $g(U)$ can be expressed in a closed form. Vanderslice [4] *et al* improved this method for the rotationless state (J=0) by using a series of quadratics over

the range of the potential so that a best least-squares choice of the spectroscopic constants is used for each vibrational level.

In this thesis the RKR potentials were constructed using a program written by Lawley [5] which required the spectroscopic constants ω_e, $\omega_e x_e$ etc., B_e, α_e etc. and the atomic masses as input. The Franck-Condon calculations required the potentials to be tabulated in steps of 0.001 $\mathring{A}$.

Bibliography

[1] R. Rydberg, Ann. Physik **73** (1931) 376.

[2] O. Klein, Z. Physik **76** (1932) 226.

[3] A.L.G. Rees, Proc. Phys. Soc. (London) **A59** (1947) 998.

[4] J.T. Vanderslice, E.A. Mason, W.G. Maisch and E.R. Lippincott, J. Mol. Spec. **3** (1959) 17.

[5] K.P. Lawley (1981) 1133.

Appendix B

Publications

State-specific collisional energy transfer in electronically excited SiF radical: dramatic contrasts with SiCl, Cameron W. Watson and Kenneth G. McKendrick, Chem. Phys. **187** (1994) 79-86.

Vibrational transition probabilities in the $B - X$ and $C - X$ systems of the SiF radical, Cameron W. Watson and Kenneth G. McKendrick, Chem. Phys. **187** (1994) 87-95.

Appendix C

Courses Attended

In accordance with the regulations of the Department of Chemistry, University of Edinburgh, I attended the following lecture courses and conferences during my period of study in addition to attending all departmental seminars and research group meetings:

1. Departmental postgraduate lectures
2. Unix I computer training course
3. 'C' programming course
4. Theoretical Chemistry
5. Lasers I and II
6. Gas Kinetics Discussion Group, Manchester University, 1992.
7. 3rd Annual Informal Northern Universities Chemical Physics Meeting, Liverpool University, 1992.
8. The Twelfth International Symposium on Gas Kinetics, Reading University, 1992.
9. 4th Annual Informal Northern Universities Chemical Physics Meeting, Nottingham University, 1993.

10. Gas Kinetics Discussion Group, Nottingham University, 1993.

11. 7th European Workshop on Molecular Spectroscopy and Photon-Induced Dynamics, Maratea, Potenza,Italy, 1993.